APPLICATION OF A NUMERICAL-BASED SOIL REACTION CURVE METHOD FOR DESIGN OF LATERALLY LOADED MONOPILES

Yiling He

A thesis submitted for the degree of
Master of Science (by Research)
at the University of Oxford

St Cross College

Hilary Term 2016

ABSTRACT

Application of a numerical-based soil reaction curve method for design of laterally loaded monopiles

A thesis submitted for the degree of Master of Science (by Research)
Yiling He
St Cross College, Oxford
Hilary term, 2016

Monopiles are the major current foundation type for offshore wind turbine foundations. The geotechnical design of monopiles usually employs conventional '*p-y*' approaches, originally developed for the design of long slender piles for the oil and gas industry. It has been recognised, however, that the *p-y* approaches may not be entirely appropriate when applied to the design of monopiles for offshore wind turbines. Evidence from full scale field measurements indicates that they can underestimate the stiffness of the soil-pile response. A joint industry project – PISA (Pile Soil Analysis) was established to address these limitations and to provide improved design methods for monopiles. The new PISA methodology addresses the pile-soil interaction with a distributed lateral load and moment along the pile shaft, along with a horizontal force and moment at the pile base. Two design methods, incorporating these soil reaction curves, the rule-based method and the numerical-based method, have been proposed. The PISA project demonstrated that the two methods provided better predictions of pile response, as shown in medium scale field tests, compared to the conventional *p-y* approaches. The PISA project focused on two reference soils. Further work is needed to apply the new methods to different design scenarios and to assess their sensitivity to different constitutive models and boundary conditions.

This thesis presents a series of 3D and 1D finite element (FE) analyses to examine the applicability of the numerical-based approach, considering a wide variation of pile geometries, load eccentricities, soil profiles and layered soils. The 3D FE analyses, which were performed in Abaqus 6.13, employed elastic perfectly plastic constitutive models and considered pile-soil interaction. Load-displacement response and soil reaction components were produced by a small number of calibration analyses in homogeneous clay and sand. A systematic procedure was developed to obtain soil reaction curves from the calibration analyses. These were subsequently used for input to a 1D model. Further 3D analyses for new design scenarios were performed, and the results computed were compared with the results predicted by the calibrated 1D model. The predictability of the calibrated 1D model was comprehensively evaluated. In addition, the soil reaction curves of rigid piles in lateral translation and rotation about the pile base were analysed.

The results demonstrated that the numerical-based method and the 1D model are capable of predicting monopile lateral response in design scenarios involving variations of pile geometries and soil properties. Compared with 3D FE results, the errors of overall load-displacement response and ultimate capacity predicted by the 1D model were less than 10%. The calibrated 1D model was also applicable in layered soil cases, with the errors being less than 15%. The rigid pile analyses indicated that load eccentricity and boundary conditions have greater influences on soil reaction curves in sand than in clay. Inspection of base soil reaction components demonstrates that a coupling effect existed between base horizontal force and base moment, which should be evaluated in future monopile design methods.

ACKNOWLEDGEMENTS

The research presented in this thesis would not have been possible without the support, assistance and encouragement from various people. I first would like to express my profound gratitude to my supervisors, Prof Byron Byrne and Prof Harvey Burd, for their valuable and constructive suggestions on my research and keeping my progress on schedule. Throughout the course of this study, I have learned a great deal from their generous academic guidance, extensive geotechnical insight, and meticulous reviews of my thesis and papers. Special thanks are due to Prof Ken Gavin and Prof Tony Blakeborough, my examiners, for the enlightening discussions we had and offering me the opportunity to improve and polish my research.

I would like to acknowledge the PISA Project as a source of inspiration for this research project and the PISA Academic Work Group for allowing me to attend their meetings, from which I was able to gain many technical insights. I am particularly indebted to the assistance from those at Oxford who made available their expertise and knowledge (including the provision of the 1D FE model), including my supervisors, Dr Ross McAdam, Stephen Suryasentana and William Beuckelaers. The research has benefitted greatly from these many useful conversations, guidance and assistance.

I would like to thank Alison May, our group secretary, for her assistance and support all along. My grateful thanks also extend to the Graduate Studies committee for their guidance and help in administration, and the Abaqus Users group in the department for giving me helpful advices and resources on solving software problems.

I owe many thanks to my friends in Civil Engineering Research group and in St. Cross College, without whom my time in Oxford would not have been such an enjoyable and memorable experience. My sincerest thanks go to Dr Christelle Abadie, Wing Nam Yiu and Jianxin Hu for our friendship and being considerate and supportive throughout my study; to Helen Dunne and Dr Brian Sheil for proofreading my work and their valuable suggestions; to Yang Li, Dr Tao Zhao, Dr Yuepeng Dong, Dr Deqiong Kong, Boshu Zhang, Chanshu Gao, and many others in the group for their support and sharing some laughs together inside and outside the office.

I do not know how to put into words my gratitude for my family, who has always been my strongest support financially and emotionally, regardless of the distance. Finally, I wish to thank my boyfriend, for his unconditional love, encouragement, patience, and always having been there for me. Thank you, Fafa.

NOMENCLATURE

A	Area under load-displacement curves or factor to account for cyclic or monotonic condition in API p-y method
D	Pile outer diameter (m)
R	Pile cross-section radius (m) or rigidity parameter
I	Section second moment of area (m^4)
I_R	Clay stiffness / strength ratio (G/s_u)
I_S	Sand stiffness coefficient
J	API p-y method empirical constant (clay)
E	Young's modulus (MPa)
G	Shear modulus (MPa)
K	Coefficient of lateral earth pressure or bulk modulus
H	Lateral load applied to pile head (MN)
V	Vertical load applied to pile head (MN)
L	Pile embedded length (m)
T	Traction vector in soil elements (kPa)
M	Bending moment (MNm)
S	Shear force (MN)
s_u	Undrained shear strength (kPa)
e	Load eccentricity with respect to ground level (m)
h	Height of lateral load application from ground level (m)
k	Initial stiffness parameter of soil reaction curves or subgrade reaction modulus
K_0	Earth pressure coefficient at rest
m	Distributed pile moment (MNm/m) or s_u increase rate with depth (kPa/m)
n	Transitional curvature parameter
p	Distributed lateral soil reaction (MN/m)
t	Pile wall thickness (mm)
v or y	Pile displacement in positive loading direction (m)
v	Poisson's ratio
z *or* x	Depth below ground level (m)
γ	Unit weight (kN/m^3)
μ	Friction coefficient
η	Soil reaction component contribution metric
θ	Rotation of pile cross-section (radians)
Φ	Radial angle about the x-axes in the pile cross-section (radians)
φ	Internal friction angle (degree)
ψ	Dilation angle (degree)
ε	Strain
σ	Stress (kPa)
τ	Shear stress (kPa)

γ	Shear strain

Subscripts

p	With respect to distributed load curves
m	With respect to distributed moment curves
M	With respect to base moment curves
S	With respect to base horizontal force curves
0	Initial value
u or ult	Value at the ultimate response
Sec	Secant value

Superscripts and macrons

$\overline{x}$	Normalised quantity
$'$	Effective quantity (after the subtraction of pore pressure)

Abbreviations

OWT	Offshore wind turbine
FE	Finite element
BS	Base horizontal force
BM	Base moment
DOF	Degree of freedom
AWG	Academic work group
ULS	Ultimate limit states
SLS	Serviceability limit states
FLS	Fatigue limit states
RLT	Rigid pile lateral translation
RBR	Rigid pile rotation about pile base

TABLE OF CONTENTS

Chapter 1

INTRODUCTION

1.1 OFFSHORE WIND ENERGY AND DEVELOPMENT

The energy challenges of the 21st century are (i) meeting the increasing global energy demand due to population growth, technology advancement and the impact of emerging economies; (ii) solving the climate change problem caused by the increasing carbon dioxide emissions and heavy reliance on fossil fuels. To address these issues, the UK government set out energy policy goals to cut carbon dioxide emissions by at least 80% by about 2050 (from the 1990 baseline) (Climate Change Act, 2008), and encouraged the development of alternative energy sources. The government has a target in line with the EU Renewable Energy Directive (Department of UK Trade & Investment, 2015), to source 15% of primary energy supply from renewable energy by 2020. Driven by government support, renewable energy has seen the fastest growth in recent years, as shown in Figure 1.1.

An important element of the renewable energy growth is wind power, in both electricity generation (see Figure 1.2) and installed capacity. Onshore wind has developed over the last three decades to be the main element of wind energy, now characterised by a mature market with well-developed technologies. In contrast, offshore wind is regarded as a promising future energy source for the long term, due to:

(1) Higher and steadier wind speed over the sea, compared to the land, resulting in 10% higher load factor;
(2) Availability of large continuous areas for exploitation in the sea;
(3) Fewer negative impacts (noise, birds and landscape disturbance) on adjacent areas.

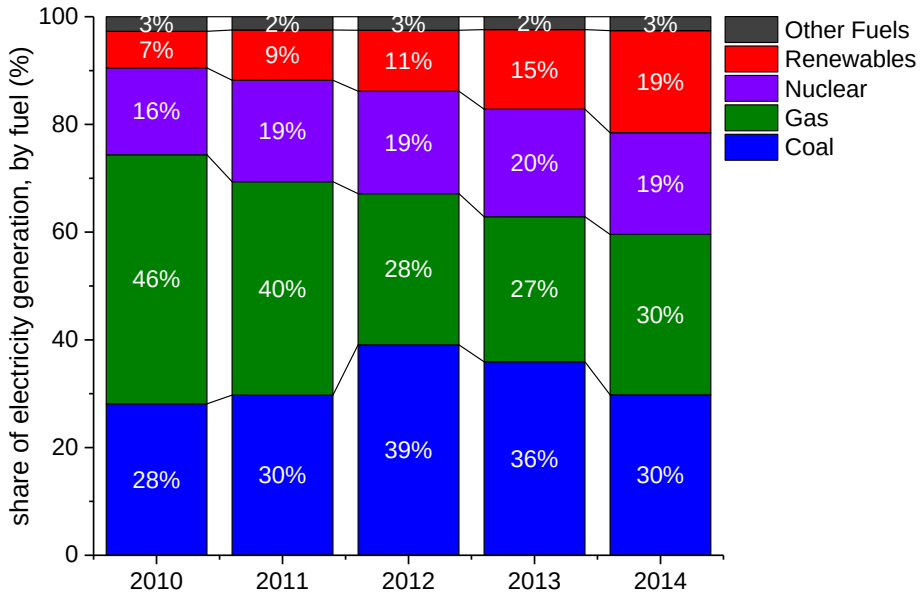

Figure 1.1 Share of electricity generation in the UK, by fuel type (Data from Department of Energy & Climate Change, 2011 to 2015[1])

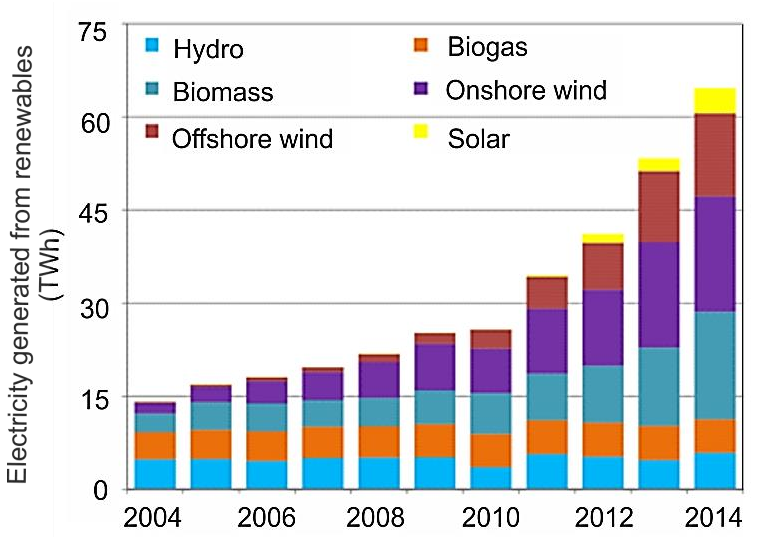

Figure 1.2 Renewable electricity generation in the UK (Figure from Department of Energy & Climate Change, 2015[2])

There are a number of challenges related to offshore wind. The demanding offshore environment poses significant design problems to be addressed. The installation and maintenance

[1] https://www.gov.uk/government/collections/digest-of-uk-energy-statistics-dukes (last accessed March 2016)
[2] https://www.gov.uk/government/collections/renewables-statistics (last accessed March 2016)

processes are complex and time-consuming. The transmission and integration of offshore wind energy into the electricity network is more complicated and expensive than for onshore wind. These factors result in a substantial increase in cost. The total capital cost of offshore wind is generally twice that of onshore (Electricity cost calculator, EWEA[3]). Note that the calculated capital cost is an upfront cost and does not account for operation and maintenance cost. The success of offshore wind going forward depends heavily on a reduction in cost. Both government and industry have begun to look for innovative solutions to bring down these costs.

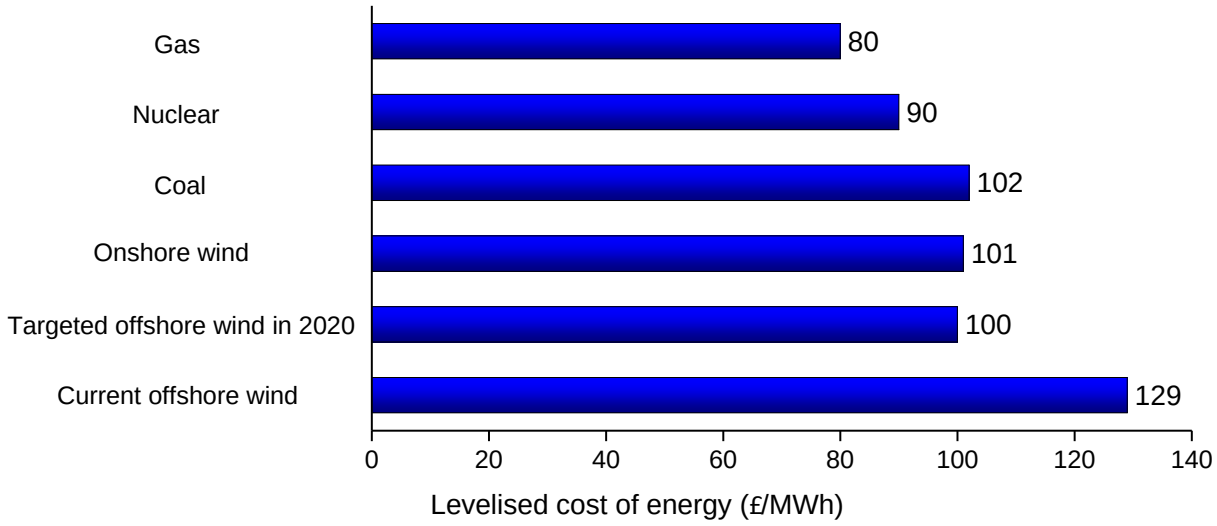

Figure 1.3 Current and targeted offshore wind cost compared with other energy sources (Data from Department of Energy & Climate Change, 2013[4]) Note: Levelised cost of energy accounts for energy generation efficiency, capital cost and operation and maintenance cost.

The leading countries with the most operational wind farms include the UK, Denmark, Germany, Belgium, the Netherlands, and Sweden. Outside Europe, the capacity of offshore wind farms around China has increased dramatically over the past few years, though progress is slow compared to the target of 5 GW by 2015 (Carbon Trust, 2014). France, the United States and China have significant potential for developing large-scale offshore wind farms, while South Korea and Japan are trying to accelerate their developments in this industry. Brazil and India have recently

[3] http://www.ewea.org/our-activities/policy-issues/economics/ (last accessed July 2016)
[4] https://www.gov.uk/government/uploads/system/uploads/attachment_data/file/269888/131217_Electricity_Generation_costs_report_December_2013_Final.pdf (last accessed March 2016)

entered the market and are also looking for future development. Overall, the offshore wind market shows clear signs of global expansion in the near future.

As the global market leader in offshore wind, the UK is on track to deliver 10 GW by 2020, with a potential investment of between £16 bn and £21 bn from 2014 to 2020 (Department of UK Trade & Investment, 2015). The UK offshore wind project pipeline, dated April 2015, shows substantial progress has been made to meet the target (see Figure 1.4), representing the largest expansion in any class of renewable energy technology.

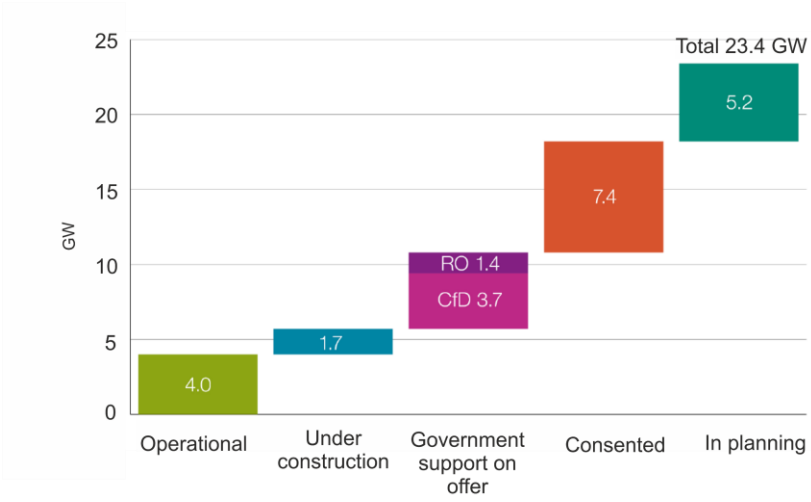

Figure 1.4 UK offshore wind project pipeline – April 2015 (Notation: RO-Renewable Obligation; CfD-Contract for Difference) (Figure from The Crown Estate, 2015[5])

The development of offshore wind farms in the UK consists of three rounds. Round 1 was launched in 2001 and involved 18 near-shore sites in England and Wales. Round 2 was formed of the three strategic areas: Greater Wash, Greater Thames and Irish Sea, which are located further offshore and in deeper waters. Rounds 1 and 2 have been largely completed. The present round, Round 3, starts construction from 2015 onwards, poses a potential threefold increase in total installed capacity (RenewableUK, 2015). Figure 1.5 shows the location of the UK offshore wind farms.

[5] http://www.thecrownestate.co.uk/media/476141/ei-key-facts-uk-offshore-wind.pdf (last accessed March 2016)

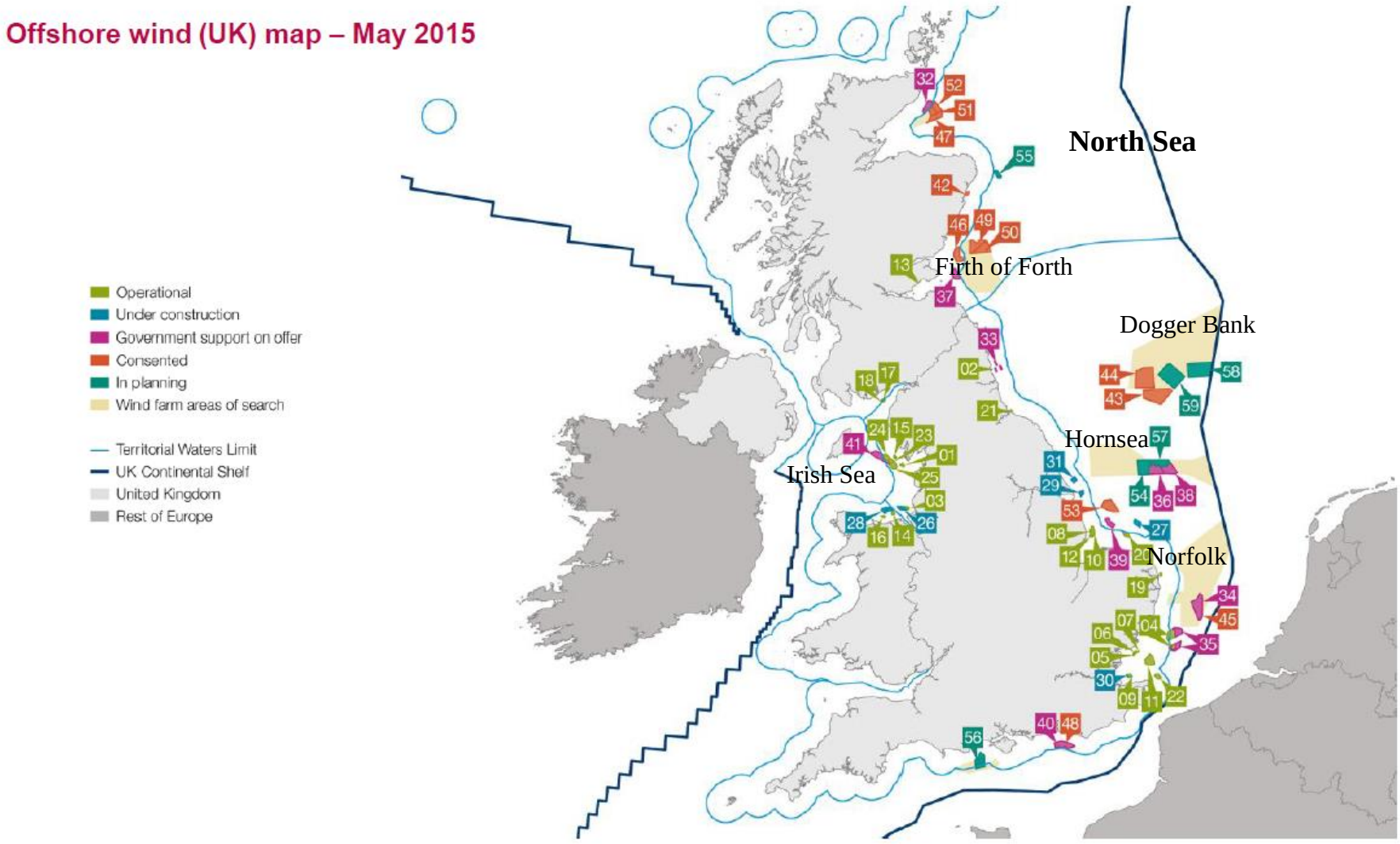

Figure 1.5 Location of offshore wind farms in the UK (the numbers of wind turbines are shown in the boxes) (Figure from Department of UK Trade & Investment, 2015)

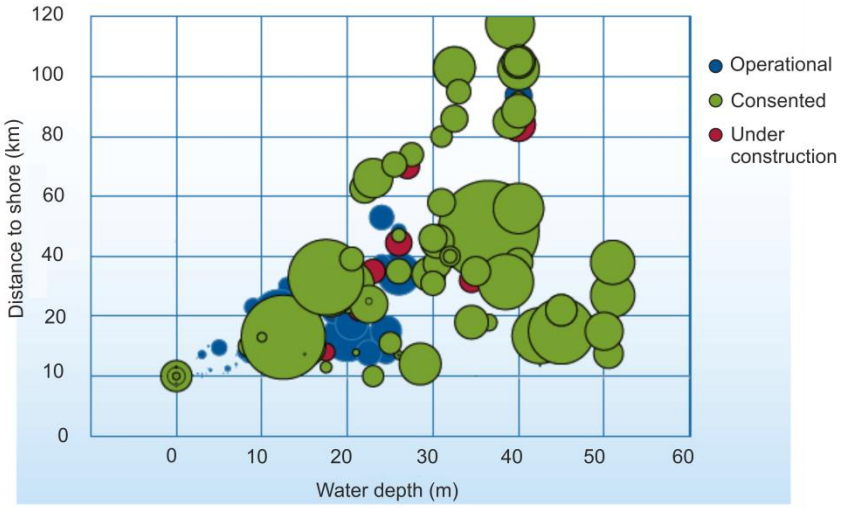

Figure 1.6 Average water depth and distance to shore of wind farms in Europe (Figure from EWEA, 2015)

The average water depth and distance to shore of wind farms in Europe are shown in Figure 1.6. Wind speeds increase with the distance from shore, and there is a clear trend of wind farms moving further offshore and into deeper water to capture these higher wind speeds. Hence, wind turbines are likely to be larger and founded on more substantial structures and foundations. This results in high cost of the foundation, which can vary from 16% to 23% of the total capital cost for an offshore wind turbine (EWEA, 2009; The Crown Estate, 2012; NREL, 2012). The cost of offshore foundations is typically at least 2.5 times higher than that of onshore foundations, and as such there is great potential for reducing the cost of offshore wind turbine foundations (EWEA, 2009). Reliable and robust foundation design methods are necessary to reduce the foundation cost and promote further development of offshore wind farms.

Offshore wind farms can be comprised of several hundred wind turbines. The structure of a typical offshore wind turbine (OWT) and the dimensions of its components are shown in Figure 1.7. The foundation is the part of the substructure that is in direct contact with the seabed, and transfers loads from the tower to the surrounding soil. It plays a crucial role for the functional ability of the whole structure, and must be able to withstand the total weight of the structure, and cope with wind, wave and current loads.

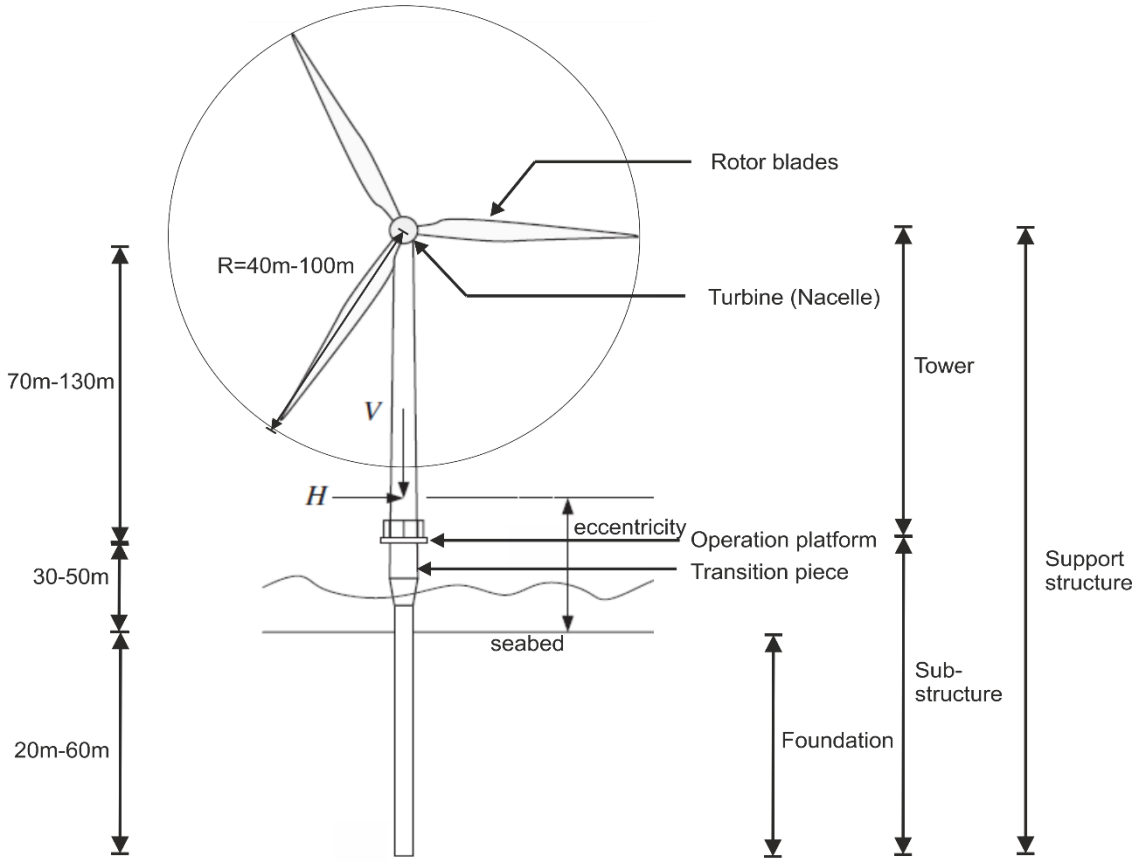

Figure 1.7 Components of a wind turbine and their typical dimensions (not to scale)

1.2 OFFSHORE WIND TURBINE FOUNDATIONS

Different foundation types are available for OWT (see Figure 1.8). Water depths, soil conditions, and loads applied to the structure are the important factors in choosing foundation types. Monopiles, jackets and tripods are currently the most conventional options, and have been widely used in practice. Several novel concepts such as suction caissons, floating structures, and 'hybrid' systems, combining monopiles and gravity bases, have been developed and gradually applied in newly developed wind farms.

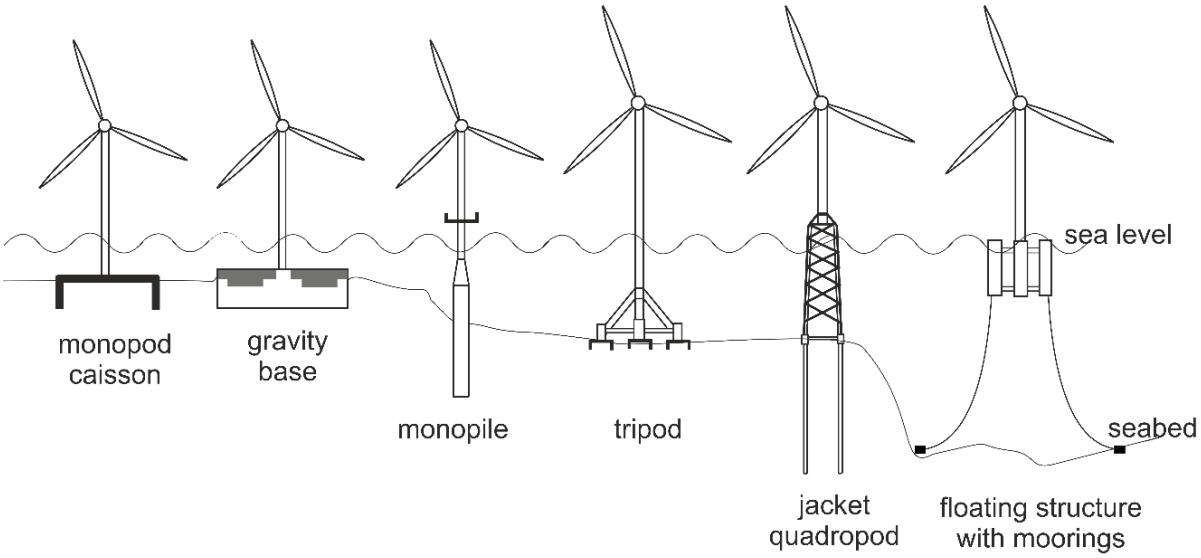

Figure 1.8 Typical foundation types for offshore wind turbines (redrawn from a figure by J. Schneider after NREL)

A monopile is a relatively simple structure made of a steel tube, as shown in Figure 1.9, and is usually connected to the tower through a transition piece. It is one of the most common foundation types because it is relatively time-efficient and cost-effective in both fabrication and installation. It is traditionally driven into the seabed by steam or hydraulic powered hammers. A new technology, known as BLUE Piling technology, drives large monopiles by using combustion generated pressures from falling water. The installation process of individual piles can take less than a day. Monopiles have been widely deployed in recent years, dominating the market with circa 90% share recorded to 2014 (EWEA, 2015). They have been successfully installed in water depths ranging from 0 – 30 m, and are promising in water depths up to 60 m.

The pile is designed to withstand a vertical load from the upper structure, and horizontal loads due to wind, waves and currents. The designed life-span for offshore wind turbines is about 20 - 25 years (LeBlanc *et al*., 2010). For a typical 5 MW wind turbine, the vertical load would be approximately 6 MN - 8 MN, and the maximum horizontal load would be 10 MN (de Vries and van der Tempel, 2007). Also, the pile is designed to satisfy pile head displacement and rotation tolerances, which are usually imposed by the manufacturers of the rotor and nacelle (DNV, 2011; Bhattacharya, 2014). A typical 5 MW wind turbine requires a pile of diameter 5 – 7.5 m to ensure adequate lateral capacity and meet the deformation requirements (Achmus *et al*, 2009). Being different from piles for oil and gas platforms, monopiles have larger diameters (4 – 10 m) and lower L/D ratios ($L/D < 10$). The monopile response is dominated by the lateral loads and overturning moment due to wind and waves.

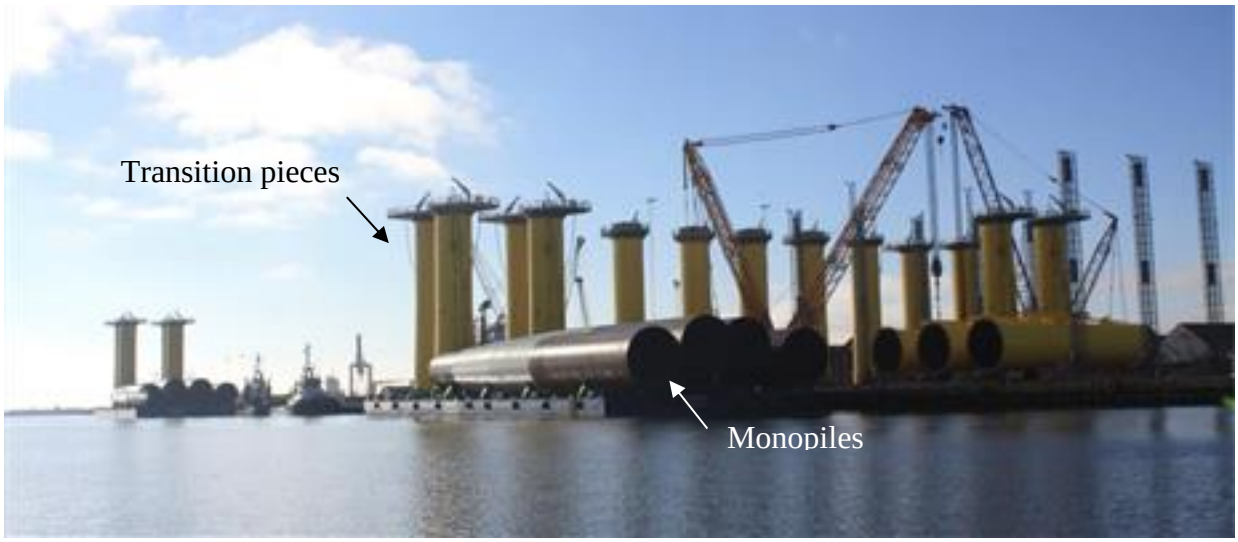

Figure 1.9 Current largest monopile installed (D = 7.5 m) at the Gode Wind Offshore Wind Farm in the German North Sea (Figure from DONG Energy, 2015[6])

The design approach for monopiles under lateral loading recommended in the current design guidelines (*i.e.* API/DNV standards) is commonly known as the *p-y* methods. They were originally developed for long and slender piles in the oil and gas industry (Matlock, 1970; Reese *et al*. 1974). These methods are based on the Winkler concept (Winkler, 1867). The soil is treated as a series of uncoupled non-linear springs along the pile, with the *p-y* curves representing the relationship between the lateral soil resistance, *p*, and the pile lateral displacement, *y*. The pile response (*e.g.* pile deflection, bending moment) is solved using beam theory. They have been widely employed and give plausible responses for long piles with large *L/D* ratios (Meyer and Reese, 1979). However, their applicability to relatively short monopiles is questionable. For instance, Hald *et al*. (2009) found that the *p-y* methods overestimated the head displacement of monopiles by 30% - 50% when compared to field measurements.

[6] http://www.dongenergy.com/en/media/newsroom/news/articles/first-foundation-successfully-installed1, (last accessed March 2016)

1.3 OVERVIEW OF PISA DESIGN METHODS (*E.G.* BYRNE *ET AL.*, 2015)

To improve the design of laterally loaded monopiles, new design methods are being developed within the PISA (PIle Soil Analysis) joint industry project. The innovation in the new design methods is that along with the conventional *p-y* curves, additional soil reaction components are taken into account, *i.e.* distributed moment due to the vertical shear stresses, τ, developed at the pile-soil interface, base horizontal force, *S*, and base moment, *M*, developed at the base of the soil plug (see Figure 1.10b). Similar to the *p-y* methods, a series of soil reaction curves representing the relationship between the soil reactions and pile deformation are incorporated within a beam model to predict pile responses.

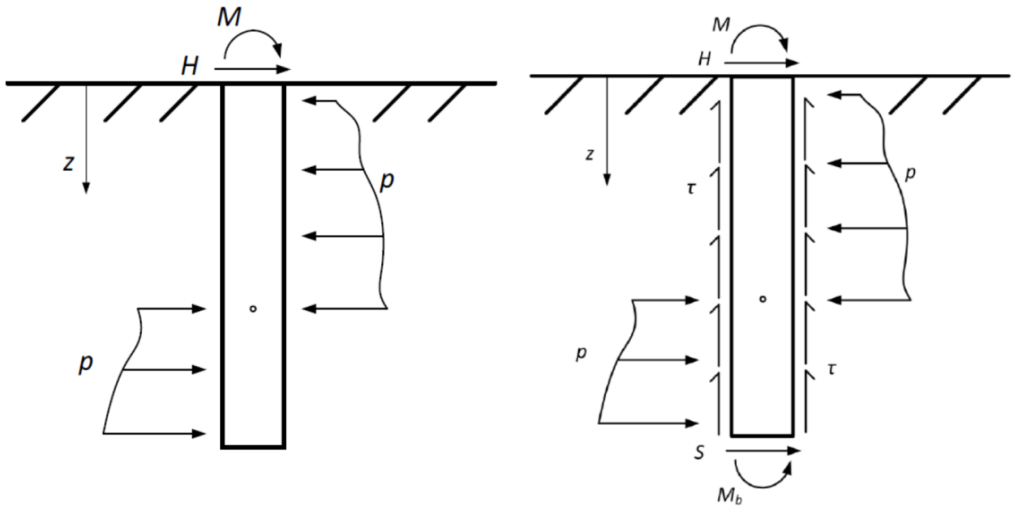

(a) (b)

Figure 1.10 Comparison of the soil reaction components used in (a) the *p-y* methods, and (b) the new design methods in PISA (Byrne *et al*., 2015)

From PISA, two design approaches, a rule-based method and a numerical-based method, are proposed. In the rule-based method, the soil reaction curves are determined from look-up tables, based on simple classification of the site soil profile; while in the numerical-based method, the soil reaction curves are extracted from detailed 3D finite element (FE) analyses. The methods proposed for PISA are hereafter referred to as 'the PISA design methods' or 'the new design methods'.

Preliminary work performed in the PISA project showed that, by considering the four soil reaction components, the new design methods gave more accurate estimates of pile responses compared with the *p-y* method, particularly for monopiles with low *L/D* ratios. However, it is still unclear whether the soil reaction curves developed by the numerical-based method can be applied to analyses considering pile geometries and load eccentricities, which are interpolated from the parameter space from which they have been developed. The PISA project considered two specific soil profiles, those at Cowden and Dunkirk, representing a stiff glacial till clay and a dense sand.

The new design approaches have not yet been validated on other soil profiles such as layered soils, which are frequently encountered in practice. Further investigation is required to confidently address these issues before the application of the new design methods can be more widely adopted.

1.4 OBJECTIVES

The primary focus of the study presented in this thesis is to examine the applicability of the numerical-based approach for design scenarios considering a wide variation of pile geometries, load eccentricities, soil profiles and layered soils. The study aims to investigate the sensitivity of the numerical-based approach to different soil models and boundary conditions. Finally, it intends to explore the feasibility of developing the soil reaction curves from a relatively small number of calibration analyses, as well as analyses of rigid piles in idealised deformation modes.

The major objectives for the study in this thesis are:

1. Perform 3D FE analyses using simple elastic perfectly plastic constitutive models;

2. Extract the soil reaction curves from a small number of calibration analyses in clay and sand for the calibration of the 1D model;

3. Develop appropriate parameterised expressions to describe the variation of soil reaction curves with depth, and validate them against known analytical solutions;

4. Investigate the relationship between the soil reaction components and loading conditions;

5. Examine whether the parameterised soil reaction curves developed from the calibration analyses can be applied to analyses considering different pile dimensions and load eccentricities, which are interpolated from the parameter space for the calibration analyses;

6. Explore the feasibility of using the soil reaction curves developed from homogeneous soil analyses for design cases considering Gibson-type soil and layered soils.

7. Explore the feasibility of developing the soil reaction curves from idealised rigid pile analyses, and compare them with those developed from the calibration analyses.

1.5 OUTLINE OF METHODOLOGY & THESIS

The development of soil reaction curves, which is the main component of this study, followed the procedure established in the PISA project. A complete investigation 'loop' for the development and validation of soil reaction curves is shown in Figure 1.11.

The investigation ‘loop’ consisted of four steps. In step 1, 3D FE analyses using simple elastic perfectly plastic constitutive models were performed using the commercial software Abaqus (Abaqus 2013, Version 6.13). In step 2, the soil reaction components were extracted systematically from a small number of 3D FE analyses (termed ‘calibration analyses’), and calculated at measurement depths along the pile shaft and at the base of the soil plug. The soil reaction curves were then normalised and parameterised in step 3. Both the ‘raw’ soil reaction curves extracted directly from the FE simulations (termed ‘numerical curves’), and the processed soil reaction curves obtained after the parameterisation (termed ‘parameterised curves’) were incorporated within a 1D model. In step 4, the results from the 1D model were compared with the results of the 3D FE calibration analyses performed in step 1. By varying pile and soil conditions, the effectiveness of the numerical-based design method and the calibrated 1D model could be examined by comparing 1D predictions with the results of further 3D FE analyses (termed ‘test analyses’).

In this thesis, Chapter 1 highlights the mechanism of four soil reaction components for laterally loaded monopiles proposed in the PISA project. As shown in step 4 in Figure 1.11, the four soil reaction components are the distributed load and distributed moment along the pile shaft, and the base horizontal force and base moment at the pile base. The distributed load component is the conventional horizontal soil reaction per unit length of the pile. The distributed moment is developed due to vertical shear stresses mobilised at the pile-soil interface. The base horizontal force and base moment are developed due to horizontal and vertical soil stress occurring at the base of the pile and the soil plug. The investigation loop to develop the four soil reaction components from 3D FE analyses is outlined in Figure 1.11.

Chapter 2 presents a review of current design guidelines and methods used for analysing the lateral responses of monopiles. The *p-y* method, recommended by the design guidelines for monopiles, is outlined. The limitations of the *p-y* method are discussed, and previous work performed in the PISA project for the development of improved design methods is presented. The calibration process adopted in PISA, which provides the basis for the calibration process used in this study, is elaborated.

The description of the 3D FE models, some key issues about 3D FE analysis, and the reaction curve extraction processes are presented in Chapter 3. The detailed procedures used to derive parameterised soil reaction curves for clay and sand, which are then used for input to the 1D model, are presented in Chapters 4 and 5, respectively. Two sets of parameterised soil reaction curves in sand and clay are given in tables. The applicability of the numerical-based approach is examined by comparing the pile response predicted by the calibrated 1D model with the results obtained from 3D FE analyses. The comparisons for analyses in clay, sand and layered soils are given and discussed in Chapters 4, 5, and 6. The findings observed from the results, and suggestions for future work are summarised in Chapter 7.

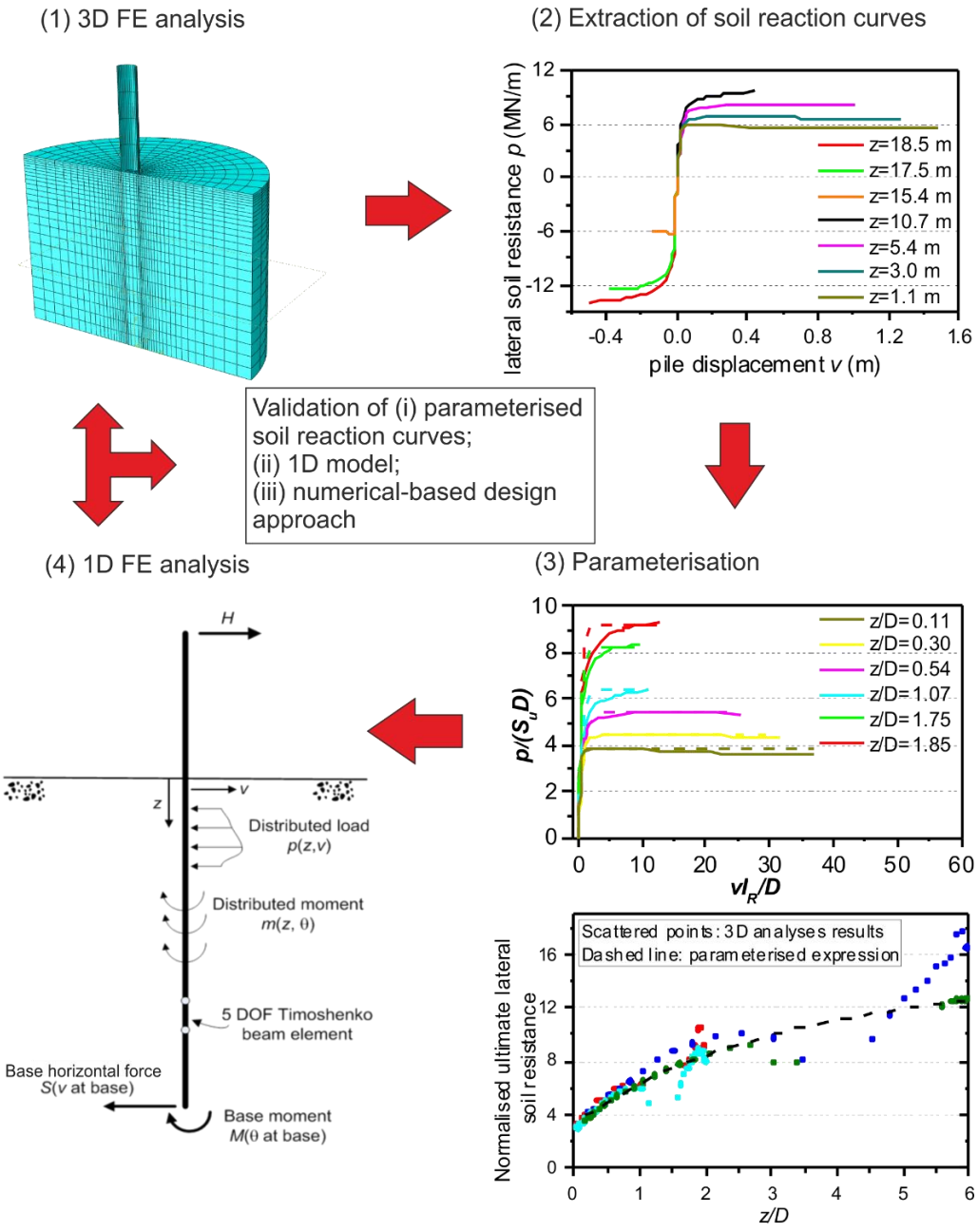

Figure 1.11 Investigation loop for Chapters 3, 4, 5, and 6

Chapter 2

LITERATURE REVIEW

2.1 DESIGN GUIDELINES AND CONSIDERATIONS FOR MONOPILES

The design of OWT is governed by guidance issued by national, European or international entities. The guidance generally covers key aspects including safety, site investigation, load conditions, design of turbines, blades and support structures, manufacturing, installation, commissioning, operation, maintenance and monitoring. Listed below are the guidelines for monopiles consulted by the industry. There are some gaps and lack of specificity in the guidelines, which will be discussed in detail in Section 2.3.4.

- DNV-OS-J101: Design of Offshore Wind Turbine Structures, Det Norske Veritas, May 2014, Norway;
- API RP-2A-WSD: Recommended Practice for Planning, Designing and Constructing Fixed Offshore Platforms – Working Stress Design, American Petroleum Institute, Nov 2014;
- IEC 61400-3: Design Requirements for Offshore Wind Turbines, International Electrotechnical Commission, Feb 2009;
- BSH Standards: Design of Offshore Wind Turbines, Bundesamt für Seeschifffahrt und Hydrographie, Dec 2007, Germany.

The DNV standard, which is often applied, is based on the partial safety factor method, which means that the different loads acting on the foundation are factored and combined for the limit state design. The design method for monopile foundations for OWT in the DNV standard refers to the same design methods adopt by API. Further in the thesis the reference to API refers to API (2014).

The design of monopiles must comply with the followings limit states:

- Ultimate Limit States (ULS): the bearing capacity and the deformation of the structure that occurs in the maximum load cases (such as extreme hurricane and tidal wave events) must be within a certain tolerance;

- Serviceability Limit States (SLS): the accumulated deformation and vibration of the structure during its normal working condition (*i.e.* under long-term cyclic loading) must enable the functional ability of the structure; the design natural frequency should avoid system dynamic resonance;
- Fatigue Limit States (FLS): particularly related to dynamic loading effects on the material and structural degradation.

ULS is usually the first case to consider for a preliminary design. The ULS design provides baseline information for the subsequent SLS design. It is necessary to use relatively simple and yet accurate methods to predict the monopile performance under monotonic lateral loading for the ULS design.

The loads acting on a monopile consist of vertical loads, *V*, horizontal loads, *H*, and moment, *M*, induced by the horizontal loads acting on the structure above seabed level (see Figure 2.1). 80-90% of the horizontal load is due to wind and waves, while the rest is generated by current movement and rotor blade operation (Peralta, 2010). Because the vertical load acting on monopiles is usually very small compared to the vertical capacity, the horizontal force and moment are considered as the dominant loads. For the ULS design, the design loads are representative of the maximum loads in 50 years, usually derived from statistical analysis of historic wind and wave data.

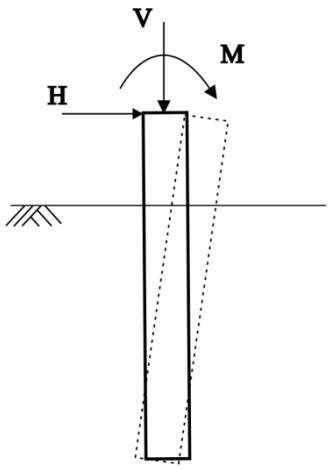

Figure 2.1 Offshore loads applied to a monopile

The ULS design consists of load analysis and deformation analysis. Load analysis, alternatively called bearing capacity analysis, is used to determine the maximum capacity of the structure before soil failure occurs. Deformation analysis is used to analyse the deformation of the structure under different loadings, in order to determine the maximum applicable loads when the deformation reaches design deformation tolerances. For OWT, which are very sensitive to tilting and rotation, deformation analysis is generally much more critical.

2.2 DEFORMATION ANALYSIS FOR LATERALLY LOADED PILES

There have been a number of methods used to assess the deformation of single laterally loaded piles. They can be categorised as closed-form solutions, semi-empirical methods and numerical-based methods, and are briefly reviewed as follows.

Closed-form solutions

In these solutions, the soil reaction is derived from theoretical assumptions. Poulos and Davis (1980) have proposed elastic continuum models to analyse laterally loaded piles. Broms (1964a, 1964b, 1965) developed closed-form solutions for the ultimate lateral loads and maximum bending moment of both long and short piles by limit state analyses. He adopted an idealised distribution of soil resistance with depth (for an example see Figure 2.2). c_u is the undrain shear strength of soils, D is the pile diameter, e is the load eccentricity, L is the pile embedded length, and M is the bending moment of the pile. In his analysis for cohesionless soils, the solutions for the deflection of a flexible pile at ground level were developed by assuming that the coefficient of subgrade reaction increases linearly with depth. Broms also developed solutions for the deflection of piles in cohesive soils assuming a constant subgrade reaction coefficient with depth.

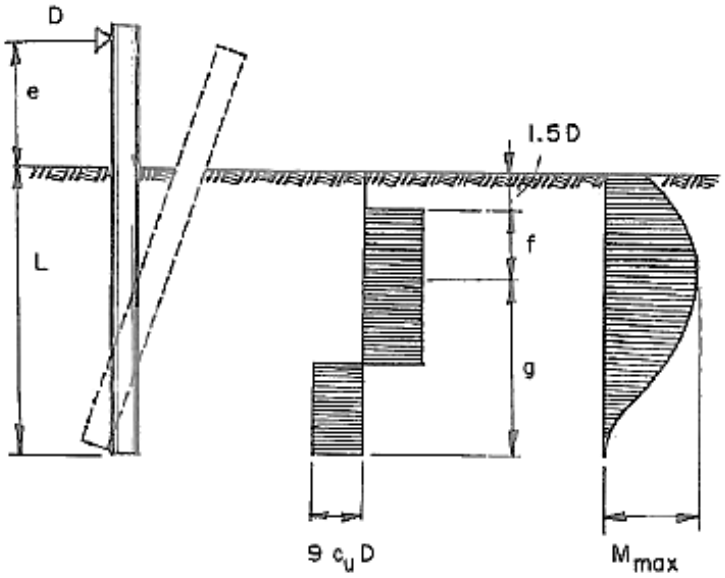

Figure 2.2 Assumed distribution of soil reaction and bending moment for a short pile in cohesive soils (Broms, 1964b)

The calculation of the monopile response was relatively straight-forward in these methods. However, Poulos' methods were only valid for the analysis of laterally loaded piles at very low load levels (Budhu and Davies, 1987). Broms' solutions can be useful in giving an approximate design with a minimum of computation (Meyer and Reese, 1979). However, comparisons with field measurements showed that his solutions for clay underestimated the actual deflection of pile by

factor of 3 (Broms, 1964b). Meanwhile, the assumption of linear increase in subgrade reaction coefficient with depth in sand is questionable (Doherty and Gavin, 2012).

Semi-empirical methods

The semi-empirical methods are also known as the subgrade reaction methods or the *p-y* methods. They are based on the Winkler concept, in which the soil is represented by a series of uncoupled non-linear springs. The soil reactions in these methods are developed from theoretical assumptions and correlations with field test results. Reese and his colleagues developed non-linear *p-y* curves for common types of soils (*e.g.* clay, sand and rock) from field test results (Reese and Cox, 1975; Reese *et al*., 1974; Reese, 1997). These methods have been widely used in the oil and gas industry, and their performance was generally regarded as being satisfactory for long piles with large *L/D* ratios (Meyer and Reese, 1979). However, the *p-y* methods were initially developed for the oil and gas industry and their applicability to the design of relatively short monopiles was questionable, which is further discussed in Section 2.3.4.

Finite element methods

Finite element methods provide a versatile tool that is capable of modelling soil continuity, soil non-linearity, pile-soil interface behaviour and 3D boundary conditions (Fan and Long, 2005). Brown *et al.* (1989) were the first to used 3D FE analyses to analyse a solid pile under monotonic lateral loading, and derived *p-y* curves from the 3D FE analyses. In recent years, researchers have focused on using advanced computer techniques to analyse laterally loaded piles under monotonic and cyclic loading (Fan and Long, 2005; Abdel-Rahman and Achmus, 2005; Haiderali and Madabhushi, 2012; Ibsen *et al*., 2013; Burlon *et al.*, 2014; Abadie, 2016). Meanwhile, progress has been made on developing advanced constitutive soil models to capture soil behaviour under complex loading conditions (Fakharian *et al.*, 2008; Bourgeois *et al.*, 2010; Giannakos *et al.*, 2012). Although 3D FE analyses can be computationally expensive and time-consuming, they are useful to gain better insight into soil behaviour and its failure mechanism compared with empirical approaches. Due to the advancement in numerical methods and in constitutive models, advanced 3D FE analyses are being increasingly used for design in the industry.

2.2.1 LAYERED SOILS

Piles, especially those for nearshore and offshore foundations, are frequently embedded in layered soils. However, limited research has been carried out to develop solutions for layered soil profiles. The pile behaviour in a two-layer system was first investigated by Davisson and Gill (1963) using a

linear *p-y* method. Reese *et al*. (1981) conducted small-scale model tests and a field test on slender piles (*L/D* ratios of 25.36 and 42.3 respectively), and found that there was relatively good agreement between experimental results and predictions using *p-y* curves derived from homogeneous soil analyses at the same depth. Georgiadis (1983) proposed an 'equivalent depth' concept for developing *p-y* curves for layered soils. This concept is schematised in Figure 2.3. In his method, the *p-y* curves for the upper soil layer are determined using appropriate expressions for a homogeneous soil deposit. The effect of upper layers on the *p-y* curves of the lower layers is accounted for by calculating the equivalent depth of the overlying layers. For each successive layer, the *p-y* curves are determined using recommendations for a homogeneous soil deposit at the equivalent depths. For example, the equivalent depth for the second layer, h_2, shown in Figure 2.3, is calculated by first solving the equivalent lateral force acting at the layer interface, as shown in Equation (2.1):

$$F_1 = \int_0^{H_1} p_u^1 dH \tag{2.1}$$

where F_1 is the force required to induce the soil failure of the pile segment embedded to the bottom of the upper layer, p_u^1 is the ultimate soil resistance of the upper layer, H_1 is the thickness of the first layer and *dH* is the incremental soil depth. Then the equivalent depth of the second layer is determined by solving Equation (2.2):

$$F_1 = \int_0^{h_2} p_u^2 dH \tag{2.2}$$

where h_2 is the equivalent depth of the first layer as if the entire soil profile consists of only the soil in the second layer. p_u^2 is the ultimate resistance of the second layer. The equivalent depth h_3 and the *p-y* curves of the third layer are obtained by the same process. This method has been incorporated in commercial pile design software *LPILE* (Reese *et al*., 2004).

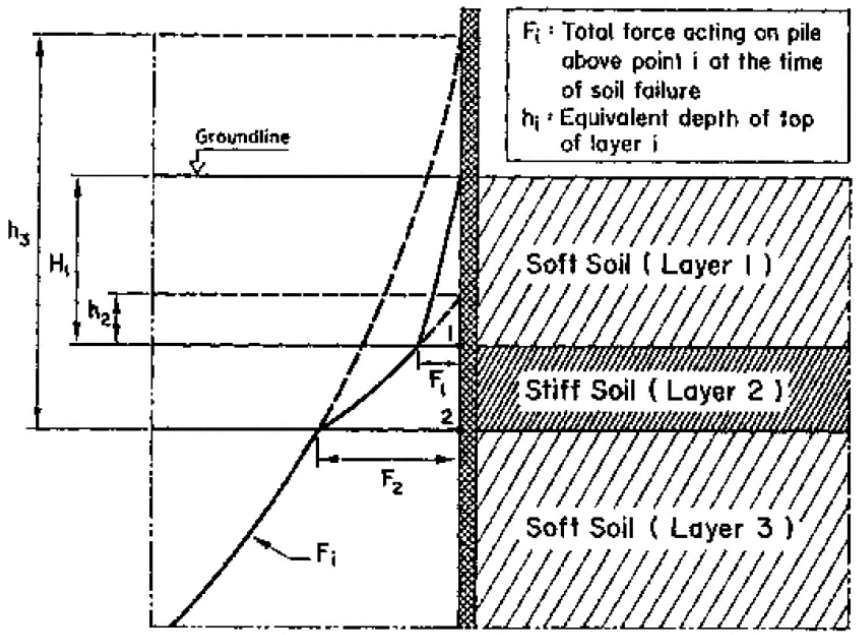

Figure 2.3 Illustration of the 'equivalent depth' method for layered soils (Georgiadis, 1983)

Continuum-based approaches were also developed to analyse a laterally loaded pile in layered soils. Ashour *et al*. (1998, 2004) proposed a semi-empirical strain wedge approach to develop *p-y* curves in layered soils, and successfully demonstrated the capability of the strain wedge approach by comparison with published full-scale test results. Yang and Jeremić (2002) extracted *p-y* curves from 3D FE analyses on a single pile in elastic-plastic clay-sand interbedded deposits, and compared the extracted curves with those developed from analyses with homogeneous soils. Their results suggested that soil layering effects occurred in both the lower and the upper layers. Basu *et al*. (2009) developed a continuum-based analytical solution for a single pile in elastic layered media, and his model was formulated using a variational approach. As yet there is no generally accepted method for the analyses of laterally loaded piles in layered soils.

2.3 REVIEW OF API *P-Y* METHODS

2.3.1 BASIC CONCEPTS

As adopted by API and further referred by DNV and other design guidelines, the *p-y* methods (*i.e.* the subgrade reaction method) are the most commonly used methods for the design of laterally loaded monopiles. They are based on Winkler's assumption, assuming that the soil is approximated by a series of uncoupled springs (Winkler, 1867). The *p-y* curves, *i.e.* the spring properties, represent the relationship between the lateral soil reaction, *p*, and the lateral pile displacement, *y*, at the same depth, *z* (see Figure 2.4). The *p-y* curves vary with depth, soil properties and pile

geometries. With these *p-y* curves, the pile displacement at any applied load level can be found by solving the differential equations (see Equations (2.3) - (2.5)) based on the Euler-Bernoulli beam theory, usually through iterative calculation methods.

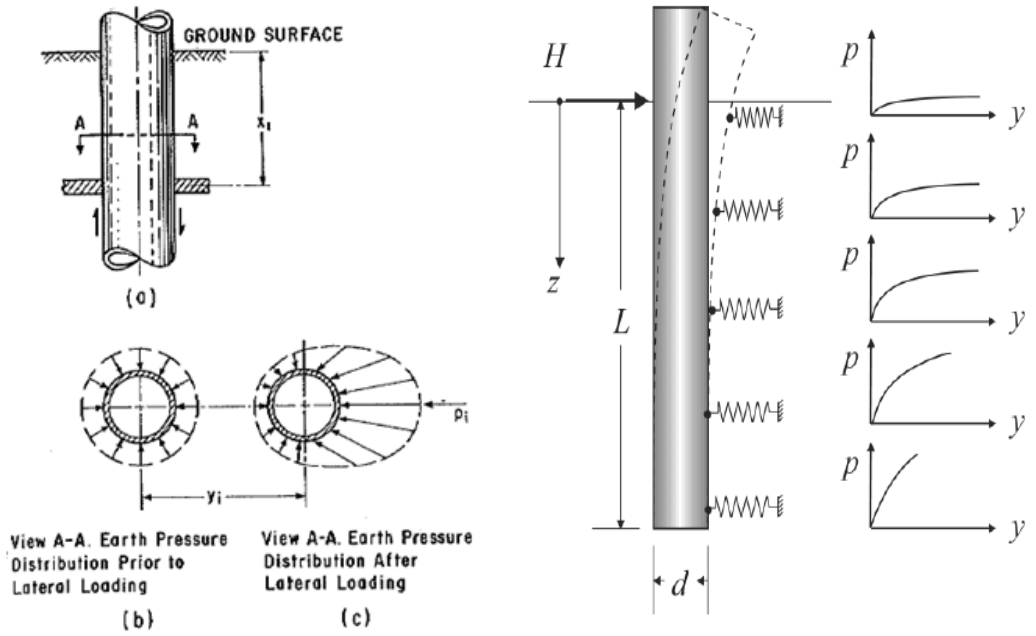

Figure 2.4 Principle of the *p-y* method (Reese *et al*., 1974; Peralta, 2010)

$$\frac{d^2}{dx^2}\left(E_p I_p \frac{d^2y}{dx^2}\right) + Q_x \frac{d^2y}{dx^2} - p(y) = 0 \tag{2.3}$$

with

$$E_p I_p \frac{d^3y}{dx^3} + Q_x \frac{dy}{dx} = Q_y \tag{2.4}$$

$$E_p I_p \frac{d^2y}{dx^2} = M \tag{2.5}$$

where $E_P I_P$ = flexural stiffness of the pile, FL^2

Q_x = axial force in the pile, F

Q_y = lateral shear force in the pile, F

M = bending moment in the pile, FL

p = lateral soil reaction, F/L

x = position along the pile length starting from the ground level, L (Note that this term is referred as z in the rest of the thesis.)

y = lateral pile displacement, L (Note that this term is denoted by v in the new design methods.)

The beam-on-springs concept was firstly introduced by Hetenyi (1946), in order to analyse a horizontal beam placed on soils. Hetenyi treated the soil as elastic springs with only one parameter – the subgrade reaction modulus, *k*, defined by Equation (2.6).

$$k = {}^{dp}/_{dy} \tag{2.6}$$

The concept was extended to the analysis of laterally loaded piles by Reese and Matlock (1956). Based on field tests performed in 1970s, along with theoretical assumptions, Reese and his colleagues developed non-linear *p-y* curves as recommended in the current design guidelines. These *p-y* curves begin with a straight line, followed by a parabola adjoined by another linear portion, and finally reach a constant ultimate strength. The expressions for the *p-y* curves for different soil types are discussed later in Section 2.3.3.

The subgrade reaction modulus plays an important role in determining pile responses at small load levels. Biot (1937) and Vesić (1961) investigated the modulus of subgrade reaction for the beam-on-elastic-soil problem through fitting with numerical solutions. They correlated this parameter with soil elastic properties (shear modulus *G* and Poisson's ratio *v*). Bowles (1997) suggested doubling Vesić's solution for piles. Their solutions were empirical, owing to significant difference in soil deformation pattern between a laterally loaded pile and a beam (*e.g.* Smith, 1987; Prasad and Chari, 1999). For laterally loaded piles, the variation of *k* with depth depends on loading conditions, pile constraint conditions, pile-soil relative stiffness, soil Poisson's ratio and so on (Guo and Lee, 2001). Guo (2001) suggested different values of *k* for rigid and flexible piles by considering the impact of load eccentricity, *e*, by numerical analyses. The expressions for a circular solid pile are summarised in Table 2.1

Table 2.1 Typical solutions for subgrade reaction modulus (extracted from Guo, 2013)

Authors	Expressions
Biot, 1937	$\frac{k}{G} \approx \frac{1.9}{(1-\upsilon)}\left(\frac{128G}{\pi(1-\upsilon)E_p}\right)^{0.108}$ (2.7) Note: E_p is the Young's modulus of the pile.
Vesić, 1961	$\frac{k}{G} \approx \frac{1.3}{(1-\upsilon)}\left(\frac{128G(1+\upsilon)}{\pi E_p}\right)^{1/12}$ (2.8)
Bowles, 1997	$\frac{k}{G} \approx \frac{2.6}{(1-\upsilon)}\left(\frac{128G(1+\upsilon)}{\pi E_p}\right)^{1/12}$ (2.9)
Guo, 2001	$\frac{k}{G} \approx \left(8.4 + \frac{\bar{e}}{0.12+0.2427\bar{e}}\right)\left(\frac{L}{D}\right)^{-0.45\left(1+\bar{e}/1+5\bar{e}\right)}$ (2.10) for rigid piles $\frac{k}{G} \approx \left(6.86 + \frac{\bar{e}}{0.146+0.2834\bar{e}}\right)\left(\frac{E_p}{G}\right)^{-\left(0.087+\bar{e}/11.5+50\bar{e}\right)}$ (2.11) for flexible piles where $\bar{e} = e/L$

2.3.2 ULTIMATE LATERAL SOIL RESISTANCE

Two main parameters used to control the *p-y* curves are the initial slope and the ultimate lateral soil resistance. The ultimate lateral soil resistance at depth (force per unit length along the pile length), p_u, is an important quantity for predicting pile lateral capacity (Randolph and Houlsby, 1984). The expressions for the ultimate lateral soil resistance with depth were developed based on theoretical assumptions on soil failure mechanism, and correlations with field test results.

Assumptions

Two distinct failure mechanisms, the wedge failure and the flow-around failure were proposed for soils at different depths. The ultimate soil resistance was derived by solving force and moment equilibrium, at depths near the ground surface and at a considerable depth below the ground surface. The pile, in both assumptions, is considered as a rigid block.

A. Wedge failure

The wedge failure assumes that, near the ground surface, the soil in front of the pile fails by shearing upward and forward, as illustrated in Figure 2.5.

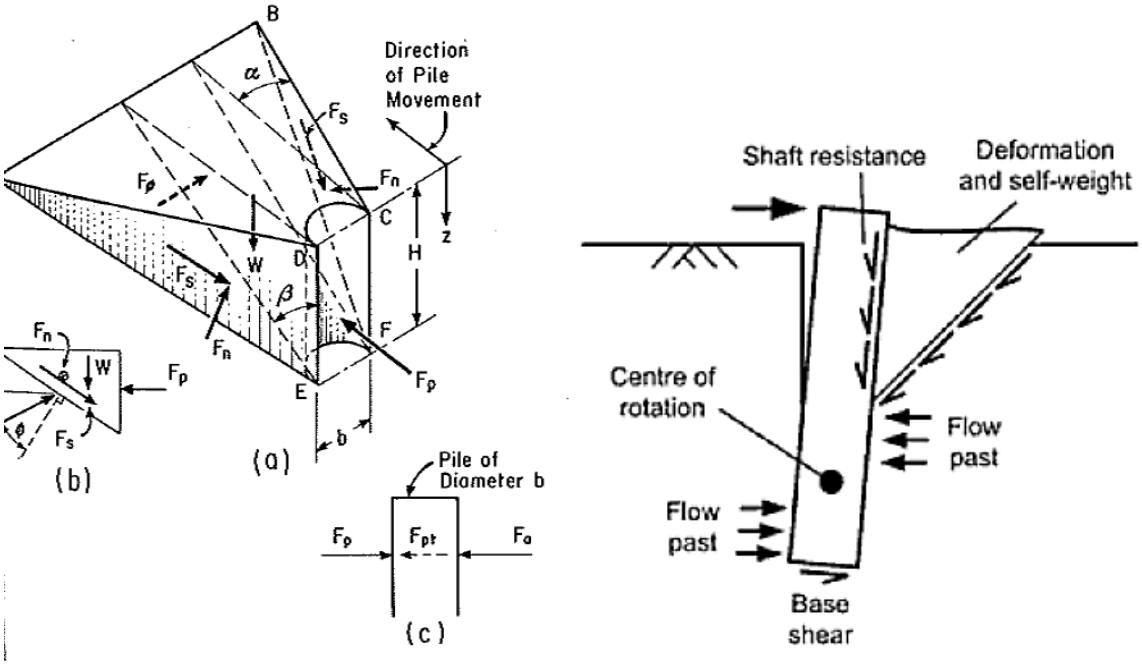

Figure 2.5 Assumed wedge failure and the failure planes (Reese *et al*., 1974, Randolph and Gourvenec, 2011)

The failure planes form a wedge-shaped block of soil in front of the pile. The ultimate soil resistance is calculated by summing the limiting shear stress acting on the wedge sides, the vertical resistance provided by the overburden pressure from the soil itself, and the resistance developed by the shear stress at the pile-soil interface (Matlock, 1970).

B. Flow-around failure

For soil at considerable depth below the ground surface, the vertical degree of freedom is considered eliminated, which means that deformation occurs in horizontal planes. The ultimate soil resistance is obtained by solving a plane strain problem. The exact solution for undrained clay was developed by Randolph and Houlsby (1984), and Martin and Randolph (2006), while the solution in sand was developed by Reese *et al*. (1974) and further simplified by Borgard and Matlock (1980). The flow-around failure is schematised in Figure 2.6.

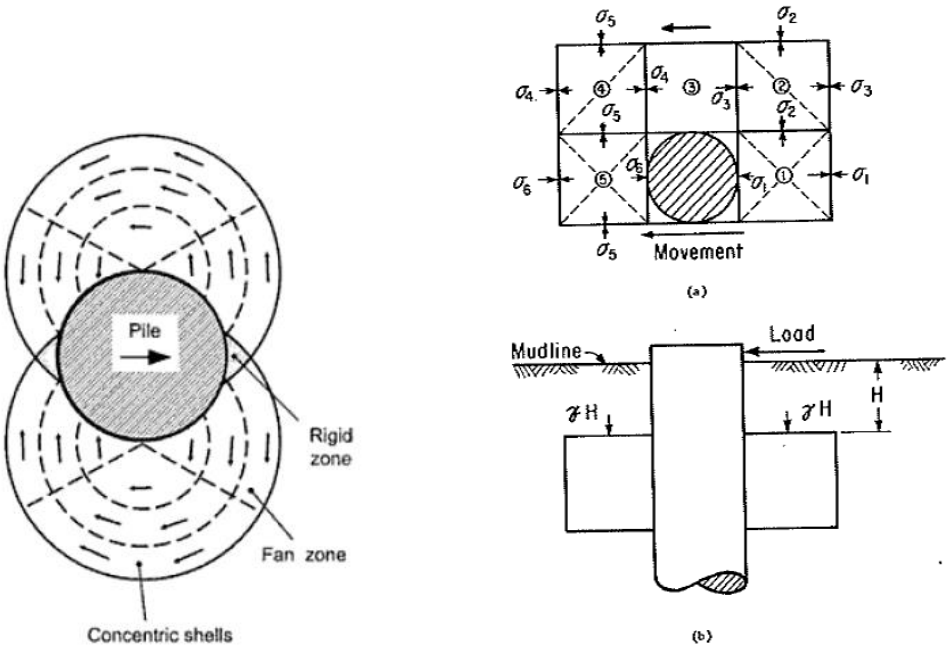

(a) clay (b) sand

Figure 2.6 Assumed flow-around failure and the associated slip lines (where the shear stress is maximum) (Randolph and Gourvenec, 2011; Reese *et al.*, 1974)

Solutions for ultimate lateral soil resistance with depth

A. Clay

For cohesive soil, several analytical solutions for the ultimate lateral soil resistance with depth have been reported in the literature (Murff and Hamilton, 1993; Matlock, 1970; Reese and Cox, 1975; and Brinch Hansen, 1961). Murff and Hamilton (1993) developed a solution using upper bound limit analysis calculations. The collapse mechanism is assumed as a combination of a conical wedge push-up mechanism for shallow depths and a plane strain flow-around mechanism at greater depths. The API *p-y* method recommended Matlock's semi-empirical solution for soft clay, and the semi-empirical solution by Reese and Cox (1975) for stiff clay. The analytical solutions for the ultimate lateral soil resistance in clay are briefly summarised in Table 2.2.

Table 2.2 Typical solutions for ultimate lateral soil resistance in clay

Authors	Expressions
Murff and Hamilton, 1993	$$p_u = \min\{(N_p s_u + \gamma z)D, N_1 s_u D\} \quad (2.12)$$ $$N_p = N_1 - N_2 \exp(-\frac{\xi z}{D}) \quad (2.13)$$ $$\xi = \begin{cases} 0.25 + 0.05\lambda & \lambda < 6 \\ 0.55, & \lambda \geq 6 \end{cases} \quad (2.14)$$ where $\lambda = s_{u0}/(s_{u1}D)$ Note: s_u is the undrained shear strength of soil. z is the soil depth from the ground level. s_{u0} is s_u at the surface, and s_{u1} is the increase rate of s_u with depth. N_1 is the limiting resistance at depth, 9.0 is used for smooth piles and 12.0 is taken for rough piles. They are consistent with Randolph and Houlsby's solution (1984). (N_2 - N_1) gives the ultimate resistance at the surface, 2.0 is assumed for smooth piles and 3.0 is assumed for rough piles in calculations.
Matlock, 1970 (API method for soft clay)	$$p_u = N_p s_u D \quad (2.15)$$ $$N_p = \begin{cases} 3 + (\frac{\gamma D}{s_u} + J)\frac{z}{D}, & \frac{z}{D} < \frac{6}{\frac{\gamma D}{s_u} + J} \\ 9, & \frac{z}{D} \geq \frac{6}{\frac{\gamma D}{s_u} + J} \end{cases} \quad (2.16)$$ Note: J is an empirical factor ranging between 0.25 and 0.5, determined by field testing. A value of 0.5 is appropriate for Gulf of Mexico clays.
Reese and Cox, 1975 (API method for stiff clay below water table)	$$p_u = A * N_p s_u D \quad (2.17)$$ $$N_p = min\begin{cases} 2 + (\frac{\gamma D}{s_u} + 2.83)\frac{z}{D}, \\ 11, \end{cases} \quad (2.18)$$ Note: The empirical factor, A, given in charts in Reese and Cox (1975), ranges from 0.2 to 0.6 for static loading and from 0.2 to 0.3 for cyclic loading.
Brinch Hansen, 1961	$$p_u = (K_q^D \gamma' z + K_c^D s_u)D \quad (2.19)$$ where K_q^D=0 for clay ($\varphi' = 0$) $$N_p = K_c^D = (K_c^0 + \alpha_c K_c^\infty \frac{z}{D})/(1 + \alpha_c \frac{z}{D}) \quad (2.20)$$ $$\alpha_c = 2\sin\left(45^\circ + 0.5\varphi'\right) K_c^0/(K_c^\infty - K_c^0) \quad (2.21)$$ $$K_c^0 = (\exp((0.5\pi + \varphi')\tan\varphi')\cos\varphi \tan\left(45^\circ + 0.5\varphi'\right) - 1)\cot\varphi' \quad (2.22)$$ $$K_c^\infty = \left(1.58 + 4.09\tan^4\varphi'\right)\left(\exp\left(\pi\tan\varphi'\right)\tan^2\left(45^\circ + 0.5\varphi'\right) - 1\right)\cot\varphi' \quad (2.23)$$ Note: $K_c^0\left(\varphi' = 0\right)$, $K_c^\infty(\varphi' = 0)$ are given in design charts in Brinch Hansen (1961).

The dimensionless ultimate resistance coefficient, N_p, given by Matlock, includes the effect of unit weight; while in Murff and Hamilton, N_p is derived directly from a weightless soil. The ultimate resistance for a soil with weight using Murff and Hamilton's solution is the sum of $N_p s_u$ and the contribution due to overburden pressure (see Equation (2.12)). Similar to Matlock's solution, Reese and Cox's solution is developed by assuming a wedge failure at shallow depths and plane strain failure at greater depths. The solution is correlated with field test data by an empirical factor. Brinch Hansen (1961) studied single rigid piles with the ultimate resistance calculated based on the assumption of passive Rankine states.

B. Sand

Several solutions for the ultimate lateral soil resistance have been developed for cohesionless soil (Brinch Hansen, 1961; Broms, 1964a; Reese *et al*., 1974; Bogard and Matlock, 1980; Barton, 1982; O'Neill and Murchison, 1983 and Zhang *et al*., 2005). Their solutions for the ultimate lateral soil resistance in sand are summarised in Table 2.3.

The dimensionless ultimate resistance coefficient for sand is defined by $N_p = p/(\gamma' z D)$. Broms (1964a) suggested $N_p = 3K_p$ in his analysis, where $K_p = \tan^2(45^\circ + 0.5\varphi')$ (the Rankine passive coefficient). Later Barton (1982) found an improved fit based on data from lateral pile tests in dense sand, which gave greater values than Broms' solution for most natural sand. Zhang *et al*. (2005) decomposed the ultimate lateral soil resistance into two components: the frontal normal reaction and the side friction reaction, depending on pile types and installation methods. Brinch Hansen developed non-linear distribution of the ultimate lateral resistance with depth, in a general c-φ' soil. For sand, the term related to soil cohesion was ignored. Reese *et al*. (1974) developed a theoretical solution assuming a wedge failure near the surface and plane strain failure at greater depths. Bogard and Matlock (1980) simplified the solutions developed by Reese *et al*. by replacing some terms with constants. Their solutions resulted in relatively little additional errors. By multiplying by the empirical factor, *A*, the modified ultimate soil resistance represents the real limiting value for the *p*-*y* curves obtained from field tests.

Table 2.3. Typical solutions for ultimate lateral soil resistance in sand

Authors	Expressions
O'Neill and Murchison, 1983 Bogard and Matlock, 1980 (API method)	$p_u = min\begin{cases}(C_1 z + C_2 D)\gamma\ 'z \\ C_3 D\gamma\ 'z\end{cases}$ (2.24) $p = Ap_u \tanh(\frac{kz}{Ap_u} v)$ (2.25) where $A = 0.9$ for cyclic loading or $A = (3.0 - 0.8\frac{z}{D}) \geq 0.9$ for static loading Note: The coefficients C_1, C_2, C_3 and k are given in design charts in API depending on soil internal friction angle and relative density.
Reese *et al*., 1974 (extracted from Zhang *et al*., 2005)	$p_u = Ap_c$ (2.26) p_c is taken as the lesser value from Equations (2.27) and (2.28) $\gamma' z\left(D(K_p - K_a) + z(K_p - K_0)\sqrt{K_p}\tan\alpha + zK_0\sqrt{K_p}\left(\frac{1}{\cos\alpha} + 1\right)\tan\varphi'\sin\beta\right)$ (2.27) $\gamma' zD(K_p^3 + K_0 K_p^2 \tan\varphi' - K_a)$ (2.28) where $K_a = \tan^2(45^\circ - 0.5\varphi')$, $K_p = \tan^2(45^\circ + 0.5\varphi')$; K_0 is the earth pressure coefficient at rest; $\beta = 45^\circ + 0.5\varphi'$; α is the angle defining the shape of the failure wedge. A is an empirical factor given in Reese *et al*. (1974).
Brinch Hansen, 1961	$p_u = (K_q^D \gamma' z + K_c^D s_u)D$ (2.29) where $s_u = 0$ for sand $K_q^D = (K_q^0 + \alpha_q K_q^\infty \frac{z}{D})/(1 + \alpha_q \frac{z}{D})$ (2.30) $\alpha_q = K_q^0 K_0 \sin(\varphi') /((K_q^\infty - K_q^0)\sin(45^\circ + 0.5\varphi'))$ (2.31) $K_q^0 = e^{(0.5\pi + \varphi')\tan\varphi'}\cos\varphi'\tan(45^\circ + 0.5\varphi') - e^{-(0.5\pi - \varphi')\tan\varphi'}\cos\varphi'\tan(45^\circ - 0.5\varphi')$ (2.32) $K_q^\infty = K_c^\infty(1 - \sin\varphi')\tan\varphi'$ (2.33) where K_c^∞ is defined in Equation (2.23).
Broms (1964a)	$N_p = 3K_p$ where $K_p = \tan^2(45^\circ + 0.5\varphi')$ (2.34)
Barton (1982)	$N_p = {K_p}^2$ where $K_p = \tan^2(45^\circ + 0.5\varphi')$ (2.35)
Zhang *et al*. (2005)	$N_p = \eta {K_p}^2 + \xi K\tan\delta$ (2.36) where η and ξ are constants related to pile types, K is equal to the lateral earth pressure coefficient at rest for driven pile, and δ is related to pile material.

2.3.3 *P-Y* CURVE EXPRESSIONS

The construction of *p-y* curves in API for stiff clay (s_u > 96 kPa), soft clay ($s_u \leq$ 96 kPa) and sand refers to three key references. The empirical expressions are briefly summarised as follows.

A. Soft clay

The expressions developed by Matlock (1970) were adopted in API. The ultimate soil resistance, p_u, is defined by Equations (2.15) - (2.16). The load-displacement relationship for laterally loaded piles in soft clay is given by a normalised curve, shown in Figure 2.7.

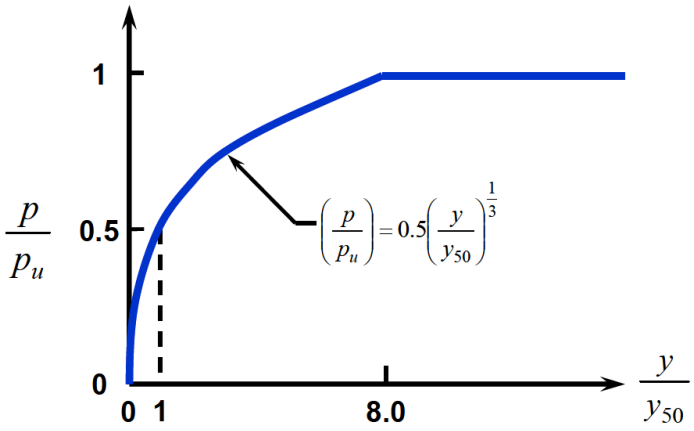

Figure 2.7 Normalised *p-y* curve for soft clay (Isenhower and Wang, 2011)

where p = actual lateral soil resistance, kPa

y = actual pile lateral displacement, mm

$y_{50} = 2.5\varepsilon_{50}D$, mm

ε_{50} = strain occurs at 50% of the maximum stress on laboratory undrained compression tests of undisturbed soil samples.

B. Stiff clay

The expressions developed by Reese and Cox (1975) were adopted in API. The ultimate soil resistance, p_c as shown in Figure 2.8, is defined by Equations (2.17) - (2.18). The load-displacement relationship for laterally loaded piles in stiff clay below water table is given by the curve shown in Figure 2.8. A_s, given in Reese and Cox (1975), is an empirical factor for static loading.

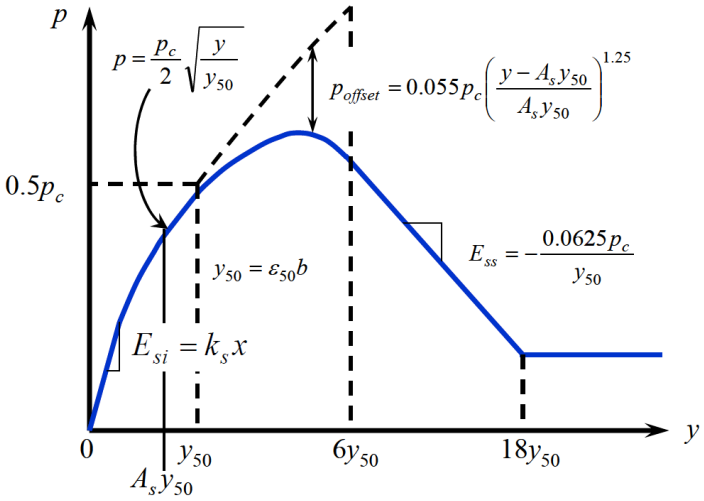

Figure 2.8 Characteristic *p-y* curve for stiff clay (Isenhower and Wang, 2011)

The symbols in Figure 2.8 share the same meanings with those in Figure 2.7. In addition, E_{si} is the initial soil modulus, which is expressed as a function with the depth, x, and an empirical factor depending on static or cyclic loading conditions, k_s. E_{ss} is the slope for the post-yielding soil response.

C. Sand

The expressions developed by O'Neil and Murchison (1983) were adopted in API. The ultimate soil resistance is defined by Equation (2.24). The load-displacement relationship for sand is defined by Equation (2.25) and illustrated in Figure 2.9. A is an empirical factor for static loading given in API (expressions see Table 2.3), and k is the initial modulus of subgrade reaction, determined as a function of soil internal fraction angle.

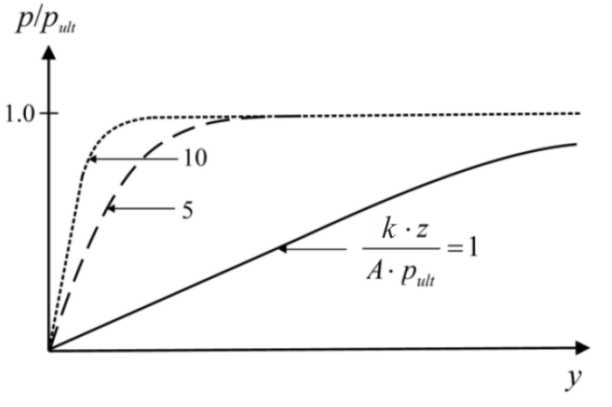

Figure 2.9 Normalised *p-y* curve for sand (Peralta, 2010)

2.3.4 LIMITATIONS

Due to the rapid expansion of offshore wind farms, design engineers are becoming more and more aware of the issues related to the application of the *p-y* methods to relatively short monopiles. The *p-y* curves were initially derived from field tests on slender piles for the oil and gas industry. However, there are some obvious differences between monopiles for OWT and piles used in the oil and gas industry, summarised in Table 2.4.

Table 2.4 Differences between OWT monopiles and oil & gas platform piles

	for OWT	for oil & gas
Pile aspect ratio, *L/D*	1-10	50-100
Pile diameter, *D* (m)	4-10	0.2-2
Applied load ratio, *H/V*	High	Low
Dominant actions	Horizontal loads Overturning moment	Vertical load (both tension and compression)

As can be seen from Table 2.4, the monopile aspect ratio is much smaller than that for the piles in the oil and gas industry, and the pile diameter for monopiles is larger than the piles used for oil and gas platforms. Furthermore, the monopiles for OWT are mainly subjected to large horizontal loads and overturning moment, with a small vertical load, while the piles in the oil and gas industry are subjected to large vertical loads and a relatively small horizontal load. The differences in both loading components and pile geometries lead to differences in pile behaviour under offshore loadings, as illustrated in Figure 2.10.

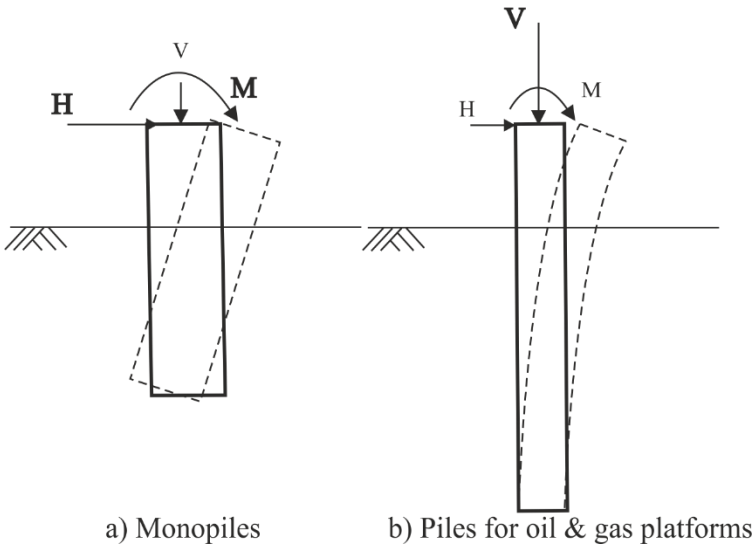

Figure 2.10 Differences in geometries, loadings and pile deformation patterns for offshore piles

Poulos and Hull (1989) defined a rigidity parameter, *R*, which depends on the pile flexural stiffness, E_pI_p, and soil Young's modulus, E_s, to classify the pile deformation mode under horizontal loads (see Equation (2.36)).

$$R = \left(\frac{E_pI_p}{E_s}\right)^{0.25} \tag{2.37}$$

They suggested that in a homogeneous soil, a pile behaved rigidly if its length was less than 1.48*R* and behaved flexibly if its length was greater than 4.44*R*. A typical monopile in relative stiff soils is more likely to behave like a rigid pile, which is supported by the "toe kick" phenomena observed in simulations presented in this thesis.

Previous research on drilled shafts and suction caissons (Davidson, 1982; Lam and Martin, 1986; Gerolymos and Gazetas, 2006 and Lam, 2013) identified that additional pile-soil interaction components, including the vertical shear stresses acting on the pile shaft, a shear force and a moment developed at the pile base, become increasingly significant when the *L/D* ratio becomes smaller. As monopile *L/D* ratios are smaller than those for piles used in the oil and gas industry, the effects due to additional pile-soil interaction components might be significant. These effects are omitted in the API *p-y* methods, which only consider lateral soil reaction.

Furthermore, permanent deformation accumulated under long-term cyclic loading, and the effect of the degradation of soil stiffness on the natural frequency of the pile-soil system is not captured by design guidance. A typical wind turbine encounters a large number of cycles (*i.e.* 10^7 to 10^8 cycles) during its service life (Leblanc *et al*., 2010). However, in the API methods, the cyclic *p-y* curves were developed based on cyclic loading tests with a limited number of cycles (up to hundreds of cycles). The extensions of the *p-y* method to cyclic loading are rudimentary and simplistic. The change in soil stiffness during long-term cyclic loading may lead to resonance, which could result in significant deformation. The design issues related to cyclic loading should be properly addressed in future design methods for monopiles. However, this is beyond the scope of the thesis.

Evidence on the limitations of the *p*-y methods applied to monopiles is shown in field tests performed at Horns Rev and in the Persian Gulf. The measurements indicated that the current design method overestimated the displacement and rotation at the pile-head by 30%-50%, and the stiffness of the measured pile response was underestimated (Hald *et al*., 2009; Hokmabadi *et al*., 2012). An improvement of the API *p-y* methods is therefore required to give better predictions of monopile responses. This is the primary focus of the PISA project.

2.4 PISA WORK

In the PISA project, state-of-the-art FE analyses, advanced laboratory tests and high-quality field tests were performed to investigate and develop new design methods. Two approaches have been developed: a) a rule-based method; and, b) a numerical-based method. Either of the design processes can be used to develop appropriate soil reaction curves, which are then used to calibrate the 1D model for monopile design. The procedures of the rule-based approach and the numerical-based approach are outlined in Figure 2.11.

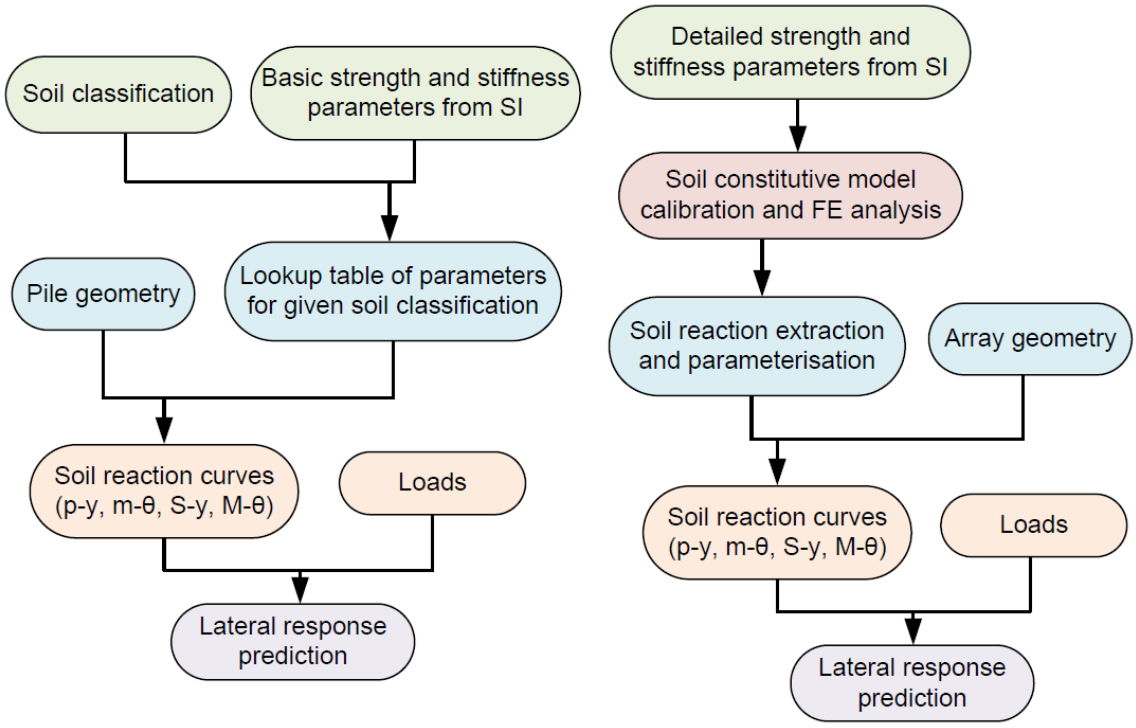

Figure 2.11 Procedures of the rule-based and numerical-based design approaches (PISA AWG, 2014a)

The application of the numerical-base design method was demonstrated in the PISA project, and as a consequence, expressions for the rule-based method were developed. Two sites were chosen to be representative of soils in the North Sea, the Cowden clay site located in northeast England and the Dunkirk sand site located in northern France. The soil parameters used in the simulations were developed from site investigation and advanced laboratory tests. Advanced 3D FE analyses were carried out using the finite element software ICFEP (Potts and Zdravković, 1999, 2001). An extended generalised version of the non-linear elasto-plastic Modified Cam Clay model was adopted for clay (Potts and Zdravković, 1999; Tsiampousi *et al*., 2013), while a bounding surface plasticity model was adopted for sand (Taborda *et al*., 2014; Manzari and Dafalias, 1997). Soil reactions were extracted from the stresses at integration points of the interface elements around

the pile shaft, and from the nodal forces acting on the pile and soil elements at the bottom of the soil plug.

11 calibration analyses were performed at each site. Soil reaction curves were developed from the calibration analyses covering a range of expected values of pile dimension and load eccentricity. To develop the generalised expressions for soil reaction curves, a procedure to normalise and parameterise the extracted soil reaction curves from 3D FE analyses was proposed. The dimensionless groups employed in the PISA project are shown in Table 2.5, where the soil parameters, I_R and I_S, are given in Equations (2.38) and (2.39), respectively.

Table 2.5 Normalisation used in the new design methods

Normalised component	Symbol	Clay normalisation*	Sand normalisation**
Distributed load	$\bar{p}$	$\frac{p}{s_u D}$	$\frac{p}{\sigma'_{vi} D}$
Distributed moment	$\bar{m}$	$\frac{m}{s_u D^2}$	$\frac{m}{pD}$
Base horizontal force	$\bar{S}$	$\frac{S}{s_u D^2}$	$\frac{S}{\sigma'_{vi} D^2}$
Base moment	$\bar{M}$	$\frac{M}{s_u D^3}$	$\frac{M}{\sigma'_{vi} D^3}$
Pile lateral displacement	$\bar{v}$	$\frac{v}{D} I_R$	$\frac{v}{D} I_S \sqrt{\frac{P_a}{\sigma'_{vi}}} [= \frac{v}{D} \frac{G}{\sigma'_{vi}}]$
Pile rotation	$\bar{\theta}$	θI_R	$\theta I_S \sqrt{\frac{P_a}{\sigma'_{vi}}} [= \theta \frac{G}{\sigma'_{vi}}]$
Depth	z/D	z/D	

Note: * Undrained shear strength s_u corresponds to the value measured in triaxial compression tests;
**σ'_{vi} corresponds to local vertical effective stress. P_a corresponds to the standard atmospheric pressure.

$$I_R = \frac{G_0}{s_u} \tag{2.38}$$

$$I_S = \frac{G_0}{\sqrt{P_a \sigma'_{vi}}} \tag{2.39}$$

A conic function was selected to describe the shape of the elemental response for the distributed load, base horizontal force and base moment, while a bilinear function was initially used for the distributed moment in the draft reports (PISA AWG, 2014a, 2014b). In the final report (PISA AWG, 2016), a modified conic function was used for all the soil reaction components. The general forms are represented by $\bar{y} = f(\bar{x})$, where $\bar{x}$ refers to normalised displacement variables

and $\bar{y}$ refers to the normalised soil reaction components. The conic and bilinear functions are given in Equations (2.40) - (2.43). Their forms are illustrated in Figure 2.12.

(a) Conic:

$$\bar{y}(\bar{x}) = \begin{cases} \sqrt[n]{\dfrac{(B+1-(1-{}^{\bar{x}}/_{\bar{x}_u})^m)}{B}} - 1, & \bar{x} < \bar{x}_u \\ \bar{y}_u, & \bar{x} \geq \bar{x}_u \end{cases} \tag{2.40}$$

$$B = \frac{1}{(1+\bar{y}_u)^n - 1} \tag{2.41}$$

$$m = Bnk\bar{y}_u \tag{2.42}$$

(b) Bilinear:

$$\bar{y}(\bar{x}) = \begin{cases} k\bar{x}, & \bar{x} < {}^{\bar{y}_u}/_{k} \\ \bar{y}_u, & \bar{x} \geq {}^{\bar{y}_u}/_{k} \end{cases} \tag{2.43}$$

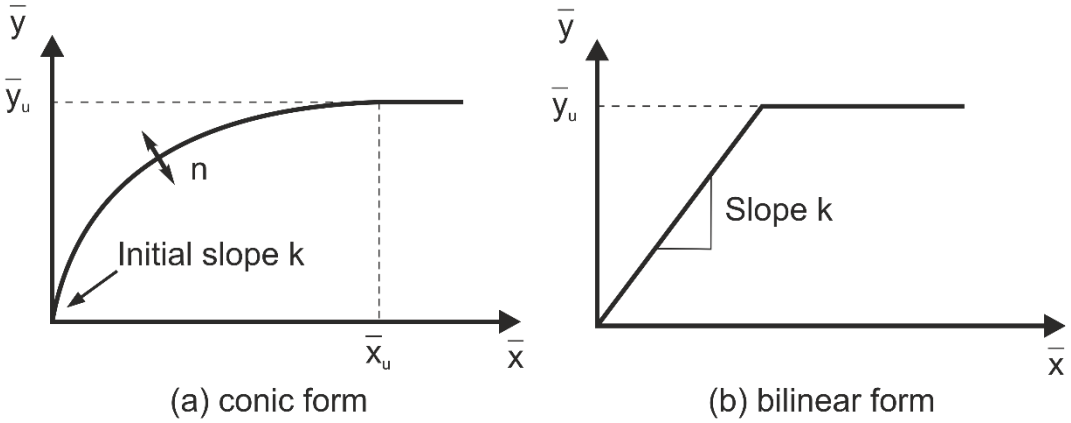

Figure 2.12 Proposed function forms for soil reaction curves

The process used in the PISA project to determine parameters from the extracted soil reaction curves is:

1. A single value of ultimate displacement $\bar{x}_u$ was selected manually at which the reactions for all depths have reached their approximate ultimate values.

2. The initial stiffness parameter was determined by fitting the linear expression $\bar{y} = k\bar{x}$ using a least squares fit over the small displacement region of $0 < \bar{x} < {}^{\bar{x}_u}/_{20}$.

3. The ultimate response of each soil reaction $\bar{y}_u$ and the curvature *n* (if applicable) were fitted using a proportional least squares fit, as given by Equation (2.44).

$$f_{error} = \sqrt{\sum_{i=1}^{last\ increment} \left(\frac{\bar{y}^i{}_{parameterised} - \bar{y}^i{}_{numerical}}{\bar{y}^i{}_{numerical}}\right)^2} \quad (2.44)$$

where $\bar{y}^i{}_{parameterised}$ is determined from Equations (2.40) - (2.43), *i* indicates the results in the i[th] increment.

Sets of parameterised expressions were developed for clay and sand. They are presented in Chapters 4 and 5 and compared with the results developed in this thesis. They can be used as input to a 1D FE model, used for fast prediction of monopile response, essential in the types of analyses carried out in the offshore wind sector.

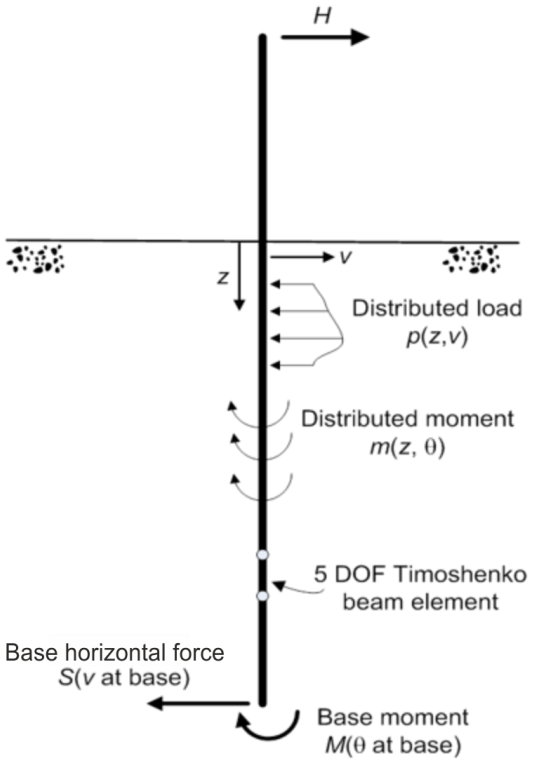

Figure 2.13 Proposed 1D model for the design of monopiles (Byrne *et al*., 2015)

The 1D model used for the design is illustrated in Figure 2.13. The pile was represented by Timoshenko beam elements, consisting of 4 DOF, which are the same as those for traditional Euler-Bernoulli beam elements, and one independent rotational DOF related to element shearing. There were 4 Gaussian integration points per element. Hermitian shape functions were used to define lateral displacement and rotation in both the pile and the soil. The model was formulated using a variational approach. According to virtual work theory for a static system, the sum of the internal and external virtual work is zero (see Equation (2.45)). The external virtual work and

internal work induced by different soil reaction components was defined by Equations (2.46) and (2.47).

$$0 = \delta W_E + \delta W_I \tag{2.45}$$

$$\delta W_E = H\delta v_T \tag{2.46}$$

$$\delta W_I = \int_{Pile} \left[EI \frac{d\delta\theta}{dz}\frac{d\theta}{dz} + GAK_s\left(\delta\theta + \frac{d\delta v}{dz}\right)\left(\theta + \frac{dv}{dz}\right) + p(z,v)\delta v + m(z,\theta)\delta\theta \right] dz + M(z,\theta)\delta\theta_b + S(z,v)\delta v_b \tag{2.47}$$

$$K_s = \frac{1+v}{2+v} \tag{2.48}$$

(v is the Poisson's ratio of the pile)

where v_T – lateral pile displacement at the application point of the horizontal load H,

θ – rotation of the pile cross-section,

EI – flexural rigidity of the pile,

A – cross-sectional area,

G – soil shear modulus,

K_s – shear factor, defined by Equation (2,47). The current PISA approach used 0.5 for this parameter.

The functions, $p(z,v), m(z,\theta), M(z,\theta)$, and $S(z,v)$, are the soil reaction curves, which are described in more detail later in the thesis. MATLAB code for the 1D model was developed in the PISA project. The 1D predictions using the calibrated 1D model were compared with the predictions using the API *p-y* methods and the results obtained from the 3D FE analyses. It was demonstrated that the calibrated 1D model gave better predictions of pile response than the *p-y* methods.

2.5 SUMMARY

This chapter presents a general review of the design guidelines for monopiles and previous research on the deformation analysis of laterally loaded piles. Differences exist in pile dimensions, load conditions and deformation pattern between monopiles for OWT and piles for the oil and gas industry. The *p-y* methods, recommended by the current design guidelines, were initially developed for long slender piles for oil and gas structures, and found to be questionable for monopiles with relatively small *L/D* ratios. The limitations of the *p-y* methods were discussed and the new design methods proposed in the PISA project were introduced. The two design approaches, the rule-based method and numerical-based method were outlined. The procedure of the numerical-based method and the calibration for the 1D model, which provides the basis for the methodology in this study, was elaborated. The PISA work has demonstrated the capability of the new design approaches for two reference soils by comparisons with medium scale field test results. Further work is required to examine the robustness of the new design methods for varied design scenarios.

Chapter 3

THREE-DIMENSIONAL FINITE ELEMENT MODELLING

3.1 INTRODUCTION

This chapter focuses on the 3D FE models used for the analysis of monopiles under lateral loading. They provide the basis for soil reaction curves for the 1D model and load-displacement results for the verification of 1D predictions. Preliminary analyses were conducted to explore model parameters, the influences of element types for soil, as well as consideration of different extraction approaches. Other effects such as the presence of a vertical load and gapping at pile-soil interface were also examined. The soil types considered in the analyses are undrained clay and drained sand. Note that the selection of the soil parameters for clay and sand, and corresponding soil reaction curve results are presented in further detail in Chapters 4, 5 and 6. For each analysis, a code is given to define the tested pile and soil conditions, formatted as AA-BB-CC. The identifiers and their meanings are presented in Table 3.1.

Table 3.1 Identifiers and their meanings for the naming scheme of the analyses

Identifier	Meaning
AA	Reference for the analysis type (C for the Calibration analyses, T for the Test analyses, P for the Preliminary analyses, RLT for the Rigid pile Lateral Translation analyses, RBR for the Rigid pile Base Rotation analyses)
BB	Reference for the tested pile condition listed in Table 3.2
CC	Reference for the tested soil condition (CS for clay, SS for sand, LS for layered soils) given in Table 4.1, Table 5.1 and Table 6.1

Table 3.2 Pile geometries and loading conditions used in the analyses in this study

Analysis reference	*D* (m)	*L* (m)	*h* (m)	*t* (mm)	*L/D*
P1	10	20	50	91	2
P5	10	60	150	91	6
P7	5	10	25	83	2
P8	5	30	25	45	6
P4	10	60	50	91	6
P10	7.5	15	37.5	68	2
P4-2	10	40	50	91	4
P4-3	10	40	80	91	4

The pile geometries and loading parameters given in Table 3.2 are defined in Figure 3.2. The pile wall thickness, *t*, has a minor influence on the pile deformation, as indicated by the numerical analyses in PISA, hence its variation was not included within the calibration analyses. The values of these parameters are partially selected from those used in the calibration analyses in PISA, which are considered representative for monopiles for future wind farms (Byrne *et al*., 2015). As shown in Figure 3.1, the first four piles are located at the boundary of the parameter space of interest; they were used in the calibration analyses, which are used to develop soil reaction curves. The last four piles are located within the range of interest; they were used in the test analyses, which are used to examine the performance of the 1D model.

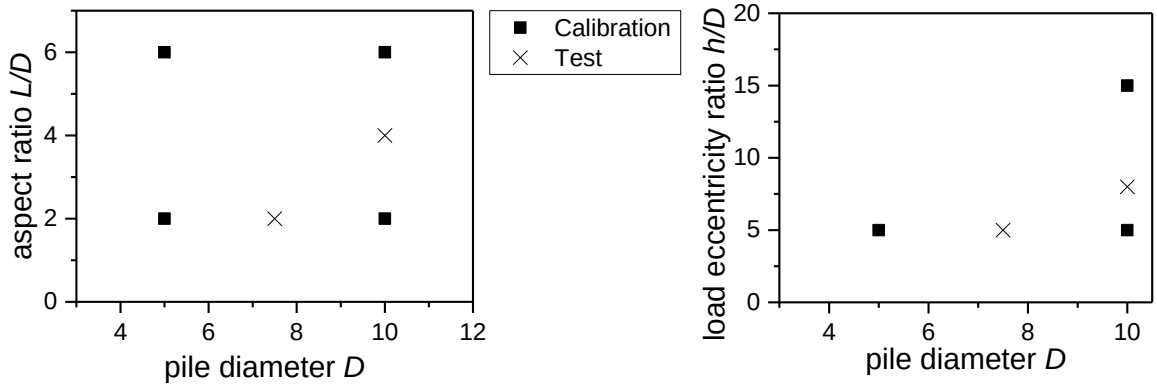

Figure 3.1 Pile parameters used in the calibration and test analyses

3.2 3D FE MODEL

The 3D models were developed using commercial finite element software Abaqus/Standard (Abaqus 2013, Version 6.13). The reasons to use Abaqus are that, (i) it is commonly used by offshore engineering consultancies and designers, and (ii) the examination and extraction of element stresses and nodal forces are relatively easy to achieve compared to other commercial software. Regarding the 3D FE models, half-symmetry was adopted to ease the computational effort, as shown in Figure 3.2. The models consist of three parts: an open-ended tubular steel pile, the surrounding soil and the soil plug. The soil plug inside the pile was assumed to exist along the pile entire length below the seabed level. This is a realistic assumption supported by design guidelines in which the length of the soil plug inside the pile are generally found to be 0.9 times the pile embedded length (Rosjberg and Gravesen, 2009).

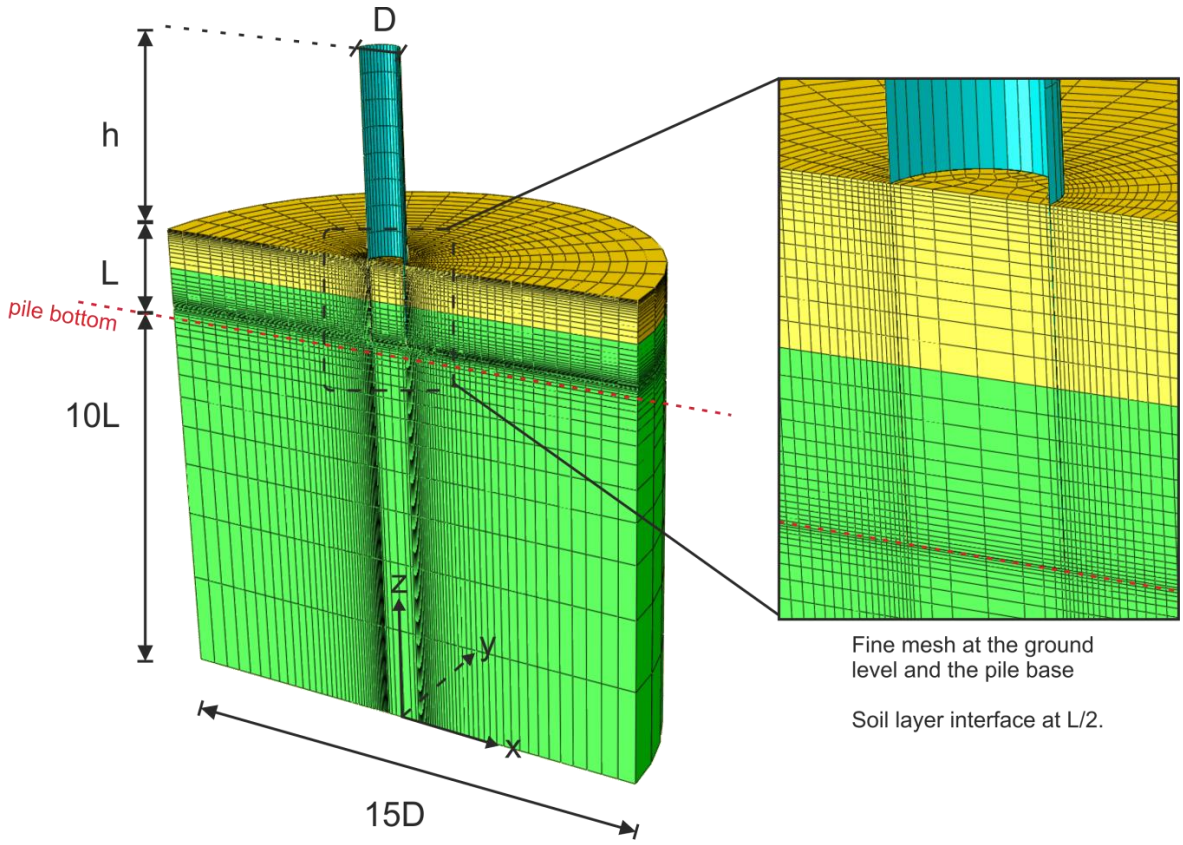

Figure 3.2 Dimensions and mesh for a representative 3D FE model (yellow and green refer to the different soil layers for the layered soil analyses)

The bottom of the soil was fixed in the three coordinate directions (x, y and z). The displacement in the y-direction at the symmetric plane (y = 0) and the rotational DOFs with respect to x- and z-axes along the edge of pile shell elements in the symmetric plane were set to zero. The soil domain dimensions were chosen to minimize the effect of the boundary constraints on pile movement. The outer diameter of the soil domain was set as 15 times the diameter of the pile, and

the bottom was set as 10 times the embedded length of the pile. These dimensions were verified by comparing the load-displacement results with those with greater dimensions and the differences were minimal. The mesh at the pile bottom was refined to ensure the accuracy of extracted base soil reaction results. A typical mesh density adopted is shown in Figure 3.2, and the quantity of elements in the final 3D FE analyses is generally between 2×10^5 and 3.5×10^5.

Three mesh sensitivity analyses with different degrees of mesh density were carried out before the final 3D FE analyses. The visual mesh comparison, number of elements, and computation time of the mesh sensitivity analyses are given in Table 3.3. The load-displacement results for different meshes are shown in Figure 3.3. As expected, the ultimate load decreases with increasing mesh density. The differences in load-displacement results using Mesh 2, which is also the adopted mesh for the final 3D FE analyses, and a finer mesh (*i.e.* Mesh 3) were marginal. However, the computation time for the analysis using a finer mesh is much higher than that of using Mesh 2. Hence, the adopted mesh is considered a good balance between computational cost and result quality.

Table 3.3 Comparisons of the mesh sensitivity analyses (P-P8-CS0 analyses)

Mesh 1	**Mesh 2**	**Mesh 3**
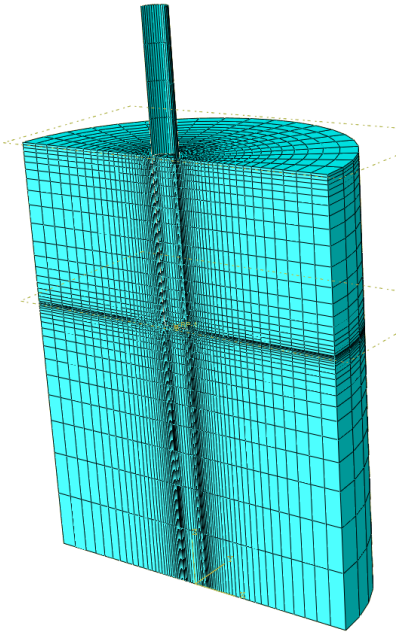	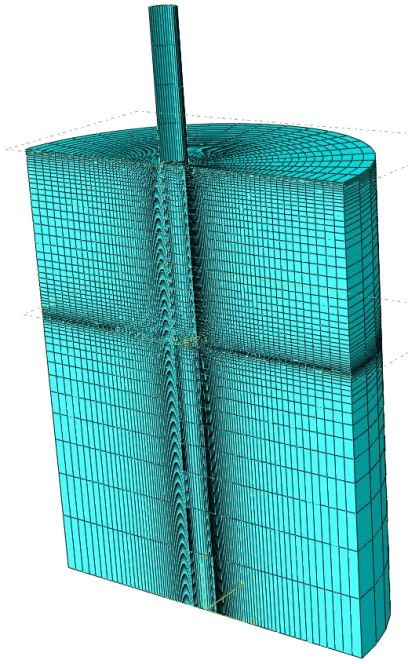	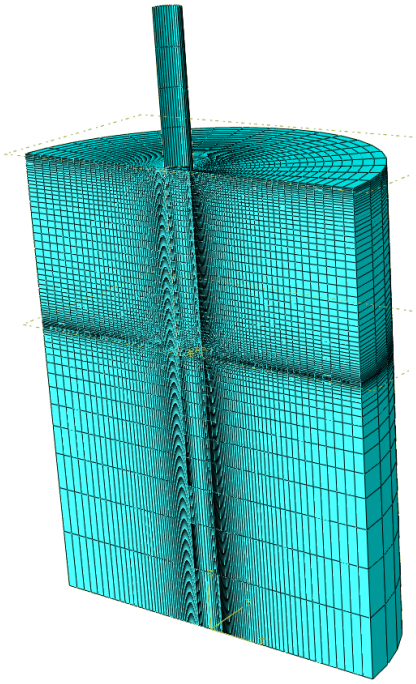
Element number		
15104	34880	45472
Computation time (Processor: Intel(R) Xeon(R) CPU E3-1270 v3 @ 3.50 GHz; RAM: 16.0 GB; Operating System: 64-bit; Parallelization: 2 processors, default multiprocessing mode)		
3.6 hrs	9.7 hrs	17.2 hrs

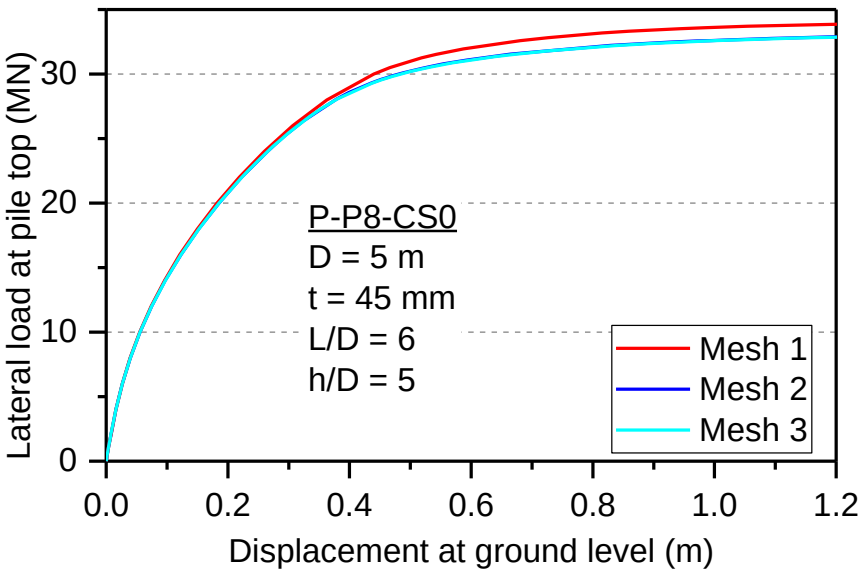

Figure 3.3 Comparison of load-displacement results for mesh sensitivity analyses (the results of Mesh 2 and Mesh 3 are overlapped)

The pile was discretised with 4-noded doubly curved reduced integration shell elements with hourglass control and finite membrane strains. The soil was discretised with 8-noded linear reduced integration solid elements, with hourglass control. The element types were selected based on quality of results, computational cost, and the ability to extract soil reaction curves. The pile behaviour was simulated using a linear elastic material, with Young's modulus of 200 GPa and a Poisson's ratio of 0.3, maintaining consistency with those used in PISA (Zdravković *et al*., 2015). The pile was assumed weightless for simplicity, as pile weight was considered to have a negligible effect on the analyses.

Elastic perfectly plastic soil models were adopted in this study. The motivation for choosing simple soil models relates to the required soil parameters for input, which can be obtained from routine site investigation. These soil models take into account basic soil properties such as elasticity and plasticity, and nonlinearity of pile response. As most analytical solutions were developed using perfectly plastic soil models, using the same soil models enable direct comparisons of the computed results with known analytical solutions. Undrained clay was modelled as elastic perfectly plastic with Von Mises failure criterion and a Poisson's ratio close to 0.5. Drained sand was modelled as elastic perfectly plastic with Mohr-Coulomb failure criterion and effective soil parameters. The layered soil analyses were performed with effective stresses to ensure consistency in overburden stress level. The selection of the soil parameters for the clay, sand and layered soil analyses are presented in further detail in Chapters 4, 5 and 6.

The contact between the monopile and the soil was modelled using Mohr-Coulomb friction law, via the contact pairs approach in Abaqus. The maximum shear stress allowed at the interface is controlled by the coefficient of friction, μ, and the adhesion parameter, α (definitions see Figure 3.4). The adhesion parameter was set as unity for simplicity. The selection of μ was based on the plasticity index in clay and effective friction angle in sand. Regarding the normal contact stress, it is either negative in compression or zero in tension ('allow gapping'), or allowed to be infinite in tension ('no gapping'). The three parts (*i.e.* the pile, the surrounding soils and soil plug) use the same mesh at the interface to ensure convergence. The interface parameters adopted in the clay, sand and layered soil analyses are given in further detail in Chapters 4, 5 and 6.

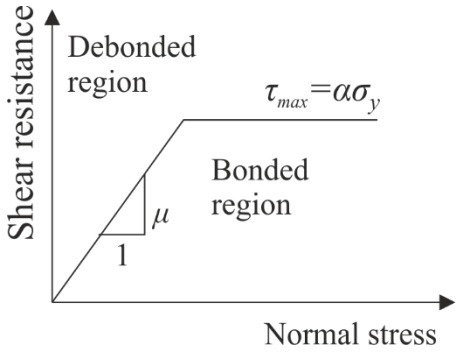

Figure 3.4 Shear resistance at contact interface (Abaqus Users' Manual, 2013) (σ_y is the minimum yield stress of the two objects in contact)

Stages of analysis

Each analysis consists of three steps. Firstly, an initial geostatic stress field was imposed without the pile. Secondly, the pile and the contact were both "activated". Lastly, the pile was displaced / loaded incrementally until failure thereby obtaining a complete load-displacement curve for each analysis.

In the clay analyses, a horizontal shell edge load was applied at the pile top. The incremental loads in the x-direction were applied uniformly around the pile top perimeter (unit: F/L), while the z- and y-axis components of the shell edge load were kept zeros during the analyses. The moment acting on the monopile about ground level was then given by $M = Hh$, where H is the total horizontal load (unit: F) applied at the top of the pile and h is the height of the pile top from the ground level. There was no displacement constraint applied to the pile. In the sand analyses, the loading step was performed in a displacement controlled manner to enable better convergence. The incremental displacement in the x-direction was applied uniformly around the pile top perimeter, while no constraint was applied to the z- and y-axis displacements and rotational DOF at the pile top. The total horizontal load acting on the pile was then obtained as the reaction to the imposed

displacement. Preliminary analyses confirmed that the load-displacement results for the piles with imposed displacement and with imposed load were the same for materials without softening.

In the 3D FE analyses, the pile was wished-in place, without considering effects of pile installation. It has been recognised by previous researchers (Randolph *et al*., 1979; Carter *et al*., 1979; Randolph and Wroth, 1979; Yang *et al*., 2010) that pile installation causes disturbance of soil around the pile shaft and potentially affects pile deformation and capacity under loading. However, for driven piles, the disturbance is limited to a zone of relatively small thickness around the pile, whereas the soil in a much larger zone is subjected to stress increase due to horizontal loading (Achmus *et al*., 2009). Therefore, FE analyses of driven pile behaviour usually neglect pile installation effects (see examples in Fan and Long, 2005; Abdel-Rahman and Achmus, 2005; Augustesen *et al*., 2009).

Pile and soil deformation

The computed deformation of a short pile (L/D = 2, D = 10 m) under lateral loading is illustrated in Figure 3.5. Displacement vectors are shown by red arrows. Von Mises stress contours are shown by coloured lines. The red contour corresponds to the extent of soil yielding around the pile.

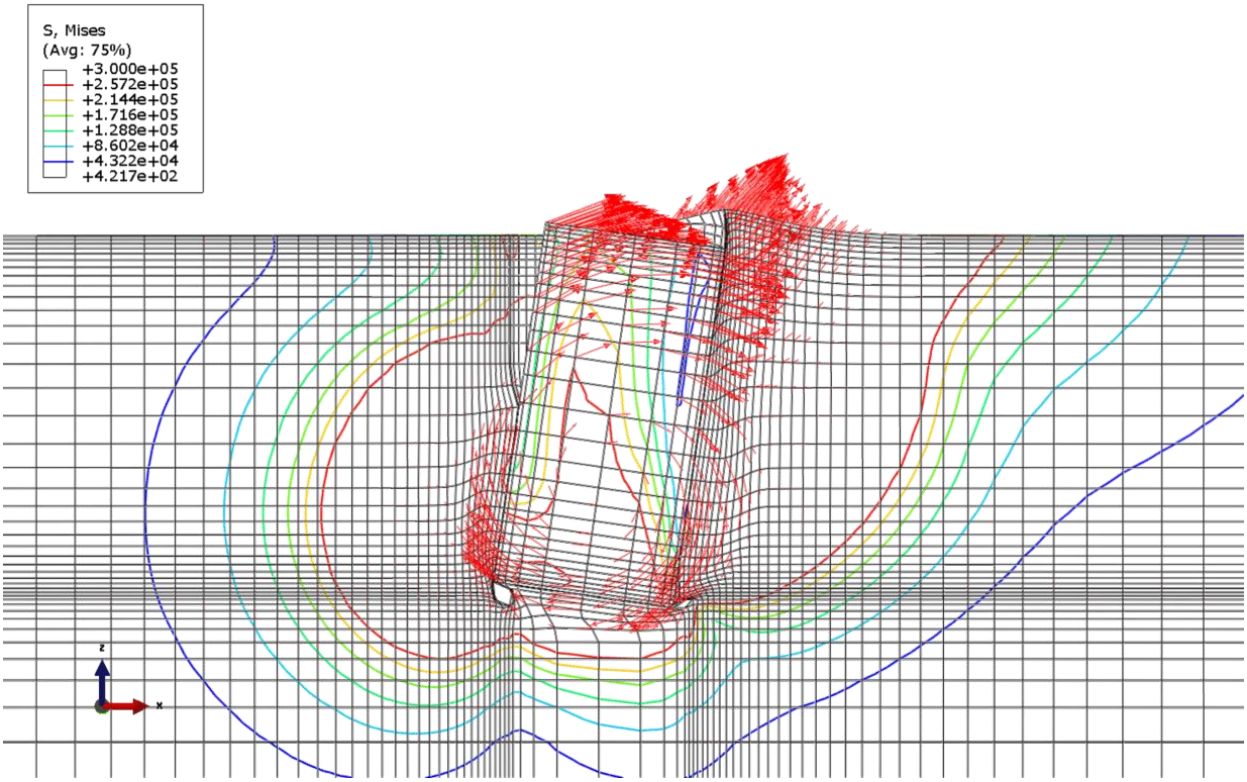

Figure 3.5 Displacement vector (red arrows) and Von Mises stress contour (coloured lines) plot at the symmetric plane (C-P1-CS0 analysis, at *H* equals to 50% of the ultimate load)

As shown in Figure 3.5, the pile behaves rigidly and rotates at depth of 3/4 of the pile embedded length. “Toe kick” is found at the pile base. On the passive side of pile, the soil at the surface moves upward and forward. The displacement vectors shown near the ground surface confirm the wedge failure assumption. Interestingly, the soil around the pile base rotates with the pile. The displacement vectors of soil at greater depth indicate that the plane strain failure mechanism is not applicable for this case; the mechanism corresponds more likely to a spherical-rotation-type failure.

3.3 EXTRACTION OF SOIL REACTION CURVES

The nodal forces of the soil elements immediately surrounding the pile (shown using red dots in Figure 3.6) were obtained from the 3D FE analysis output. The nodal forces were output to data files and then post-processed in a MATLAB programme (ver. 2015a).

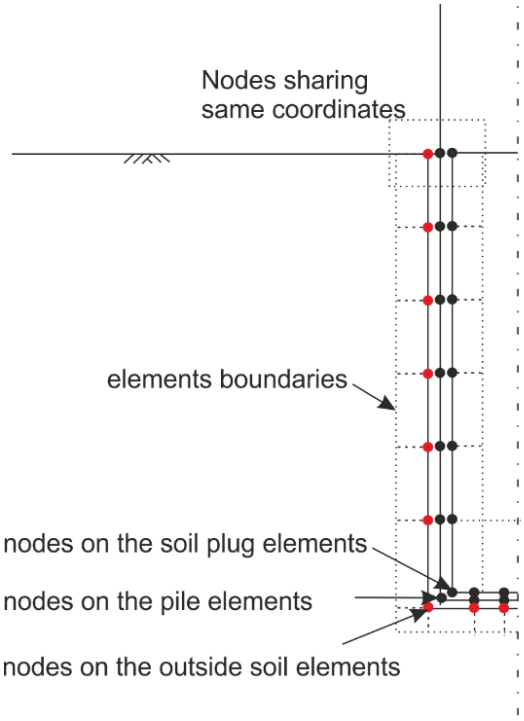

Figure 3.6 Half-section view of the FE model with nodes and elements at the interface

Regarding the sign convention used for the calculation, the positive displacement direction was defined the same as the applied force direction, and the soil pressure was assumed positive in the direction opposite to the pile displacement. The sign convention for the soil reactions and pile deformation is given in Figure 3.7.

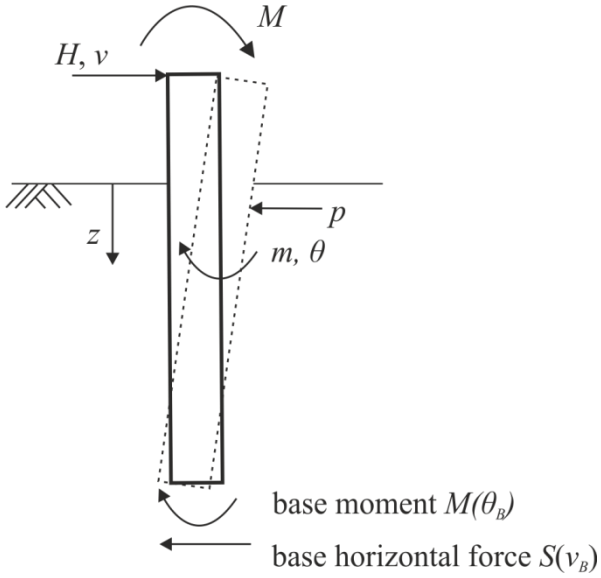

Figure 3.7 Sign convention for the applied loads, soil reactions and pile deformation

The distributed lateral soil reaction (*i.e.* the soil resistance per unit length along the pile, unit: *F*/*L*) was derived from the reference locations, which was defined at the middle of the element area at the interface (see Figure 3.6). As the soil elements considered are eight-noded hexahedral elements with assumed strain stabilization and uniform reduced integration (Abaqus Analysis User's Manual 6.13, 2013; Belytschko and Bindeman, 1992), the stress field in an element is uniform. Hence, the distributed lateral soil reaction was calculated by dividing the sum of the horizontal nodal forces of a ring of elements at the same depth by the shared length of the ring of elements along the pile length direction. The pile lateral displacement was interpolated from the average nodal displacement of the shell elements at the same depth.

The distributed moment (unit: *FL*/*L*) was obtained at the same reference locations as those for the distributed lateral soil reaction, by multiplying the distributed vertical shear forces with the distance from the neutral axis of the pile. The distributed vertical shear forces (unit: *F*/*L*) of a soil element acting at the pile (shown as τ in Figure 3.8) was calculated by dividing the sum of the vertical nodal forces by the length of the element along the pile length direction. Because the mesh around the pile was refined, the distance from the neutral axis of the pile was measured from the reference location on a plane, as illustrated in Figure 3.8. The rotation of the pile cross-section was found by plotting the vertical nodal displacement against the distance of the node from the central axis of the pile cross-section, and calculating the slope of the best linear fit.

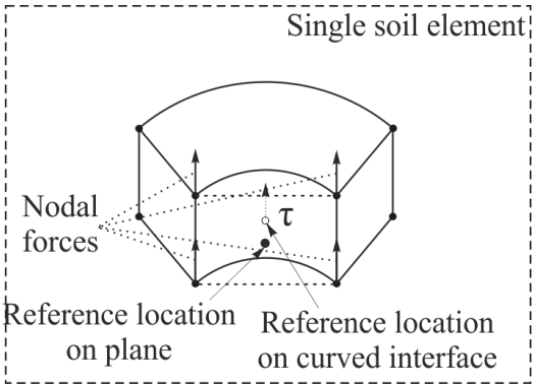

Figure 3.8 Illustration of the calculation of the distributed vertical shear force

The calculations of the distributed lateral reaction and moment presented here were based on the assumption that the stress field in an element is uniform. For second-order elements, an alternative method was used and is discussed in the next section.

The calculations of the base soil reaction components involved summing the nodal forces from the soil elements located immediately below the pile base and soil plug. The base horizontal force was calculated from the sum of the horizontal nodal forces. The base moment was calculated with reference to the same nodes as those for the base horizontal force, but by summing the product of the vertical nodal forces and the lateral distances from the pile neutral axis.

Figure 3.9 shows the typical extracted soil reaction curves. It is clear that the distributed soil reaction curves vary with depth. The negative displacements indicate that “toe kick” occurred at the pile base. And the rotation point location was about 3/4 of the pile embedded length for this case.

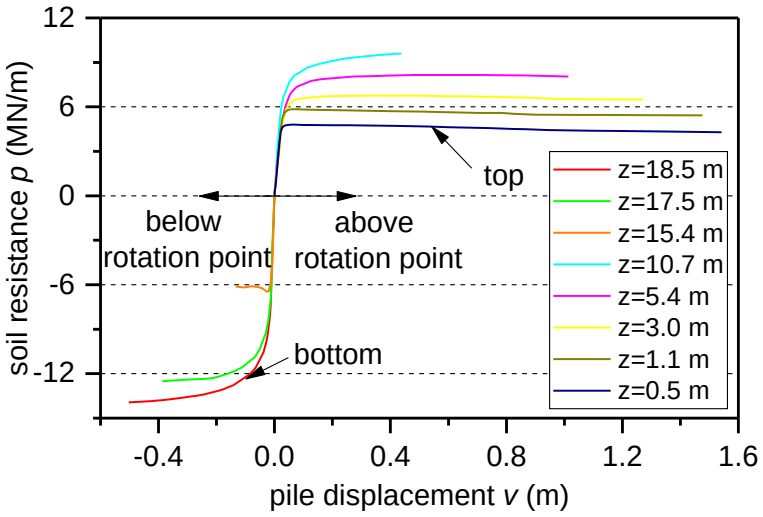

(a) Distributed load curves

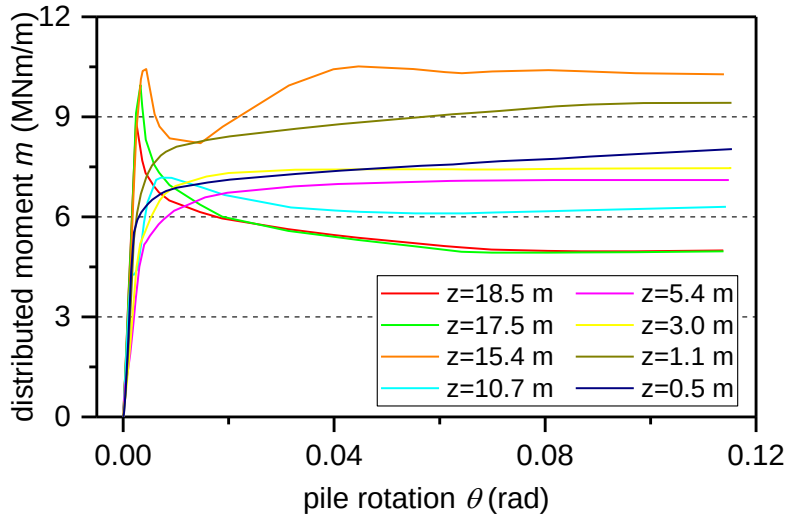

(b) Distributed moment curves

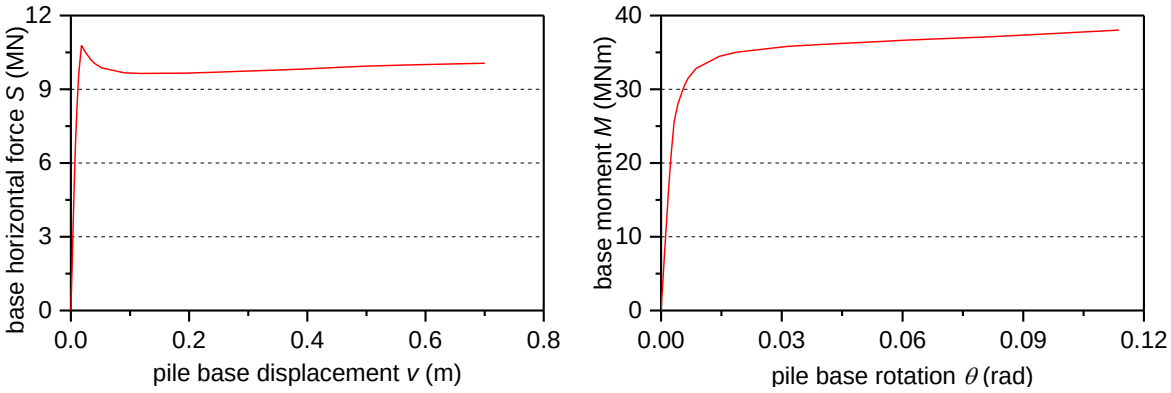

(c) Base horizontal force curve (d) Base moment curve

Figure 3.9 Typical extracted soil reaction curves (C-P1-CS0 analysis)

For each analysis, an initial equilibrium check was performed, by calculating the errors between the sum of the soil reaction components and the applied loads. The moment was calculated with respect to the ground level. Figure 3.10 shows typical results obtained from this equilibrium

check. The agreement between the total horizontal forces calculated from the extracted data and the applied load was satisfactory, with overall errors within 2% for all displacements.

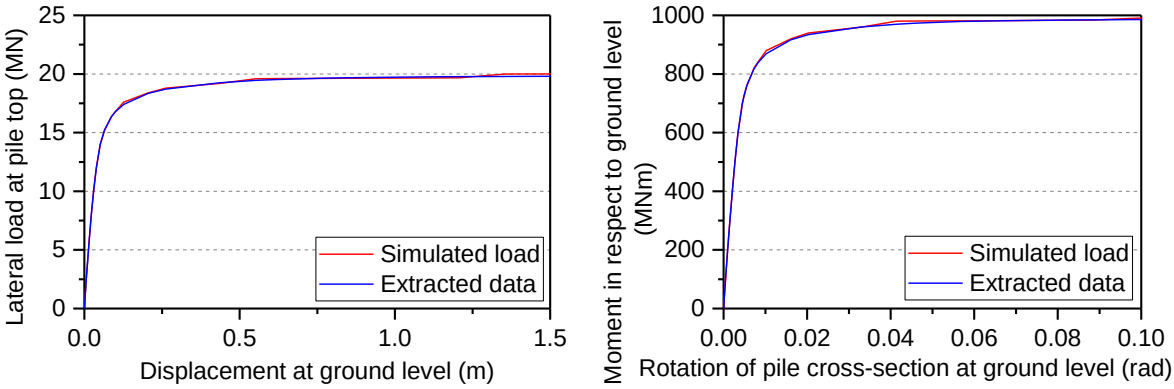

Figure 3.10 Typical equilibrium check results for the extracted data (C-P1-CS0 analysis)

3.4 CHOICE OF ELEMENT TYPES AND ALTERNATIVE EXTRACTION METHODS

To decide the soil element type used for the 3D analyses, a series of preliminary analyses were performed. The soil, pile conditions and mesh layout remained the same in these analyses. To avoid volumetric locking for nearly incompressible material such as undrained clay, elements with reduced integration are often used. The three reduced integration element types: C3D8R, C3D20R and C3D27R in the element library in Abaqus were selected for the preliminary analyses (see Figure 3.11). Their integration point schemes are given in Table 3.4. Both the load-displacement response and soil reaction curves obtained from the preliminary analyses are compared.

It is worth mentioning that the C3D8R element in Abaqus is different from first-order reduced integration elements in classic finite element theory. The single-point reduced-integration scheme in Abaqus is based on the "assumed uniform strain formulation": the strains are not obtained at the first-order Gauss point but are obtained as the (analytically calculated) average strain over the element volume (Abaqus Users' Manual). The assumed uniform strain method, proposed by Flanagan and Belytschko (1981), and further developed by Belytschko and Bindeman (1993), ensures that the first-order reduced-integration elements pass the patch test and retain accuracy when elements are skewed. The C3D8R element is free from volumetric locking in three-dimensional non-linear problems. The two second-order element types in Abaqus using Gaussian quadrature are the same as those in classic finite element theory (Cook *et al.*, 2002; Zienkiewicz *et al.*, 2005).

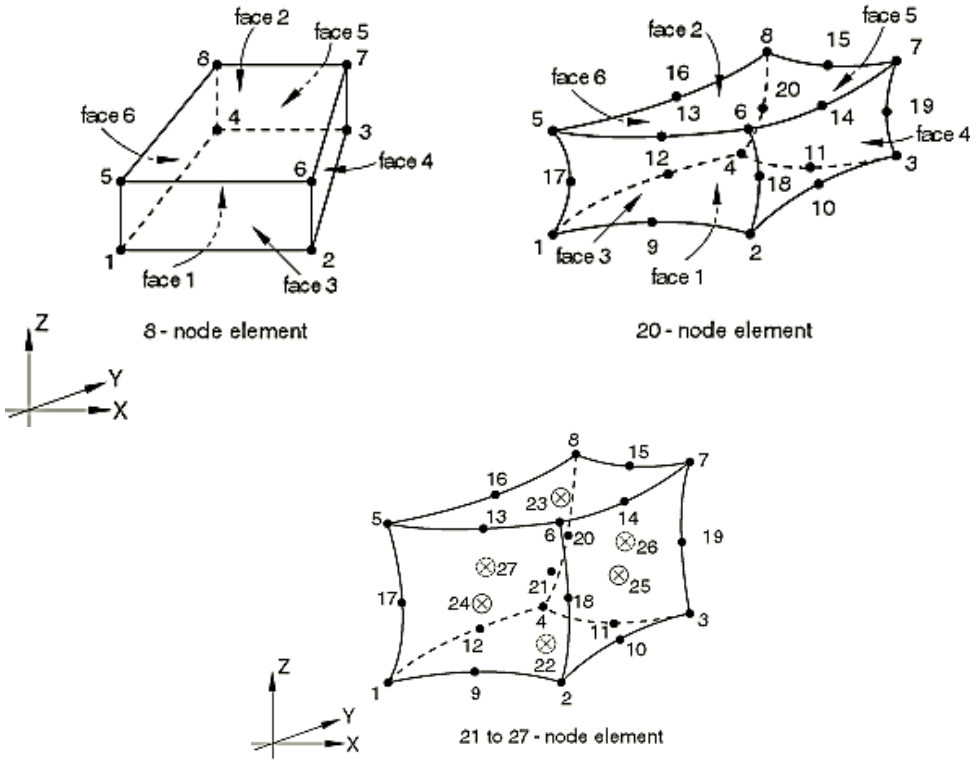

Figure 3.11 Node distribution for C3D8R, C3D20R, C3D27R elements in Abaqus (Abaqus Analysis User's Manual 6.13, 2013)

Table 3.4 Integration scheme for C3D8R, C3D20R, C3D27R elements

Element type	Integration point scheme
C3D8R	1*1*1
C3D20R, C3D27R	2*2*2

For second-order elements, an alternative method proposed by Fan and Long (2005) was used to calculate the soil reactions. The soil reaction curves were calculated from the stresses at the integration points of the soil elements immediately surrounding the pile. The distributed lateral soil resistance is the *x*-component of the total stress acting on the interface. The *x*-component stress in a soil element can be represented by traction vector, T_x, calculated as follows:

$$T_x = \sigma_{xx} n_x + \sigma_{xy} n_y + \sigma_{xz} n_z \tag{3.1}$$

$$n_x = cos\theta_x = \frac{x}{R} \tag{3.2}$$

$$n_y = cos\theta_y = \frac{y}{R} \tag{3.3}$$

$$n_z = cos\theta_z = 0 \tag{3.4}$$

where x, y are the coordinates of the nodes;

σ_{xx} is the normal stress in the x-direction;

σ_{xy}, σ_{xz} are the shear stress in the xy- and xz-plane;

R is the radius of the pile cross-section.

To calculate the total soil resistance in the x-direction, p_x, per unit length along the pile, the soil resistance was integrated over the circumference of the pile cross-section, and p_x was expressed as:

$$p_x = \int T_x \, dL \tag{3.5}$$

where dL is the infinitesimal length along the pile perimeter.

The distributed moment per unit length along the pile is the z-component of the total stress acting on the interface times the distance from the y-axis (supposing the pile rotates about the y axis). Similar to T_x, the traction vector of the z-component of stress in a soil element is defined as:

$$T_z = \sigma_{zx} n_x + \sigma_{zy} n_y + \sigma_{zz} n_z \tag{3.6}$$

The distributed moment was then calculated as:

$$m = \int T_z \cdot R \cdot \cos(\Phi) \, dL \tag{3.7}$$

where Φ is the radial angle between the element integration points and the x-axes.

The calculations for the horizontal displacement, the rotation of the pile cross-section and the base soil reactions were the same as the calculation used for the first-order elements.

Figure 3.12 and Figure 3.13 show the comparisons of the load-displacement results and the ultimate load and moment responses for the three tested element types. It is evident that the differences in the overall load-displacement curves were minor. From Figure 3.13, stress oscillations at the pile base are shown in the soil reaction curves for C3D20R and C3D27R. The ultimate soil reaction for quadratic elements was slightly lower than that for linear elements, as expected. The ultimate soil reactions with depth obtained by two different extraction methods were in good agreement. Table 3.5 indicates that the use of second-order elements is computationally much more expensive than C3D8R element. Considering the computation time, the amount of output data and the smoothness of the extracted results, C3D8R was used for soil elements in all the 3D analyses.

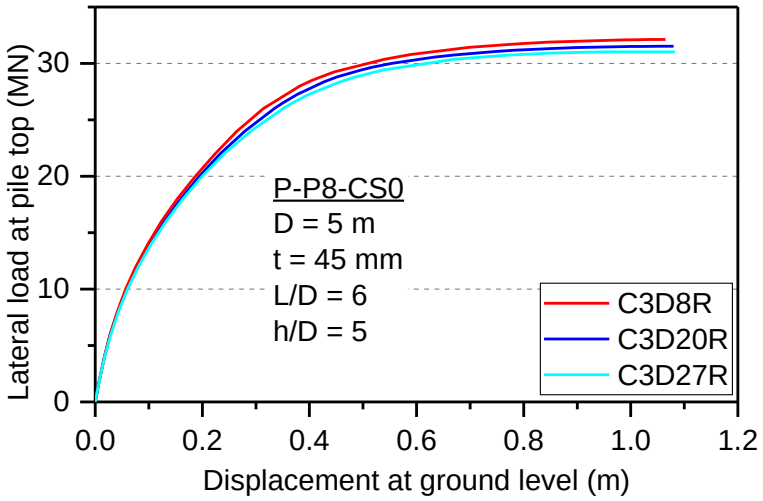

Figure 3.12 Comparison of load-displacement curve with C3D8R, C3D20R, C3D27R

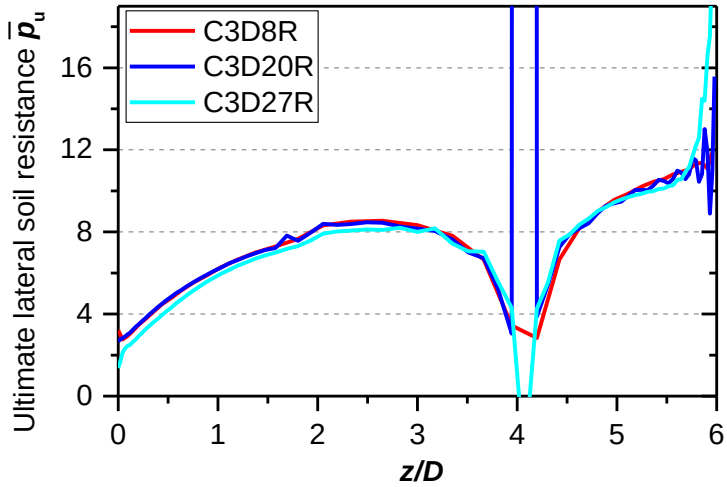

(a) Ultimate lateral soil resistance with depth

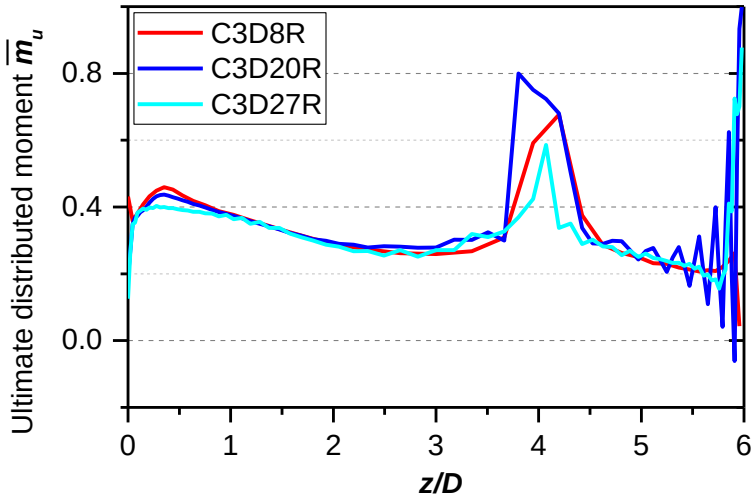

(b) Ultimate distributed moment with depth

Note: Notation of parameters is given in Table 4.2. Normalisation is given in Table 2.5.

Figure 3.13 Comparison of soil reaction parameters for C3D8R, C3D20R, C3D27R elements (P-P8-CS0 analyses)

Table 3.5 Comparison of computation time for C3D8R, C3D20R, C3D27R (P-P8-CS0 analyses)

Element type	Computation time
C3D8R	4 hours
C3D20R	2.4 days
C3D27R	6.4 days

3.5 COMPLEMENTARY MODELLING CONSIDERATIONS

Besides the choices of constitutive models and element types, a number of factors which might have an influence on the results were initially investigated, including the presence of a vertical load, gapping and pseudo-cohesion parameter for sand.

3.5.1 EFFECT OF VERTICAL LOADS

In reality, monopiles are always subjected to vertical loads from self-weight and the weight of the superstructure. The presence of vertical loads could affect the lateral deflection of the monopile. Two series of analyses were carried out to investigate the influence of vertical loads, in sand and clay. For each series, the first simulation was performed with a large vertical load only. The load-settlement curves were obtained to determine the ultimate vertical capacity, V_u. Then simulations with different vertical loads, proportional to the ultimate vertical capacity, were completed. A vertical load was applied at the pile top in the first load step, and then the imposed lateral displacement at the pile top increased from zero in the second load step, while the vertical load was held constant.

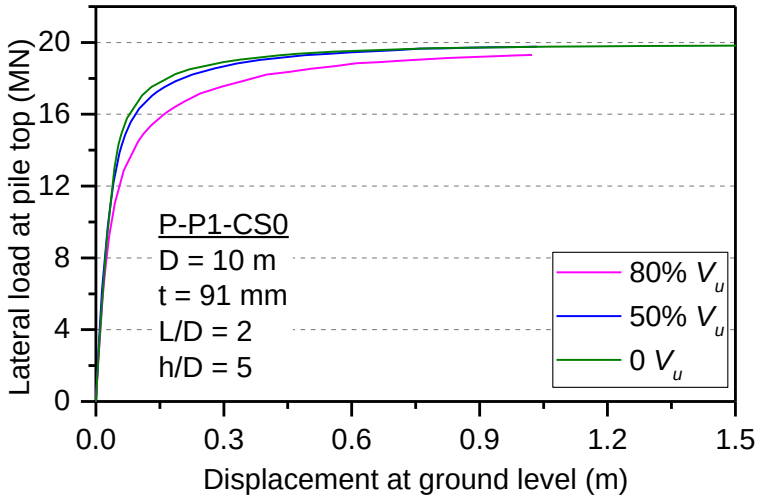

Figure 3.14 Effect of a vertical load on laterally loaded monopiles in homogeneous clay

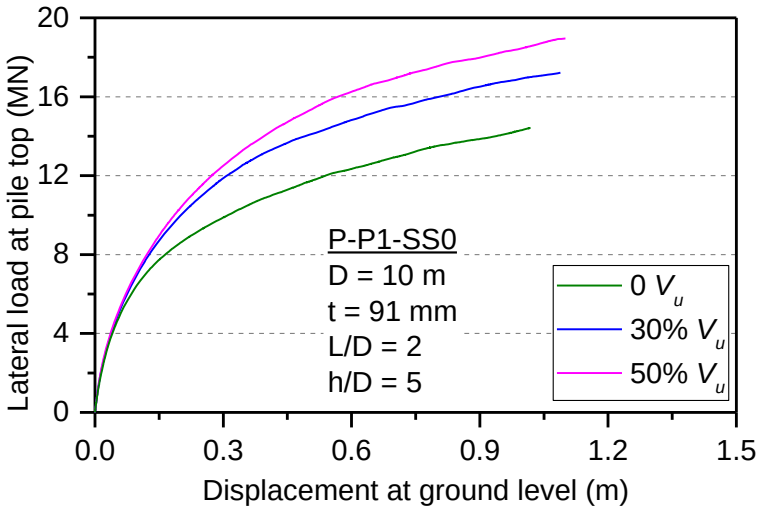

Figure 3.15 Effect of a vertical load on laterally loaded monopiles in homogeneous sand

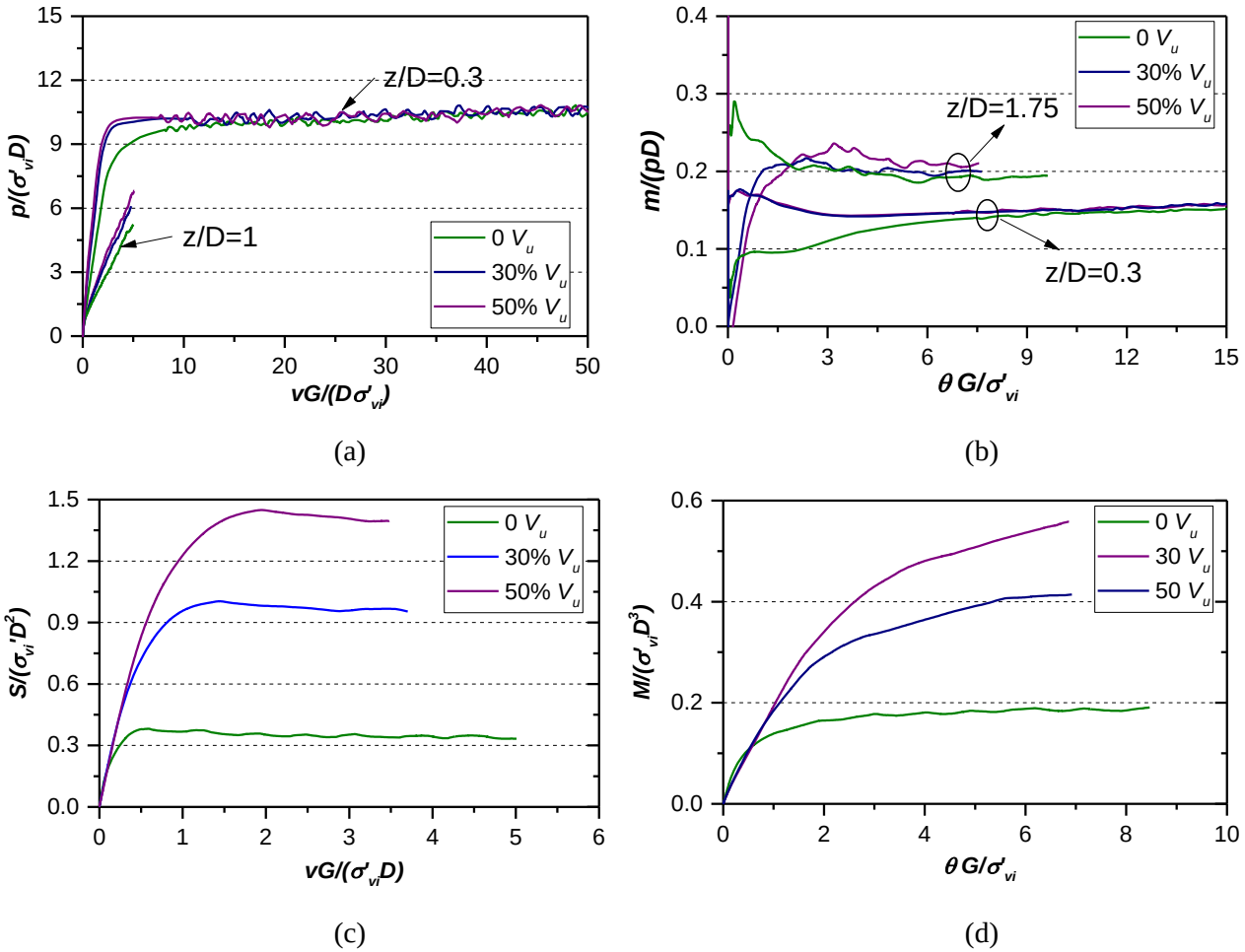

Figure 3.16 Effect of a vertical load on individual soil reaction components in sand

Figure 3.14 and Figure 3.15 show that the presence of the vertical load slightly reduces the ultimate lateral capacity of monopiles in clay. However, with 80% of the ultimate vertical load, the change in lateral displacement at the ground level is less than 10%. In sand, the increase in vertical loads increases significantly the ultimate lateral capacity of monopiles. The zero vertical load case

yields the most conservative pile response. These findings are consistent with the findings by Karthigeyan *et al*. (2007).

The effects of a vertical load on the individual soil reaction component for the sand analyses were shown in Figure 3.16. For clarity, the distributed components were only compared at two different depths. It is interesting to note that the vertical load has significant effects on the base soil reaction components, while the effects on the distributed soil reaction components around the pile shaft are relatively small. The reason for increase in pile horizontal capacity is mainly due to the increase in confining stress at the pile base, which leads to significantly higher base horizontal force and base moment. This finding suggested that the installation effect in sand can be taken into account by expressing the base soil reaction components as function of vertical loads. While for clay, the constitutive model used is pressure-independent. Hence, the change in pile lateral capacity is marginal. The reduction of lateral capacity can be attributed to early failure developed at the pile-soil interface, due to the presence of a vertical load, as stated by Karthigeyan *et al*. (2007).

As the actual percentage of the design vertical load to the bearing capacity for a typical 5 MW turbine is generally less than 10%, the vertical load effects on lateral response are marginal in sand and clay. Therefore, no vertical load was considered in the analyses presented in Chapters 4, 5, and 6.

3.5.2 EFFECT OF GAPPING

In idealised conditions, no gapping condition at the pile-soil interface for a sand analysis is expected, due to zero cohesion in the soil. However, gapping was observed from the field tests conducted in PISA, which might be due to cementation or the partial saturation of the soil in the test site. These issues are not expected to occur in offshore condition. In preliminary sand analyses, both zero-tension and full-tension conditions at the interface were examined. As shown in Figure 3.17, there is no difference in the load-displacement results between these two conditions. Zero-tension condition was used in the sand analyses. Note that suction might be developed at the gap between pile and soil in practice, which is beyond the scope of this thesis.

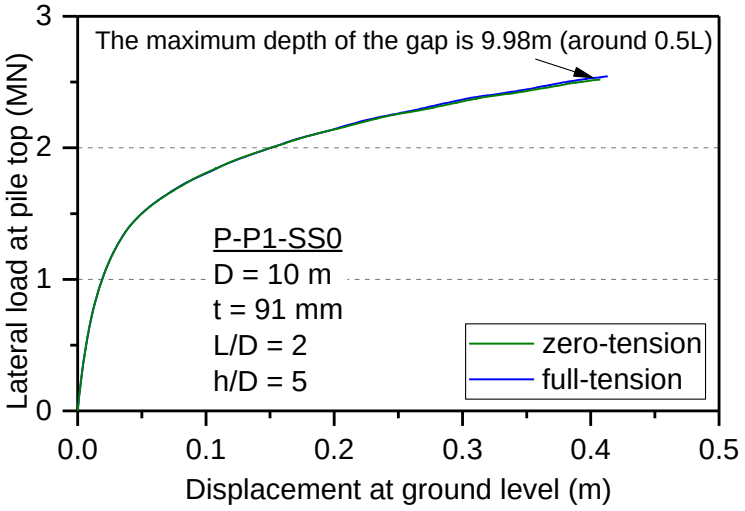

Figure 3.17 Effect of gapping on the lateral behaviour of monopiles in sand

3.5.3 EFFECT OF PSEUDO-COHESION

For the use of Mohr-Coulomb model for modelling sand, zero cohesion leads to a numerical singularity and thus is not allowed in Abaqus. A small amount of cohesion was initially applied to the analyses. As can be seen from Figure 3.18, the use of 1 kPa for the cohesion parameter shows a good balance between the convergence and accuracy. The value of the cohesion parameter is kept as 1 kPa for the sand and layered soil analyses.

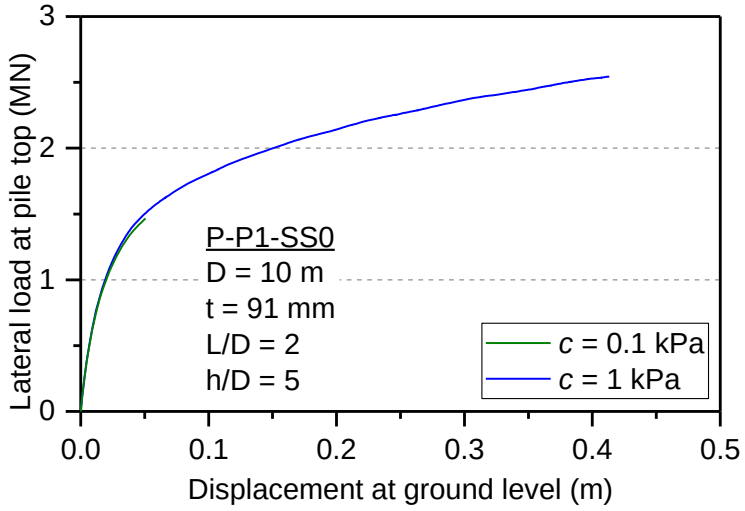

Figure 3.18 Effect of pseudo-cohesion for sand on monopile lateral response

3.6 CONCLUDING REMARKS

This chapter describes the work carried out for establishing 3D FE models for the analyses of single laterally loaded monopiles. A series of preliminary analyses were carried out to investigate the influence of varied element types in conjunction with different extraction methods. The effects of a vertical load, gapping and the use of pseudo-cohesion parameter for sand were also examined. The final 3D FE model described in Section 3.2 serves as a reference model for the analyses presented in the following chapters.

Inspection of the computed soil displacement vectors indicated that the failure of the soil at shallow depths corresponded to a wedge-type failure, while that of the soil at greater depths corresponded to a spherical rotation failure.

The results from the preliminary 3D FE analyses indicated that the differences in load-displacement results from the analyses using different element types (C3D8R, C3D20R and C3D27R) in Abaqus were less than 5%. They also demonstrated that the extracted soil reactions from the analyses using these elements were in good agreement. The use of linear element C3D8R provided satisfactory result accuracy while greatly diminished computational effort compared with the other two quadratic elements, and was thus employed in the reference model. Regarding the effect of vertical loads on the lateral response of monopiles, it was found that the pile lateral capacity increased significantly with the increase of a vertical load in sand, while decreased marginally in clay. As a result of the presence of the vertical load, the increase in horizontal capacity in sand is mainly due to the increase in the base soil reaction components. In addition, gap formation at the pile-soil interface had no real effect on the pile response in sand.

Chapter 4

LATERALLY LOADED MONOPILES IN UNDRAINED CLAY

4.1 INTRODUCTION

This chapter presents the study on predicting the lateral response of monopiles in undrained clay using the numerical-based approach outlined in Chapter 2. The objectives of this study were as follows: (1) to develop the soil reaction curves from a limited number of analyses, denoted "calibration analyses", as input for the 1D model; (2) to evaluate the predictive capabilities of the 1D model by performing a series of "test analyses", including applications to different pile dimensions and soils with different stiffness / strength profiles from the calibration analyses; (3) to explore the suitability of developing the soil reaction curves from idealised rigid pile analyses.

Soil profile used in the calibration analyses

Cowden clay was used in the simulations as it was considered representative of clay deposits in the North Sea. The soil was modelled using the elastic perfectly plastic model with a Von Mises yield criterion. The uniform undrained shear strength, s_u, and initial shear modulus, G_0, adopted in the calibration analyses were selected based on the Cowden soil profile, shown by the dashed line in Figure 4.1. The constant value of maximum shear modulus is chosen to be representative of soil shear modulus at shallow depths. The secant shear stiffness was taken at 0.1% deviatoric strain from the shear stiffness degradation curve. The 0.1% deviatoric strain lies in the characteristic strain range for foundation analyses (Atkinson and Sallfors, 1991; Mair, 1993). From Figure 4.2, G_{sec} at 0.1% deviatoric strain is about $0.3G_0$. In the calibration analyses, G_{sec} was set to 37.5 MPa, and the stiffness / strength ratio was therefore 250. A value of 0.49 was assigned to Poisson's ratio to approximate the undrained condition. A saturated bulk unit weight of 21.2 kN/m^3 was used in the analyses. The friction coefficient between steel piles outside surface and clay was estimated using the tan δ_{peak} curve given in Figure 4.3. As the average plasticity index PI = 18 was reported by Powell and Butcher (2003) for Cowden clay, the friction coefficient at the pile-soil interface, μ, was taken as 0.4. Gapping at the pile-soil interface was allowed.

To evaluate the predictive capabilities of the numerical-based approach for non-homogeneous soils, three Gibson type soil profiles were considered in the test analyses. A Gibson soil assumes the soil stiffness increases linearly with depth (Gibson, 1967; Gibson and Sills, 1975). As the ratio I_R=G/s_u was kept constant with depth for all analyses, the soil s_u varied linearly with depth, z, in Gibson soil, according to the Equation (4.1):

$$s_u(z) = s_u(0) + mz \tag{4.1}$$

where m is the rate of increase with depth in s_u.

The soil parameters used in the analyses are summarised in Table 4.1. The homogeneous soil profile, CS0, was used in the calibration and rigid pile analyse, while the Gibson-type soil profiles, CS1 - CS3, were used in the test analyses.

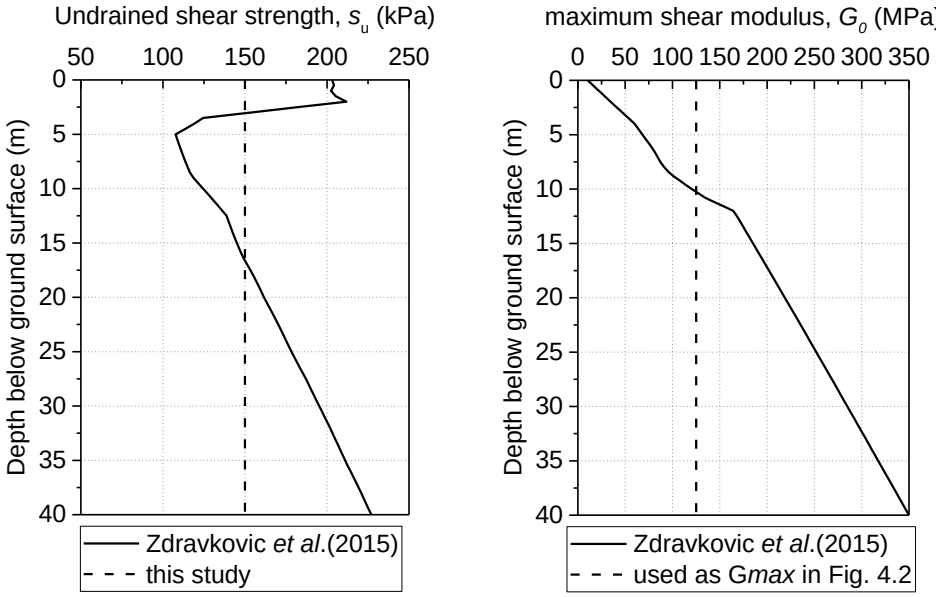

Figure 4.1 Profile of s_u and maximum shear modulus for the calibration analyses (Note: the G used in the simulations is the secant shear modulus at 0.1% deviatoric strain.)

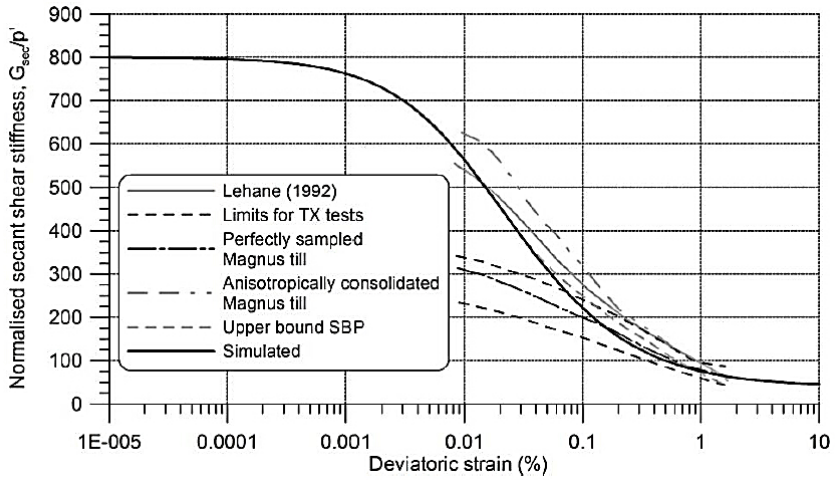

Figure 4.2 Shear stiffness degradation for Cowden clay (Zdravković *et al.*, 2015)

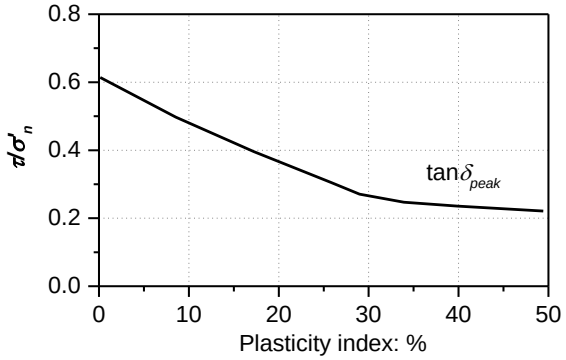

Figure 4.3 Pile-clay interface friction (Lehane *et al*., 2000)

Table 4.1 Soil parameters for the clay analyses

Soil parameter	Value			
Shear modulus at seabed level, G_{sec} (z = 0) (MPa)	37.5	25	12.5	12.5
Undrained shear strength at seabed level, s_u (0) (kPa)	150	100	50	50
s_u increase rate with depth, m (kPa/m)	0	5	10	5
Poisson's ratio, v	0.49			
Saturated bulk unit weight, γ (kN/m^3)	21.2			
Earth pressure coefficient at rest, K_0	1.0			
Friction coefficient at pile-soil interface, μ	0.4			
Analysis reference	CS0	CS1	CS2	CS3

4.2 POST-PROCESSING OF SOIL REACTION CURVES

4.2.1 NORMALISATION

The soil reaction curves extracted from four calibration analyses, C-P1-CS0, C-P5-CS0, C-P7-CS0, C-P8-CS0, were firstly normalised by local pile dimensions and soil properties. The normalisation enables soil reaction curves to be re-dimensioned for any combination of pile dimensions and soil properties with depth. The same dimensionless groups from PISA (see Table 2.5) were employed.

Figure 4.4 and Figure 4.5 show the normalised distributed load and distributed moment curves for different normalised depths, *z/D*. It is clear that the normalised soil reaction curves vary with depth. Hence, simplified parameterised expressions are required to describe the variations of normalised soil reaction curves with depth.

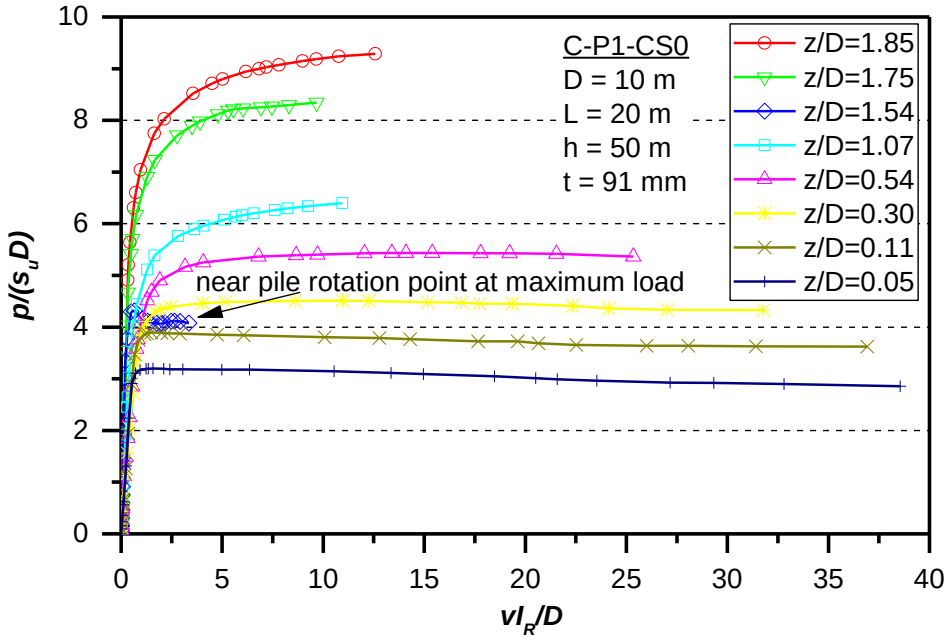

Figure 4.4 Representative normalised distributed load curves for C-P1-CS0 analysis

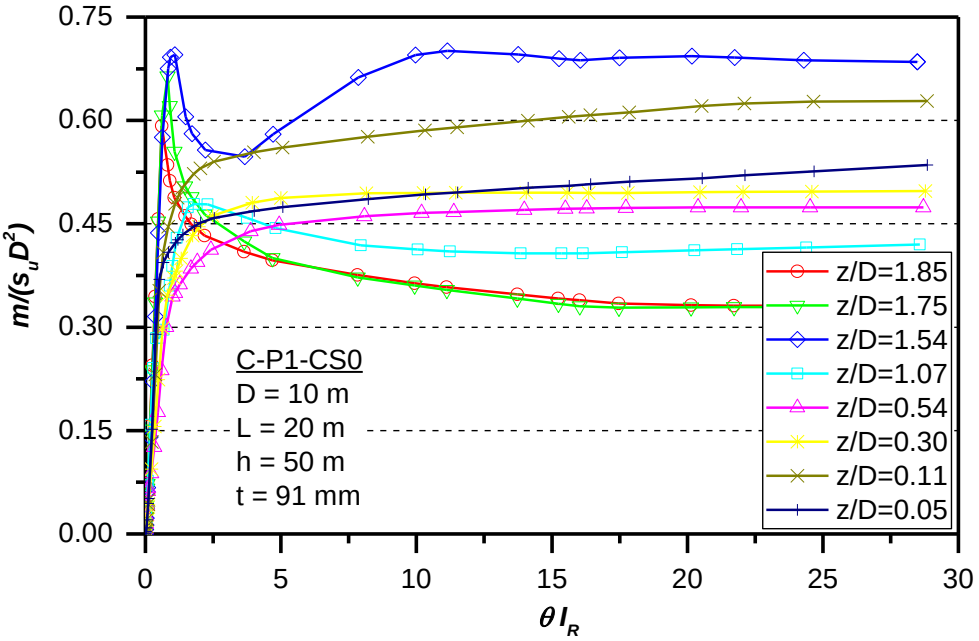

Figure 4.5 Representative normalised distributed moment curves for C-P1-CS0 analysis

Figure 4.5 shows that for the results for shallow depths (z/D < 1), the distributed moment curves increase continuously and show no peaks; while for the results at greater depths (z/D > 1), the curves firstly peak at small rotations, then decrease until they plateau. The cause of the difference between the distributed moment curves at shallow and great depths might be related to the depth of the forming gap. Note that the depth of the gap varies with applied load. The soil mechanism behind this could be complicated and is beyond the scope of this thesis. No further study is conducted to investigate the cause for this phenomenon.

4.2.2 PARAMETERISATION

Parameterisation is the procedure of finding the functions to describe the variations of soil reaction curves with depth. The same conic and bilinear functions from PISA (see Figure 2.12) were employed to fit to the numerical data. The characteristics of the soil reaction curves are described by the fitted curve parameters. Simplified expressions are then developed to describe the variations of the curve parameters with depth. They enable the parameterised curves to be derived for any depth of interest. Both the numerical and parameterised curves are subsequently used in the 1D model.

The procedure for the derivation of the curve parameters adopted in the PISA project is explained in Chapter 2. In this study, a systematic calibration process, based on PISA, is developed to obtain the parameterised expressions from homogeneous soil analyses. The calibration process for this study was implemented in MATLAB (ver. 2015a).

Because the curve shape for each soil reaction component is slightly different, the post-processing method is discussed for each individual soil reaction component. The subscripts for the curve parameters, for the different soil reaction curves and their meaning are given in Table 4.2.

Table 4.2. Subscripts for the curve parameters

Subscript	Meaning
p	with respect to distributed load curves
m	with respect to distributed moment curves
S	with respect to base horizontal curves
M	with respect to base moment curves
u	quantity at the ultimate response

4.2.2.1 Lateral distributed load

The conic function (see Figure 2.12 and Equations (2.40) - (2.42)), from PISA, was adopted to fit the distributed load curves. It was controlled by four parameters which are relevant to the desired properties of the soil reaction: the initial stiffness, k_p, the ultimate resistance, $\bar{p}_u$, the ultimate displacement, $\bar{v}_u$, and the transitional curvature, n_p. It was noted that the ultimate resistance and the ultimate displacement parameters should be derived from the numerical curves. A limiting local gradient was imposed to find the value of ultimate response from the numerical curves. A parameter, *k*, was introduced to indicate whether the soil reaction curve at a particular level has reached its ultimate response. The process of determining the curve parameters for the conic function is shown in the flow chart in Figure 4.6. A proportional least squares approach was used (see Equation

(2.44)). Because the numerical data became irregular around the pile rotation point, the ultimate values from depths around rotation point were not taken into account.

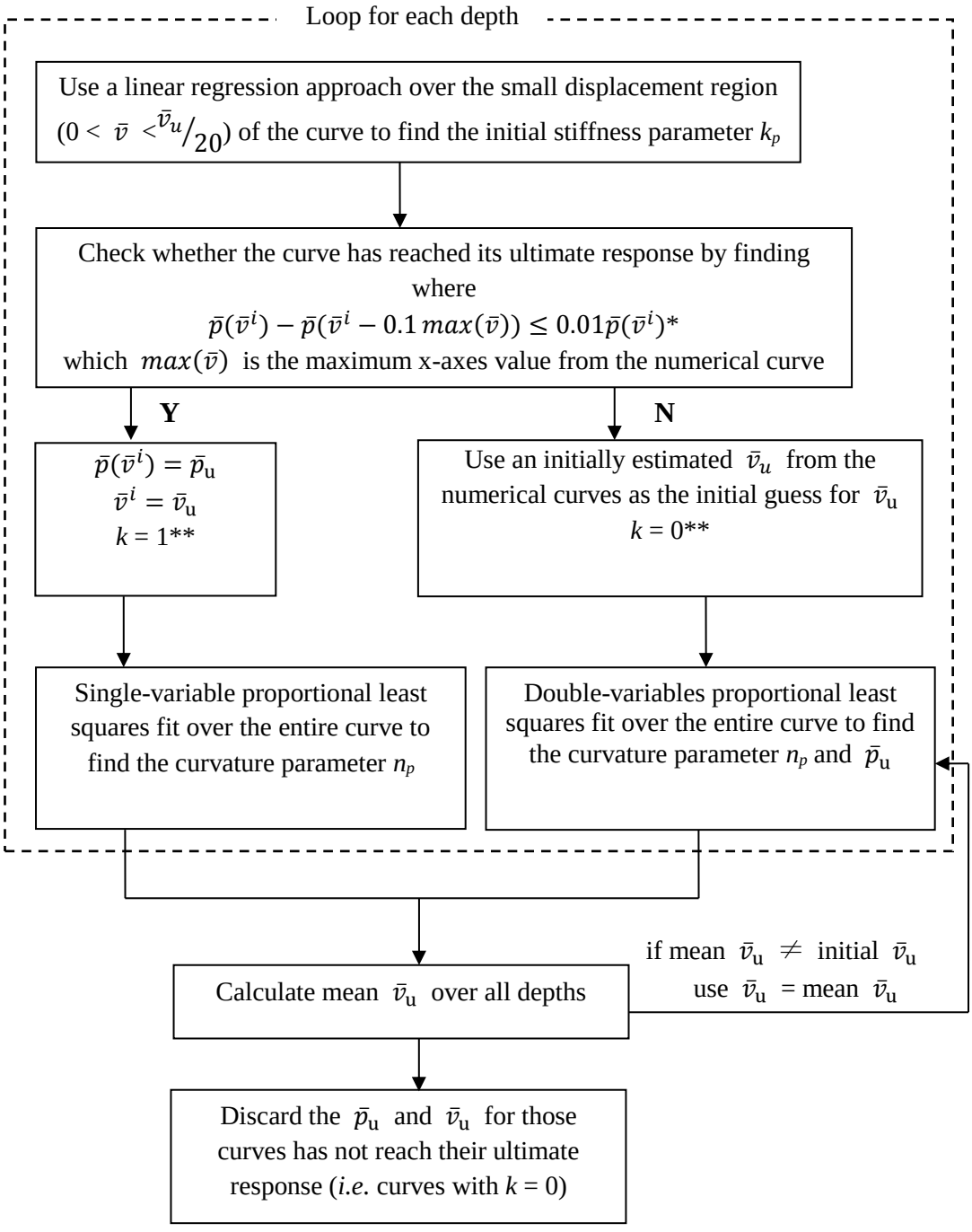

Note: * Superscript *i* indicates the data in the i[th] increment;
**k is an indicator of whether the curve has reached its ultimate response.

Figure 4.6 Process to derive the curve parameters for distributed load curves

Typical curve fitting results are shown in Figure 4.7. The ultimate response and the initial stiffness of the numerical curves were well fitted by the parameterised curves. However, the fit seems poor at the region $\frac{3}{4}\bar{p}_u < \bar{p} < \bar{p}_u$ for some depths.

As this poor fit might be due to the curvature parameter, the value of *n* is varied to better fit the data. As shown in Figure 4.8, the parameterised curve becomes flatter as the curvature parameter increases. However, as the curvature value increases, the parameterised curve intersects with the numerical curve at some point and results in greater differences at the region $0 < \bar{p} < \frac{3}{4}\bar{p}_u$. This indicates that the chosen function might be restricted to fit some particular curve form. As the proportional least squares method was adopted, the best fit curvature parameter aims to better fit the data for the region $0 < \bar{p} < \frac{3}{4}\bar{p}_u$.

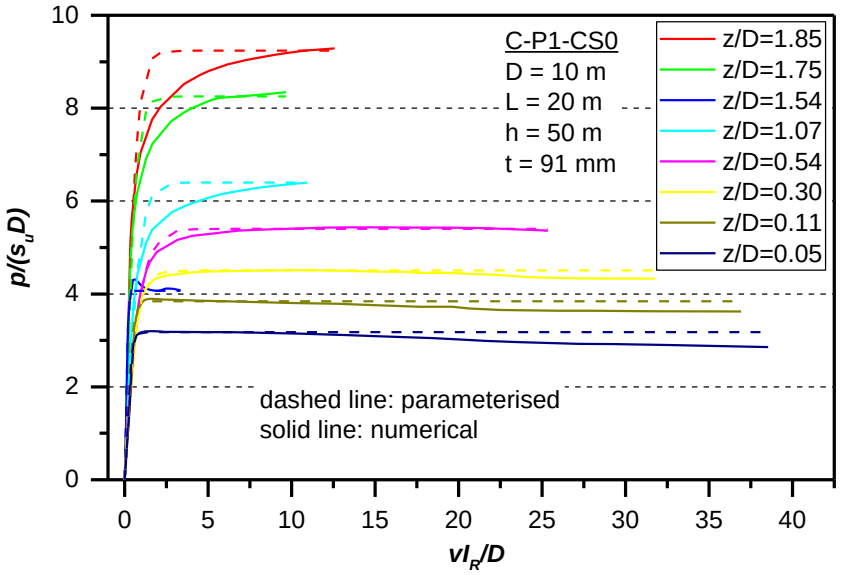

Figure 4.7 Representative curve fitting results for distributed load curves

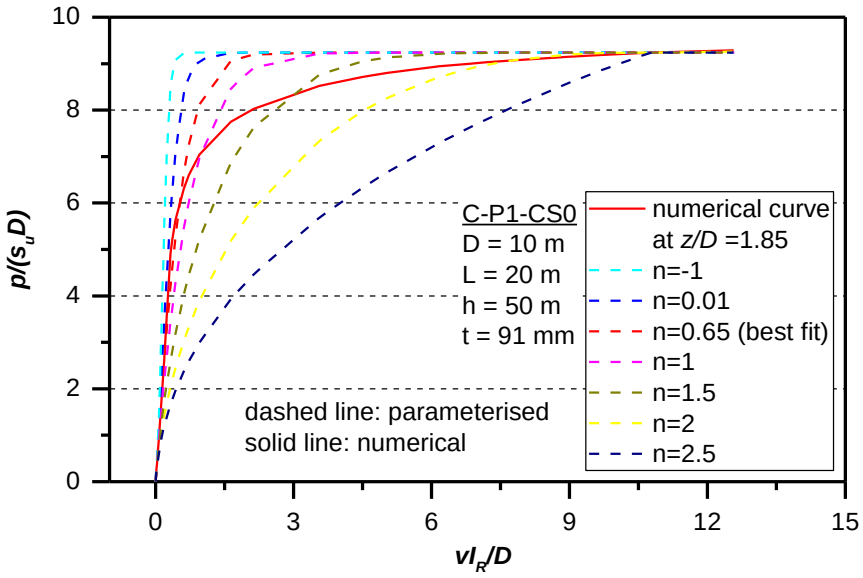

Figure 4.8 Variation of the curvature parameter for fitting distributed load curves

The curve parameters were evaluated at each measurement depth and plotted against *z/D* (see Figures 4.9 - 4.11), also plotted are the expressions adopted for the parameterised curves. The

variations of the parameters with *z/D* were described by simple expressions (see Table 4.3). Regarding the ultimate response parameter shown in Figure 4.11, the exponential parameterised function based on the analytical solutions by Murff and Hamilton (1993) was adopted. The constants in the exponential function were determined by a proportional least squares fit over the pile embedded length. The ultimate displacement parameter was taken as the mean value of the calibration analyses. Since there is no known expression for the initial stiffness parameter k_p or the curvature parameter n_p, they were represented by constants. As the measurement depths were not evenly spaced due to the fine mesh at the ground surface and pile tip, choosing the arithmetic mean value was not suitable. Instead, an integration average method was used to derive these constants. It consisted of the following steps:

1. Calculate the average height of the area under the curve for each analysis;
2. Calculate the arithmetic mean value of the average height for all analyses.

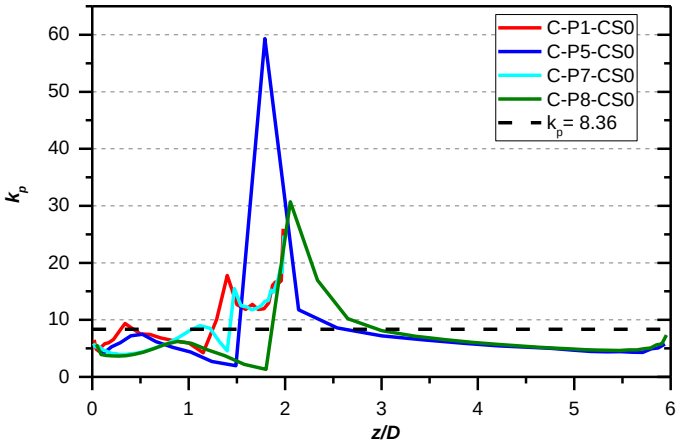

Figure 4.9 Initial stiffness parameter k_p

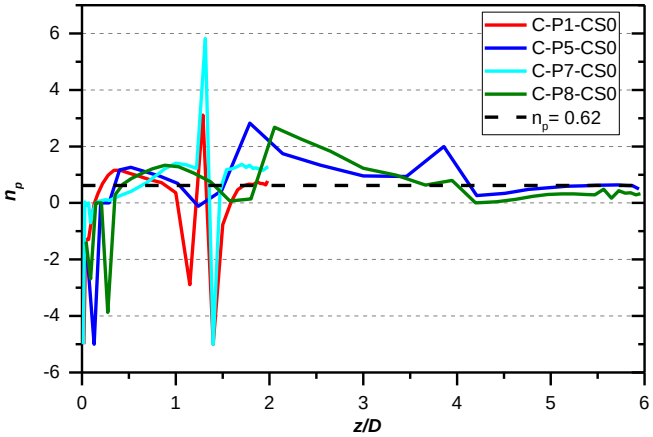

Figure 4.10 Curvature parameter n_p

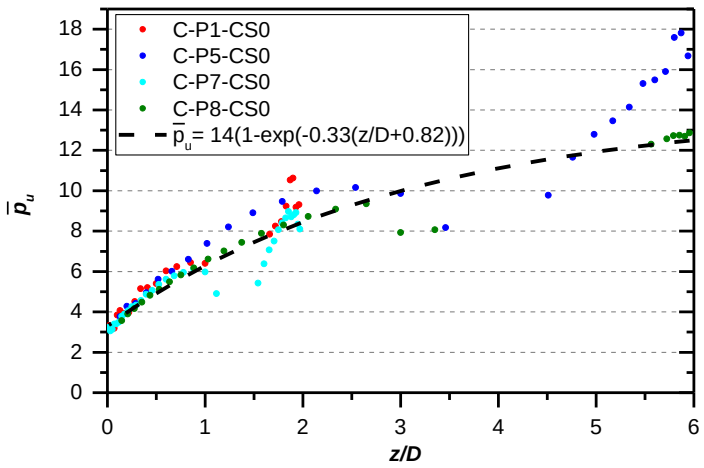

Figure 4.11. Ultimate response parameter $\bar{p}_u$

The parameterised expression for the normalised ultimate lateral soil resistance is compared with the analytical solutions (given in Table 2.2) in Figure 4.12. The empirical coefficient, *J*, in Matlock's solution was chosen as 0.5 since no information about this value is known for Cowden clay. The normalised ultimate lateral soil resistance obtained using Murff and Hamilton's method for both smooth and rough piles are shown. Soil weight was considered in all solutions. As the frictional coefficient was 0.4 in the analyses, the parameterised expression for shallow depths lie between Murff and Hamilton's solutions for smooth and rough piles, as expected. However, at greater depths, the extracted data are significantly higher than Murff and Hamilton's solutions, and keep increasing with *z/D*. This could be due to the fact that the soil fails according to a spherical rotation failure mechanism rather than a plane strain failure. Because the soil weight was considered in the 3D analyses, the extracted ultimate response consisted of the contribution due to soil unit weight. The API solutions for both stiff and soft clay were calculated for piles with diameter D = 10 m. They both under-predicted the ultimate resistance for *z/D* range from 0 to 6. Also, Brinch Hansen's approach yields significantly lower $\bar{p}_u$ for same *z/D*, which is consistent with the conclusion by Kasch (1977). The chosen expression for $\bar{p}_u$ aimed to better fit the data for shallow depths, and was developed based on the solution by Murff and Hamilton (1993).

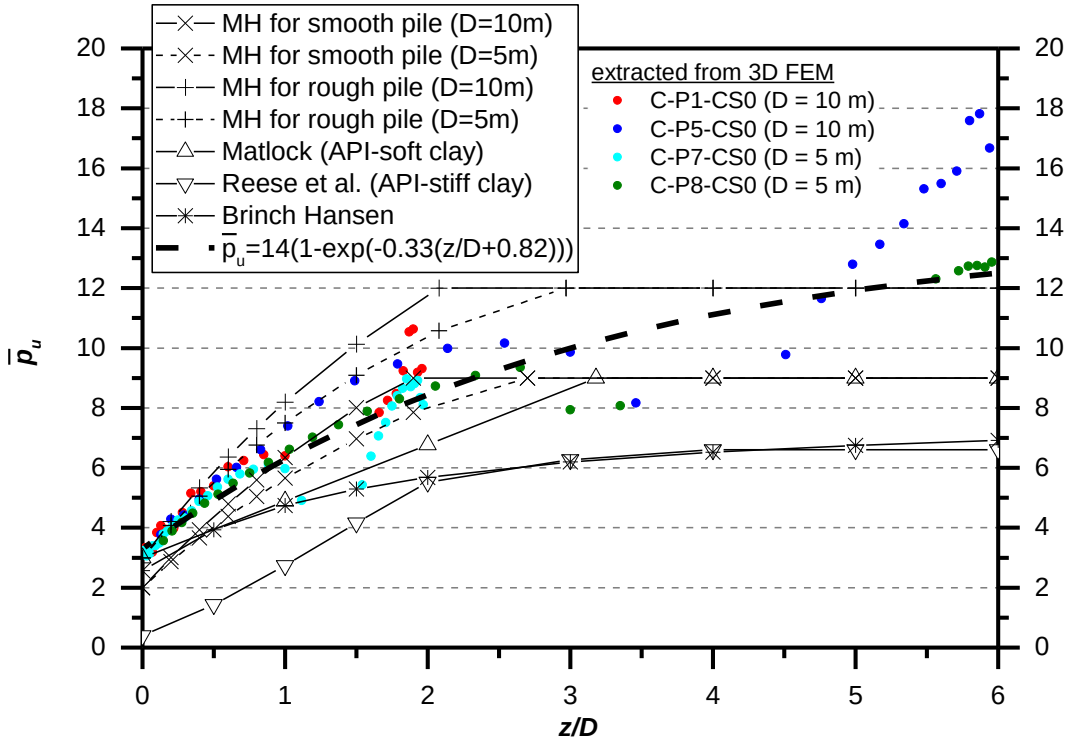

Figure 4.12 Comparison between the parameterised ultimate response and the analytical solutions outlined in Table 2.2

4.2.2.2 Distributed moment

The bilinear function from PISA was used to fit the distributed moment curve (see Figure 2.12 and Equation (2.43)), assuming that the peak at the beginning has negligible effect on the overall pile response. The function is controlled by the initial stiffness parameter k_m and the ultimate moment parameter $\bar{m}_u$. The ultimate rotation $\bar{\theta}_u$ was then calculated by $\bar{m}_u/k_m$. The curve fitting process for the normalised distributed moment curve consisted of two steps:

1. Use a linear regression approach to find the initial stiffness for the region up to 0.005 normalised rotation;

2. Use a single-variable proportionally least squares fit to find the ultimate moment $\bar{m}_u$.

The typical curve fitting results are shown in Figure 4.13. The ultimate response and the initial stiffness of the numerical curves were well fitted by the parameterised curves.

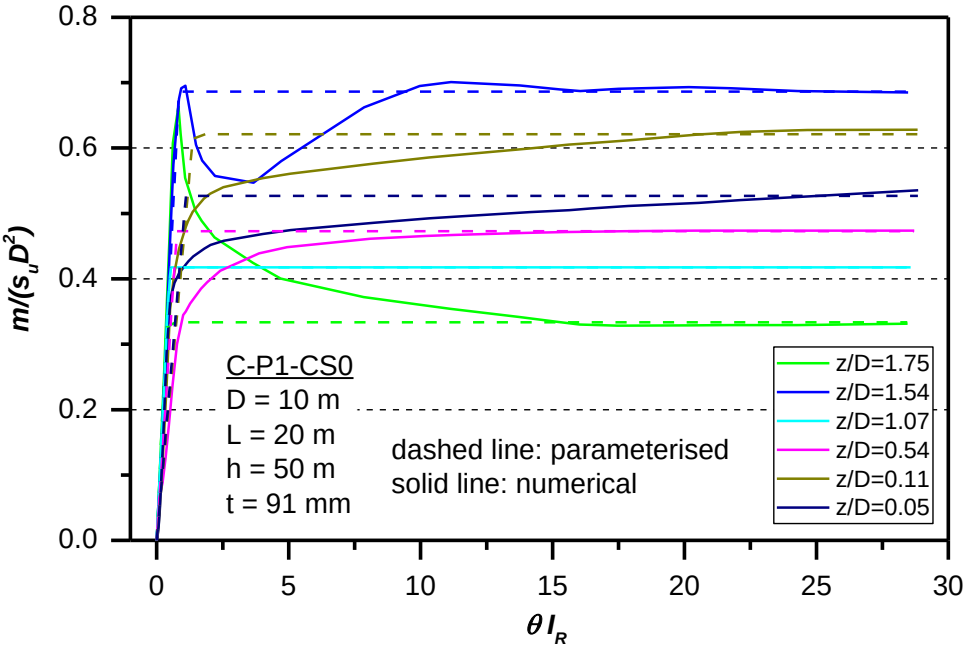

Figure 4.13 Representative curve fitting results for distributed moment curves

The curve parameters were evaluated at each measurement depth and plotted against *z/D* (See Figure 4.14 and Figure 4.15). The expressions for parameterised curves are shown by dashed lines. From Figure 4.15, it appears that the computed ultimate moment decreases with normalised depths, similar to the results from PISA.

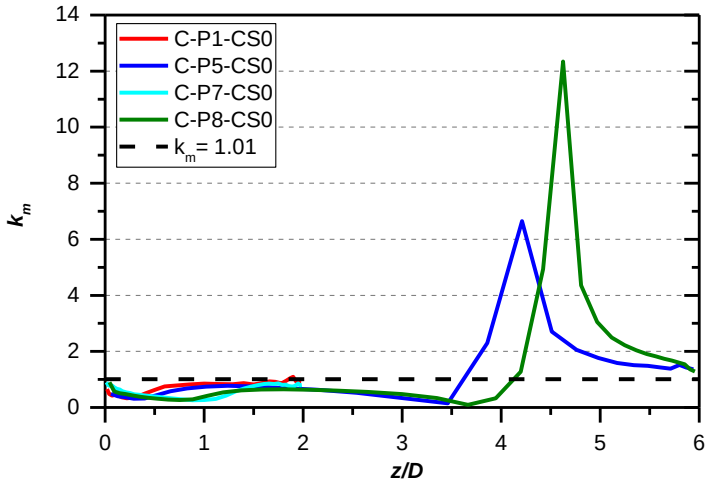

Figure 4.14 Initial stiffness parameter k_m

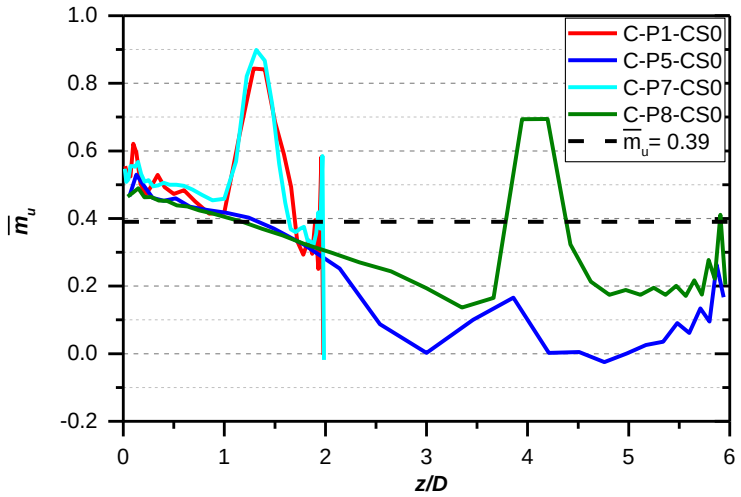

Figure 4.15 Ultimate moment parameter $\bar{m}_u$

It is noted that the numerical data were irregular around the rotation point. However, agreement at depths around the rotation point was not essential because the soil resistance at these depths contributed less compared to other depths. Since there is little knowledge about the form of these parameters with depth, again for simplicity, their variations with depth were estimated by constants. These constants were derived from the integration average method.

4.2.2.3 Base horizontal force

The conical function from PISA was also used to fit the base horizontal force curve. The same process used to derive the curve parameters for the distributed load curve was used for the base horizontal force curves (see Figure 4.6).

The curve fitting results for the calibration analyses are given in Figure 4.16. The results for the same *L/D* ratio were repeatable. The ultimate response and the initial stiffness of the numerical curves were well fitted by the parameterised curves. The curve parameters are plotted against *z/D* and presented in Figures 4.17 - 4.20. The expressions for the parameterised curves are shown by dashed lines. These plots show that the computed initial stiffness parameter decreased with the normalised depth, while the computed ultimate response and ultimate displacement parameters increased with the normalised depth. Because of the lack of information for piles with intermediate *L/D* ratios, linear interpolation was used to derive the parameterised expressions. The curvature parameter n_p was negative (see Figure 4.8) as the transition from elastic deformation to plastic deformation was steep, which might indicate that the bilinear function could be used in this case.

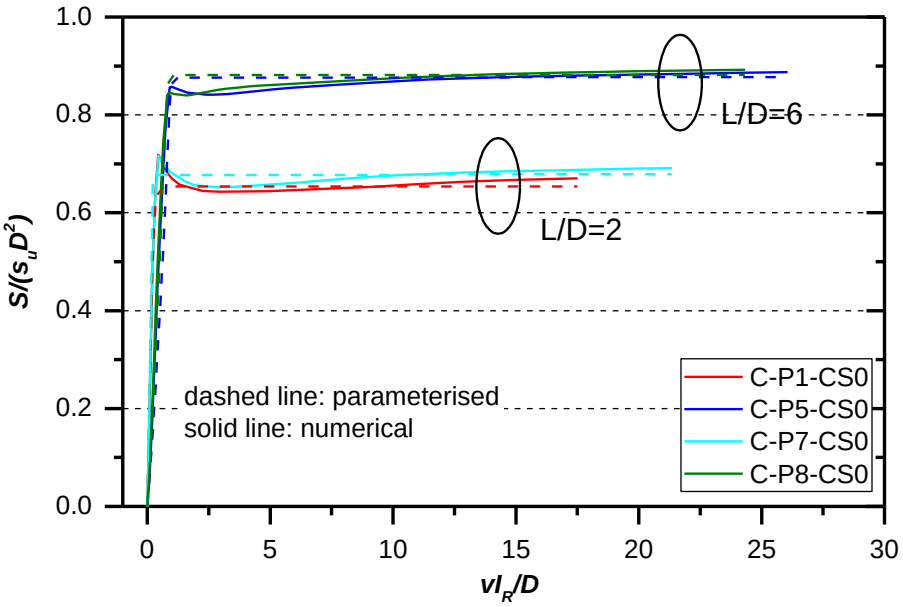

Figure 4.16 Curve fitting results for base horizontal curves

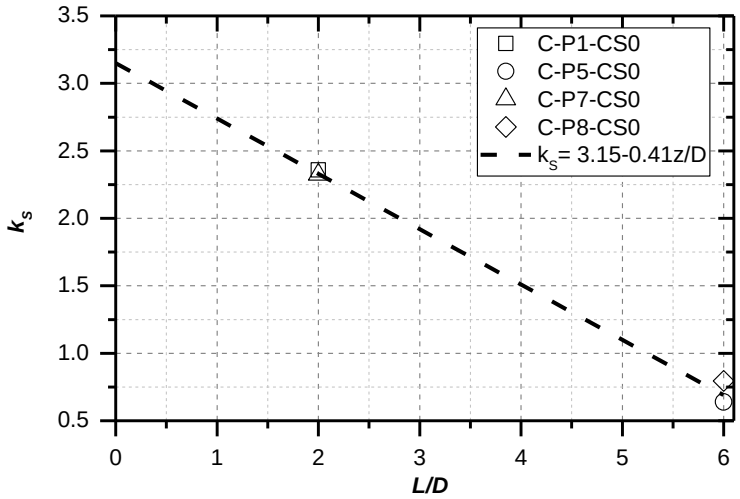

Figure 4.17 Initial stiffness parameter k_S

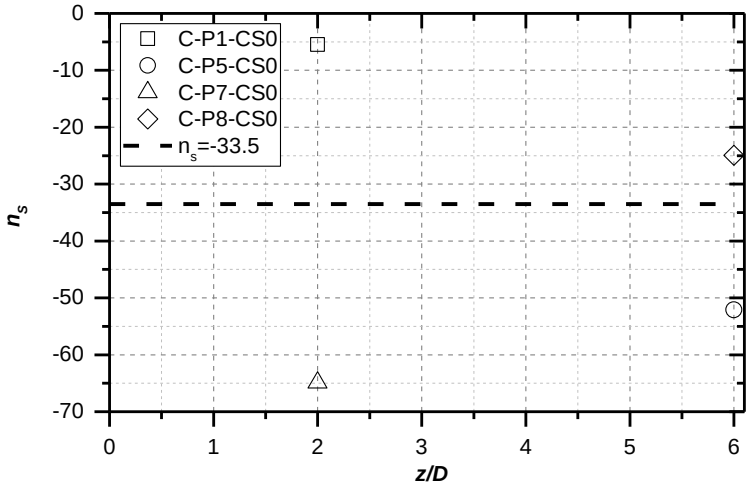

Figure 4.18 Curvature parameter n_s

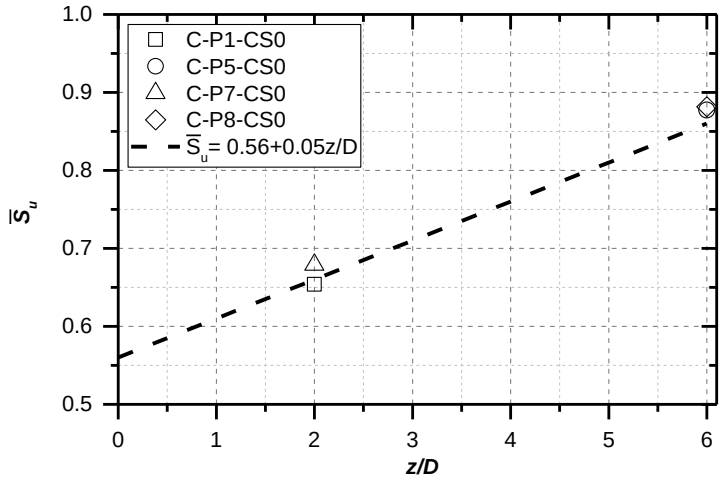

Figure 4.19 Ultimate response parameter $\overline{S}_u$

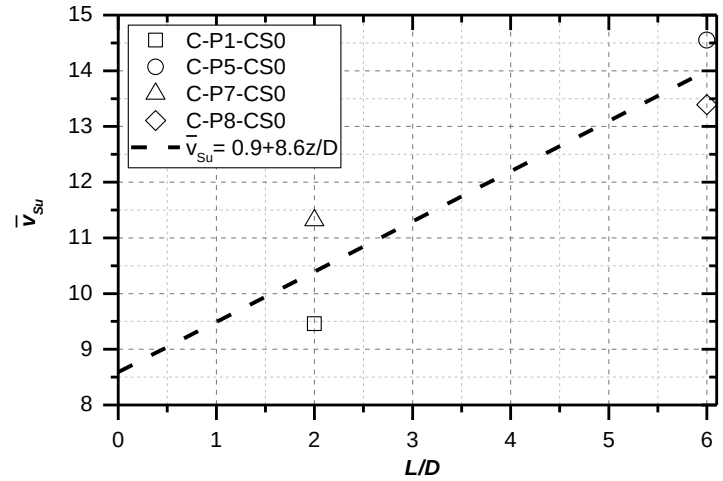

Figure 4.20 Ultimate displacement parameter $\overline{v}_{Su}$

4.2.2.4 Base moment

The normalised base moment curve has a similar shape to the distributed load curve. Hence, the same conical function was used to fit to the numerical curves.

The curve fitting results for the calibration analyses are given in Figure 4.21. It can be seen that the curve fitting results for the same *L/D* ratio were repeatable. The ultimate response and the initial stiffness of the numerical curves were well fitted by the parameterised curves. The parameterised expressions are shown by the dashed lines in Figures 4.22 - 4.25. Linear functions are used to derive the parameterised expressions. It is shown that the computed ultimate moment and ultimate base rotation parameters both decreased with the normalised depth. It appears that the initial stiffness and curvature parameters were influenced by the load eccentricity ratio (see P5 and P8 extracted results).

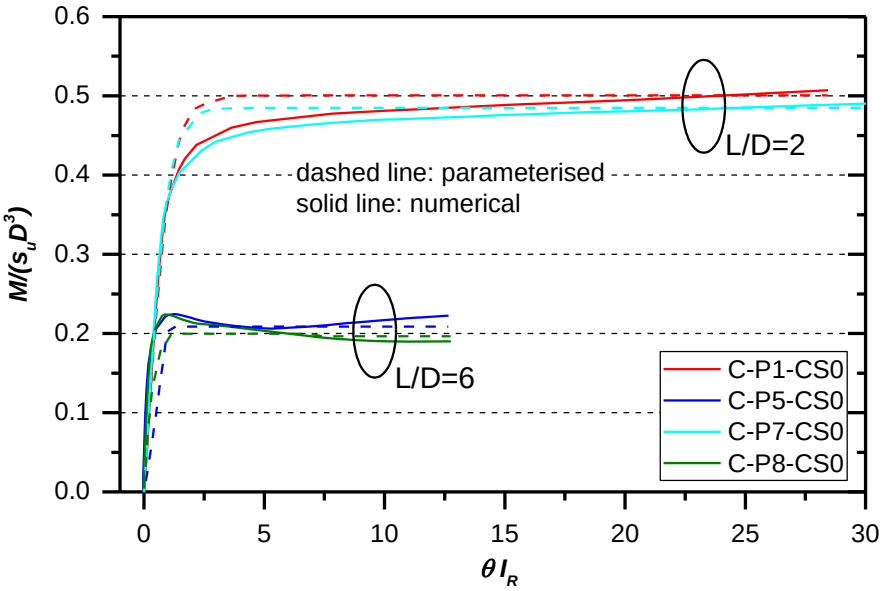

Figure 4.21 Curve fitting results for base moment curves

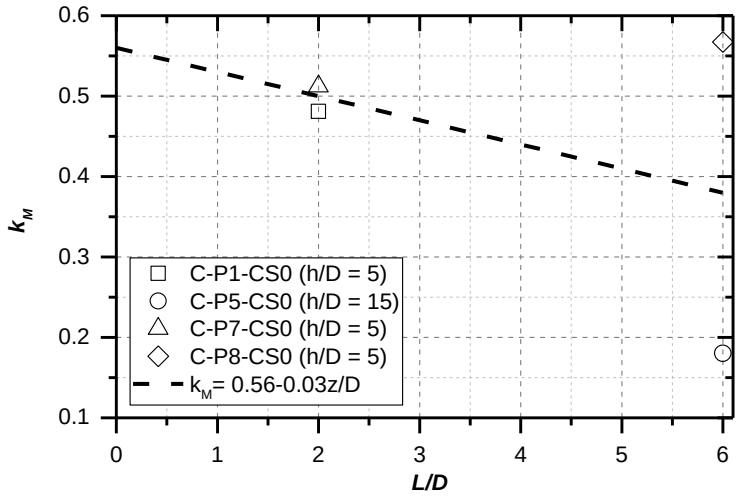

Figure 4.22 Initial stiffness parameter k_M

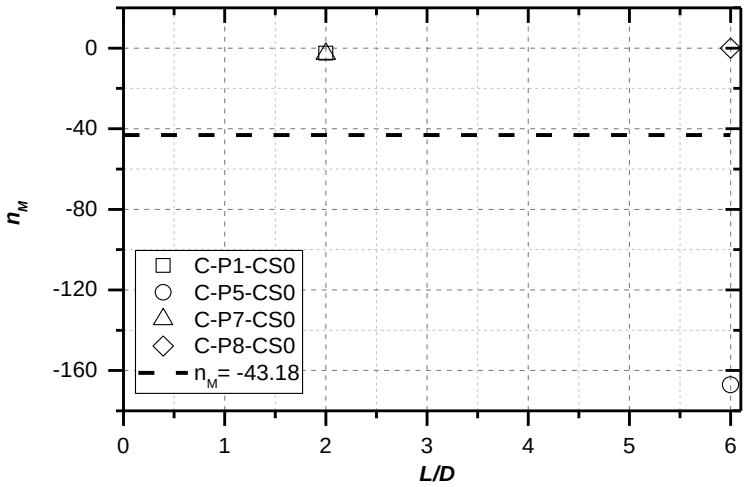

Figure 4.23 Curvature parameter n_M

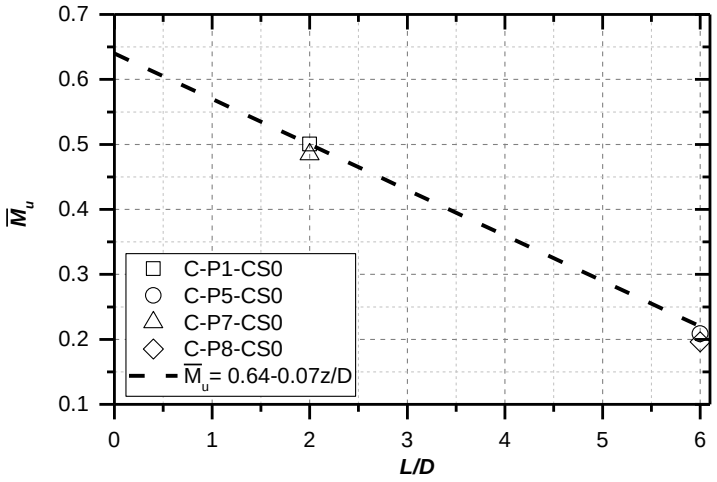

Figure 4.24 Ultimate moment parameter $\bar{M}_u$

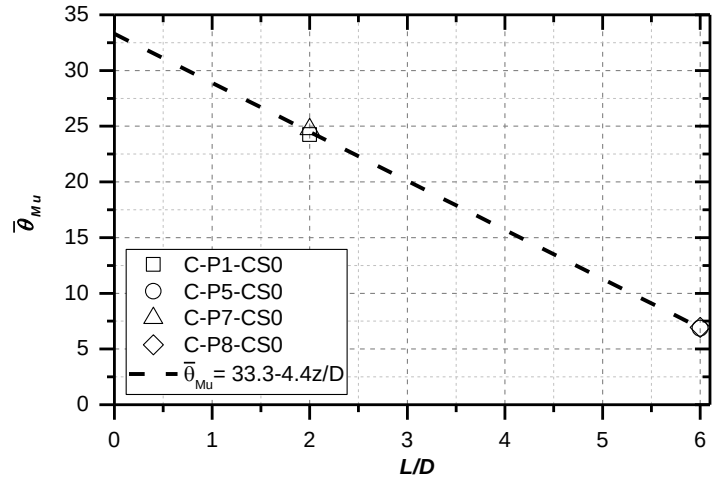

Figure 4.25 Ultimate rotation parameter $\bar{\theta}_{Mu}$

4.2.2.5 Comments on the parameterised expressions

The derived parameterised expressions were simple mathematical approximations of the extracted data from the limited cases analysed, and they do not suggest any interrelationship between the curve parameters and the normalised depth in reality. It is expected that the derived expressions do not follow those developed in PISA, because that the expressions depend on soil models used in the 3D FE analyses. However, the expressions were developed by following the same procedure of the numerical-based design method proposed in PISA, hence, by applying these expressions, the predictive capability of the numerical-based design method and the 1D model can be examined.

It is worth mentioning that only two *L/D* ratios were studied in the calibration analyses. The parameterised expressions of the base soil reactions were determined solely based on the four

analyses considered. Hence, those linear expressions should be used with caution for analyses considering other *L/D* ratios.

The parameterised expressions for all the soil reaction curves are summarised in Table 4.3.

Table 4.3 Summary of the expressions for the parameterised curve parameters for clay derived from this study and the PISA project (calibrated for 2 < *L/D* < 6)

	Parameter	This study	AWG PISA (2014a)
Distributed load	k_p	8.36	$-\frac{4}{3}\frac{z}{D}+10$
	n_p	0.62	$-\frac{8}{15}\frac{z}{D}+4.2$
	$\bar{p}_u$	$14(1-e^{-0.33(z/D+0.82)})$	$9.5(1-e^{-0.6(z/D+0.4)})$
	$\bar{v}_u$	12	200
Distributed moment	k_m	1.01	$\begin{cases} -\frac{22}{225}\frac{z}{D}+0.5, & \frac{z}{D}<4.5 \\ 0.06, & \frac{z}{D}\geq 4.5 \end{cases}$
	$\bar{m}_u$	0.39	$\begin{cases} 0.32, & \frac{z}{D}<2.8 \\ -\frac{27}{320}\frac{z}{D}+0.56, & \frac{z}{D}\geq 2.8 \end{cases}$
Base horizontal force	k_S	$3.15-0.41\frac{z}{D}$	$2.8-\frac{1}{3}\frac{z}{D}$
	n_S	-33.5	$9.3-\frac{23}{30}\frac{z}{D}$
	$\bar{S}_u$	$0.56+0.05\frac{z}{D}$	$0.8+0.3\frac{z}{D}$
	$\bar{v}_{Su}$	$0.9+8.6\frac{z}{D}$	500
Base moment	k_M	$0.56-0.03\frac{z}{D}$	0.32
	n_M	-43.18	$9.3+0.7\frac{z}{D}$
	$\bar{M}_u$	$0.64-0.07\frac{z}{D}$	$0.73-\frac{7}{120}\frac{z}{D}$
	$\bar{\theta}_{Mu}$	$33.3-4.4\frac{z}{D}$	200

4.3 APPLICATION OF SOIL REACTION CURVES TO THE 1D MODEL

To validate the extraction process and the extracted soil reaction curves, 1D analyses using the numerical soil reaction curves were carried out. Meanwhile, to validate the parameterisation and the parameterised soil reaction curves, 1D analyses using the parameterised soil reaction curves were carried out. The predicted load-displacement results from the 1D analyses are compared with the results obtained from the 3D simulations. The contribution of each soil reaction component to the overall pile response is also discussed.

4.3.1 NUMERICAL SOIL REACTION CURVES

For each calibration analysis, the numerical soil reaction curves were incorporated within the 1D model. The pile and soil conditions adopted for the 1D analysis were those used in the 3D FE calibration analyses. The load-displacement results from the 1D and 3D analyses are shown in Figures 4.26 - 4.29. For the legend in these figures, p refers to the distributed load; m refers to the distributed moment; the base horizontal force is denoted by BS and the base moment is denoted by BM. To investigate the contribution of each soil reaction component, the soil reaction curves were added to the 1D model one by one. In the results, the analyses that account for only the distributed load curves are shown by dotted lines; the analyses with the distributed load and distributed moment curves are shown by dash-dotted lines; the analyses with the distributed load, distributed moment and base horizontal force curves are shown by dashed lines, and the analyses with all soil reaction curves are shown by solid lines. The results predicted by the 1D model with numerical soil reaction curves and those obtained from the corresponding 3D FE analyses are represented by different colours.

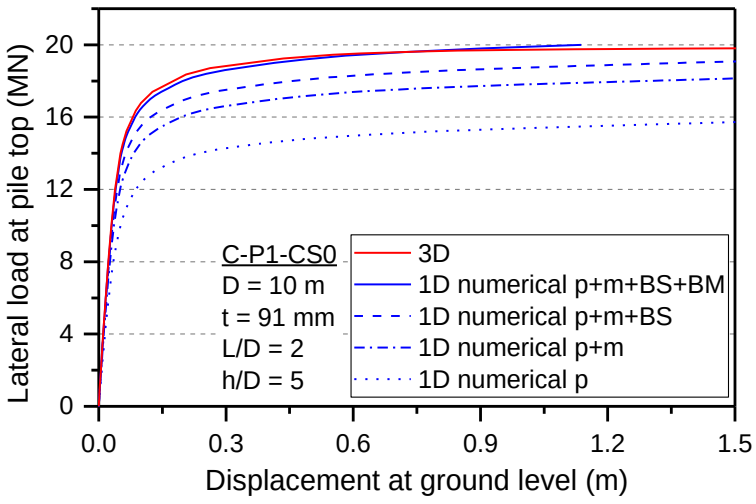

Figure 4.26 Comparison between 1D (numerical) and 3D results for C-P1-CS0 analysis

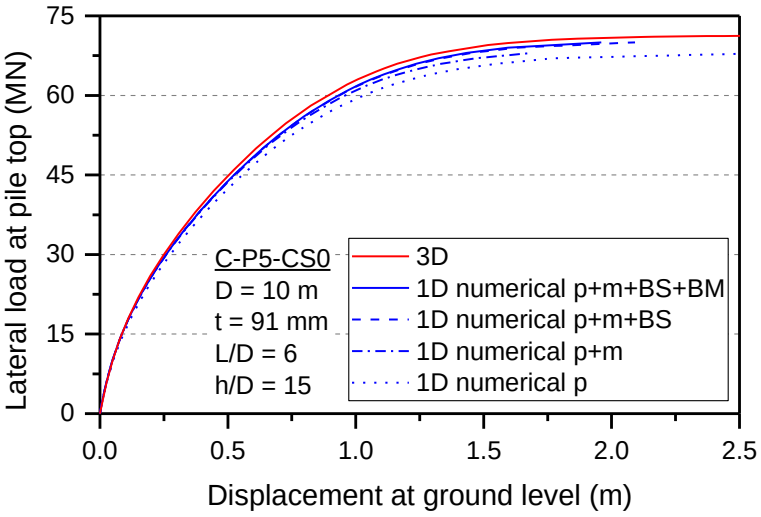

Figure 4.27 Comparison between 1D (numerical) and 3D results for C-P5-CS0 analysis

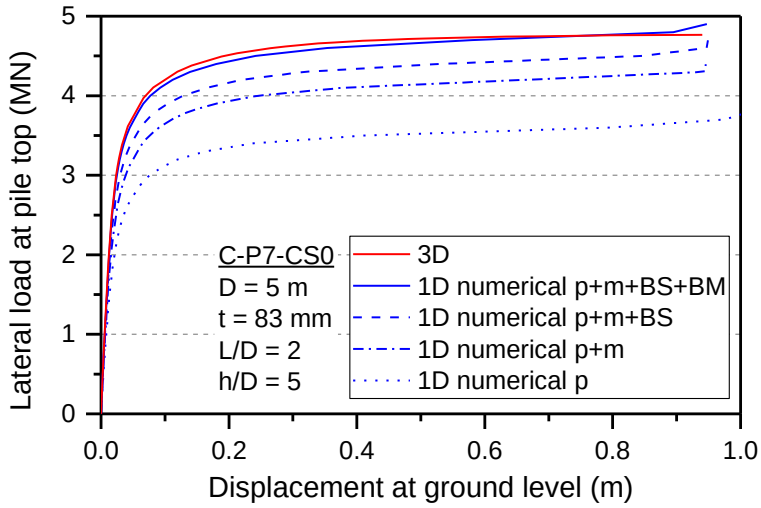

Figure 4.28 Comparison between 1D (numerical) and 3D results for C-P7-CS0 analysis

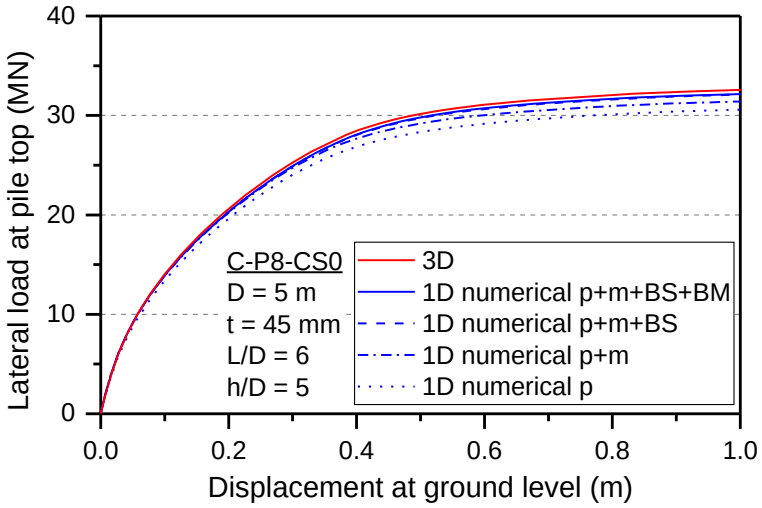

Figure 4.29 Comparison between 1D (predicted) and 3D results for C-P8-CS0 analysis

The 1D analyses with all soil reaction components showed excellent agreement with the 3D FE results, which implied that the extraction process for the soil reaction curves was validated. By taking into account the four soil reaction components, the 1D model was capable of predicting monopile lateral response as well as 3D FE analyses.

Contribution of additional soil reaction components

While the contribution of the soil reaction components can be calculated at any load level, in this thesis, it was evaluated by comparing the area under the numerical curves for the displacement range from zero to the ultimate displacement (0.1*D* as proposed in PISA). The contribution metric for each component was given as a percentage defined using Equation (4.2).

$$\eta = \frac{A_{one\ component\ only}}{A_{all\ components}} \times 100\% \tag{4.2}$$

where *A* is the area under the curve over the ground displacement up to 0.1*D*.

Table 4.4 Contribution of each soil reaction component to pile lateral response (%)

Analysis	*L/D*	*D* (m)	η_p	η_m	η_S	η_M
C-P1-CS0	2	10	76.75	12.60	6.31	4.34
C-P7-CS0	2	5	75.36	13.14	7.13	4.37
C-P5-CS0	6	10	96.46	2.94	0.58	0.02
C-P8-CS0	6	5	96.03	3.03	0.88	0.06

Table 4.4 and Figures 4.26 - 4.29 show that the distributed load component is the major component and contributed the most to pile capacity. The effect of additional soil reaction components was more significant for short piles (*L/D* = 2) than for long piles (*L/D* = 6), as it accounted about 25% of the total area under the curve (*i.e.* total energy until failure). These findings indicate that it is important to consider the additional soil reaction components to give accurate predictions of the lateral responses for monopiles with low *L/D* ratios.

4.3.2 PARAMETERISED SOIL REACTION CURVES

The results of the 1D analyses using the parameterised soil reaction curves (shown by dashed lines) are compared with the corresponding 3D FE results (shown by solid lines) in Figures 4.30 - 4.33.

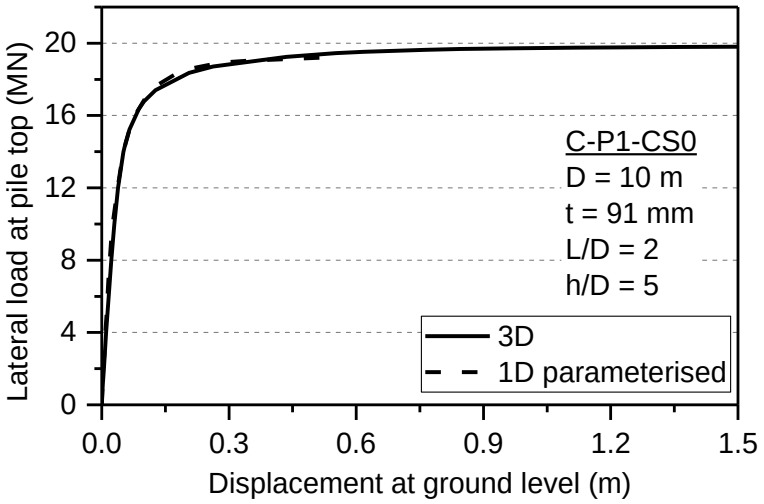

Figure 4.30 1D (parameterised) and 3D results for C-P1-CS0 analysis

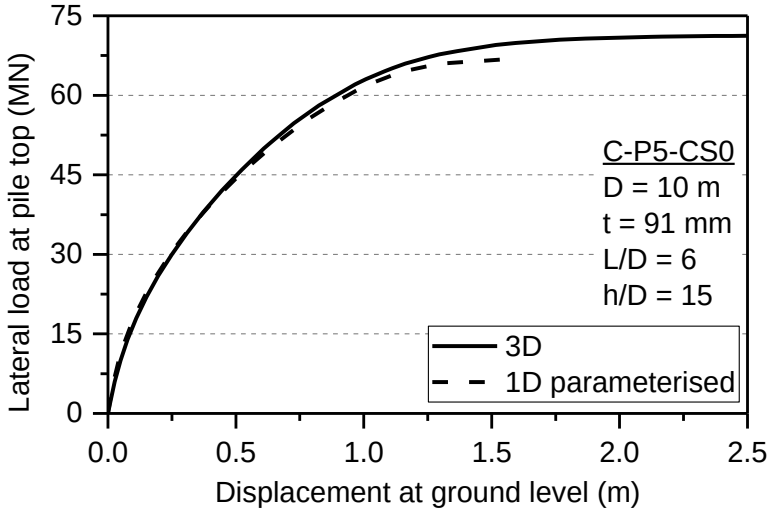

Figure 4.31 1D (parameterised) and 3D results for C-P5-CS0 analysis

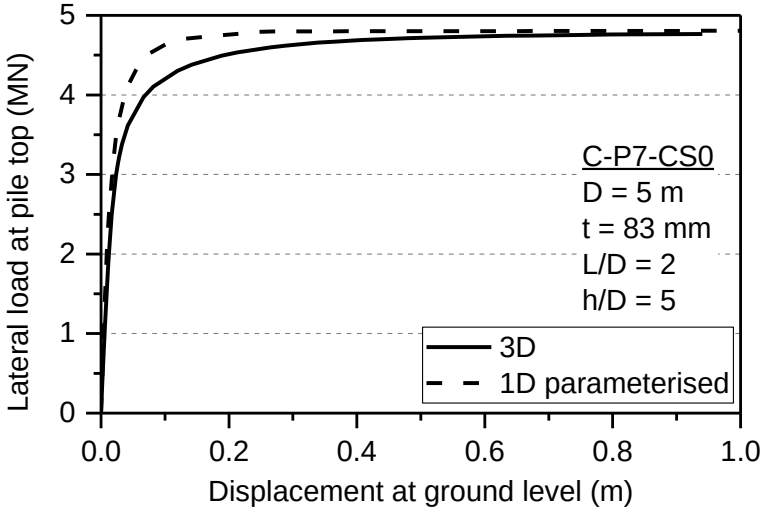

Figure 4.32 1D (parameterised) and 3D results for C-P7-CS0 analysis

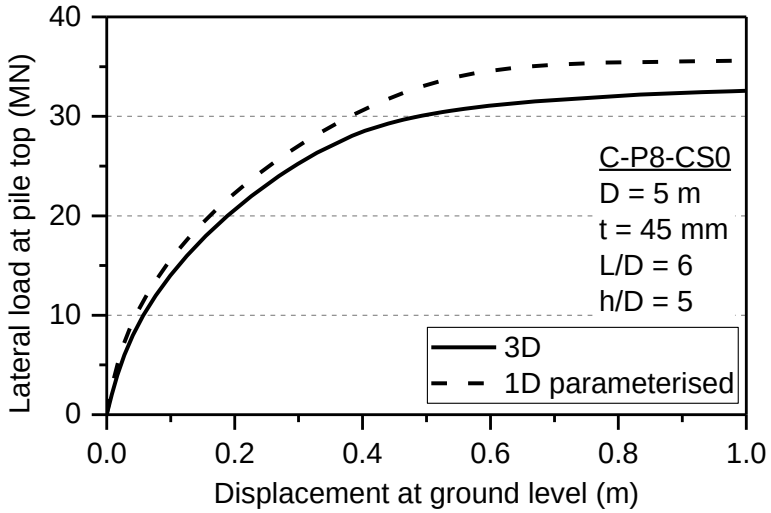

Figure 4.33 1D (parameterised) and 3D results for C-P8-CS0 analysis

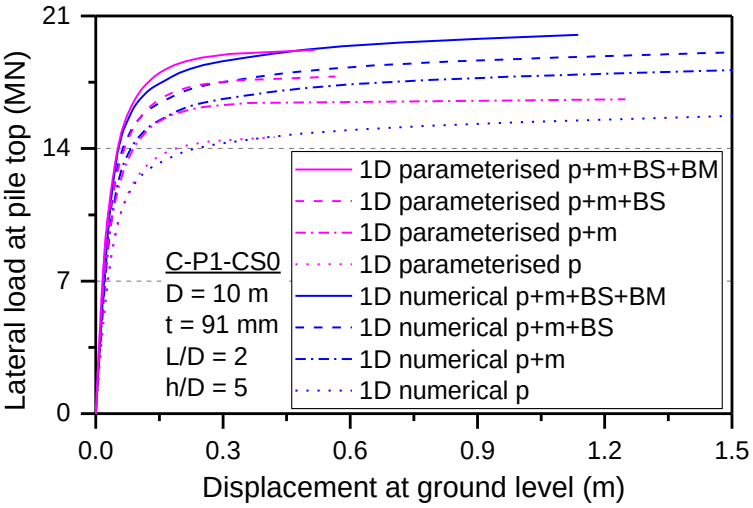

Figure 4.34 Comparison between 1D (parameterised) and 1D (numerical) results for C-P1-CS0 analysis

Although there were differences in the pre-failure response between the 1D and 3D FE results for the piles with small diameter (P7 and P8), overall, the agreement between the 1D and 3D FE results was quite satisfactory. This implied that the parameterisation of the soil reaction curves was validated. The largest discrepancy occurred for P8 analysis, which was only about 10% in ultimate capacity. On the other hand, as shown in Figure 4.34, it is interesting to note that the parameterised curves are able to predict well the pile response for the decomposition of the soil reaction components. Therefore, the parameterisation process and expressions developed were proven to be effective, and the parameterised curves were used as input to 1D model.

4.4 PREDICTABILITY STUDIES

4.4.1 VARIATION OF PILE DESIGN PARAMETERS

To investigate whether the calibrated 1D model can be applied to analyses involving pile geometries which are different from those used in the calibration analyses, four test analyses considering four additional piles, P4, P10, P4-2, P4-3, were performed. Further 3D analyses on the additional piles were also carried out. The pile geometries and load eccentricities of the additional piles were given in Table 3.2, which were chosen within the parameter range used in the calibration analyses (see Table 4.5). The soil profile used in the 1D and 3D analyses remains the same as that adopted in the calibration analyses.

Table 4.5 Pile parameters explored in the calibration analyses

Parameter	Range simulated
Aspect ratio, *L/D*	2 - 6
Diameter, *D* (m)	5 – 10
Load eccentricity ratio, *M/HD*	5 – 15
Thickness ratio, *D/t*	60 - 110

The parameters of the additional piles were selected to study the influence of a particular factor. T-P4-CS0 analysis was performed to study a different combination of the pile parameters. T-P10-CS0 analysis aims to examine the effect of changing pile diameter. T-P4-2-CS0 and T-P4-3-CS0 analyses were performed to evaluate the effect of *L/D* ratio. In addition, the effect of *h/D* was investigated in T-P4-3-CS0 analysis. The 1D predictions are compared with the results obtained from the 3D FE analyses in Figures 4.35 - 4.38.

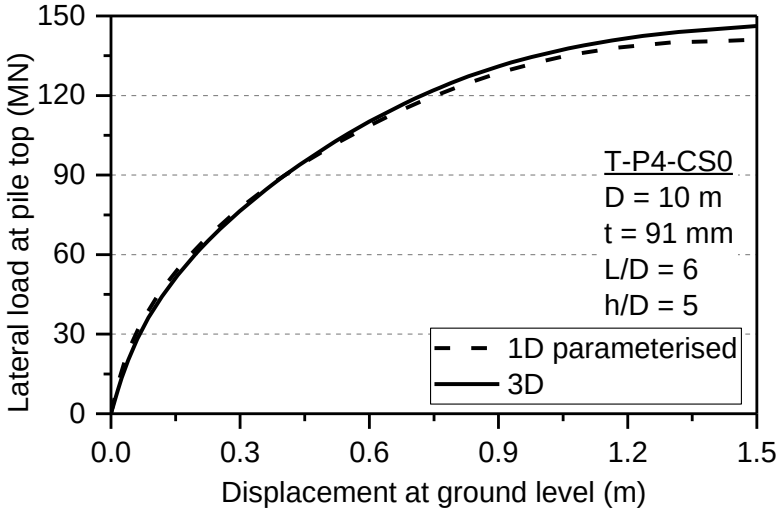

Figure 4.35 Comparison between 1D (predicted) and 3D results for T-P4-CS0 analysis

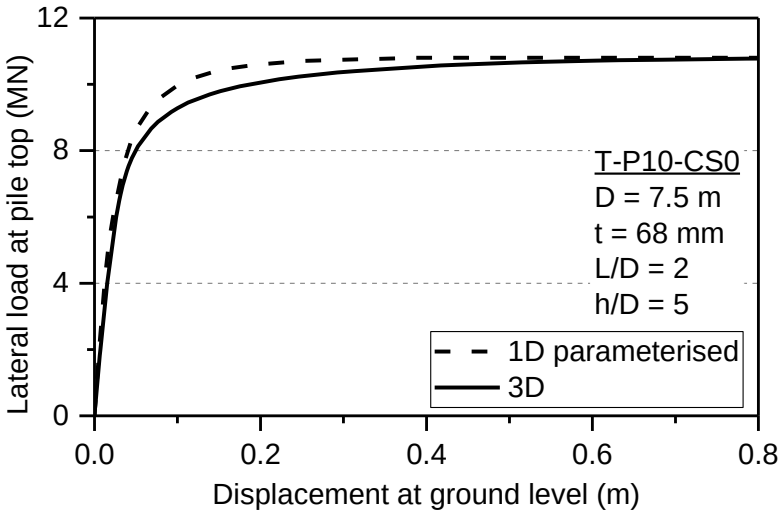

Figure 4.36 Comparison between 1D (predicted) and 3D results for T-P10-CS0 analysis

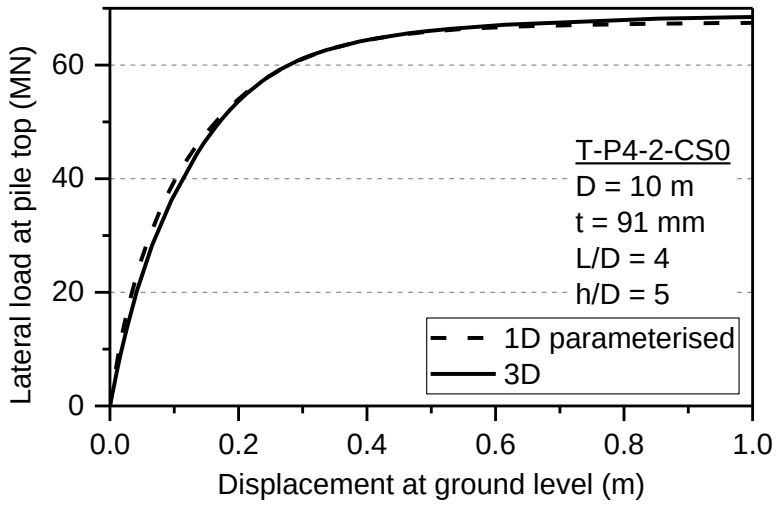

Figure 4.37 Comparison between 1D (predicted) and 3D results for T-P4-2-CS0 analysis

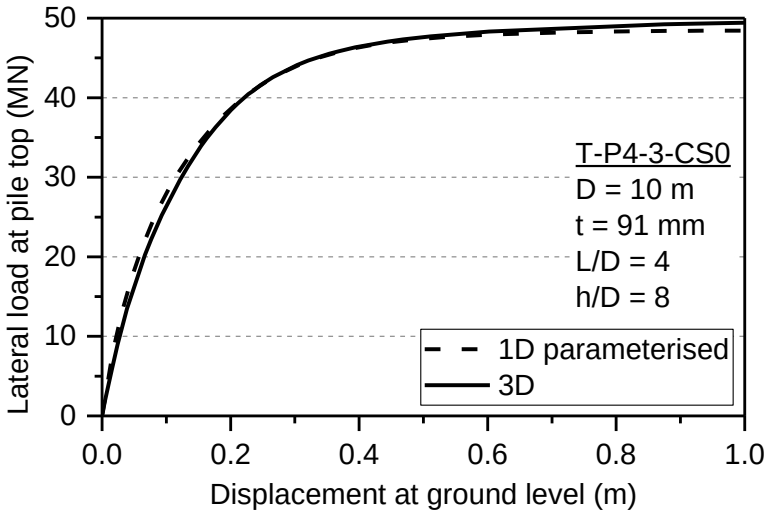

Figure 4.38 Comparison between 1D (predicted) and 3D results for T-P4-3-CS0 analysis

From the comparison shown in Figures 4.35 - 4.38, the 1D predictions matched quite well with the 3D FE results. The most significant error was shown from the results of T-P10-CS0 analysis in Figure 4.36, which might be due to the change in pile diameter. It seems that the variations of pile *L/D* ratios and load eccentricity ratios did not significantly influence the effectiveness of the calibrated 1D model.

For the load-displacement results, the difference between the 1D and 3D FE results vary with displacement. To compare the differences among the various analyses, a normalised error defined by Equation (4.3) was used.

$$normalised\ \ load\ \ error = \frac{H_{\mathrm{err}}}{H_{\mathrm{ult}}} \times 100\% \qquad (4.3)$$

where H_{err} is the absolute difference between the 1D and 3D FE results at a particular displacement level; H_{ult} is the applied load at 0.1*D* ground level displacement obtained from the 3D FE results. For analyses whose load-displacement result has not reached 0.1*D* ground level displacement, H_{ult} is taken as the maximum applied load from the 3D FE results. The normalised load error was plotted against the normalised displacement, which is the pile displacement at ground level divided by 0.1*D*. Figure 4.39 shows that the normalised errors for the four analyses presented in this section were less than 10%, which indicates that the parameterised soil reaction curves are applicable to analyses considering pile dimensions and load eccentricities which are interpolated from those used in the calibration analyses.

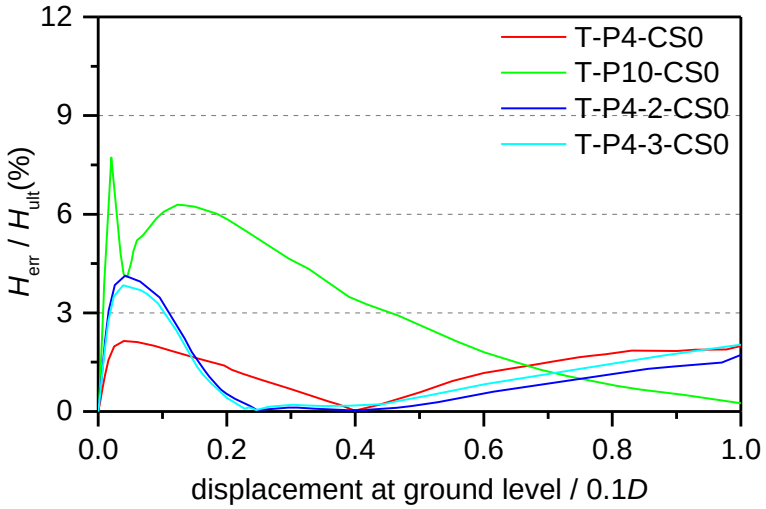

Figure 4.39 Normalised errors for analyses regarding variations of pile design parameters

4.4.2 NON-HOMOGENEOUS SOIL PROFILES

To investigate whether the parameterised curves developed from homogeneous soil simulations can be applied to non-homogeneous soils, test analyses considering three non-homogeneous profiles, as given in Table 4.6 and Figure 4.40, were performed. The load-displacement predictions were obtained using the calibrated 1D model. The comparisons between the 1D predictions and 3D FE results are shown in Figures 4.41 - 4.46.

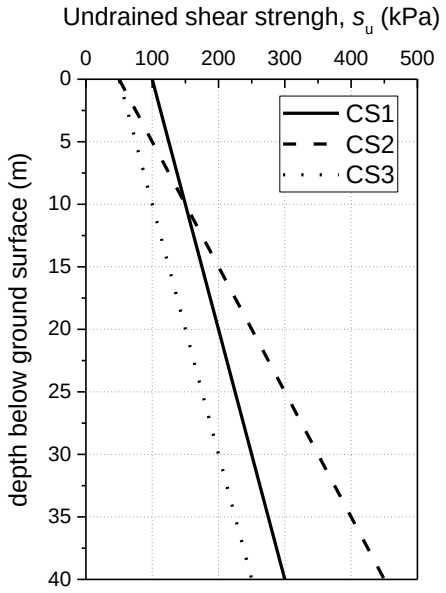

Figure 4.40 Illustration of s_u profiles for the test analyses

Table 4.6 Reference for the different clayey soil profiles used in the test analyses

Reference	Values
CS1	$s_u(0)$ = 100 kPa, m =5 kPa/m, I_R = 250, $G(0)$ = 25 MPa
CS2	$s_u(0)$ = 50 kPa, m =10 kPa/m, I_R = 250, $G(0)$ = 12.5 MPa
CS3	$s_u(0)$ = 50 kPa, m =5 kPa/m, I_R = 250, $G(0)$ = 12.5 MPa

The soil profiles were selected to study the influence of a particular factor. The effect of the magnitude at the ground surface $s_u(z = 0)$ was analysed in CS1 and CS3, and the increasing rate with depth, m, was analysed in CS2 and CS3. The clay stiffness / strength ratio, I_R, remains the same constant for the three soil profiles. Regarding pile conditions, a short pile (P10) and a long pile (P4) were considered in the analyses.

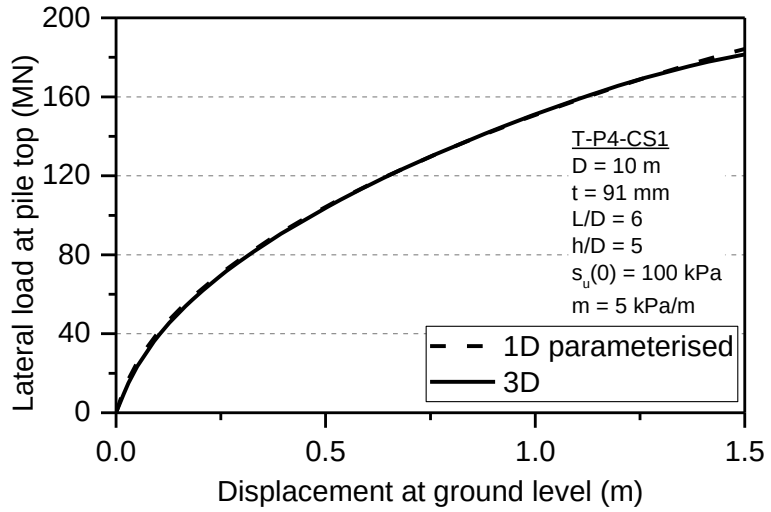

Figure 4.41 Comparison between 1D (predicted) and 3D results for T-P4-CS1 analysis

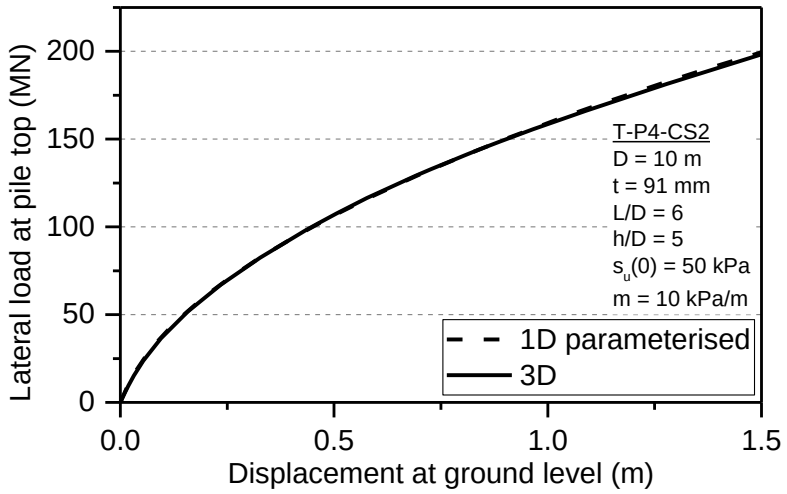

Figure 4.42 Comparison between 1D (predicted) and 3D results for T-P4-CS2 analysis

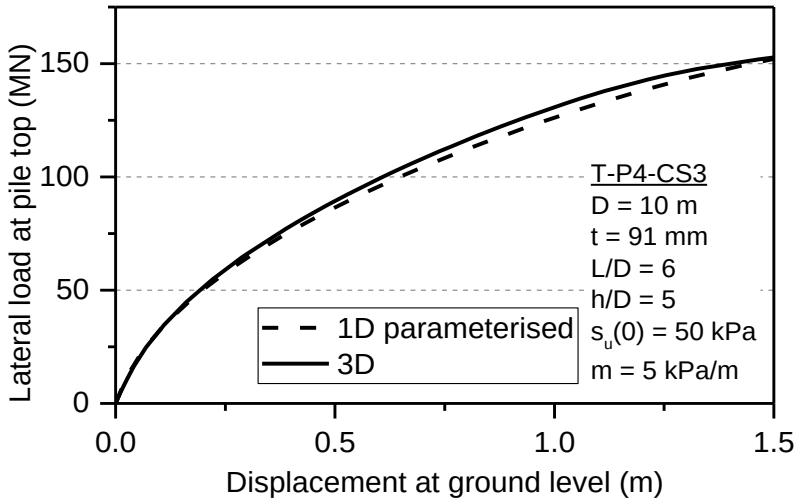

Figure 4.43 Comparison between 1D (predicted) and 3D results for T-P4-CS3 analysis

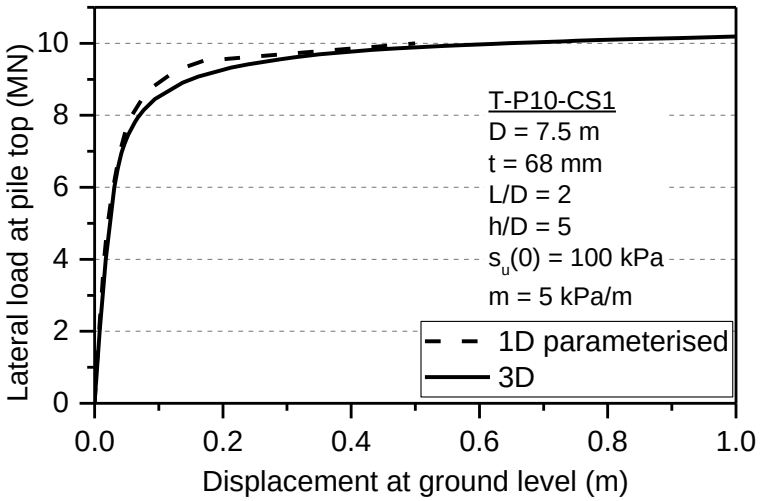

Figure 4.44 Comparison between 1D (predicted) and 3D results for T-P10-CS1 analysis

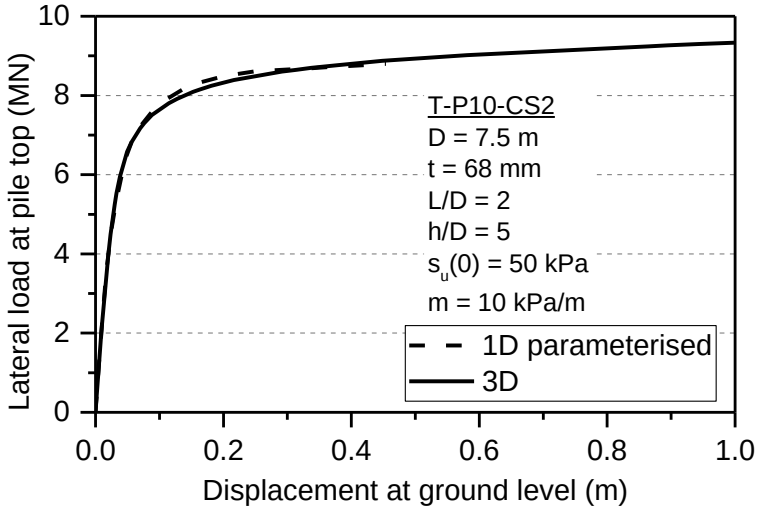

Figure 4.45 Comparison between 1D (predicted) and 3D results for T-P10-CS2 analysis

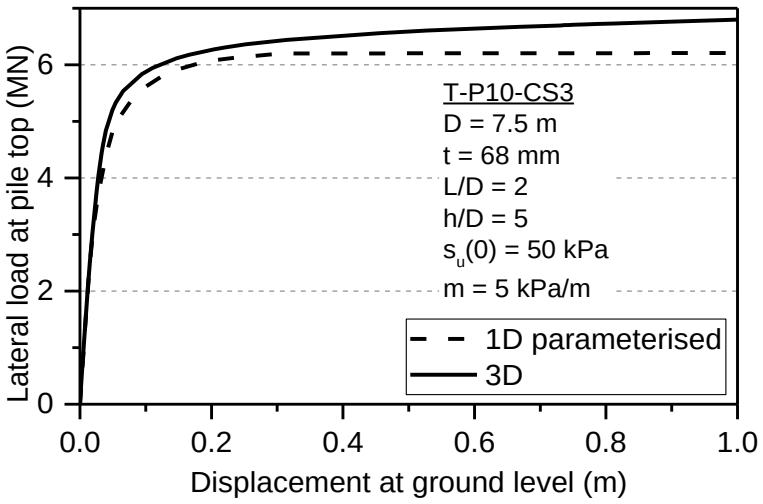

Figure 4.46 Comparison between 1D (predicted) and 3D results for T-P10-CS3 analysis

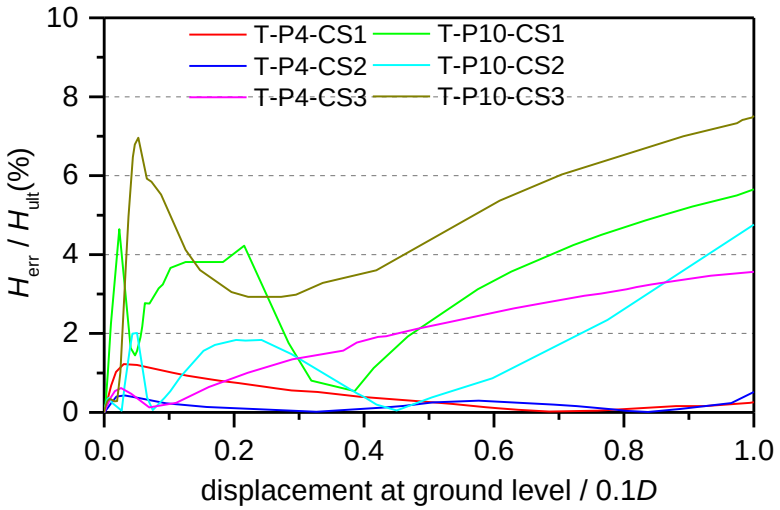

Figure 4.47 Normalised errors for analyses regarding non-homogeneous soil profiles

It can be seen from the above figures that the 1D model with the soil reaction curves extracted from homogeneous soil analyses gave quite satisfactory results for the non-homogeneous soil profiles. The maximum normalised errors for the test analyses were less than 10%, and the errors were larger for the short piles than for the long piles. It indicated that the variations of soil properties with depth did not influence the effectiveness of the calibrated 1D model.

4.5 RIGID PILE ANALYSIS FOR IDEALISED DEFORMATION MODES

The objective of the study is to explore the suitability of developing soil reaction curves from 3D FE analyses for rigid piles in idealised deformation modes, as this would reduce computational effort and alleviate the complexity of processing the soil reaction curves around the pile rotation point. Two idealised lateral deformation modes were considered: rigid lateral translation (RLT) and rigid base rotation (RBR), as illustrated in Figure 4.48.

For the RLT analyses, a forced horizontal displacement was applied to the whole pile; while for the RBR analyses, a forced rotation about a reference point, set as the midpoint at pile base, was applied to the whole pile. The pile dimensions adopted in the rigid pile analyses were the same as those used in the calibration analyses. The soil reaction curves were extracted from the RLT and RBR analyses and then compared with the numerical curves developed from the calibration analysis. These idealised analyses also investigated the relationship between the soil reaction curves and loading conditions.

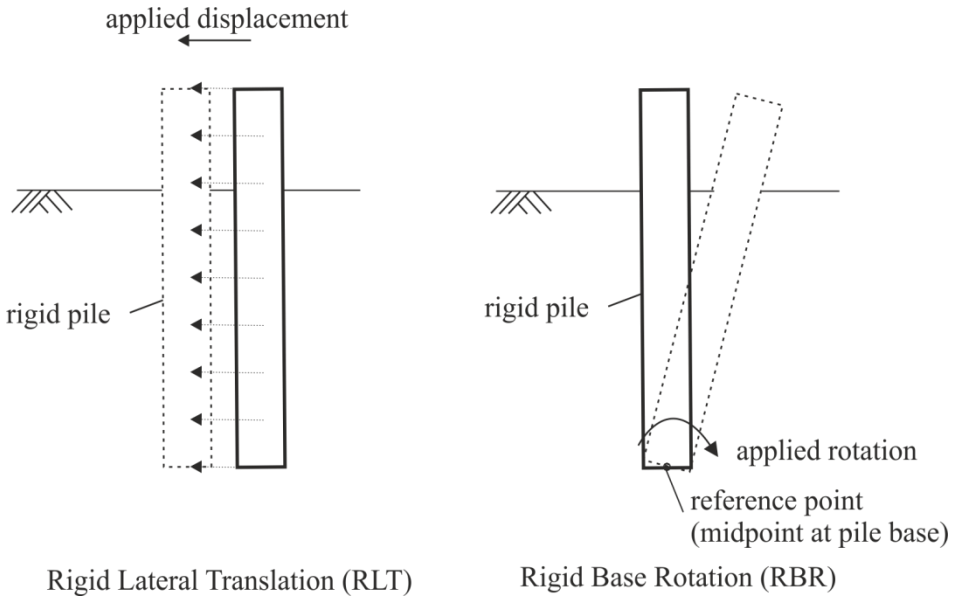

Figure 4.48 Illustration of RLT and RBR analyses

The comparisons of the curve parameters (including the initial stiffness, k_p, ultimate resistance, $\bar{p}_u$, ultimate displacement, $\bar{v}_u$, and transitional curvature parameter, n_p) of the lateral distributed load curves between the rigid pile and the calibration analyses are shown in Figures 4.49 - 4.53.

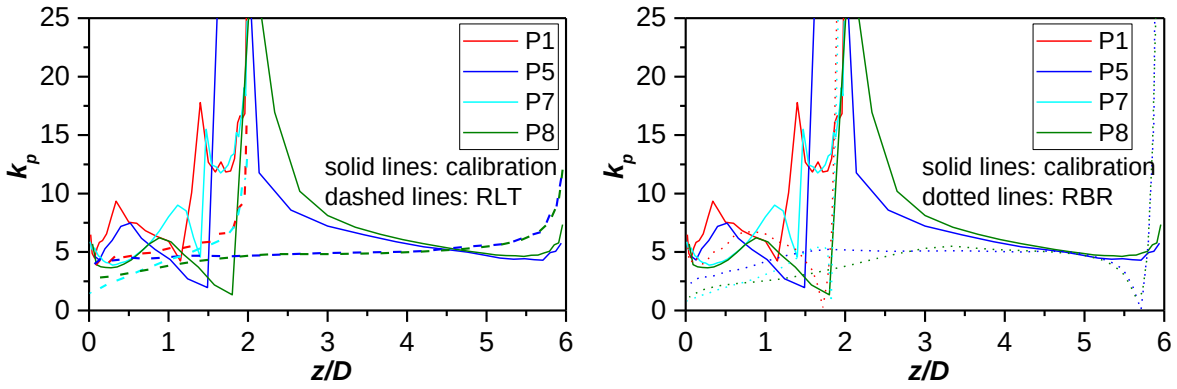

(a) RLT and calibration (b) RBR and calibration

Figure 4.49 Comparison of k_p from the calibration, RLT and RBR analyses

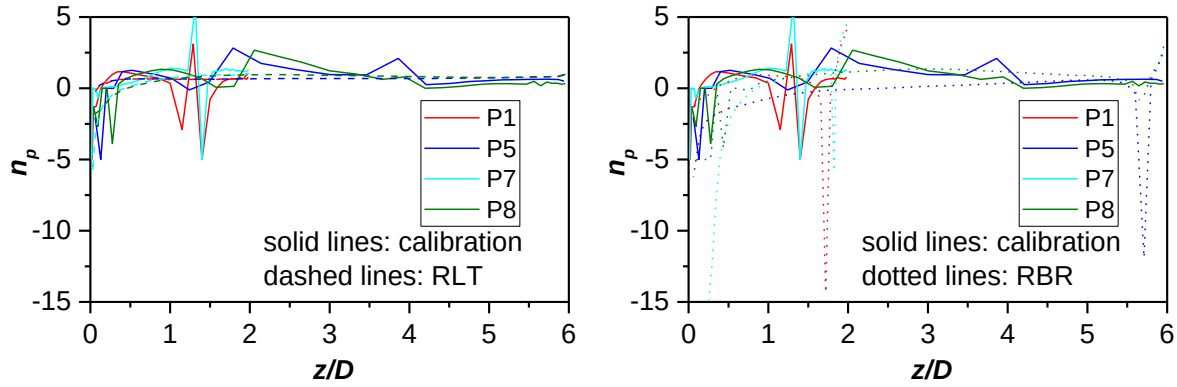

(a) RLT and calibration (b) RBR and calibration

Figure 4.50 Comparison of n_p from the calibration, RLT and RBR analyses

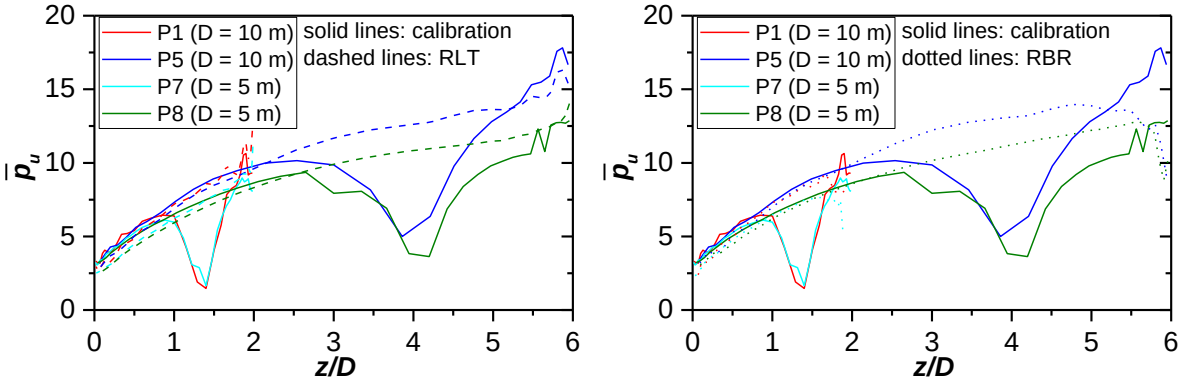

(a) RLT and calibration (b) RBR and calibration

Figure 4.51 Comparison of $\bar{p}_u$ from the calibration, RLT and RBR analyses

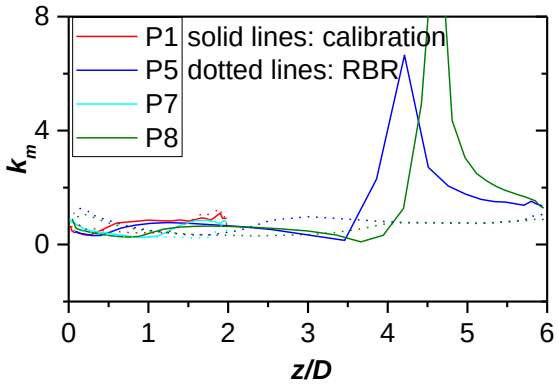

Figure 4.52 Comparison of k_m from the calibration and RBR analyses

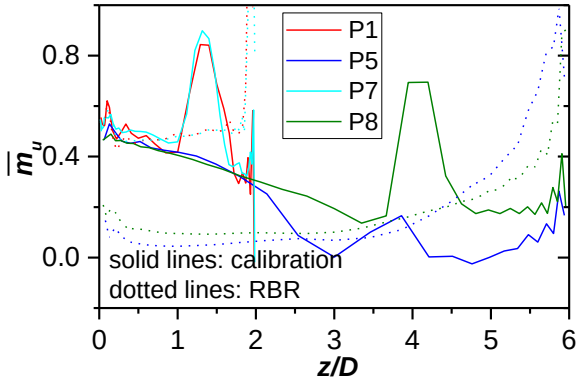

Figure 4.53 Comparison of $\bar{m}_u$ from the calibration and RBR analyses

Figure 4.49 and Figure 4.50 show that the initial stiffness and the curvature parameters are constant with depth for the RLT analyses, while they increase slightly with depth for the RBR analyses. On the other hand, their values were repeatable for the same *L/D* ratio among the RLT analyses, while their values changes with piles for the RBR analyses. From Figure 4.51, it can be seen that the ultimate response parameters obtained from the RLT and RBR analyses are similar and both match well with the results from the calibration analyses. The results again confirm that the normalised ultimate response parameter varies with *z/D* and pile diameters. The results also

indicate that restraint conditions on pile do not affect the ultimate lateral soil resistance. This finding is consistent with the findings by Matlock (1970) and Murff and Hamilton (1993).

Regarding the distributed moment curves, as the distributed moment are zero in the RLT analyses, only the results from the RBR analyses were compared with those from the calibration analyses (see Figures 4.52 and 4.53). There was no significant difference in the initial stiffness parameter between the calibration and RBR analyses, expect at greater depths for long piles, while there was significant difference in the ultimate moment parameter. The ultimate moment parameter from the RBR analyses appears to be dependent on pile *L/D* ratio (see Figure 4.53).

Because the extracted distributed load curves from the RLT analyses did not have irregular results around the pile rotation point, these curves were incorporated within the 1D model to see whether they could produce the same results as the 1D analyses with the distributed load curves extracted from the calibration analyses. The RBR analyses were not incorporated into the 1D analysis, because for the RBR case, the pile was forced to rotate about its base, which means there is no horizontal displacement and soil reaction at the pile base. As such, the soil reaction curves developed from the RBR analyses were not used for the 1D analysis. The load-displacement results obtained from the 1D analyses with the distributed load curves extracted from the RLT and those from the calibration analyses are compared in Figures 4.54 - 4.57.

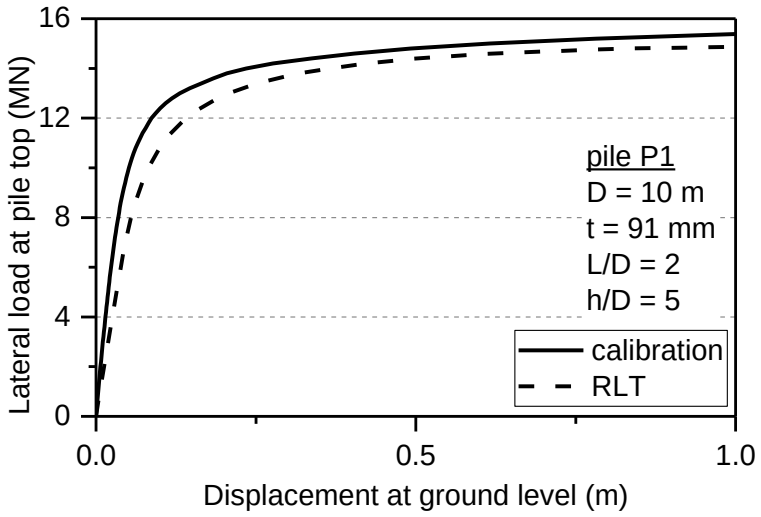

Figure 4.54 Comparison of 1D predictions from C-P1-CS0 and RLT-P1-CS0 analyses

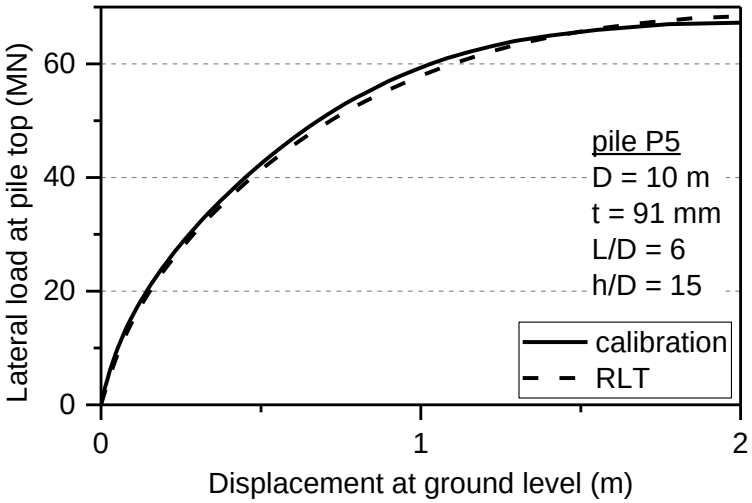

Figure 4.55 Comparison of 1D predictions from C-P5-CS0 and RLT-P5-CS0 analyses

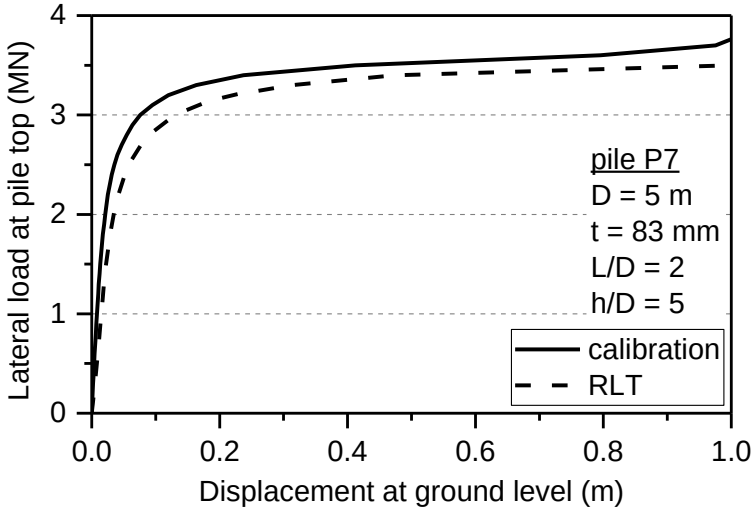

Figure 4.56 Comparison of 1D predictions from C-P7-CS0 and RLT-P7-CS0 analyses

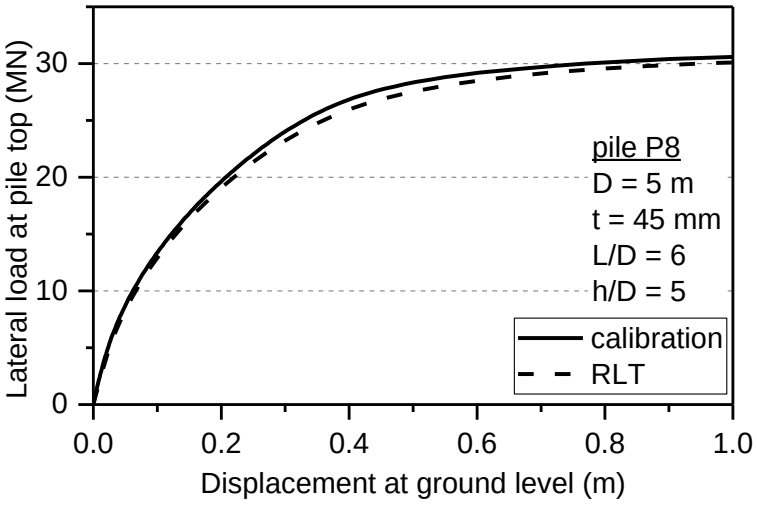

Figure 4.57 Comparison of 1D predictions from C-P8-CS0 and RLT-P8-CS0 analyses

As can be seen from Figures 4.54 - 4.57, the numerical curves from the RLT analyses over-predicted ground displacement when compared with the results from the calibration analyses at the same load. Smaller *L/D* ratios resulted in larger differences. Hence, it was concluded that developing the distributed load curves from RLT analyses was not suitable for monopiles with low *L/D* ratios.

4.5.1 COUPLING OF BASE HORIZONTAL FORCE AND BASE MOMENT

In bearing capacity problems for shallow footings, the limiting horizontal load and the limiting moment load are interdependent and they form a failure envelope. The RLT and RBR analyses investigated whether there was also a similar relationship between the two base soil reaction components. The normalised base horizontal force is plotted against the normalised base moment in Figure 4.58. Each curve corresponds to the results from a particular analysis. Each point on these curves corresponds to the results at a particular load level.

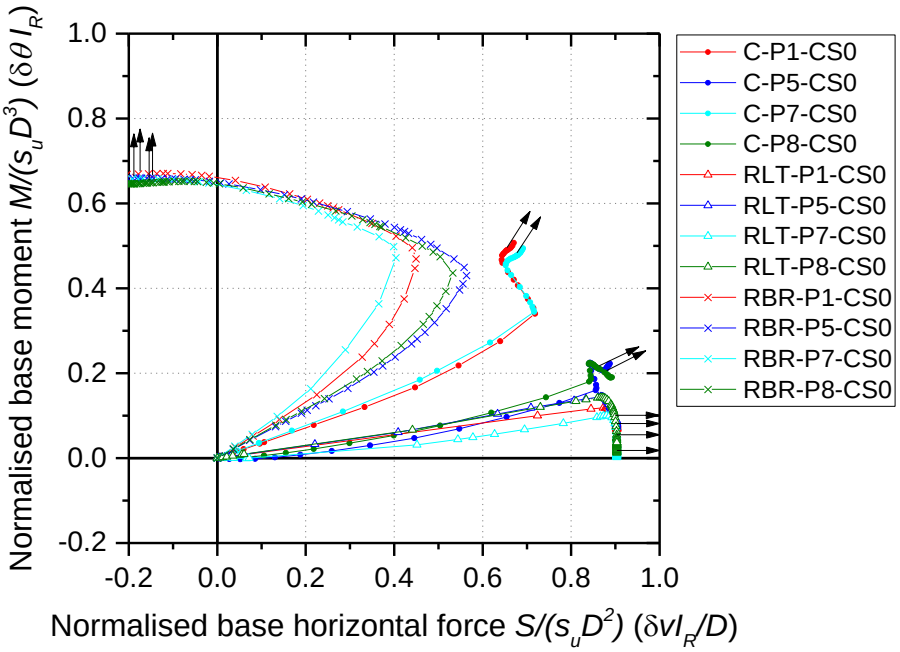

Figure 4.58 Normalised base moment vs normalised base horizontal force, and incremental normalised plastic displacement vectors for clay

The yield point was determined by taking the results at a load level at which both the base moment and base horizontal force reach their ultimate values to ensure that the incremental displacement vectors equal to the incremental plastic displacement vectors. The results indicated that there is a coupling effect between the ultimate base horizontal force and the ultimate base moment. It was found that when the ultimate base horizontal force was high, the ultimate base

moment was low, and vice versa. In addition, a consistent elliptical shape was shown for the failure envelope. The coupling between base horizontal force and base moment resulted in non-zero values in the non-diagonal terms in the stiffness matrix for the base pile element. The normalised incremental displacement vectors are shown by arrows in Figure 4.58. They have a large normal component to the ellipse, which indicates that an associated flow rule might be applicable. This points towards the development of an appropriate coupled model at the base.

4.6 LIMITATIONS AND ASSUMPTIONS

In this chapter, a series of numerical analyses were conducted to investigate the robustness of the numerical-based design approach for predicting the lateral response of monopiles in undrained clay. The limitations and the assumptions related to the analyses in this chapter are discussed as follows:

1. It was recognised that pile installation causes disturbance of soil around pile shaft. However, for driven piles, the disturbance is limited to a zone of relatively small thickness around the pile, whereas the soil in a much larger zone is subjected to stress increase due to horizontal loading (Achmus *et al*., 2009). Hence this effect was omitted in the finite element analyses.
2. The interface properties might have an influence on the distributed load and distributed moment curves, and on their contribution to the overall lateral pile response. However, a parametric study on the interface parameters was not performed due to time limits.
3. Two assumptions were made during the calibration process of soil reaction curves. Firstly, the ultimate displacement parameter for the distributed load curve was assumed constant with depth. Secondly, it was assumed that the initial peak of the distributed moment curve did not significantly affect the pile response. Both assumptions were verified by the good agreement between the predictions of 1D analysis with parameterised soil reaction curves and 3D FE results.

4.7 CONCLUDING REMARKS

In this chapter, the numerical-based design approach was applied to the analyses of laterally loaded monopiles in undrained clay. The soil reaction curves developed from the calibration analyses were parameterised and incorporated within the 1D model. The procedure used to derive the soil reaction curves were described in detail. Both the extraction and parameterisation process were validated. A set of parameterised expressions for clay were established, and were employed to calibrate the 1D model.

The extracted curves of ultimate lateral resistance with depth matched well with the solution by Murff and Hamilton (1993), which indicated that the normalised ultimate lateral resistance increases exponentially with the normalised depth. Meanwhile, a coupling effect was found between the two base soil reaction components. The increase in the ultimate base horizontal force resulted in a decrease in the ultimate base moment, and vice versa. A consistent elliptical shape of the failure envelopes was observed.

The predictive capability of the calibrated 1D model was examined by a series of test analyses considering a range of pile dimension, load eccentricity and soil profiles. The load-displacement results predicted by the 1D model using parameterised soil reaction curves matched very well with 3D FE results for all test analyses. The maximum errors for all test analyses were less than 10%. The good match indicated that (1) the parameterised soil reaction curves were able to capture soil and pile behaviour under lateral loading; (2) the soil reaction curves developed from homogeneous soil analyses could be used to predict lateral response of monopiles in Gibson soils; (3) the parameterised soil reaction curves developed from the calibration analyses could be applied to analyses considering pile geometries and load eccentricities interpolated from the parameter space used in the calibration analyses.

An attempt to develop soil reaction curves from rigid piles in lateral translation and rotation about the pile base was made. The analysis results indicated that it was infeasible to develop soil reaction curves from idealised rigid pile analyses for piles with low L/D ratios.

Chapter 5

LATERALLY LOADED MONOPILES IN SAND

5.1 INTRODUCTION

This chapter examines the performance of the numerical-based design approach for the analysis of laterally loaded monopiles in sand. Similar to the previous chapter, the study aims to (1) develop soil reaction curves from four calibration analyses; (2) test the predictive capability of the calibrated 1D model by performing analyses considering pile and soil conditions that are different from those employed in the calibration analyses; (3) explore the suitability of developing the soil reaction curves from idealised rigid pile analyses. The pile dimensions and load eccentricities considered are given in Table 3.2.

Soil profile used in the calibration and test analyses

The soil parameters for the calibration analyses were taken from Abdel-Rahman and Achmus (2005) for typical dense sand in North Sea. Most North Sea deposits are over-consolidated. The linearly elastic perfectly plastic constitutive model with a Mohr-Coulomb yield criterion was adopted in the 3D FE analyses. The Young's modulus was taken as the average value of the surface soil (depth < 20 m) from the profile adopted by Abdel-Rahman and Achmus (2005). The pile-soil interface friction coefficient was taken the same as that adopted by Abdel-Rahman and Achmus (2005). Gapping at pile-soil interface was not allowed. The homogeneous sand profile, SS0, was used in the calibration analyses, and the additional sand profiles, SS1 and SS2, were used in the test analyses. Regarding the additional sand profiles, the variations of stiffness with depth and effective unit weight were considered. The soil parameters of the sand profiles are given in Table 5.1. The variations of friction angle and relative density were not considered in the test analyses because these parameters were not used in the dimensionless groups for normalisation (see Table 2.5). This indicates that the normalised soil reaction curves developed from the calibration analyses are friction angle and relative density dependent. The earth pressure coefficient at rest was taken as K_0 = 1-sin φ' for sand, the same as that used in Reese *et al*. (1974).

Table 5.1 Soil parameters for the sand analyses

Soil parameters	Value		
Secant shear modulus at seabed level, $G(z = 0)$ (MPa)	20	0	20
Constant stiffness with depth, (Y/yes, N/no)	Y	N	Y
Stiffness/effective stress ratio, *Is* (given in Eq. (2.39))	Non-constant	200	Non-constant
Effective unit weight, γ' (kN/m^3)	11	11	13
Effective internal friction angle, φ' (°)	35		
Dilation angle, ψ (°)	5		
Poisson's ratio, v	0.25		
Earth pressure coefficient at rest, K_0	0.426		
Analysis reference	SS0	SS1	SS2

5.2 POST-PROCESSING OF SOIL REACTION CURVES

5.2.1 NORMALISATION

The soil reaction curves developed from four calibration analyses: C-P1-SS0, C-P5-SS0, C-P7-SS0, C-P8-SS0, were first normalised by the dimensionless groups from PISA (see Table 2.5). The normalised distributed moment component is related to the distributed load component, because of the pressure-dependent nature of sand shear strength.

Figure 5.1 and Figure 5.2 show the normalised distributed load and distributed moment curves at different normalised depths (z/D). As shown in Figure 5.1, the deeper soil has not reached its failure state, even though the soil at the surface has already developed significant displacement. The reason for this might be soil dilation. Under loading, a dense sand might be expected to dilate, in other words, it expands in volume during shearing. As the boundary of the soil domain was constrained, soil dilation leads to an increase in the mean effective stress (higher confining pressure). This in turn results in higher shear strength. The fluctuation of the soil resistance at large deformation might be due to stress oscillations in soil elements.

Figure 5.2 shows that the form of distributed moment curves for depths above the rotation point appears to be different from those for depths below the rotation point. The reason behind this might be the same as for the clay analyses, as discussed in Section 4.2.1.

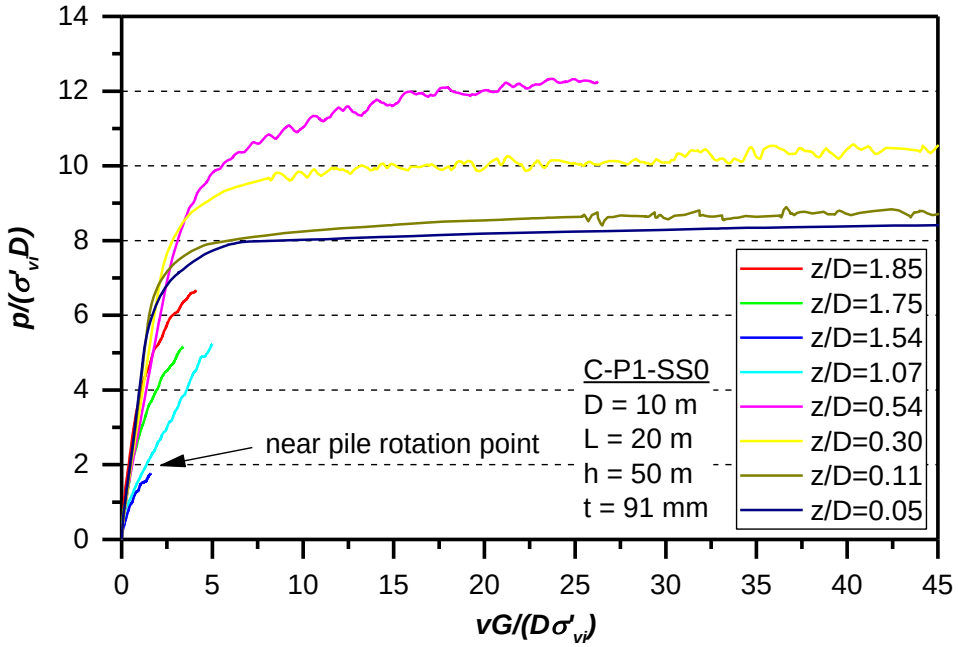

Figure 5.1 Representative normalised distributed load curves for C-P1-SS0 analysis

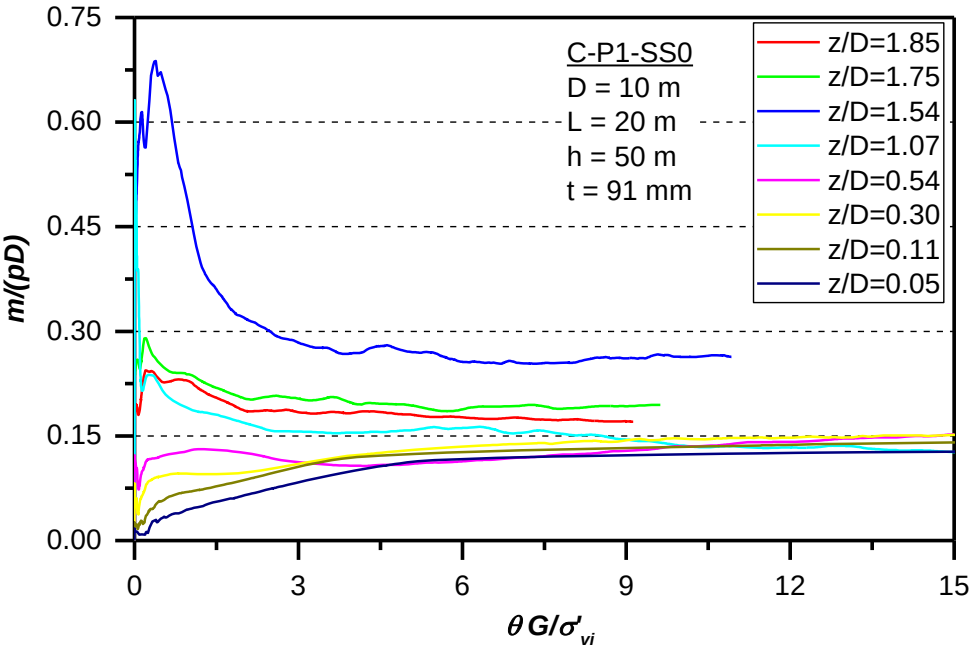

Figure 5.2 Representative normalised distributed moment curves for C-P1-SS0 analysis

5.2.2 PARAMETERISATION

The parameterisation process for sand was analogous to that used for clay. The only difference, due to data oscillations shown on the numerical curves, was that the local gradient criterion for the ultimate response parameter was less stringent than that used for clay. The curve fitting results and parameterised expressions are presented separately for each soil reaction component. The subscript nomenclature for curve fitting parameters was given in Table 4.2.

5.2.2.1 Lateral distributed load

The conic function for PISA was used to fit the numerical distributed load curves (see Equations (2.40) - (2.42)). The typical curve fitting results are shown in Figure 5.3. The numerical curves are well fitted by the parameterised curves. The parameters for the parameterised curves at the measurement depths were obtained by the procedure outlined in Figure 5.4. Similar to the procedure for clay analyses, *k* is used to indicate whether the curve has reached its ultimate response. Due to the fact that soil reaction curves at great depths have not reached their ultimate response, only the ultimate response at the shallow depths was considered.

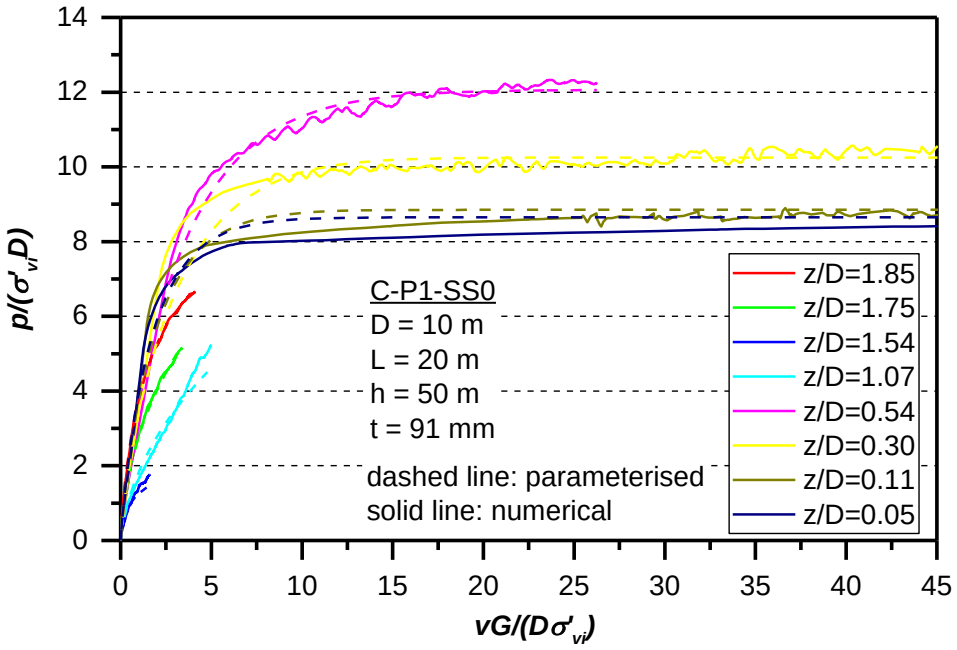

Figure 5.3 Representative curve fitting results for distributed load curves

The curve parameters were evaluated at each measurement depth and plotted against *z/D* (see Figure 5.5 and Figure 5.6). The normalised ultimate displacement was assumed as constant with depth, and determined by the mean value of the calibration analyses. The initial stiffness parameter and the curvature parameter are expressed by constants for simplicity and determined using the integration average method described in the previous chapter.

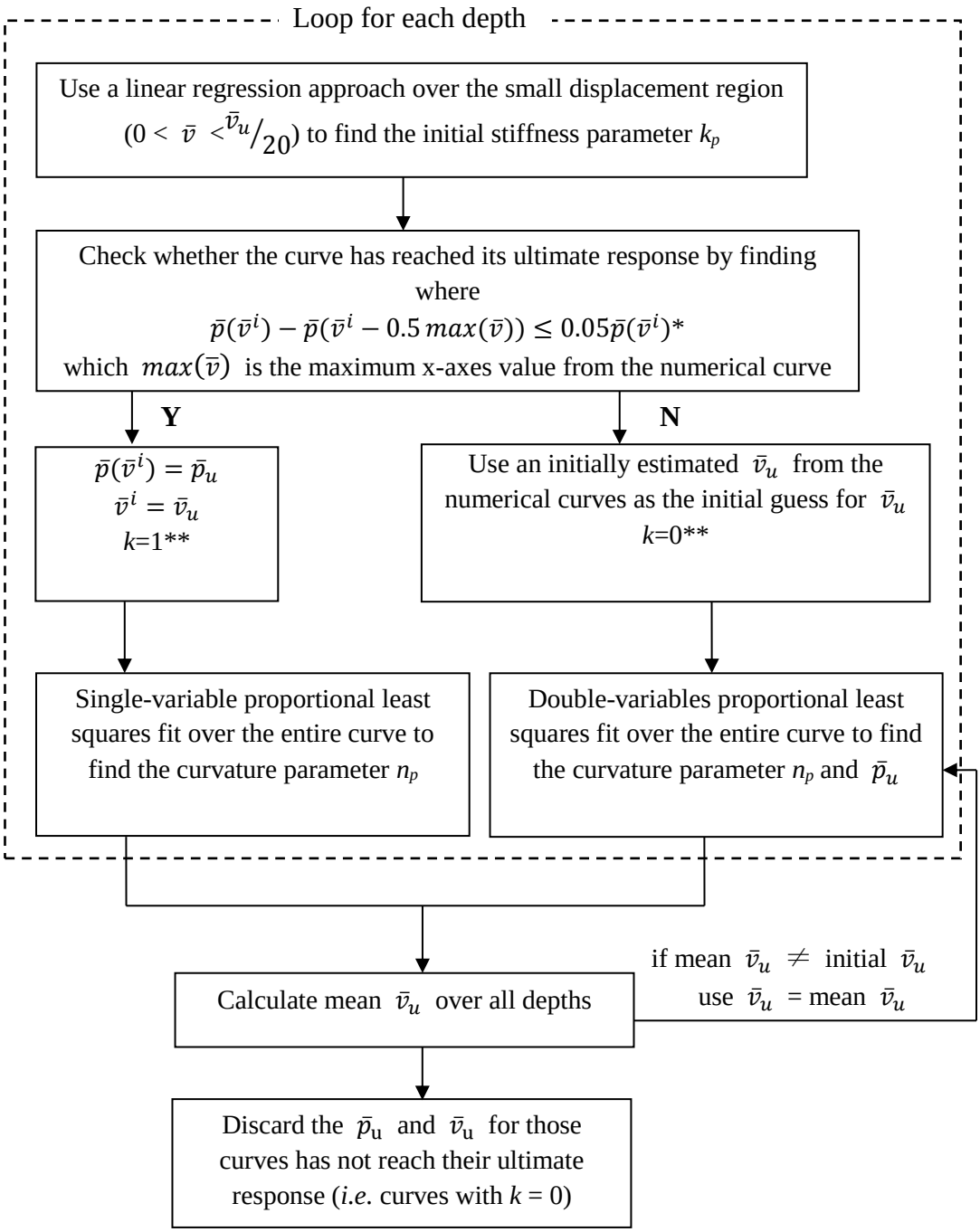

Note: * Superscript *i* indicates the data in the i[th] increment;
**k is an indicator of whether the curve has reached its ultimate response.

Figure 5.4 Process to derive the curve parameters for distributed load curves

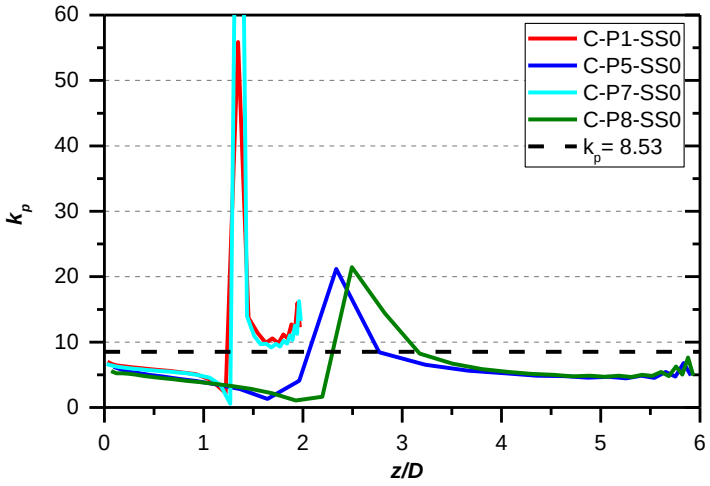

Figure 5.5 Initial stiffness parameter k_p

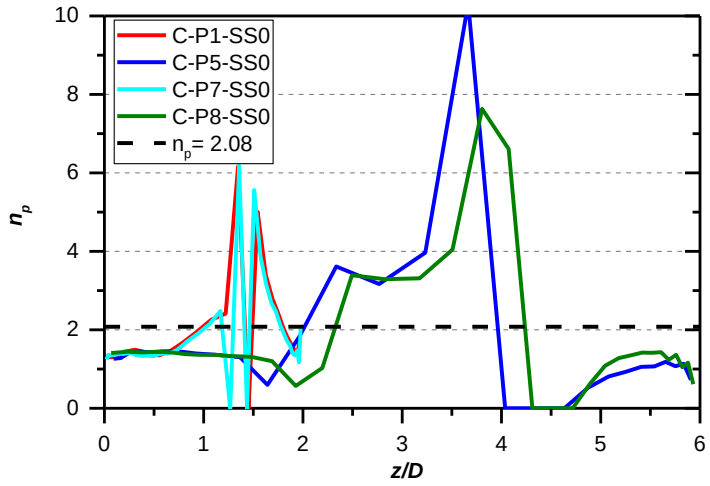

Figure 5.6 Curvature parameter n_p

Figure 5.7 shows the extracted results and the parameterised expression for the ultimate response parameter. A linear relationship is clearly shown between the extracted data and the normalised depth at shallow depths, hence a linear function was used to fit the numerical data at small *z/D* (up to the maximum *z/D* where the soil was considered as reached failure). A constant was assumed for large *z/D*. The parameterised expression was compared with solutions developed in previous research. The constant solutions obtained by empirical methods are given in Table 5.2. These solutions significantly over-predicted the normalised ultimate response at shallow depths, thus they were not likely to give accurate predictions for monopiles with low *L/D* ratio. The parameterised expression is compared with the non-linear analytical solutions (given in Table 2.3) in Figure 5.7. It shows that Brinch Hansen (1961) predicted a significantly lower $\bar{p}_u$ compared to the computed values at shallow depths. Both the API results and the prediction by Reese *et al*. (1974) are reasonably close to the extracted results shown in Figure 5.7, giving a maximum error of

about 20% for *z/D* up to 1.2. Fan and Long (2005) postulated that soil dilation led to a significant increase in the ultimate soil resistance, which none of the methods mentioned above had considered. Since no data were available at greater depths, there was little evidence to favour any of the solutions to describe $\bar{p}_u$.

Table 5.2 Constant values for $\bar{p}_u$ for sand derived from empirical-based methods

	Broms (1964a)	Barton (1982)	Zhang *et al*. (2005) *
Calculated $\bar{p}_u$	11.07	13.61	11.03
Note: * $N_p = \eta K_p{}^2 + \xi K \tan\delta$, where η is taken as 0.8 and ξ is taken as 1 for circular piles, K is equal to the lateral earth pressure coefficient at rest for driven pile, and δ is chosen as $0.5\varphi'$ for smooth steel pile.			

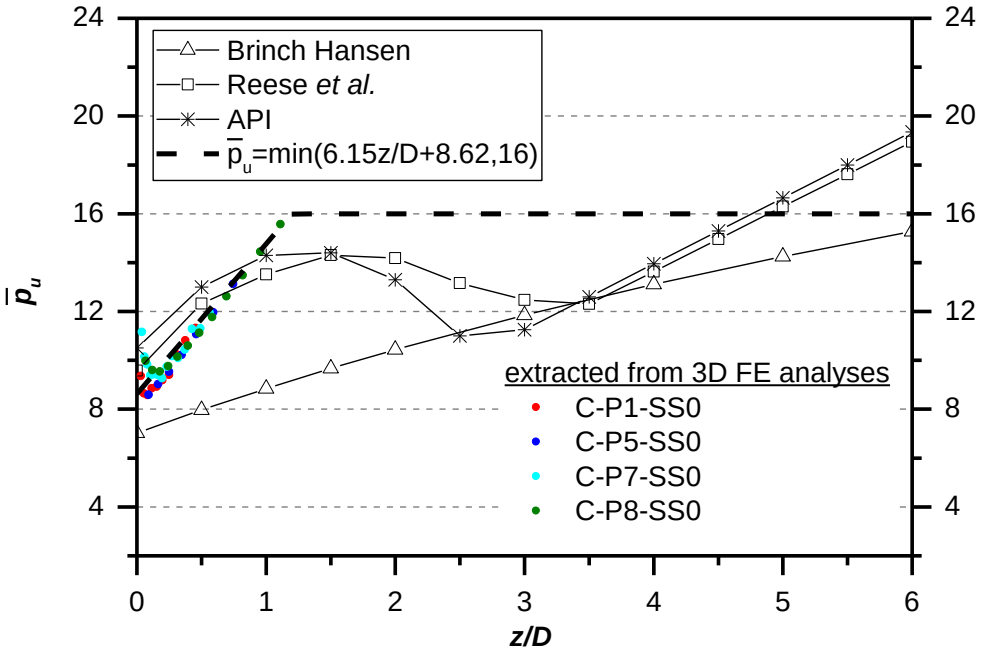

Figure 5.7 Comparison between the parameterised ultimate response and the non-linear solutions outlined in Table 2.3

The initial stiffness parameter, k_p, is an important parameter in determining the load-deflection behaviour of piles, especially at small load levels. It has a similar physical meaning as the subgrade reaction modulus discussed in Chapter 2. A direct comparison of the extracted data with the empirical solutions outlined in Table 2.1 was not conducted, due to the fact that simple linearly-elastic models were used in the 3D simulations. The simple constitutive model does not represent complex soil behaviour in reality. However, by plotting the initial stiffness parameter k_p extracted from both sand and clay analyses, as shown in Figure 5.8, a primary check on the extracted results and parameterised expressions is completed. The results for sand and clay analyses

match well, as expected, and the extracted results confirmed again a consistent decrease with normalised depth.

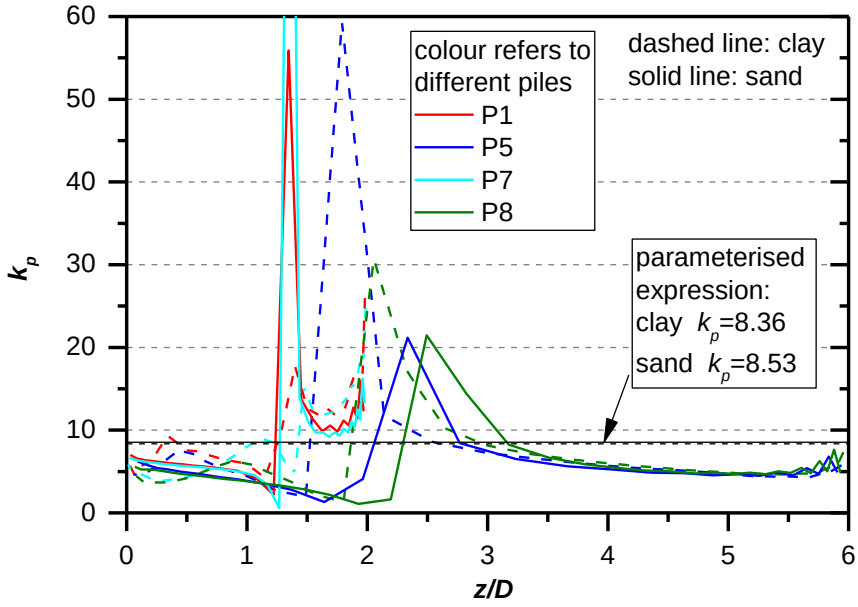

Figure 5.8 Comparison of k_p from the sand and clay calibration analyses

5.2.2.2 Distributed moment

The process used to fit the distributed moment curves for clay (see Chapter 4.2.2(b)) was repeated for sand, using the same bilinear function (see Equation (2.43)). The representative curve fitting results are shown in Figure 5.9. The initial stiffness and ultimate moment of the numerical curves were well fitted by the parameterised curves.

The curve parameters were evaluated at each measurement depth and plotted against *z/D* (See Figure 5.10 and Figure 5.11), also plotted are the values adopted for the parameterised curves. These parameters were assumed constant with depth, with the values derived from the integration average method. As shown in Figure 5.10, the computed initial stiffness parameter varies significantly with depth (*e.g.* k_m^{max}/k_m^{min} is of the order of 10^2) and the calculated mean value does not seem to be a representative value for k_m. However, it was found that choosing different constants for k_m did not significantly affect the load-displacement response predicted by the 1D model in preliminary analyses. The computed ultimate moment slightly decreased with normalised depth (see Figure 5.11), which was consistent with the results obtained in the PISA project.

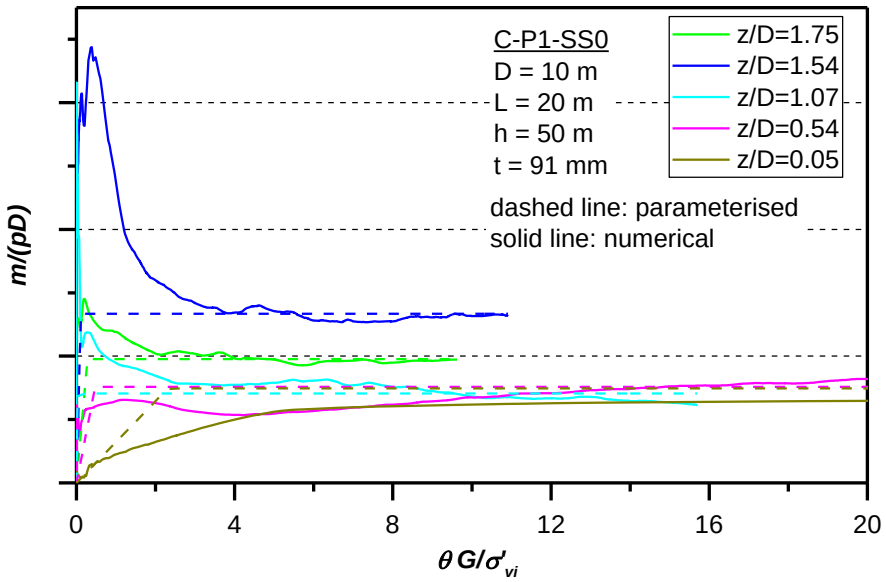

Figure 5.9 Representative curve fitting results for distributed moment curves

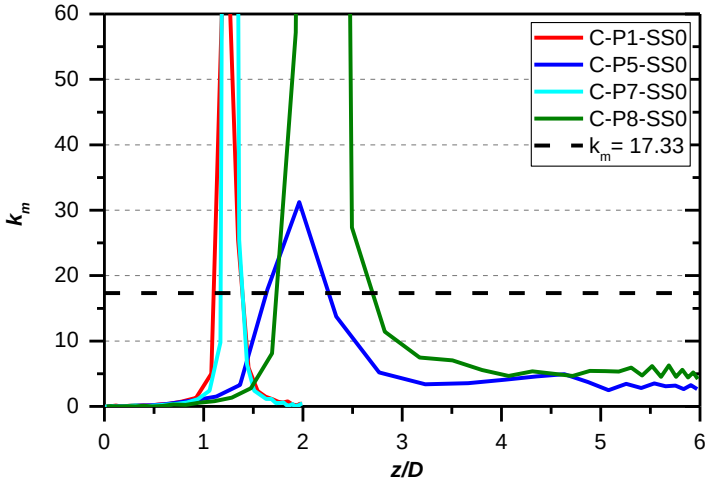

Figure 5.10 Initial stiffness parameter k_m

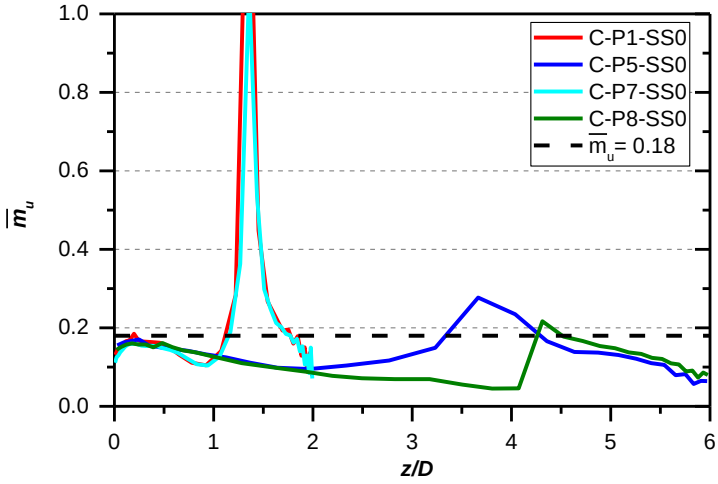

Figure 5.11 Ultimate moment parameter $\bar{m}_u$

5.2.2.3 Base horizontal force

The conical function from PISA was used to fit the base horizontal force curve. The same process used to derive the curve parameters for the distributed load curve was employed for the base horizontal force curve (see Figure 5.4). The curve fitting results for the calibration analyses are shown in Figure 5.12. The numerical curves were well fitted by the parameterised curves.

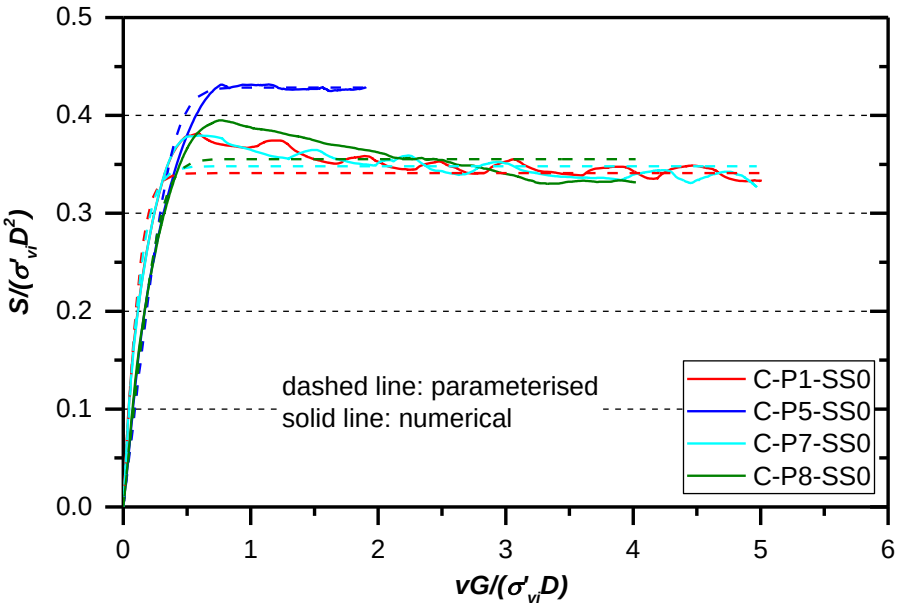

Figure 5.12 Curve fitting results for base horizontal force curves

The curve parameters are plotted against *z/D* in Figures 5.13 - 5.16, also plotted the expressions for the parameterised curves. The results for piles with *L/D* = 2 (P1 and P7) showed a slightly higher computed initial stiffness compared to the results for piles with *L/D* = 6 (P5 and P8). It appears that larger load eccentricity ratios, *h/D*, (*i.e.* P5) resulted in higher ultimate responses.

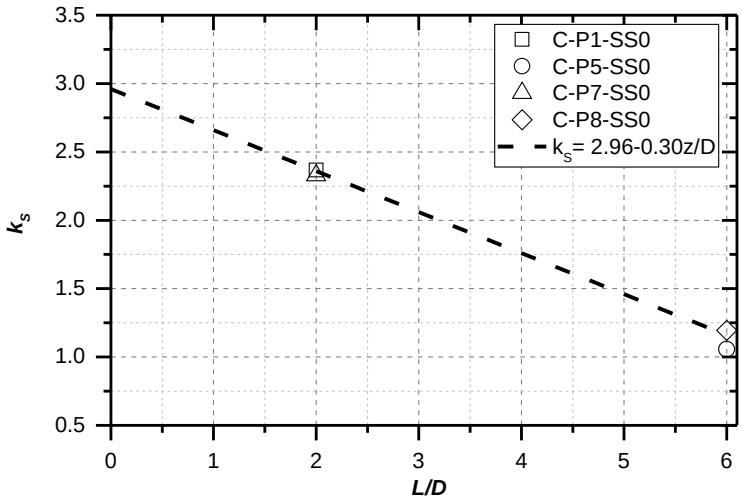

Figure 5.13 Initial stiffness parameter k_S

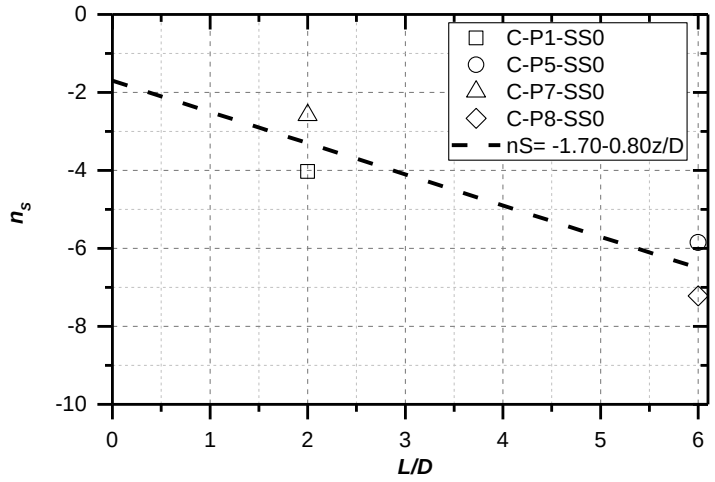

Figure 5.14 Curvature parameter n_s

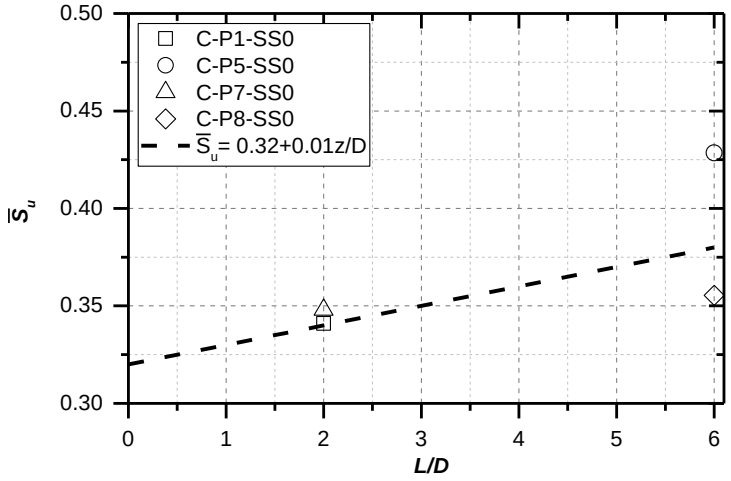

Figure 5.15 Ultimate response parameter $\overline{S}_u$

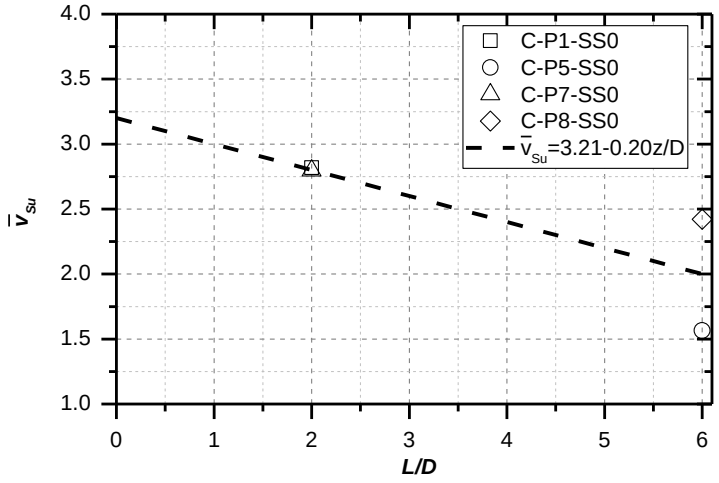

Figure 5.16 Ultimate displacement parameter $\overline{v}_{Su}$

5.2.2.4 Base moment

The same conical function as used for fitting the distributed load curves was adopted to fit the base moment curve. The curve fitting results for the calibration analyses are shown in Figure 5.17. The curve fitting results for the same *L/D* ratio were repeatable. The curve parameters are plotted against *z/D* and presented in Figures 5.18 - 5.21, also plotted the expressions for the parameterised curves. The results show that the computed initial stiffness parameter increased with normalised depth, while the computed ultimate moment and ultimate base rotation both decreased with normalised depth.

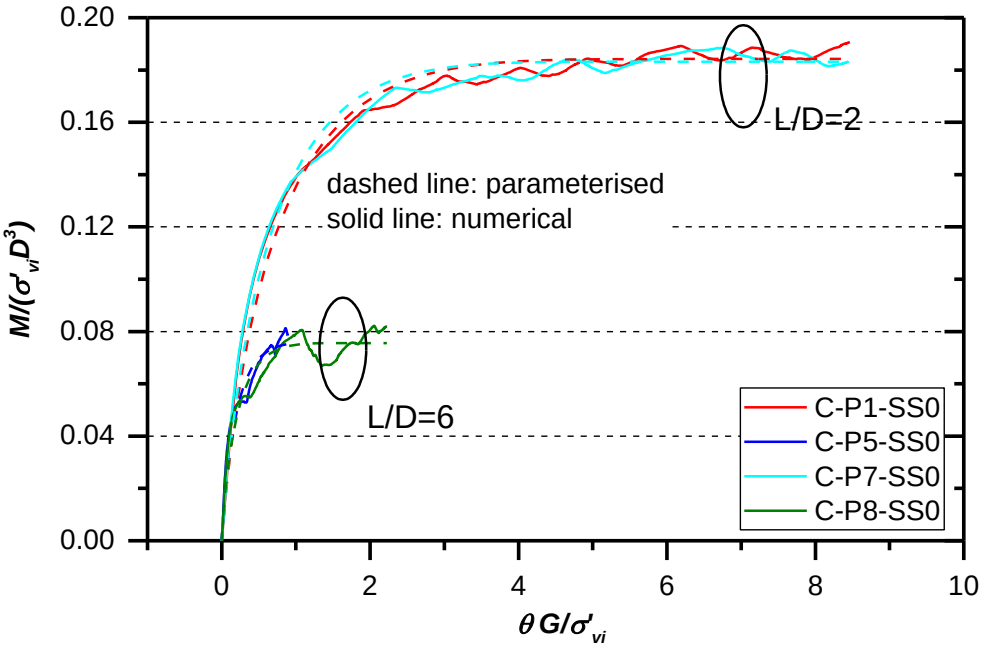

Figure 5.17 Curve fitting results for base moment curves

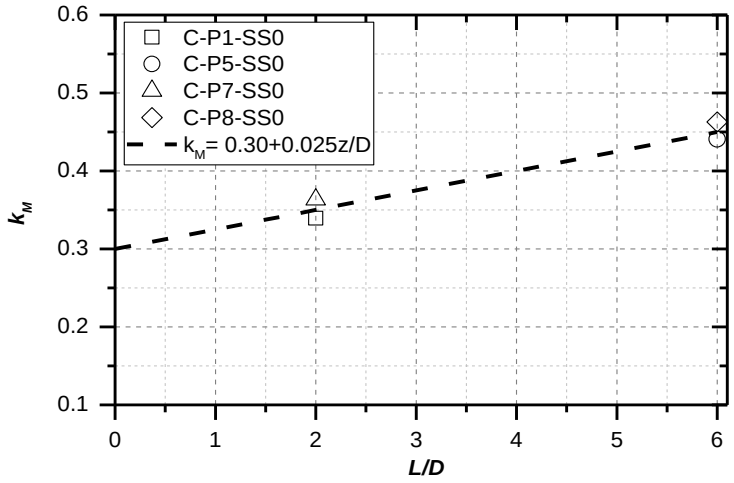

Figure 5.18 Initial stiffness parameter k_M

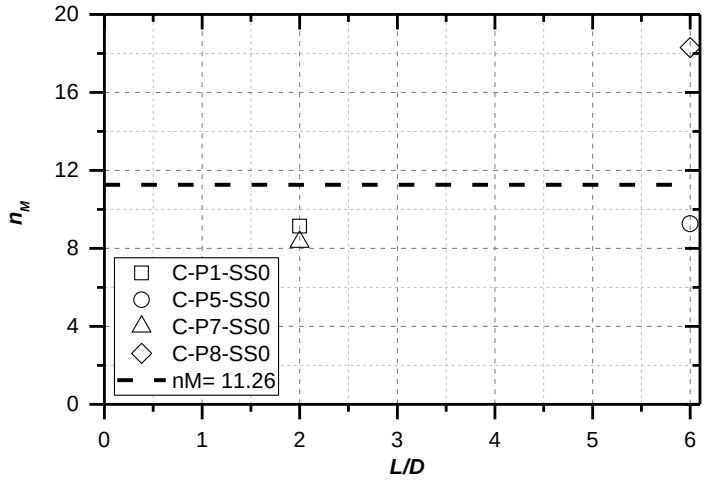

Figure 5.19 Curvature parameter n_M

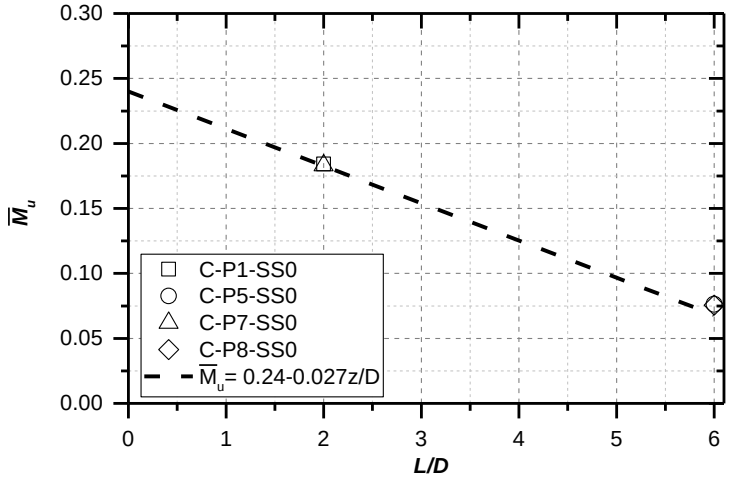

Figure 5.20 Ultimate moment parameter $\overline{M}_u$

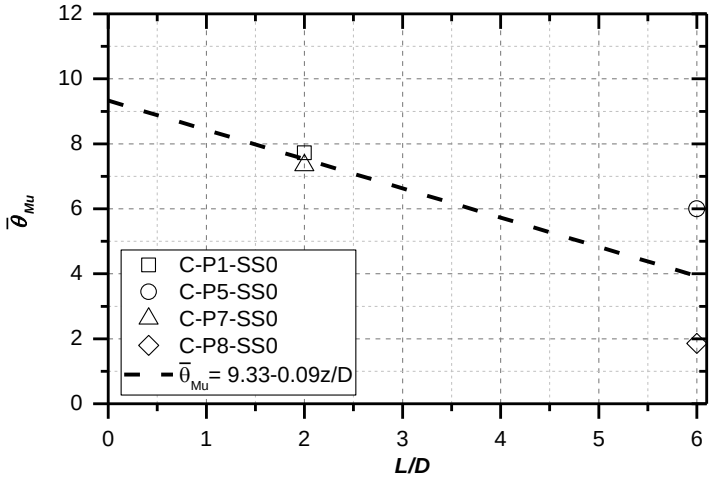

Figure 5.21 Ultimate rotation parameter $\overline{\theta}_{Mu}$

5.2.2.5 Comments on the parameterised expressions

The parameterised expressions for the soil reaction curves are summarised and compared with the expressions developed in the PISA project in Table 5.3. As mentioned in Section 4.2.2.5, the differences between the expressions developed in this study and those from PISA are expected. The expressions were developed by following the same procedure of the numerical-based design method proposed in PISA, hence, by applying these expressions, the predictive capability of the numerical-based design method and the 1D model can be examined.

Table 5.3 Summary of the expressions for the parameterised curve parameters for sand from this study and the PISA project (calibrated for $2 < L/D < 6$)

		This study	AWG PISA (2014b)
Distributed load	k_p	8.53	3.5
	n_p	2.08	2.1
	$\bar{p}_u$	$\begin{cases} 8.62 + 6.15\frac{z}{D}, & \frac{z}{D} < 1.2 \\ 16, & \frac{z}{D} \geq 1.2 \end{cases}$	18
	$\bar{v}_u$	126	90
Distributed moment	k_m	17.33	20
	$\bar{m}_u$	0.18	$\begin{cases} -\frac{1}{6}\frac{z}{D} + 0.27, & \frac{z}{D} < 0.6 \\ 0.17, & \frac{z}{D} \geq 0.6 \end{cases}$
Base horizontal force	k_S	$2.96 - 0.30\frac{z}{D}$	$2.8 - 0.3\frac{z}{D}$
	n_s	$-1.70 - 0.80\frac{z}{D}$	11
	$\bar{S}_u$	$0.32 + 0.01\frac{z}{D}$	$1.1 - \frac{67}{600}\frac{z}{D}$
	$\bar{v}_{Su}$	$3.21 - 0.20\frac{z}{D}$	$35 - \frac{23}{6}\frac{z}{D}$
Base moment	k_M	$0.30 + 0.025\frac{z}{D}$	0.23
	n_M	11.26	18
	$\bar{M}_u$	$0.24 - 0.027\frac{z}{D}$	$0.55 - \frac{7}{120}\frac{z}{D}$
	$\bar{\theta}_{Mu}$	$9.33 - 0.09\frac{z}{D}$	200

5.3 APPLICATION OF SOIL REACTION CURVES TO THE 1D MODEL

1D analyses using the numerical and parameterised soil reaction curves were carried out. The load-displacement results predicted using the 1D model were compared with the results obtained by 3D FE analyses. The contribution of each soil reaction component to overall pile response is also discussed.

5.3.1 NUMERICAL SOIL REACTION CURVES

For each calibration analysis, the numerical soil reaction curves were incorporated within the 1D model. The pile and soil conditions used in the 3D FE analyses were adopted in the 1D analyses. The load-displacement results from the 1D and 3D analyses are shown in Figures 5.22 - 5.25. The notation used in the legend refers to Section 4.3.1.

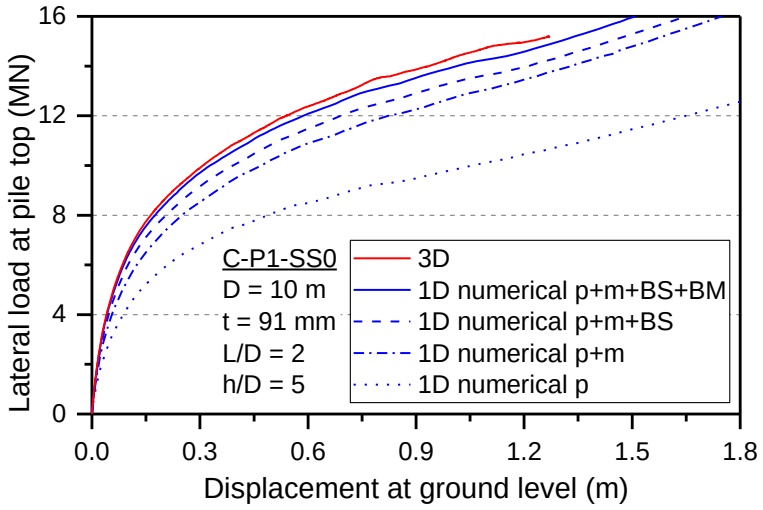

Figure 5.22 Comparison between 1D (numerical) and 3D results for C-P1-SS0 analysis

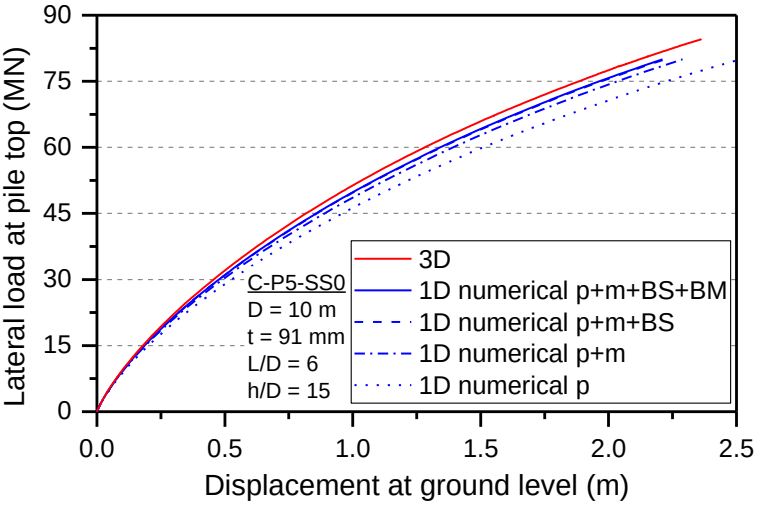

Figure 5.23 Comparison between 1D (numerical) and 3D results for C-P5-SS0 analysis

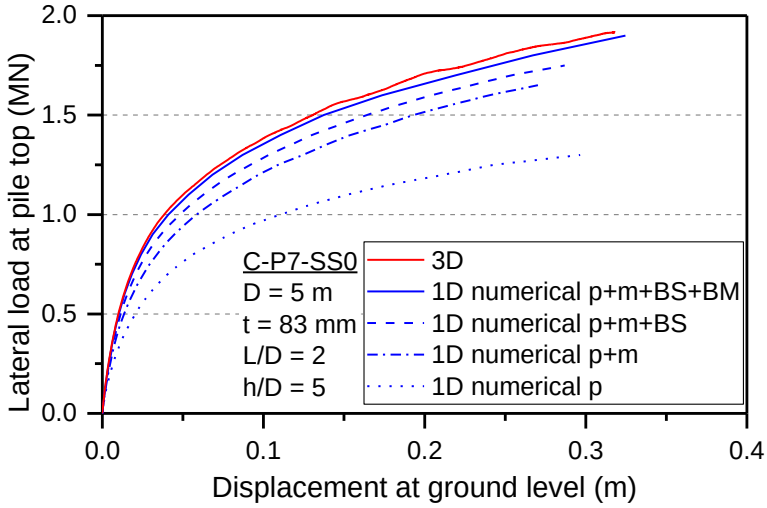

Figure 5.24 Comparison between 1D (numerical) and 3D results for C-P7-SS0 analysis

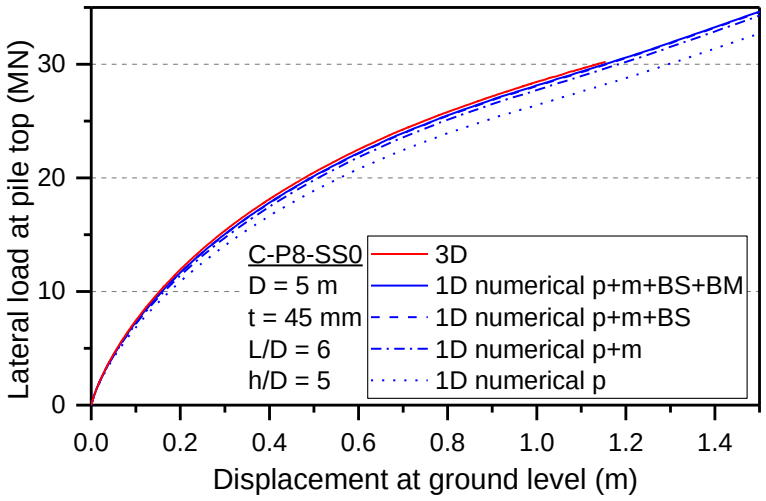

Figure 5.25 Comparison between 1D (numerical) and 3D results for C-P8-SS0 analysis

Figures 5.22 - 5.25 show that the agreement between the 1D predictions with all soil reaction components and 3D FE results are quite satisfactory. The maximum errors were less than 5%. It indicated that the extraction process and the 1D model were both validated.

Contribution of additional soil reaction components

Table 5.4 shows the contribution metric for each soil reaction component, which was defined by Equation (4.2). Compared to the clay analyses, the contribution metric for the distributed moment was higher for the sand analyses, which might be due to the fact that this component is dependent on the distributed load. The results given in Table 5.4 imply that it is important to consider the additional soil reaction components to accurately predict the responses for monopiles with low *L/D* ratios.

Table 5.4 Contribution of the soil reaction component to pile lateral response (%)

Analysis	*L/D*	*D* (m)	η_p	η_m	η_S	η_M
C-P1-SS0	2	10	70.18	19.18	5.60	5.04
C-P7-SS0*	2	5	71.14	18.71	5.35	4.80
C-P5-SS0	6	10	93.25	4.57	2.02	0.16
C-P8-SS0	6	5	93.48	4.50	1.83	0.19

Note: *Because the load-displacement response for C-P7-SS0 analysis did not reach the ultimate displacement criterion, the shown value considers the area up to 0.05*D* ground displacement instead.

5.3.2 PARAMETERISED SOIL REACTION CURVES

The results of the 1D analyses with parameterised soil reaction curves (shown by dashed lines) are compared with the corresponding 3D FE results (shown by solid lines) in Figures 5.26 - 5.29.

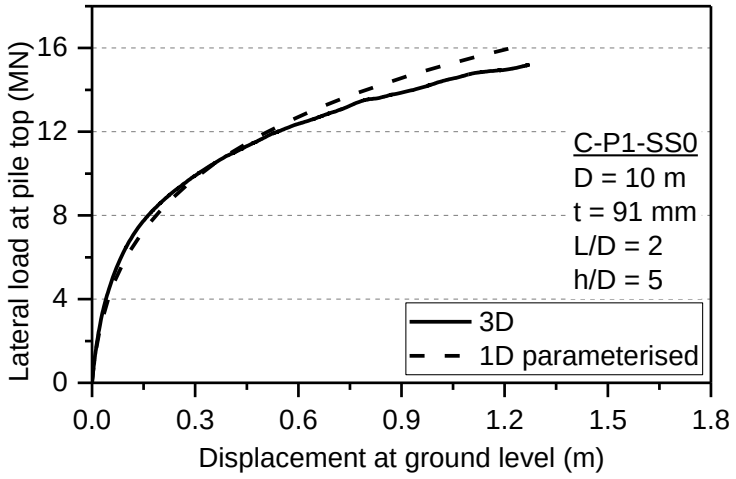

Figure 5.26 1D (parameterised) and 3D results for C-P1-SS0 analysis

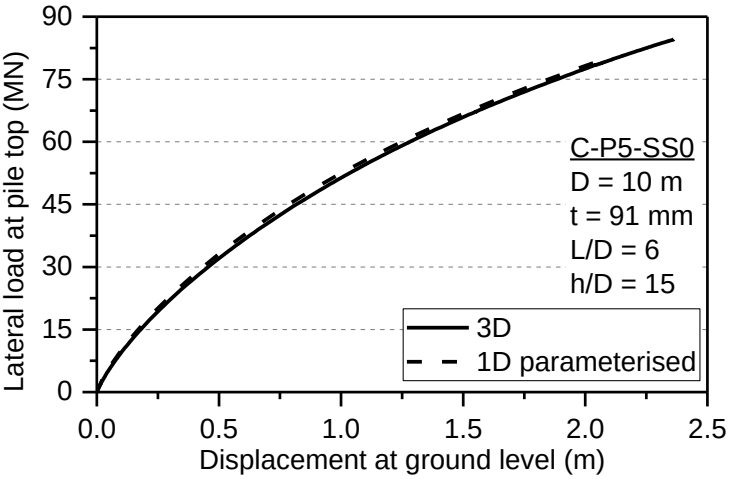

Figure 5.27 1D (parameterised) and 3D results for C-P5-SS0 analysis

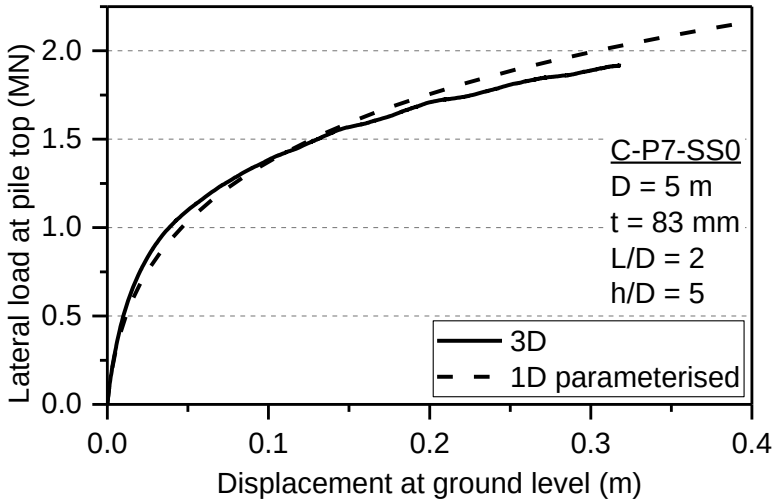

Figure 5.28 1D (parameterised) and 3D results for C-P7-SS0 analysis

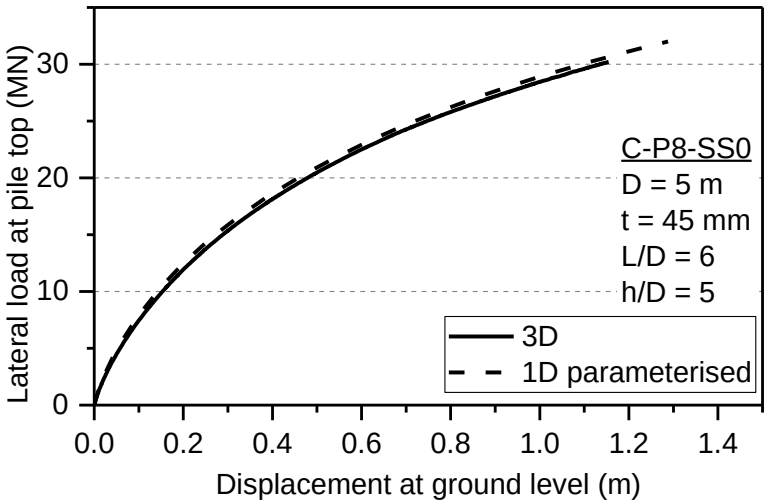

Figure 5.29 1D (parameterised) and 3D results for C-P8-SS0 analysis

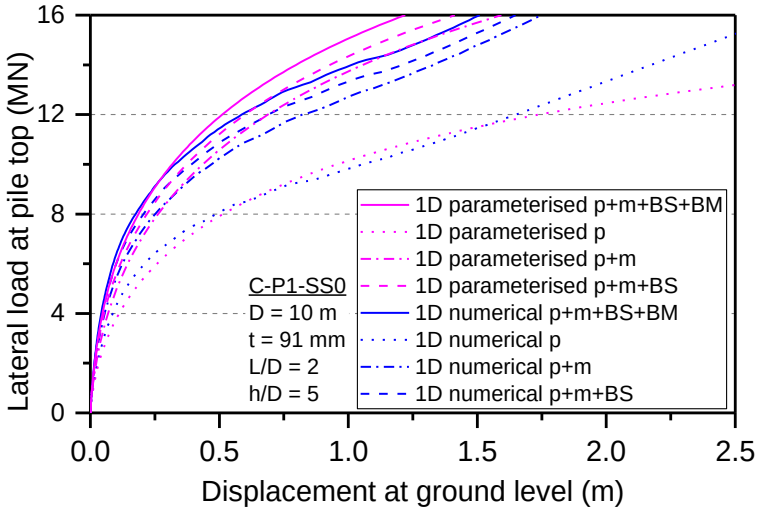

Figure 5.30 Comparison between 1D (parameterised) and 1D (numerical) results for C-P1-SS0 analysis

Despite the fact that most soil curve parameters were simply assumed constant with depth, the parameterised curves yielded predictions that matched closely the 3D FE results, although the predicted displacement was slightly conservative at higher loads. The maximum errors for the calibration analyses were within 10%. However, it was not clear whether these piles have reached their ultimate capacity. Figure 5.30 shows that the decomposition of the soil reaction component was well captured by the parameterised soil reaction curves. Therefore, the parameterisation process and expressions developed were proven to be effective, and the parameterised curves were used as input to 1D model.

5.4 PREDICTABILITY STUDIES

A series of test analyses were carried out to examine the predictability of the calibrated 1D model in different design scenarios. In the test analyses, pile geometries and soil conditions which are different from those used in the calibration analyses were considered.

5.4.1 VARIATION OF PILE DESIGN PARAMETERS

Test analyses using the additional piles, P4, P10, P4-2, P4-3 as given in Table 3.2, were performed. The four test analyses (T-P4-SS0, T-P10-SS0, T-P4-2-SS0, T-P4-3-SS0) investigate the influence of varying pile diameters (T-P10-SS0), *L/D* ratios (T-P4-2-SS0, T-P4-3-SS0), load eccentricity ratios *h/D* (T-P4-3-SS0) and different combination of design parameters (T-P4-SS0).

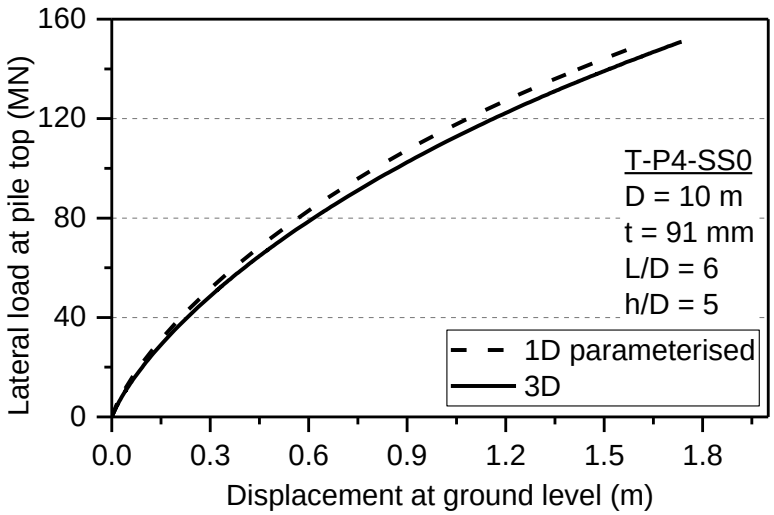

Figure 5.31 Comparison between 1D (predicted) and 3D results for T-P4-SS0 analysis

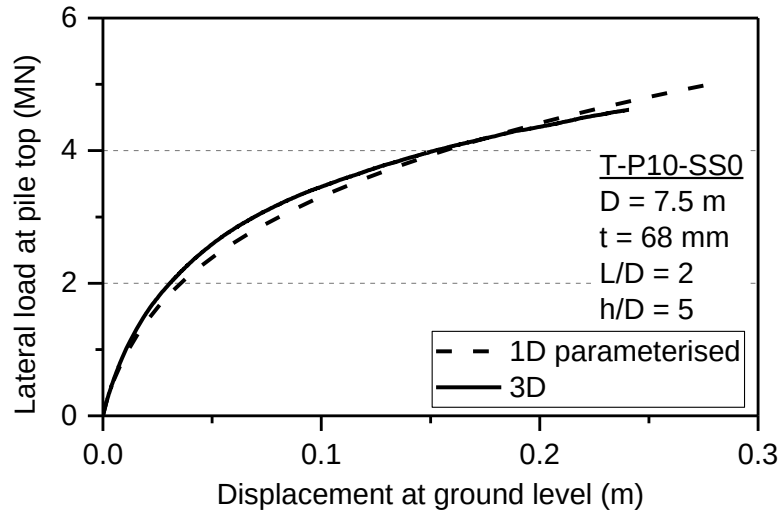

Figure 5.32 Comparison between 1D (predicted) and 3D results for T-P10-SS0 analysis

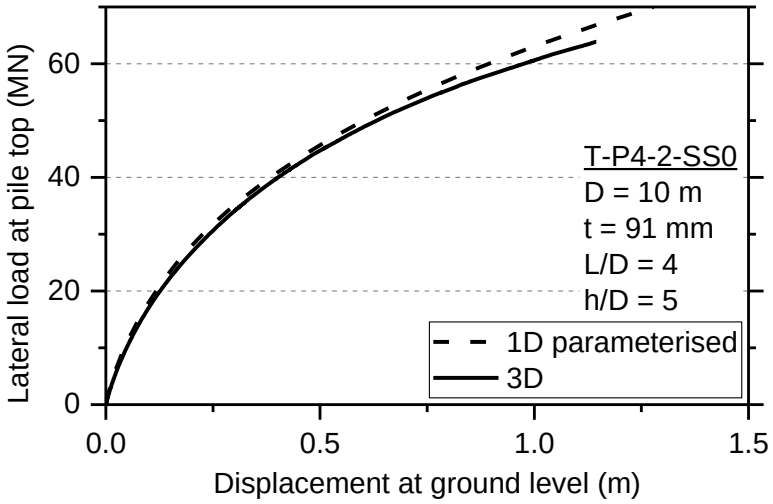

Figure 5.33 Comparison between 1D (predicted) and 3D results for T-P4-2-SS0 analysis

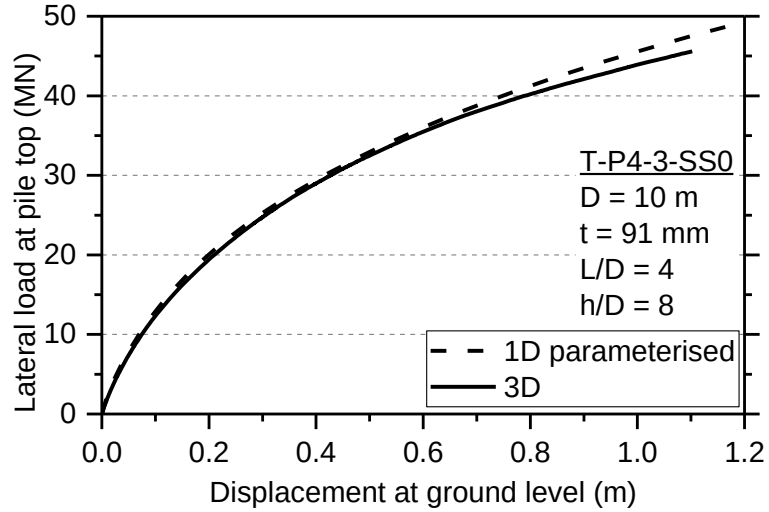

Figure 5.34 Comparison between 1D (predicted) and 3D results for T-P4-3-SS0 analysis

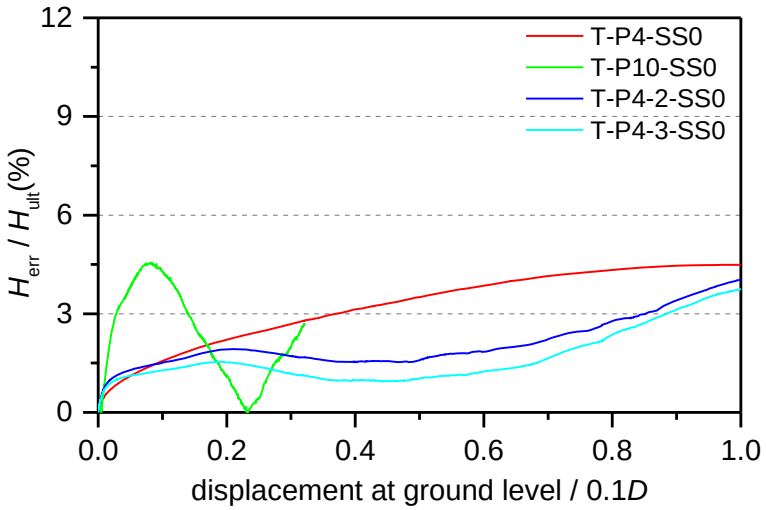

Figure 5.35 Normalised errors for analyses regarding variations of pile design parameters

The 1D predictions are compared with results obtained from the corresponding 3D FE analyses in Figures 5.31 - 5.34. As shown from the results, there was excellent agreement between the 1D predictions and 3D FE results. The maximum errors for the analyses were less than 10%.

5.4.2 VARIATION OF SOIL CONDITIONS

To investigate whether the parameterised curves developed from homogeneous soil analyses can be applied to soil which is different from that used in the calibration analyses, two additional soil profiles were considered in the test analyses, as given in Table 5.1 and Figure 5.36.

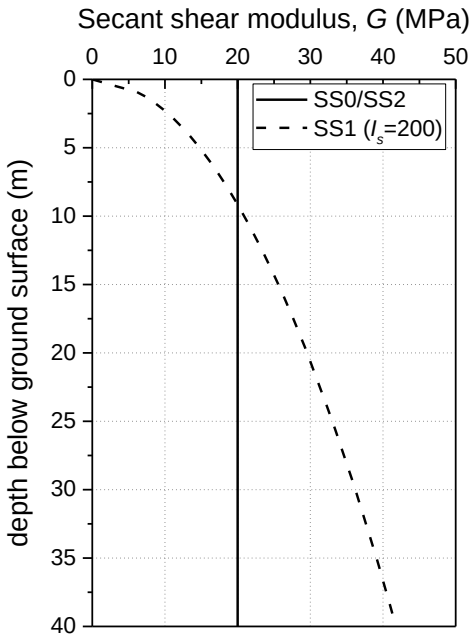

Figure 5.36 Illustration of *G* profiles for sand test analyses

In the soil profile SS0 used in the calibration analyses, *G* was assumed constant with depth. For natural sand, *G* usually varies with the square root of the mean effective stress (Wroth and Houlsby, 1985), which corresponds to a constant I_s with depth. A sand profile, SS1, with a constant I_s was considered in the test analyses. The soil profile SS1 was the same as adopted in Abdel-Rahman & Achmus (2005). The soil profile SS2 used a higher effective density to investigate the effect of soil density on the robustness of the calibrated 1D model. The stiffness for the soil profile SS2 remained constant with depth. A short pile (P10) and a long pile (P4) were considered in the test analyses. The comparisons between the 1D predictions and the 3D FE results are shown in Figures 5.37 - 5.40.

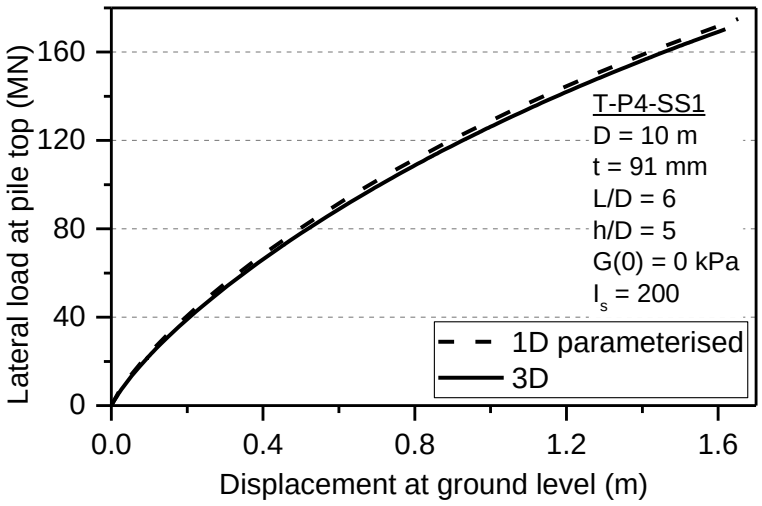

Figure 5.37 Comparison between 1D (predicted) and 3D results for T-P4-SS1 analysis

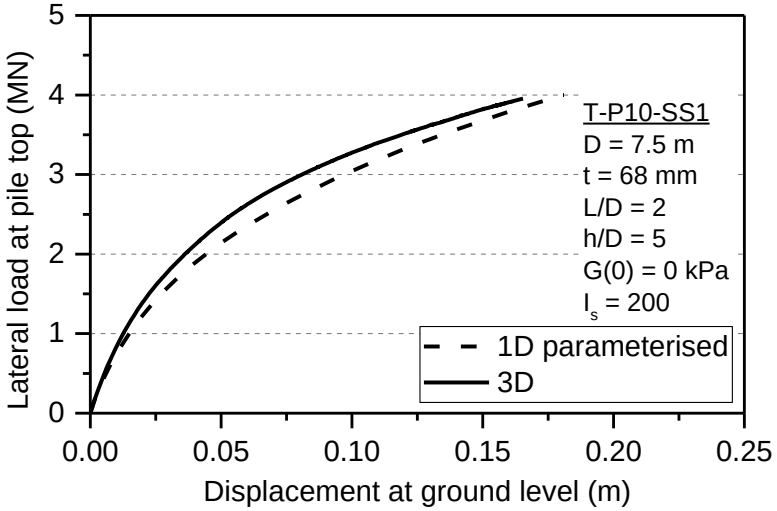

Figure 5.38 Comparison between 1D (predicted) and 3D results for T-P10-SS1 analysis

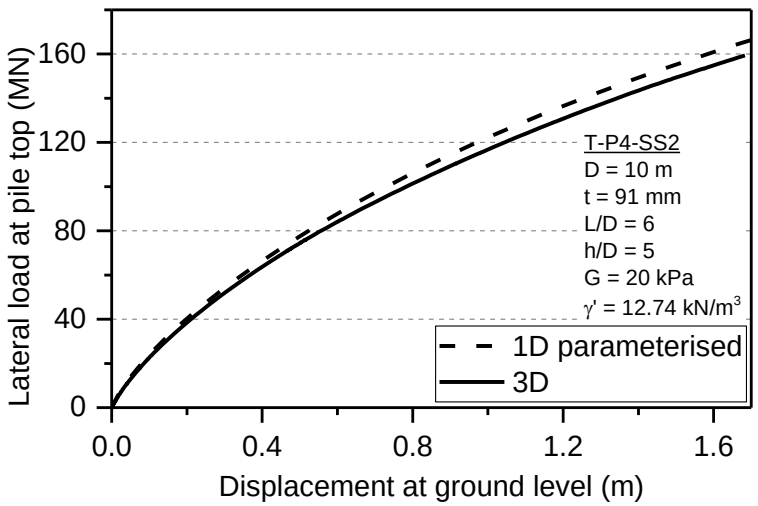

Figure 5.39 Comparison between 1D (predicted) and 3D results for T-P4-SS2 analysis

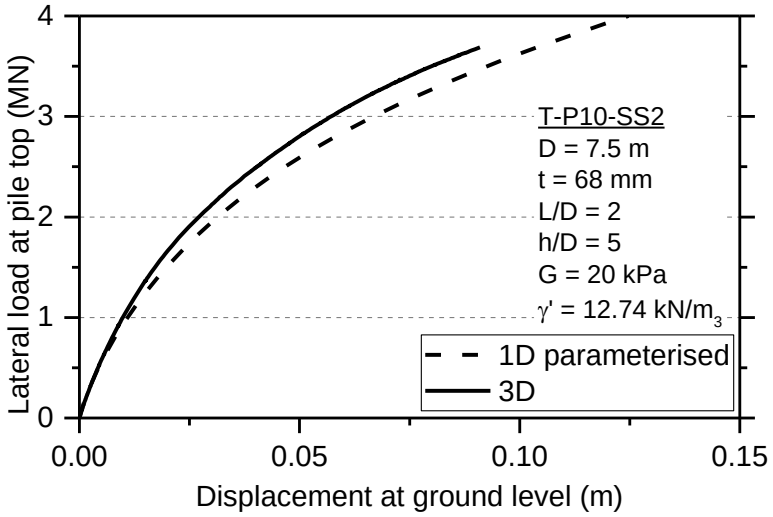

Figure 5.40 Comparison between 1D (predicted) and 3D results for T-P10-SS2 analysis

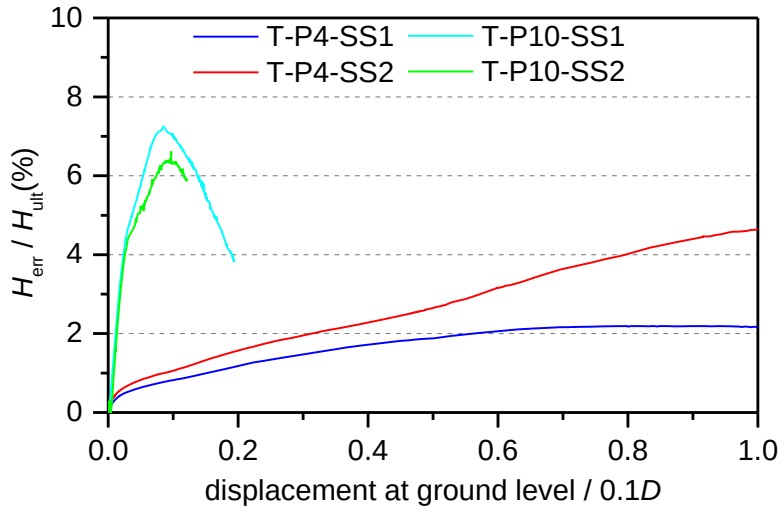

Figure 5.41 Normalised errors for analyses regarding variations of soil conditions

For the results for the short pile (P10), the predicted displacement was larger than the 3D FE results at the same load levels. For these analyses there appeared to be some convergence problems, particularly for the short pile, and this limited the maximum displacement achieved in the analyses. It was shown that the form of the curve was well captured by the 1D predictions. Overall, the agreement between the 1D predictions and 3D FE results was satisfactory.

5.5 RIGID PILE ANALYSIS FOR IDEALISED DEFORMATION MODES

In this section, the rigid pile was subjected to either forced lateral translation (RLT) or rotation around the pile base (RBR), as illustrated in Figure 4.48. The pile and soil properties adopted in the rigid pile analyses were the same as those used in the calibration analyses. The soil reaction curve parameters extracted from these rigid pile analyses were compared with those extracted from the calibration analyses.

The comparisons of the curve parameters of the lateral distributed soil reaction curves between the rigid pile and calibration analyses are given in Figures 5.42 - 5.46.

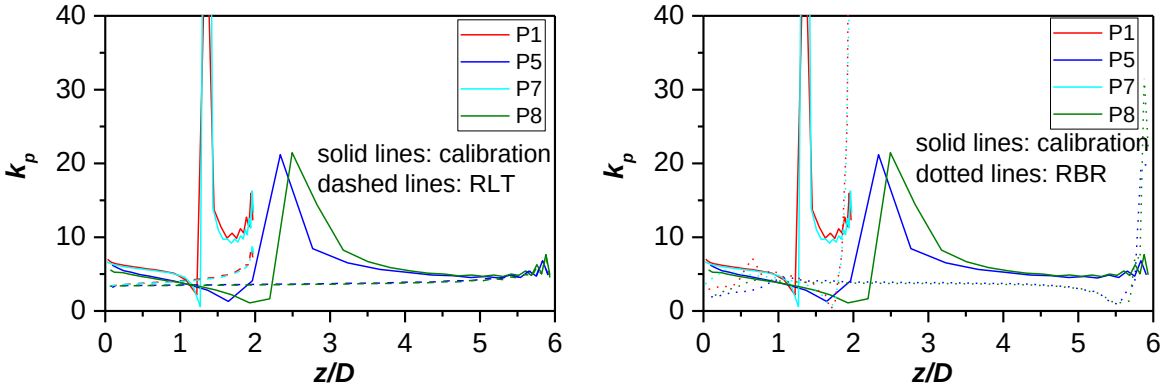

(a) RLT and calibration (b) RBR and calibration

Figure 5.42 Comparison of k_p from the calibration, RLT and RBR analyses

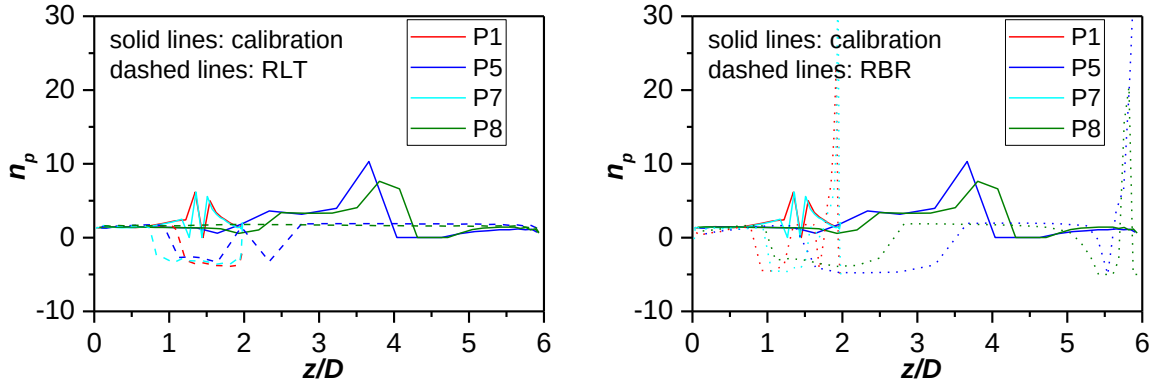

(a) RLT and calibration (b) RBR and calibration

Figure 5.43 Comparison of n_p from the calibration, RLT and RBR analyses

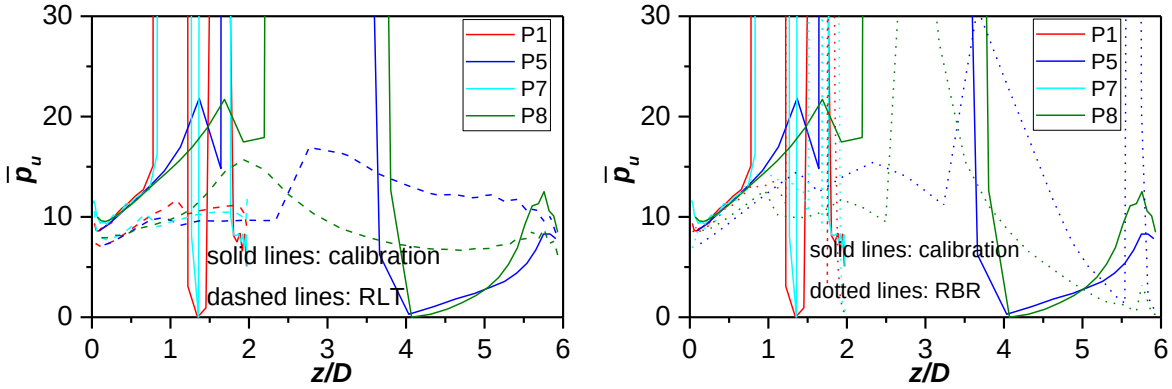

(a) RLT and calibration (b) RBR and calibration

Figure 5.44 Comparison of $\bar{p}_u$ from the calibration, RLT and RBR analyses

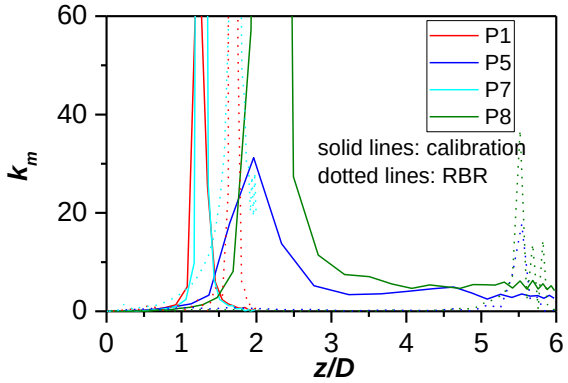

Figure 5.45 Comparison of k_m from the calibration and RBR analyses

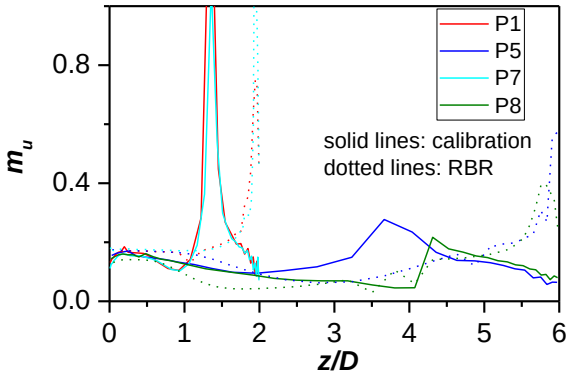

Figure 5.46 Comparison of $\bar{m}_u$ from the calibration and RBR analyses

Figure 5.42 and Figure 5.43 show that the initial stiffness and curvature parameters for distributed load curves extracted from the calibration and rigid pile analyses were different. For the RLT analyses, k_p and n_p appeared to be constant with depth. For the RBR analyses, k_p is almost constant with depth, except near the surface and around pile tip. There were fluctuations in n_p data due to the fact that for depths where the soil reaction curves do not reach their ultimate values, it was difficult to find the corresponding $\bar{p}_u$, which in return affected the derivation of n_p. Interestingly, for $z/D < 1$, the $\bar{p}_u$ from the calibration analyses was about 20% higher than from the RLT analyses. This implied that the moment load had a significant effect on this parameter, and the

rotation of the pile increased the ultimate lateral response at those depths. For the comparison of distributed moment curve parameters, the main difference occurred in $\bar{m}_u$ around pile tip. The $\bar{m}_u$ obtained in RBR analyses was higher than those from the calibration analyses.

Both the ultimate distributed lateral response and ultimate distributed moment varied with load conditions. Hence developing the soil reaction curves from the rigid pile analyses was not pursued any further in this study.

5.5.1 COUPLING OF BASE HORIZONTAL FORCE AND BASE MOMENT

The normalised base horizontal force is plotted against the normalised base moment in Figure 5.47. It can be seen that there is a coupling effect between the base horizontal force and the base moment for sand, similar to that for clay. The ultimate base horizontal force increased while the ultimate base moment decreased. It can be observed from the results that the failure envelopes for the four analyses considered are not consistent. The normalised incremental displacement vectors have a large normal component to the ellipse, which indicated that an associated flow might be used.

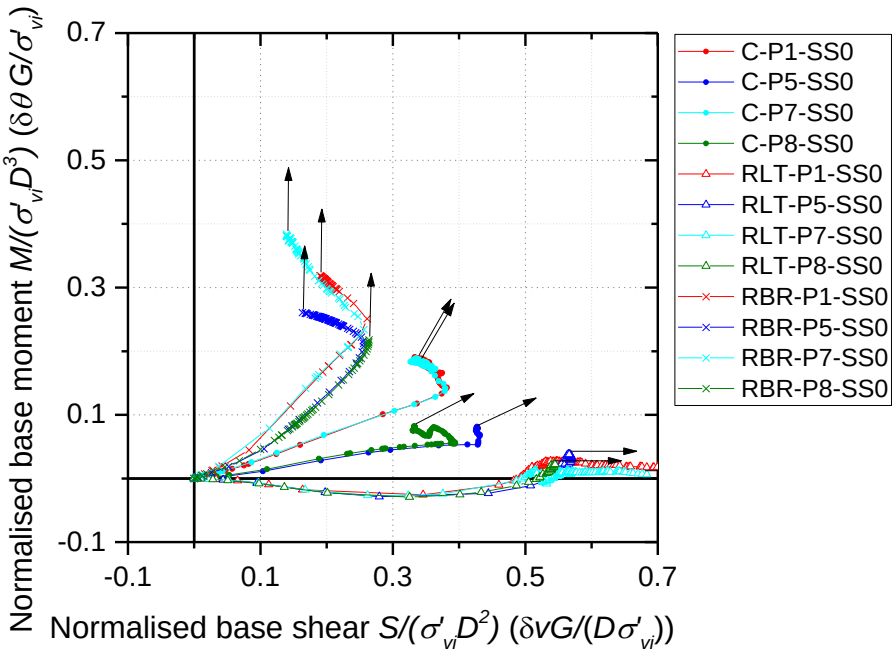

Figure 5.47 Normalised base moment vs normalised base horizontal force, and incremental normalised plastic displacement vectors for sand

5.6 LIMITATIONS

In the 3D FE analysis, it was identified that modelling dense sand was more problematic than modelling undrained clay in Abaqus. There were two numerical issues related to the chosen constitutive model. First, it was more difficult for the solution to converge at large deformation compared with the analyses for clay, which might be due to sand dilation at great depths. Second, the extracted soil reaction curves were not smooth at large displacement, which affected the curve fitting quality for the parameterisation. These consequences of the numerical issues in 3D FE analyses also affected the performance of the calibrated 1D model.

5.7 CONCLUDING REMARKS

This chapter presents the study of the lateral response of monopiles in sand by the numerical-based approach. The calibration process used to develop soil reaction curves was described. A set of parameterised expressions for sand were established, and were employed to calibrate the 1D model.

The results showed that the extracted normalised ultimate lateral response increased linearly with depth at shallow depths, and it matched reasonably well with the expression proposed in API. A coupling effect between the base soil reaction components was found, similar to that shown in the clay analyses. The load-displacement responses predicted by the calibrated 1D model were in good agreement with the results from the 3D FE analyses covering a range of pile dimensions and soil properties. The maximum errors for all the test analyses were less than 10%. This confirmed that (1) the parameterised soil reaction curves successfully captured soil and pile behaviour under lateral loading; (2) the numerical-based approach was proven applicable in design scenarios considering variations of pile and soil conditions.

An attempt to develop soil reaction curves from rigid piles in idealised deformation modes was made. The results of the analyses indicated that soil reaction curves were inconsistent with those from the calibration analyses. Inspection of soil reaction curves showed that the applied moment has an influence on the ultimate distributed lateral response and ultimate distributed moment.

Chapter 6

APPLICATION IN LAYERED SOILS

6.1 INTRODUCTION

This chapter aims to study the suitability of applying the soil reaction curves derived from homogeneous soil analyses to layered soils. The parameterised soil reaction curves developed from the calibration analyses in clay and sand were both incorporated within the 1D model. Two simple layered soil profiles were considered: uniform sand over uniform clay (denoted 'S/C'), and uniform clay over uniform sand (denoted 'C/S') (see Figure 6.1). The layered soil profiles are given in Table 6.1.

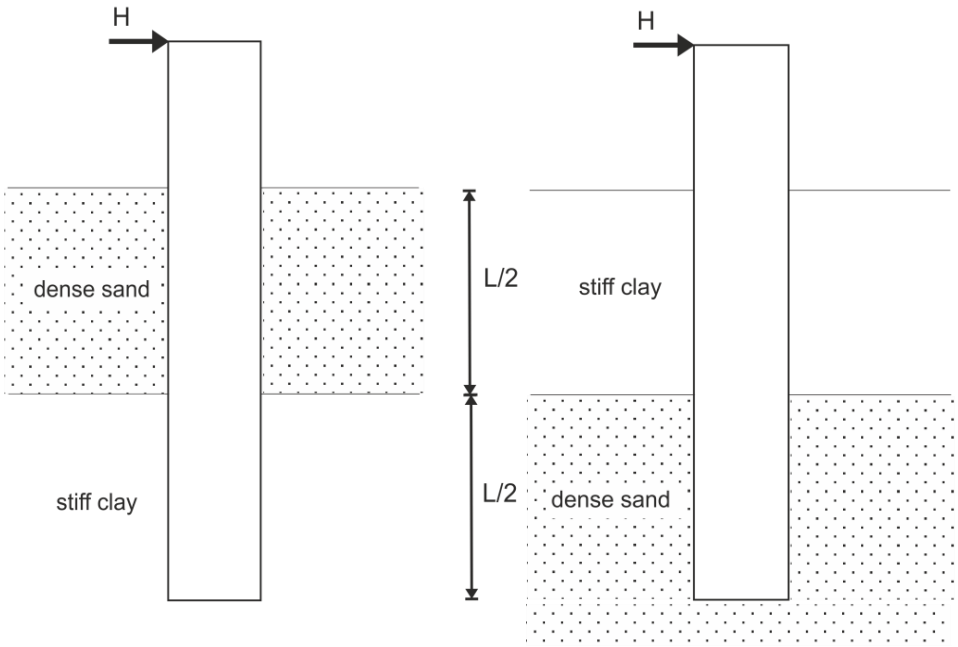

(a) S/C (b) C/S

Figure 6.1 Tested soil profiles for layered soil analysis

Table 6.1 Composition of the layered soil profiles

Analysis reference	Upper layer soil reference	Lower layer soil reference
S/C	SS0	CS0*
C/S	CS0*	SS0

*Note: Effective soil density was used for the clay layer.

Regarding the soil density used in 3D FE analyses, total soil unit weight was used for the clay analyses due to undrained conditions, while effective unit weight was used for the sand analyses due to drained conditions. For the layered soil analyses, to preserve consistency of the effective vertical stress level in the sand layer, both layers used effective unit weight. However, the clay layer is still treated undrained in the layered soil analyses. The undrained shear strength remains the same as that used for the homogeneous clay analyses, and assumed constant with depth.

Regarding pile conditions in the analyses, a long pile P4 (L/D = 6) and a short pile P10 (L/D = 2) were considered. The 1D analyses were performed by assuming that the soil reaction curves were the same as if the entire soil was uniform.

6.2 COMPARISON OF LOAD-DISPLACEMENT RESULTS

Application of parameterised soil reaction curves

The load-displacement response predicted by the calibrated 1D model is compared with 3D FE results in Figures 6.2 - 6.5.

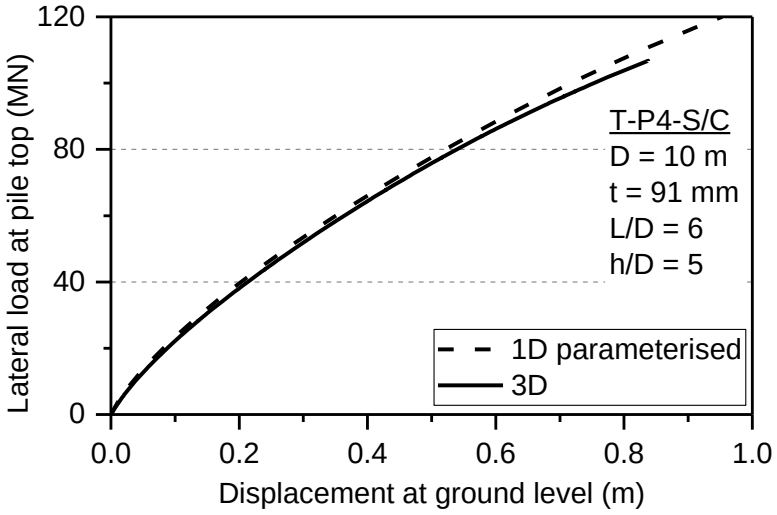

Figure 6.2 Comparison between 1D (predicted) and 3D results for T-P4-S/C analysis

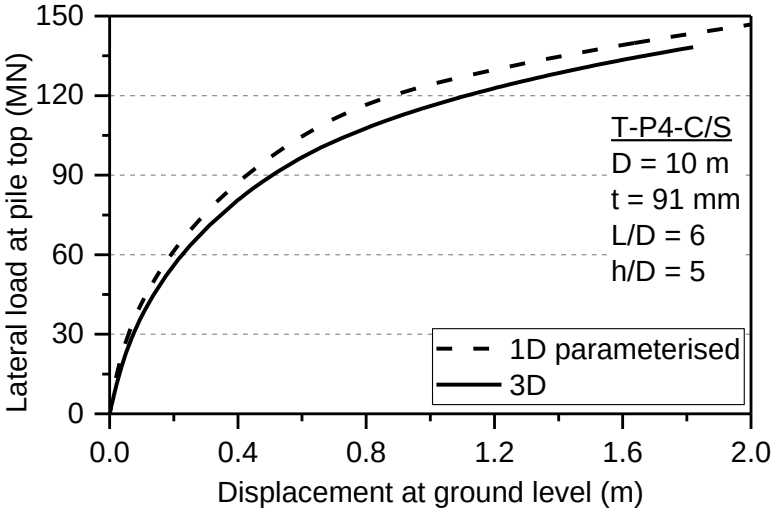

Figure 6.3 Comparison between 1D (predicted) and 3D results for T-P4-C/S analysis

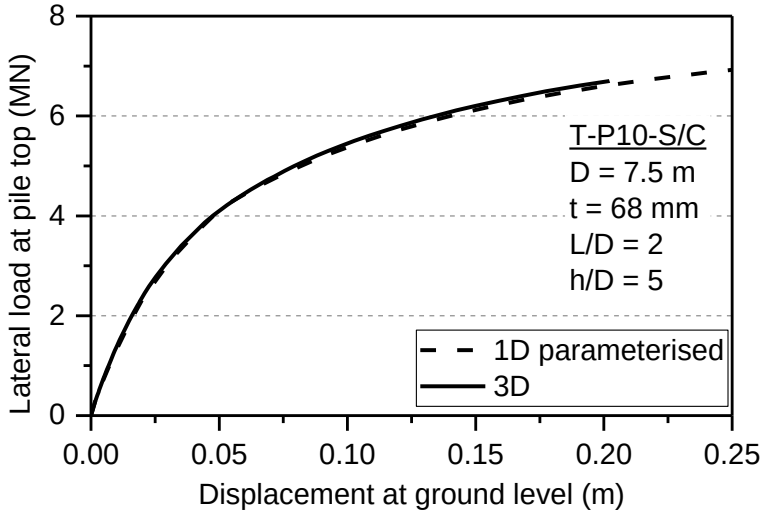

Figure 6.4 Comparison between 1D (predicted) and 3D results for T-P10-S/C analysis

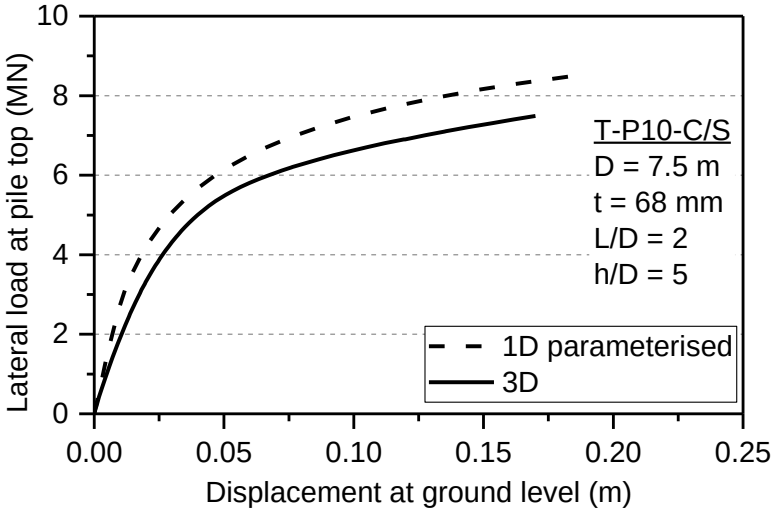

Figure 6.5 Comparison between 1D (predicted) and 3D results for T-P10-C/S analysis

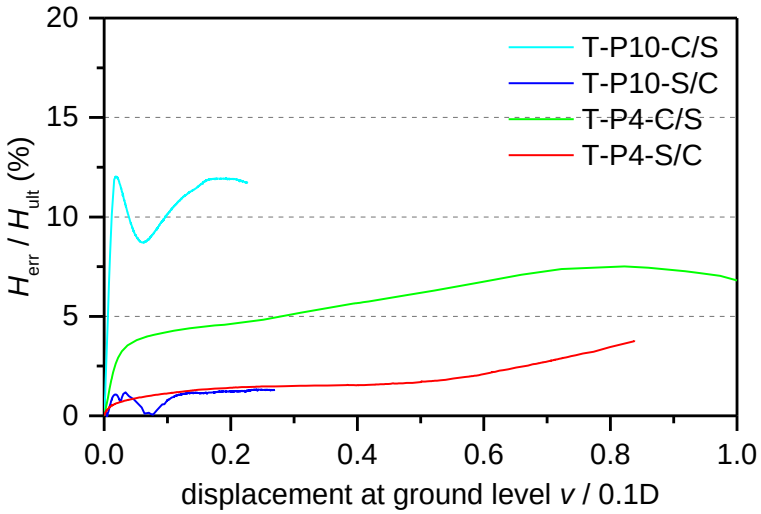

Figure 6.6 Normalised errors for layered soil analyses

The 1D analyses using the parameterised curves develop from the homogeneous soils analyses produced satisfactory results for both the long and short piles, which matched well with the 3D FE results. The results for the analyses with clay over sand showed (Figure 6.3 and Figure 6.5) that the 1D predictions slightly overestimated the ultimate lateral capacity compared to 3D FE results. The maximum errors between the 1D predictions and 3D FE results for the layered soil analyses were less than 15%. The close fit supports the reasonableness of using the parameterised soil reaction curves developed from homogeneous soils analyses for layered soil analyses.

Application of numerical soil reaction curves

It was unclear whether the differences between the 1D results predicted using the parameterised soil reaction curve and the 3D FE results were due to the parameterisation of soil reaction curves or the effect of soil layering. Therefore, the numerical soil reaction curves developed from homogeneous soil analyses were incorporated within the 1D model. The load-displacement results using the numerical soil reaction curves are compared with the 3D FE results in Figures 6.7 - 6.10.

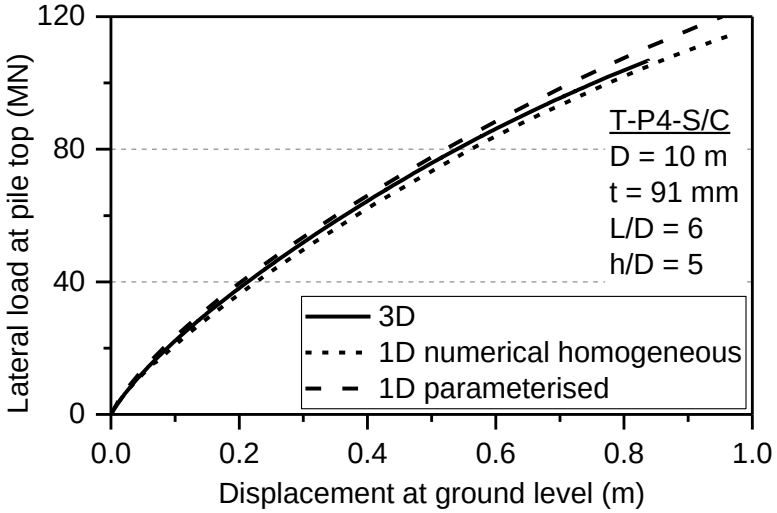

Figure 6.7 Comparison between 1D (predicted) and 3D results for T-P4-S/C analysis

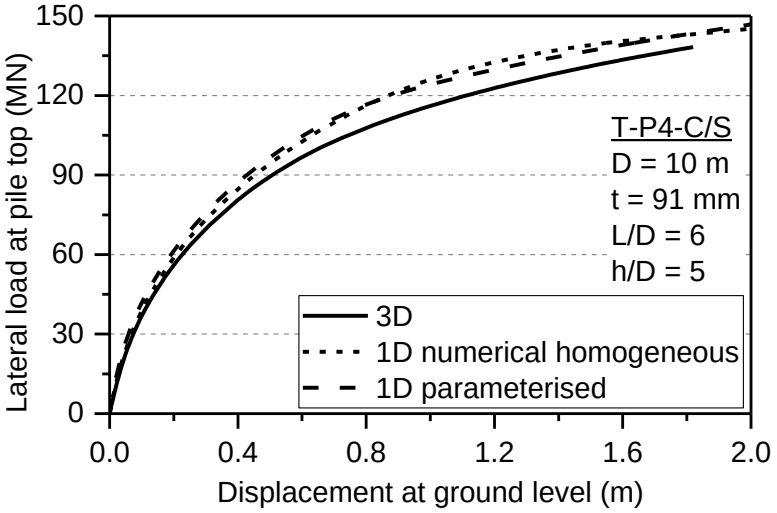

Figure 6.8 Comparison between 1D (predicted) and 3D results for T-P4-C/S analysis

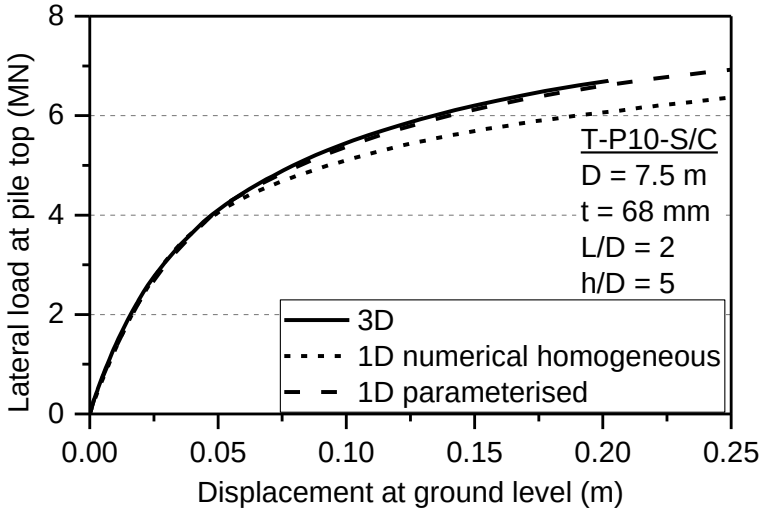

Figure 6.9 Comparison between 1D (predicted) and 3D results for T-P10-S/C analysis

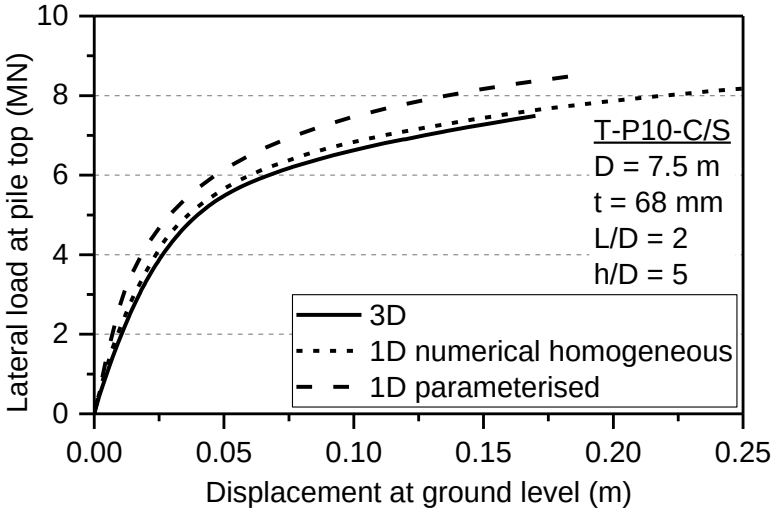

Figure 6.10 Comparison between 1D (predicted) and 3D results for T-P10-C/S analysis

Compared with the 3D FE results, the ultimate capacity predicted using the numerical curves was underestimated in the cases of sand over clay (Figure 6.7 and Figure 6.9), while overestimated in the cases of clay over sand (Figure 6.8 and Figure 6.10). The main differences were observed in T-P4-C/S (Figure 6.8) and T-P10-S/C (Figure 6.9) analyses.

The differences between the predictions using the numerical and parameterised curves indicated that the parameterisation for soil reaction curves affected the 1D predictions. The effect is more pronounced for the short pile (P10) than for the long pile (P4). Although the effect of parameterisation is present, its influence on the predicted load-displacement results remains small (less than 10% for all the layered soil analyses).

6.3 COMPARISON OF SOIL REACTION CURVES

In this section, both the distributed load and the distributed moment curves extracted from the layered soil analyses were compared with those extracted from the homogeneous soil analyses. For clarity, the following figures show the comparison at four depths only (0.1L, 0.4L, 0.6L and 0.9L). These depths were chosen to represent the depths near the clay/sand interface (0.4L and 0.6L, right column), and the depths far away from the clay/sand interface (0.1L and 0.9L, left column).

A. Distributed load

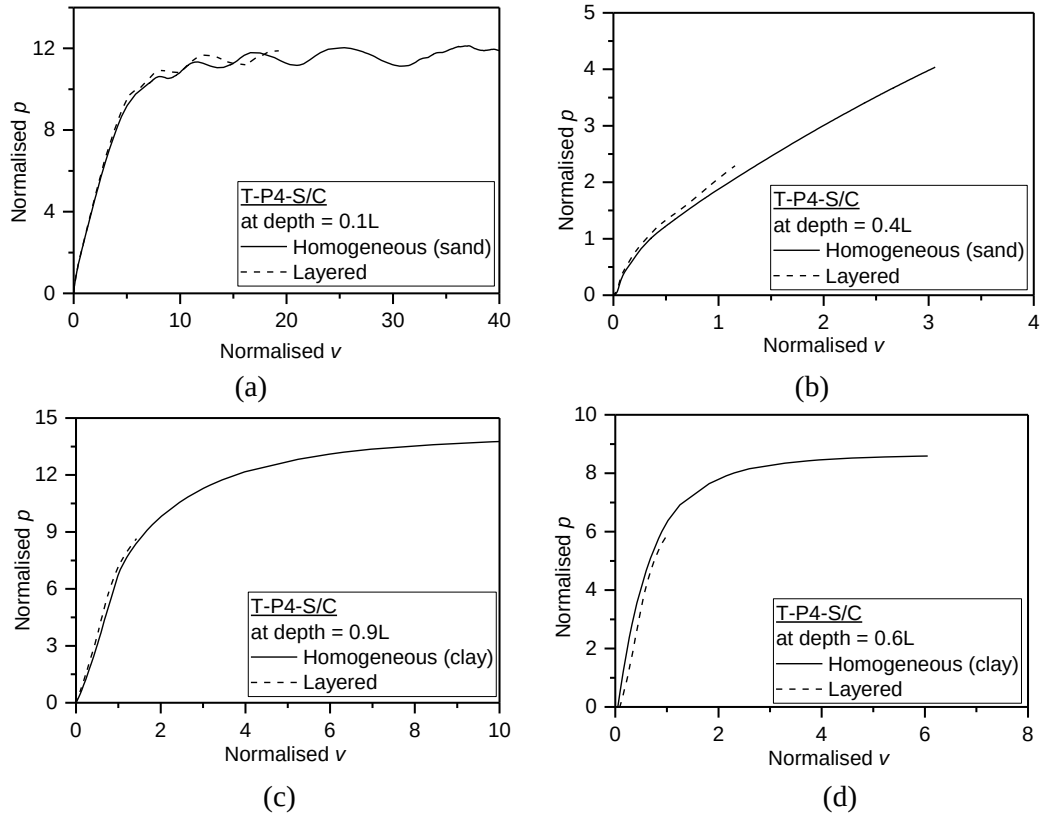

Figure 6.11 Comparison of the distributed load curves from T-P4-S/C and those from the homogeneous soil analyses

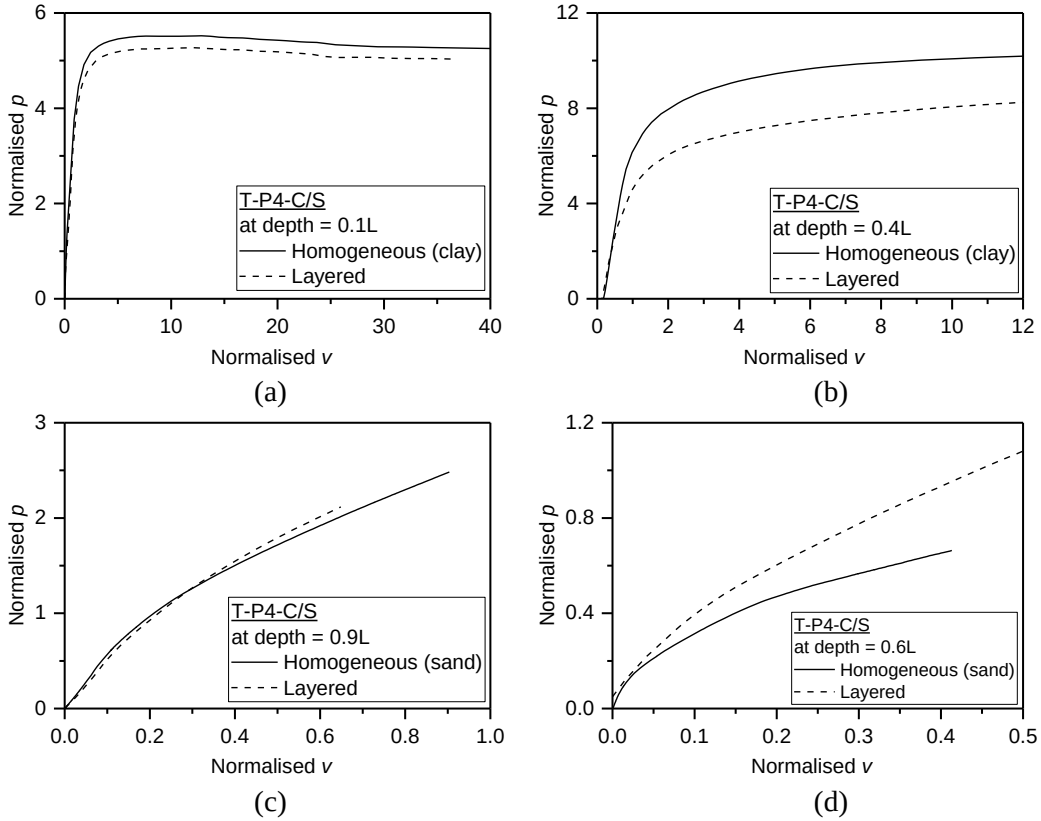

Figure 6.12 Comparison of the distributed load curves from T-P4-C/S and those from the homogeneous soil analyses

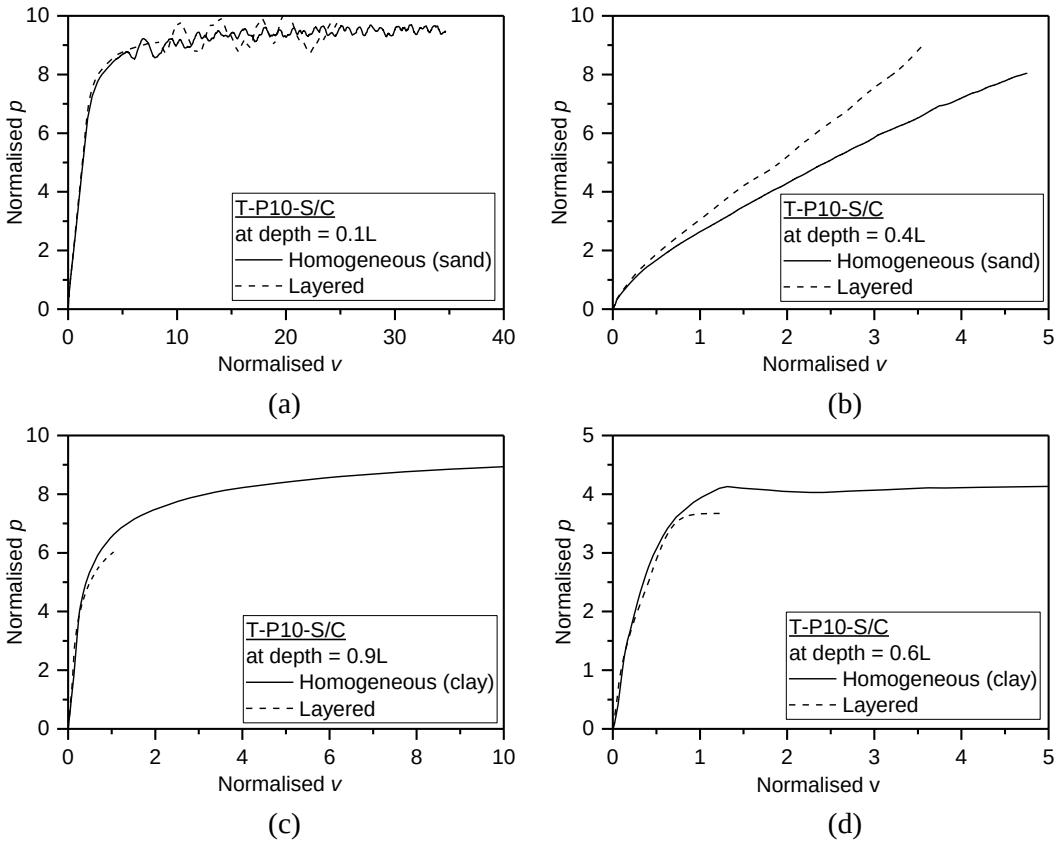

Figure 6.13 Comparison of the distributed load curves from T-P10-S/C and those from the homogeneous soil analyses

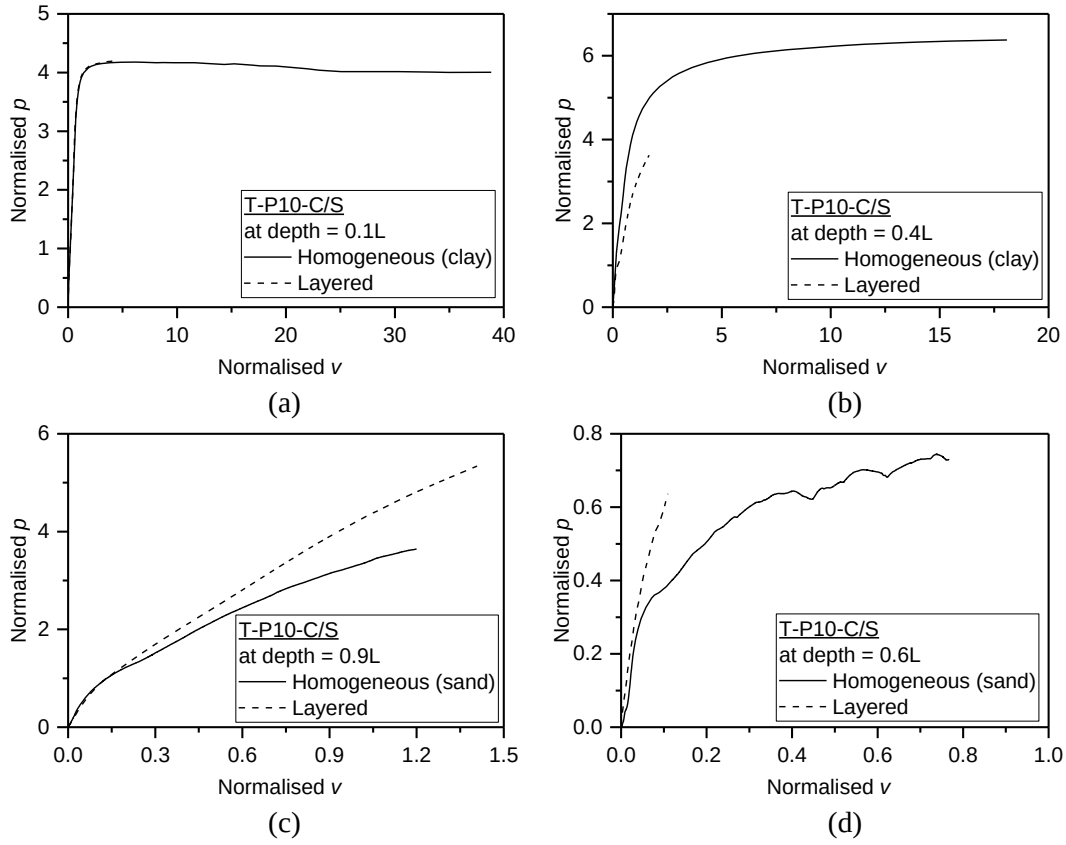

Figure 6.14 Comparisons of the distributed load curves from T-P10-C/S and those from the homogeneous soil analyses

The distributed load curves extracted from the layered soil and homogeneous soil analyses are compared in Figures 6.11 - 6.14. For sand over clay (Figure 6.11 and Figure 6.13), generally there was good agreement between the results from the layered soil and homogeneous soil analyses. For the short pile, the differences are present at 0.4*L*, 0.6*L* and 0.9*L*, where the ultimate responses for layered soils were about 10% lower than that for the homogeneous clay, and about 20% higher than that for the homogeneous sand. For the T-P4-C/S analysis, the main difference can be seen in the ultimate response in the clay layer, which was 5% at 0.1*L* and 30% at 0.4*L*. There were differences in the sand layer, but the normalised *p* values in this layer were very small compared that in the clay layer. For the T-P10-C/S analysis, there were differences in the ultimate response at 0.4*L*, 0.6*L* and 0.9*L*. Although, the difference was about 50% at 0.6*L*, it was considered less significant because the normalised *p* value is very small compared with the values at 0.4*L* and 0.9*L*.

The initial stiffness of the distributed load curves extracted from the layered soil and homogeneous soil analyses were in good agreement for all the analyses. There seemed to be soil layering effect on the ultimate lateral response in both the upper and the lower layer. The difference was the smallest at the surface (0.1*L*) as expected.

B. Distributed moment

It was found that for sand layer, if the distributed moment was normalised by the distributed load, there would be numerical singularities around the rotation point and at the surface. Therefore, for the results presented in this section, we compared the normalised distributed moment for sand which is defined by Equation (6.1).

$$\bar{m} = \frac{m}{\sigma'_{vi} D^2} \tag{6.1}$$

The comparisons between the distributed moment curves extracted from the layered soil and homogeneous soil analyses are shown in Figures 6.15 - 6.18.

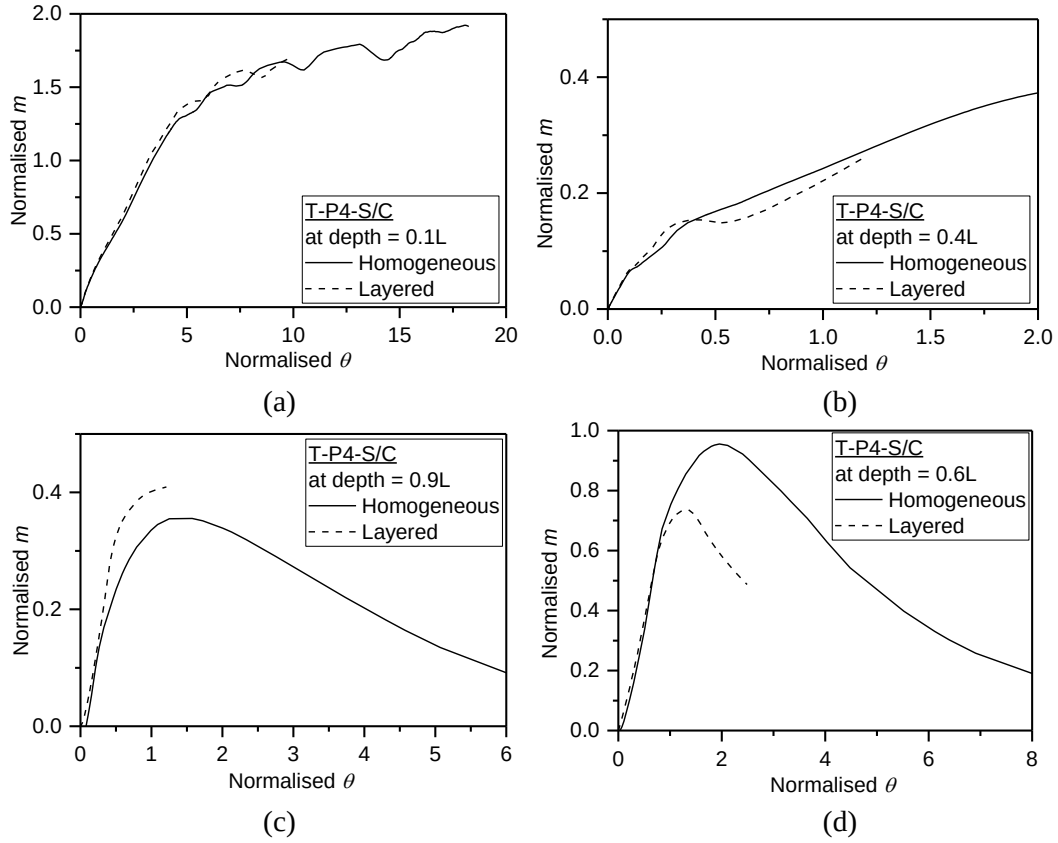

Figure 6.15 Comparison of the distributed moment curves from T-P4-S/C and those from the homogeneous soil analyses

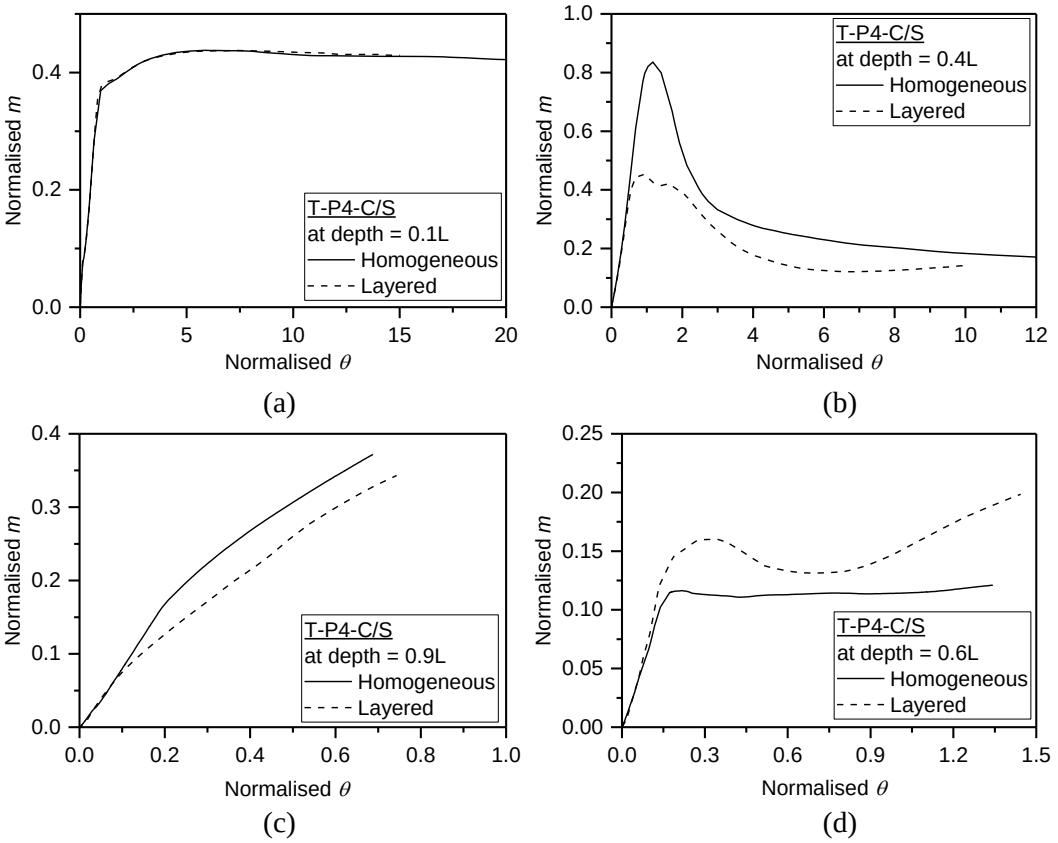

Figure 6.16 Comparison of the distributed moment curves from T-P4-C/S and those from the homogeneous soil analyses

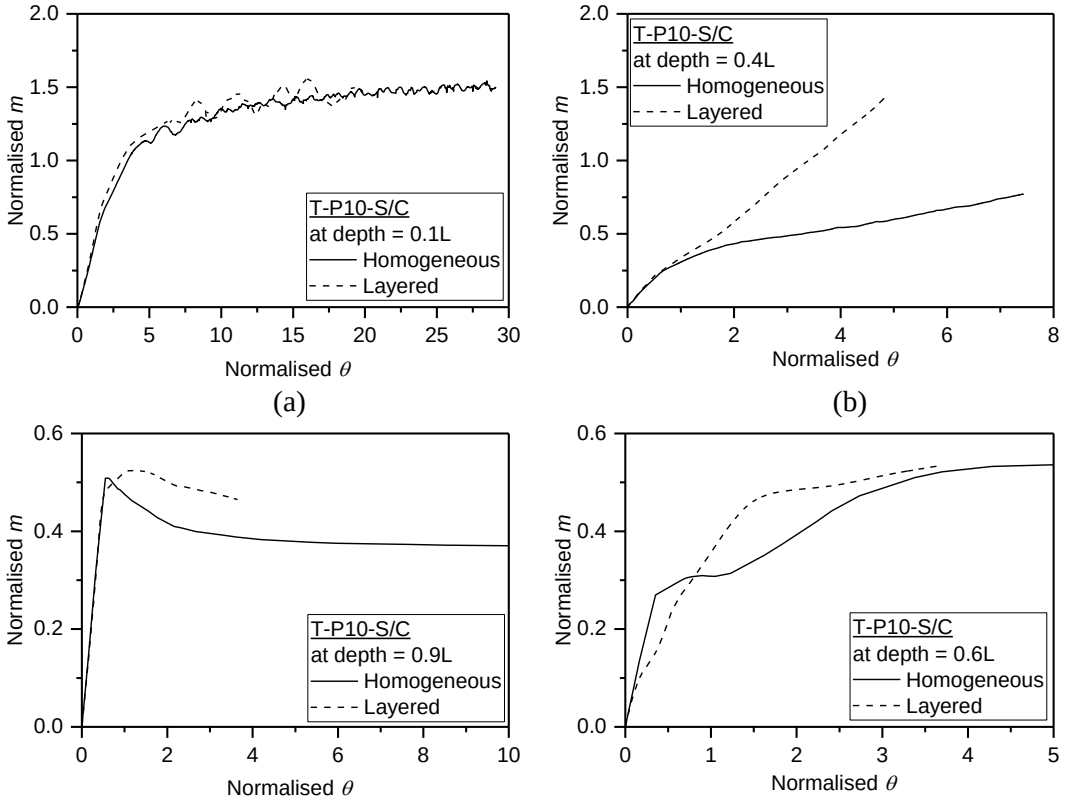

Figure 6.17 Comparisons of the distributed moment curves from T-P10-S/C and those from the homogeneous soil analyses

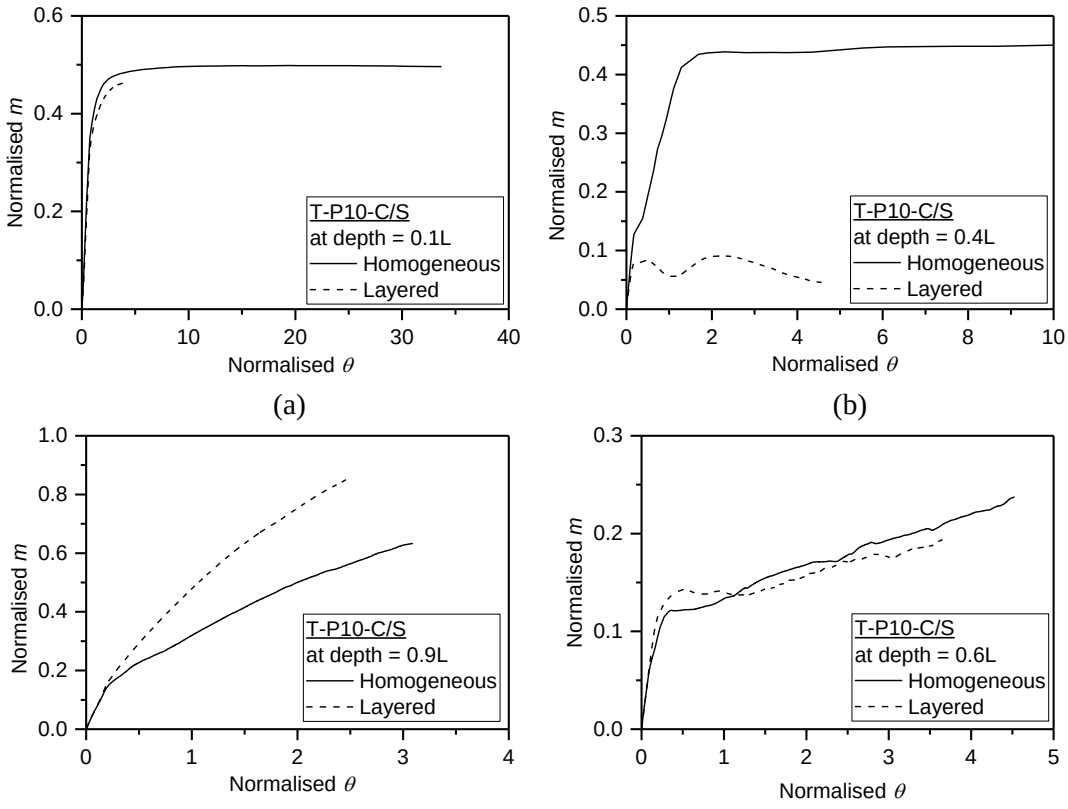

Figure 6.18 Comparisons of the distributed moment curves from T-P10-C/S and those from the corresponding homogeneous soil analyses

For T-P4-S/C analysis, the results for 0.1*L* and 0.4*L* were in good agreement. The ultimate moment obtained from the layered soil analyses was higher than that obtained from the homogeneous soil analyses at 0.9*L*, but was lower than that at 0.6*L*. This might indicate that the soil layering effect varied with depth within the same soil layer, which was also shown for T-P4-C/S analysis. Regarding the analyses with the short pile, there were differences in the ultimate moment at 0.4L, 0.6L and 0.9L, where there were also differences in the ultimate lateral response.

There was no significant difference in the initial stiffness of the distributed moment curves. There seemed to be soil layering effect on the ultimate lateral response in both the upper and the lower layer. The difference was the smallest at the surface (0.1*L*) as expected.

The results of the base horizontal force and the base moment components were similar to the distributed components close to pile tip (depth = 0.9*L*). Due to limited space, these results are not presented herein.

Note that soil layering is a complex problem, as its effect might depend on soil depths, pile *L/D* ratios or soil reaction components, some of which are interdependent. The differences in pile response due to different factors might be balanced out in some cases. Further research is required to identify the exact cause for the differences. The overall agreement between the 1D predictions and 3D FE results for the cases investigated appears to support the applicability of the calibrated 1D model for layered soil analyses.

6.4 CONCLUDING REMARKS

This chapter verified the capability of the calibrated 1D model in predicting lateral response of monopiles in layered soils, using soil reaction curves developed from the homogeneous soil analyses. Both the load-displacement response and soil reaction curves were analysed. The load-displacement response demonstrated that there was satisfactory agreement between the 1D predictions and 3D FE results for the layered soil analyses, with the maximum errors within 15%. Soil layering effects were assessed by comparing numerical soil reaction curves from the homogeneous soil analyses with those from the layered soil analyses. The comparisons showed that the differences in the initial stiffness were not significant, and there were differences in the ultimate response in both upper and lower layers. Further study is required to investigate these differences.

Chapter 7

CONCLUSIONS

This thesis has been concerned with the design of laterally loaded monopiles using the numerical-based design approach proposed in the PISA project. Numerical studies have explored the predictability of the new design method for various design scenarios, including variations of pile geometries, load eccentricities, soil profiles and layered soil conditions; and investigated the key soil reaction curve parameters and soil failure mechanisms. In addition, the soil reactions of rigid piles in lateral translation and rotation about the pile base were analysed. Potential improvements for the PISA method and further research needs are suggested.

7.1 SUMMARY OF FINDINGS

This thesis describes a series of 3D and 1D FE analyses to examine the performance of a numerical-based design method for various design scenarios. The objectives of this study, as set out in Chapter 1, were achieved. The key findings are categorised into four main areas of research: (a) 3D FE modelling; (b) extraction of soil reaction curves; (c) parameterisation of soil reaction curves; and (d) 1D FE analysis; and summarised in the following sections.

(a) 3D FE modelling

1. 3D FE analyses using elastic perfectly plastic constitutive models were performed. Non-linearity of pile response, pile-soil interaction, and 3D boundary conditions were considered. Phenomena such as “toe kick” and pile-soil separation were successfully reproduced.
2. The FE analyses were facilitated by careful selection of soil element type. Parallel studies using varied element types (C3D8R, C3D20R, C3D27R) demonstrated that the analyses using linear element (C3D8R) obtained close results to those using quadratic elements and required the least computation time.

3. The results from the 3D analyses matched well with those from the 1D analyses. This suggests that the PISA design methods, accounting for four soil reaction components, are suitable for the design of laterally loaded monopiles.
4. Close inspection of computed soil displacement vector indicated that soil at shallow depths moved upward and outward, corresponding to a wedge failure mechanism, while soil at great depths rotated with the pile, suggesting a spherical rotation failure mechanism.
5. Preliminary 3D FE analyses performed to investigate the effect of vertical loads suggested that a vertical load had a marginal effect on the lateral response of monopiles in clay, while it clearly resulted in a favourable effect on the lateral capacity of monopiles in sand. These findings were consistent with previous research. It is also found that the increase in lateral capacity in sand was mainly due to the increase in the base soil reaction components.
6. Preliminary 3D FE analyses performed to examine the influence of gapping and pseudo-cohesion of sand showed that their influences on pile response were marginal.
7. It is recognised that constitutive models play an important role in 3D FE analysis. The study in this thesis is limited to the use of simple constitutive models and basic soil parameters, and thus can be viewed as a baseline study.

(b) Extraction of soil reaction curves

8. The soil reaction curves obtained from 3D FE analyses using linear elements were verified through comparisons with those obtained using quadratic elements. For analyses using linear elements, the soil reaction curves were calculated directly from the nodal forces from the surrounding soil elements, while for analyses using quadratic elements, the soil reaction curves were calculated from the stresses at the integration points from the soil elements. The differences of the results obtained from the two extraction methods were marginal.
9. The extracted soil reactions were verified by comparing the applied horizontal load and moment with the sum of the soil reactions at the pile-soil interface and at the base of soil plug. The differences were within 2% for all the analyses.
10. The normalised ultimate lateral response was compared with analytical solutions. For the distributed load curves in undrained clay, the parameterised expression agreed well with the analytical solution developed by Murff and Hamilton (1993). However, the extracted results at greater depths were higher than the analytical predictions, which might be due to the spherical rotation mechanism shown in the 3D FE results. For sand, there was clearly a linearly increase trend between the normalised ultimate resistance and normalised depth at shallow depths. The extracted results agreed reasonably well with the expression in the API method.

11. The rigid pile analyses demonstrated that the ultimate lateral response in clay was independent of the moment applied to the pile, whilst in sand, the ultimate lateral soil response seemed to increase with the applied moment load.
12. Discrepancies were observed between the distributed load and moment curves extracted from the rigid pile analyses and those from the main calibration analyses. The discrepancies were less pronounced in the analyses for clay than for sand. It was suggested that the soil reaction curves from the rigid pile analyses were infeasible for the design of free-head monopiles.
13. Plotting the base horizontal force against the base moment revealed a coupling effect between the two components. The displacement vector plot suggested that an associated flow rule might be used.
14. There were no significant differences between the initial stiffness for the soil reaction curves extracted from the layered soil and homogeneous soils analyses. However, differences were present in the ultimate responses. From the analysis results, it appeared that there were layering effects in both the upper and lower layers.

(c) Parameterisation of soil reaction curves

15. A systematic and objective process was applied to fit the variations of soil reaction curve parameters with depth. The simple expressions selected in this study were validated by the close fit between the 1D and 3D FE results. It might be useful to choose more detailed expressions to further improve curve fitting quality for soil reaction curves, which however would require more parameters to be determined.
16. The parameterised expressions (see Table 4.3, Table 5.3) developed from a small number of calibration analyses yielded satisfactory predictions on all test analyses involving a range of pile geometries, load eccentricities and soil profiles. The errors of ultimate lateral capacity for all test analyses were within 10%.
17. The extraction and parameterisation process, including the dimensionless groups used in the normalisation, were verified in this study.

(d) 1D FE analysis

18. The robustness of the 1D model was validated by the excellent agreement between the 1D predictions using the numerical soil reaction curves and 3D FE results for the calibration analyses.
19. All the four soil reaction components contribute to the overall lateral capacity and the contribution of each soil component depends on both soil type and load eccentricities. The total contribution of base horizontal force, base moment and distributed moment was about 25%

- 30% for piles with low *L/D* ratios. Additionally, the contribution of the distributed moment component in sand was higher than that in clay for the calibration analyses considered.

20. For the layered soil analyses, the overall maximum errors between the 3D FE results and the 1D predictions using the parameterised soil reaction curves developed from homogeneous soil simulations were less than 15% for the cases considered. The close fit supports the feasibility of using the parameterised soil reaction curves developed from homogeneous soil profiles for layered soil profiles.
21. Comparisons with the 3D FE test analyses showed that the calibrated 1D model can be used to analyses considering pile geometries and load eccentricities interpolated from the parameter space used in the calibration analyses.

7.2 FUTURE WORK AND FUTURE DIRECTIONS

1. In future research, the effect of more complex soil properties, such as hardening and stiffness degradation, on different soil reaction components might be investigated by adopting advanced constitutive models in 3D FE analyses.
2. For the future development of the 1D model, the coupling of base horizontal force and base moment might be achieved by developing additional expressions for the non-diagonal terms in the base element stiffness matrix. The shape of failure envelope could be determined by performing tracking analyses or a series of constant *H/M* ratio analyses.
3. As layering effects were shown in the soil reaction curves from the layered soil analyses, it is suggested that the application of parameterised soil reaction curves from homogeneous soil analyses needs to be cautious, especially in the cases where the strengths of adjacent layers vary significantly (*e.g.* soft clay and dense sand interbedding). More research is needed to clarify the effects of soil layering on the soil reactions in adjacent soil layers.
4. For practical offshore applications, varied forms of scour protection are sometimes employed to prevent scouring occurring around piles. The presence of scour protection changes the fixation length of the pile, and thus affects monopiles' static and dynamic behaviour. The effects of scour protection on monopile lateral response and on pile-soil interaction require further investigation.
5. Installation effects could be incorporated in the 3D analyses. For driven monopiles, research on installation effects in clay were carried out by Randolph *et al*. (1979), Carter *et al*. (1979), Randolph and Wroth (1979) and their findings indicated that installation effects can be simulated by assuming increase in soil stiffness and strength in radial directions around the pile shaft due to consolidation.
6. Cyclic loading is one of the main concerns in the design of offshore foundations. The effects of cyclic loading on monopile response and on the natural frequency of the pile-soil system require future investigation. Additional analyses on the PISA cyclic loading pile tests are currently underway. It is expected that the new design methods proposed within the PISA project would be further developed to properly address this issue.

REFERENCES

Abadie, C. (2016). Cyclic Lateral Loading of Monopile Foundations in Cohesionless Soils. Dphil thesis. University of Oxford.

Abaqus. (2013). User's manual, Version 6.13.

Abdel-Rahman, K. and Achmus, M. (2005). Finite element modelling of horizontally loaded monopile foundations for offshore wind energy converters in Germany. *Proceedings of the International Symposium on Frontiers in Offshore Geotechnic (ISFOG 2005)*, Perth, Australia, 391–396.

Achmus, M., Kuo, Y. and Abdel-Rahman, K. (2009). Behavior of monopile foundations under cyclic lateral load. *Computers and Geotechnics* **36**, 725-735.

API, American Petroleum Institute. (2014). Recommended Practice for Planning, Designing and Construction Fixed Off-shore Platforms - Working Stress Design, API Recommended Practice 2A-WSD (RP2A-WSD), 21st Edition, Dalllas.

Ashour, M., Norris, G. and Pilling, P. (1998). Lateral Loading of a Pile in Layered Soil Using the Strain Wedge Model. *Journal of Geotechnical and Geoenvironmental Engineering* **124**, No.4, 303-315.

Ashour, M., Pilling, P. and Norris, G. (2004). Lateral Behavior of Pile Groups in Layered Soils. *Journal of Geotechnical and Geoenvironmental Engineering* **130**, No.6, 580-592.

Atkinson, J.H. and Sallfors, G. (1991). Experimental determination of soil properties. *Proc. 10th ECSMFE*, vol.3, 915-956. Florence.

Augustesen, A.H., Brødbæk, K.T., Møller, M., Sørensen, S.P.H., Ibsen, L.B., Pedersen, T.S. and Andersen, L. (2009). Numerical Modelling of Large-Diameter Steel Piles at Horns Rev. *Proceedings of the 12th International Conference on Civil, Structural and Environmental Engineering Computing*, Paper 239.

Barton, Y.O. (1982). Laterally loaded model piles in sand. PhD thesis. Cambridge University.

Basu, D., Salgado, R. and Prezzi, M. (2009). A continuum-based model for analysis of laterally loaded piles in layered soils. *Géotechnique* **59**, No.2, 127-140.

Belytschko, T. and Bindeman, L. P. (1993). Assumed Strain Stabilization of the Eight Node Hexahedral Element. *Computer Methods in Applied Mechanics and Engineering* **105**, 225–260.

Bhattacharya, S. (2014). Challenges in Design of Foundations for Offshore Wind Turbines. *IET Engineering & Technology Reference*, 1-9.

Boit, M.A. (1937). Bending of Infinite Beams on an Elastic Foundation. *Journal of Applied Mechanics Trans. Am. Soc. Mech. Eng.*, **59**, A1-A7.

Borgard, D. and Matlock, H. (1980). Simplified calculation of *p-y* curves for laterally loaded piles in sand, Earth Technology Corporation, Inc., Houston.

Bowles, J.E. (1998). Foundation Analysis and Design. 6th Edition, McGrow-Hill International Press

Brinch Hansen, J. (1961). The ultimate resistance of rigid piles against transversal forces. *Bulletin No.12*, Danish Geotechnical Institute, Copenhagen, Denmark, 5-9.

Broms, B.B. (1964a). Lateral resistance of piles in cohesionless soils. *Journal of the Soil Mechanics and Foundation Division* (ASCE) **90**, No.SM3, 25-63.

Broms, B.B. (1964b). Lateral resistance of piles in cohesive soils. *Journal of the Soil Mechanics and Foundation Division* (ASCE) **90**, No.SM2, 123-156.

Broms, B.B. (1965). Design of Laterally Loaded Piles. *Journal of the Soil Mechanics and Foundation Division* (ASCE) **91**, No.SM3, 79-99.

Budhu, M. and Davies, T.G. (1987). Nonlinear analysis of laterally loaded piles in cohesionless soils. *Canadian Geotechnical Journal* **24**, 289-296.

Byrne, B.W., McAdam, R., Burd, H.J., Houlsby, G.T., Martin, C.M., Zdravković, L., Taborda, D.M.G., Potts, D.M., Jardine, R.J., Sideri, M., Schroeder, F.C., Gavin, K., Doherty, P., Igoe, D., Muir Wood, A., Kallehave, D. and Skov Gretlund, J. (2015). New design methods for large diameter piles under lateral loading for offshore wind applications. *Proc 3rd International Symposium on Frontiers in Offshore Geotechnics (ISFOG 2015)*. Oslo, Norway, 705-710.

Carbon Trust. (2014). Offshore wind in China. Available at: http://www.carbontrust.com/news/2014/09/china-offshore-wind. Posted by Al-Karim Govindji. Last accessed March 2016.

Carter, J.P., Randolph, M.F. and Wroth, C.P. (1979). Stress and pore pressure changes in clay during and after the expansion of a cylindrical cavity. *International Journal for Numerical and Analytical Methods in Geomechanics* **3**, 305-322.

Cook, R.D., Malkus, D.S., Plesha, M.E. and Witt, R.J. (2002). Concepts and Application of Finite Element Analysis. John Wiley & Sons.

Davisson, M.T. and Gill, H.L. (1963). Laterally loaded piles in a layered soil system. *Journal of the Soil Mechanics and Foundations Engineering* (ASCE) **89**, No.SM3, 63-94.

Davidson, H.L. (1982). Laterally loaded drilled pier research, Vol.1: Design methodology, Vol.2: Research documentation. Final Report by GAI Consultants Inc., to Electric Power Research Institute (EPRI).

Department of UK Trade & Investment. (2015). UK Offshore Wind: Opportunities for trade and investment. Available at: http://www.renewableuk.com/download.cfm/docid/0FA64066-4BD3-49BB-BD65A6B628AE23FF. Last accessed March 2016.

De Vries, W.E. and Van der Tempel, J. (2007). Quick monopile design. *Proceedings of the European Offshore Wind conference and Exhibition*. Berlin, Germany, 4-6th Dec, 2007.

DNV, Det Norske Veritas. (2014). Design of Offshore Wind Tur-bine Structures. Offshore Standard, Norway.

EWEA, European Wind Energy Association. (2009). Wind Energy – The Facts. Available at: http://www.wind-energy-the-facts.org/home--about-the-project.html. Last accessed March 2016.

EWEA, European Wind Energy Association. (2015). The European offshore wind industry – key trends and statistics 2014. Available at: http://www.ewea.org/fileadmin/files/library/publications/statistics/EWEA-European-Offshore-Statistics-2014.pdf. Last accessed March 2016.

Fan, C. and Long, J.H. (2005). Assessment of existing methods for predicting soil response of laterally loaded piles in sand. *Computer and Geotechnics* **32**, 274-289.

Flanagan, D.P. and Belytschko, T. (1981). A Uniform Strain Hexahedron and Quadrilateral with Orthogonal Hourglass Control. *International Journal for Numerical Methods in Engineering* **17**, 679–706

Georgiadis, M. (1983). Development of *p-y* curves for layered soil. *Proc. Geotech. Practice in Offshore Engineering* (ASCE), **1**, 536-545.

Gerolymos, N. and Gazetas, G. (2006). Development of Winkler model for static and dynamic response of caisson foundations with soil and interface nonlinearities. *Soil Dynamics and Earthquake Engineering* **26**, No.5, 363-376.

Gibson, R.E. (1967). Some results concerning displacements and stresses in a non-homogeneous elastic half-space. *Géotechnique* **17**, 58-67.

Gibson, R.E. and Sills, G.C. (1975). Settlement of a strip load on a non-homogeneous orthotropic incompressible elastic half-space. *Q.J. Mech. Appl. Math.* **28**, 233-243.

Guo, W.D. and Lee, F.H. (2001) Load transfer approach for laterally loaded piles. *Int. J. Numer. and*

Anal. Meth. in Geomech. **25** (11), 1101-1129.

Guo, W.D. (2013). Theory and practice of pile foundations. Boca Raton, Fla.: CRC Press.

Haiderali, A. and Madabhushi, G. (2012). Three-Dimensional Finite Element Modelling of Monopiles for Offshore Wind Turbines. *2012 Word Congress on Advances in Civil, Environmental, and Materials Research (ACEM' 12)*, 3277-3295. Seoul, Korea, August 26-30.

Hald, T., Mørch, C., Jensen, L., LeBlanc Bakmar, C. and Ahle, K. (2009). Revisiting monopile design using *p-y* curves results from full scale measurements on Horns Rev. DONG Energy A/S, *Proceedings of European Offshore Wind Conference and Exhibition*.

Hetenyi, M. (1946). Beams on elastic foundations. University of Michigan Press, Ann Arbor, Mich., United States.

Hokmabadi, A.S., Fakher, A. and Fatahi, B. (2012). Full scale lateral behaviour of monopiles in granular marine soils. *Marine structures* **29**, No.1, 198-210.

Ibsen, L.B., Roesen, H.R., Wolf, T.K., Hansen, M. and Rasmussen, K.L. (2013). Assessment of *p-y* Curves from Numerical Methods for a Non-Slender Monopile in Cohesionless Soil. *Proceedings of the 23th International offshore and polar engineering conference*. Anchorage, Alaska, USA, 436-443.

Institute of Government, The Climate Change Act (2008). (2012). Available at: http://www.instituteforgovernment.org.uk/sites/default/files/climate_change_act.pdf. Last accessed March 2016.

Isenhower, W.M. and Wang, S. (2011). Technical Manual for LPILE, Version 6. Ensoft, Inc.

Karthigeyan, S., Ramakrishna, V. and Rajagopal, K. (2007). Numerical Investigation of the effect of vertical load on the lateral response of piles. *Journal of Geotechnical and Geoenvironmental Engineering* **133**, No.5, 512-521.

Kasch, V.R., Coyle, H.M., Bartoskewitz, R.E. and Sarver, W.G. (1977). Lateral load test of a drilled shaft in clay. Research report No.211-1, Texas Transportation Institute, Texas A&M University.

Lam, I.P.O. and Martin, G.R. (1986). Seismic Design of High-way Bridge Foundations. US Department of Transportation Report, No. FHWA/RD-86/102.

Lam, I.P.O. (2013). Diameter effects on *p-y* curves. *Deep Marine Foundations – A Perspective on the Design and Construction of Deep Marine Foundations*.

LeBlanc, C., Houlsby, G.T. and Byrne, B.W. (2010). Response of stiff piles in sand to long-term cyclic lateral loading. *Géotechnique* **60**, No.2, 79-90.

Lehane, B.M., Chow, F.C., McCabe, B.A. and Jardine, R.J. (2000). Relationships between shaft capacity of driven piles and CPT end resistance. *Proc. Institution of Civil Engineers*, *Geotechnical Engineering* **143**, 93-101.

Mair, R.J. (1993). Developments in geotechnical engineering research: application to tunnels and deep excavations. *Proceedings of Institution of Civil Engineers, Civil Engineering*, 27-41.

Manzari, M.T. and Dafalias, Y.F. (1997). A critical state two-surface plasticity model for sands. *Géotechnique* **47**, No. 2, 255-272.

Martin, C.M. and Houlsby, G.T. (2000). Combined loading of spudcan foundations on clay: laboratory tests. *Géotechnique* **50**, No.4, 325-338.

Martin, C.M. and Randolph, M.F. (2006). Upper-bound analysis of lateral pile capacity in cohesive soil. *Géotechnique* **56**, No.2, 141-145.

Matlock, H. (1970). Correlations for Design of Laterally Loaded Piles in Soft Clay. *Proceedings of the 2nd Annual Offshore Technology Conference*, OTC 1204, Houston, Texas, 577-588.

Meyer, B.J. and Reese, L.C. (1979). Analysis of Single Piles Under Lateral Loading. Research Report 244-1, Center for Transportation Research, Bureau of Engineering Research, University of Texas at Austin, Austin, TX.

Murff, J.D. and Hamilton, J.M. (1993). P-ultimate for undrained analysis of laterally loaded piles. *Journal of Geotechnical Engineering* **119**, No.1, 91-107.

NREL, National Renewable Energy Laboratory. (2012). 2010 Cost of Wind Energy Review. Technical report. Available at: http://www.nrel.gov/docs/fy12osti/52920.pdf. Last accessed March 2016.

O'Neill, M.W. and Murchison, J.M. (1983). An Evaluation of *p-y* Relationships in Sands. Research report No. GT-DF02-83, Department of Civil Engineering, University of Houston, Houston, Texas.

Peralta, P. (2010). Investigations on the behavior of large diameter piles under long-term lateral cyclic loading in cohesionless soil. PhD thesis, Leibniz University Hannover.

PISA AWG (Academic Work Group). (2014a). Draft Design Methodology, report of PISA project, DONG Energy document, (Confidential).

PISA AWG (Academic Work Group). (2014b). Draft Sand Design Methodology, report of PISA project, DONG Energy document, (Confidential).

PISA AWG (Academic Work Group). (2016). Draft PISA Final report, report of PISA project, DONG Energy document, (Confidential).

Potts, D.M. and Zdravković, L. (1999). Finite element analysis in geotechnical engineering: theory. London, Thomas Telford.

Potts, D.M. and Zdravković, L. (2001). Finite element analysis in geotechnical engineering: application. London, Thomas Telford.

Poulos, H.G. and Davis, E.H. (1980). Pile Foundation Analysis and Design. John Wiley & Sons Australia.

Poulos, H.G. and Hull, T.S. (1989). The role of analytical mechanics in foundation engineering. *Foundation Engineering, Current Principals and Practices* (ASCE) **2**, 1578-1606.

Powell, J.J.M. and Butcher, A.P. (2003). Characterisation of a glacial clay till at Cowden, Humberside. *Characterisation and Engineering Properties of Natural Soils. Tan et al. eds.* Balkema, **2**, 983-1020.

Prasad, Y.V.S.N. and Chari. T.R. (1999) Lateral capacity of model rigid piles in cohesionless soils. *Soil and Foundations* **39** (2), The Japanese Geotechnical Society, 21-29.

Randolph, M.F., Carter, J.P. and Wroth, C.P. (1979). Driven piles in clay – the effects of installation and subsequent consolidation. *Géotechnique* **29**, No.4, 361-393.

Randolph, M.F. and Wroth, C.P. (1979). An analytical solution for the consolidation around a driven pile. *International Journal for Numerical and Analytical Methods in Geomechanics* **3**, 217-229.

Randolph, M.F. and Houlsby, G.T. (1984). The limiting pressure on a circular pile loaded laterally in cohesive soil. *Géotechnique* **34**, No.4, 613-623.

Randolph, M. and Gourvenec, S. (2011). Offshore Geotechnical Engineering. 2 Park Square, Milton Park, Abingdon, Oxon OX14 4RN: Spon Press.

Reese, L.C. and Matlock, H. (1956). Non-dimensional solutions for laterally loaded piles with soil modulus assumed proportional to depth. *Proceedings of 8th Texas Conference Soil Mechanics and Foundation Engineering*, University of Texas.

Reese, L.C., Cox, W.R. and Koop, F.D. (1974). Analysis of Laterally Loaded Piles in Sand. *Proceedings of the 6th Offshore Technology Conference*, paper No. OTC 2080, Houston, Texas, 473-483.

Reese, L.C. and Cox, W.C. (1975). Field Testing and Analysis of Laterally Loaded Piles in Stiff Clay, *Proceedings of the 7th Offshore Technology Conference*, paper No. OTC 2312, Houston, Texas, 671-690.

Reese, L.C., Allen, J.D. and Hargrove, J.Q. (1981). Laterally loaded piles in layered soils. *Proc. 10th. Int. Conf. Soil Mech. And Found. Engrg*. Stockholm: A.A. Balkema, **2**, 819-822.

Reese, L.C. (1997). Analysis of laterally loaded piles in weak rock. *J. Geotech. Geoenv. Engng. Am. Soc. Civ. Engrs.* **123**, No.11, 1010-1017.

Reese, L.C., Wang, S.T., Isenhower, W.M. and Arrellage, J.A. (2004). Computer program LPILE plus version 5.0 user's manual. Ensoft, Inc., Austin, Texas.

RenewableUK. (2015). Available at: http://www.renewableuk.com/en/renewable-energy/wind-energy/offshore-wind/index.cfm. Last accessed March 2016.

Rojsberg, S. and Gravesen, H. (2009). OWA Offshore Wind Farm Foundations, UK Round 3, Design Basis, Version 1, Grontmij Carl Bro.

Smith, T. (1987). Pile Horizontal Soil Modulus Values. *J. Geotech. Engrg.*, **113** (9), 1040–1044.

Taborda, D.M.G., Zdravković, L., Kontoe, S., and Potts, D.M. (2014). Computational study on the modification of a bounding surface plasticity model for sands. *Computers and Geotechnics* **59**, 145-160.

Tsiampousi, A., Zdravković, L. and Potts, D.M. (2013). A new Hvorslev surface for critical state type unsaturated and saturated constitutive models. *Computers and Geotechnics* **48**, 156-166.

The Crown Estate. (2012). Offshore Wind Cost Reduction Pathways Study. Available at: http://www.thecrownestate.co.uk/media/5493/ei-offshore-wind-cost-reduction-pathways-study.pdf. Last accessed March 2016.

Vesić, A.B. (1961). Beams on Elastic Subgrade and Winkler's Hypothesis. *Proceedings of the 5th International Conference on Soil Mechanics and Foundation Engineering*, Paris, 845-850.

Winkler, E. (1867). Die Lehre Von Elasticitaet Und Festigkeit. 1st Edn., H. Dominicus, Prague.

Wroth, C.O. and Houlsby, G.T. (1985). Soil mechanics – property characterisation and analysis procedure. *Proceedings 11th International Conference on Soil Mechanics and Foundation Engineering*. San Francisco, No.1, 1-50.

Yang, Z.X., Jardine, R.J., Zhu, B.T., Foray, P. and Tsuha, C.H.C. (2010). Sand grain crushing and interface shearing during displacement pile installation in sand. *Géotechnique* **60**, No.6, 469-482.

Yang, Z. and Jeremić, B. (2002). Numerical analysis of pile behaviour under lateral loads in layered elastic-plastic soils. *International Journal of Numerical Analytical Method Geomechanics* **26**, 1385-1406.

Zdravković, L., Taborda, D.M.G., Potts, D.M., Jardine, R.J., Sideri, M., Schroeder, F.C., Byrne, B.W., McAdam, R., Burd, H.J., Houlsby, G.T., Martin, C.M., Gavin, K., Doherty, P., Igoe, D., Muir Wood, A., Kallehave, D. and Skov Gretlund, J. (2015). Numerical modelling of large

diameter piles under lateral loading for offshore wind applications. *Proc. 3rd International Symposium on Frontiers in Offshore Geotechnics* (ISFOG 2015). Oslo, Norway, 759-764.

Zienkiewicz, O.C., Taylor, R.L. and Zhu, J.Z. (2005). The Finite Element Method Its Basis and Fundamentals. Elsevier Ltd.

Zhang, L., Silva, F. and Grismala, R. (2005). Ultimate Lateral Resistance to Piles in Cohesionless Soils. *Journal of geotechnical and geoenvironmental engineering (ASCE)* **131** (1), 78-83.